UNIVERSIDADE DE SÃO PAULO
ESCOLA POLITÉCNICA

DAIANE IGLESIA DOLCI

Adjoint-based stability and sensitivity analyses applied for fluid flow and fluid-structure interaction problems

São Paulo,
2020

DAIANE IGLESIA DOLCI

Adjoint-based stability and sensitivity analyses applied for fluid flow and fluid-structure interaction problems

Revised version

Doctor's thesis presented to Escola Politécnica da Universidade de São Paulo in fulfillment of the requeriments for the Doctor of Science degree.

Area: Mechanical Engineering of Energy and Fluids.
Supervisor: Prof. Dr. Bruno Souza Carmo

São Paulo,
2020

Este exemplar foi revisado e corrigido em relação à versão original, sob responsabilidade única do autor e com a anuência de seu orientador.

São Paulo, ______ de ____________________ de __________

Assinatura do autor: ________________________

Assinatura do orientador: ________________________

Catalogação-na-publicação

Iglesia Dolci, Daiane
Adjoint-based stability and sensitivity analyses applied for fluid flow and fluid-structure interaction problems / D. Iglesia Dolci -- versão corr. -- São Paulo, 2020.
165 p.

Tese (Doutorado) - Escola Politécnica da Universidade de São Paulo. Departamento de Engenharia Mecânica.

1.Adjoint-based sensitivity analysis 2.Linear stability analysis 3.Bifurcation 4.Fluid-structure interaction I.Universidade de São Paulo. Escola Politécnica. Departamento de Engenharia Mecânica II.t.

Acknowledgements

Firstly my acknowledgement to God.

My sincere gratitude to my supervisor Bruno Souza Carmo by support, by comprehension, and by assisting me in the development of this research. Also, I thank him for his trust and patience. For sure, he was and is very important in my growth and maturity as a researcher. I would also like to thank Rafael Gioria for his patience and for helping me in the first steps of this research.

My heartfelt thanks to my boyfriend, and partner Vagner. I thank him by the love, by understanding me, by the support and by sharing the hard and happy moments in these last years.

To my mother, who is responsible for personal formation and education. She supported me and gave me love in all the moments of my life.

To my dear friend/sister Roberta, even far away, I know that she is with me, always cheering.

I cannot forget to thank my supervisor in the master's degree stage Gilcilene. She introduced me to the research and was responsible by made me discover a love for computational fluid mechanics.

I would like to thank the professors and colleagues from NDF (Fluid Dynamics lab). Mainly my dears João, Patino, and Sara. I thank them for understanding the stress days, by helping me and for sure for the relaxing moments.

To the professors and also to the friends that I did at Pós-MAC. I hold great affection for them, mainly for Hemily (Emilia), Marília (Mah) and José (Zezinho).

To my dear friends from UEMS, they were really important to me. I thank professor Luiz Orestes Cauz, who introduced me the applied mathematics. I also thank professor Wilson Barbosa da Costa by incentivizing me to the entrance in the researcher's career.

Abstract

This thesis focuses on numerical computations of adjoint-based stability and sensitivity analyses for fluid flow and fluid-structure interaction problems. Nektar++ was the software used in the simulations, which is based in Spectral/*hp* Element Method. New results of the adjoint-based sensitivity with respect to non-geometric variables (Reynolds number, inlet velocity and external forcing) for internal and external steady flows are introduced. To verify this methodology, comparisons with data obtained by other methods to provide sensitivity measures (like central finite difference) are performed. The adjoint method showed to be applicable to compute the quantitative sensitivities. For global linear analysis, adjoint-based stability and sensitivity methodology are first reviewed for fluid flow problems. Numerical simulations are carried out and verified for the flow around a fixed circular cylinder. Next, this thesis introduces a theoretical extension of stability and sensitivity analyses for fluid-structure interaction (FSI) systems. The displacement of the structure is governed by the linear mass-spring-damper equation, and the structure and flow equations are coupled using the non-inertial frame of reference method. The linearization of the FSI system is carried out using the *transpiration* approach and the Newmark-*beta* solver is used to integrate the mass-spring-damper system in time. Stability and sensitivity analyses are carried out from generalized eigenvalues problems solved by the Arnoldi method.

A review of the main recent results of linear stability analysis for an elastically-mounted cylinder is presented. Next, adjoint-based receptivity and sensitivity analyses are applied for this FSI problem. New sensitivity analyses with respect to external forcing are performed. In all the cases, comparisons with the sensitivity results for the flow around a fixed cylinder are made. The fields of receptivity and sensitivity show different configurations. Based on the results from the sensitivity analysis to a steady forcing, simulations of the flow subject to open-loop control are carried out. The steady forcing is proportional to the square of the base flow velocity, which is a forcing similar to the insertion of a small cylinder in the domain. The conclusion is that an elastically-mounted cylinder may respond differently than the fixed cylinder, where can happen cases in which the insertion of an external forcing at a point of the domain stabilizes the flow system. On the other hand, this same forcing can induce a higher growth rate of the least stable mode of the FSI system.

This thesis also investigates the character of the primary bifurcation for an oscillating elastically-mounted cylinder. Analyzing the bifurcation around a critical Reynolds number, it is noticed that the nonlinear character of the bifurcation changes completely for some cases, when compared to what is observed for a fixed cylinder. In these cases, the bifurcation is subcritical, while for a fixed cylinder it is supercritical. Finally, this work introduces calculations of optimal energy growth not yet assessed for Reynolds number (Re) below of the primary instability of the fixed cylinder ($Re < 47$). In this case, the results are also compared with those obtained for a fixed cylinder. The optimal energy of the fixed and elastically-mounted cylinders stays close. However, the optimal initial conditions of the fixed and elastically-mounted cylinders can be noticeably different.

Keywords: *Adjoint-based sensitivity, linear stability, bifurcation, elastically-mounted cylinder.*

Resumo

Esta tese atenta-se aos cálculos numéricos de análises de estabilidade e sensibilidade usando o método adjunto, onde as aplicaçoes são feitas para problemas de fluido-dinâmica e para um problema de interação fluido-estrutura. O software usado nas simulações numéricas foi o Nektar++, o qual é baseado no método de elementos espectrais/*hp*. Este trabalho começa com a introdução de formulaçoes matemáticas que fornecem resultados de sensibilidade em relação às variáveis não geométricas (número de Reynolds, velocidade de entrada e força externa). Os cálculos são aplicados para escoamentos estacionários internos e externos. As expressões matemáticas de sensibilidade calculadas pelo método adjunto são comparadas com as sensibilidades calculadas pelo método de diferenças finitas central, onde o método adjunto mostra-se capaz de fornecer cálculos quantitavos de sensibilidades para escoamentos estacionários. No contexto de análise linear global, inicialmente é feita uma revisão das metodologias de estabilidade e sensibilidade usando o método adjunto para problemas de fluid-dinâmica. Simulações numéricas para o escoamento em torno de um cilindro são apresentadas e verificadas a partir de comparações com resultados bem estabelecidos na literatura. Em seguida, esta tese introduz uma extensão teórica das análises de estabilidade e sensibilidade para sistemas de interação estrutura-fluido (IFS), num caso particular em que o movimento da estrutura é governado pela equação linear massa-mola-amortecedor. O acoplamento das equações da estrutura e do fluido é feito pelo método não inercial e a linearização do sistema de IFS é realizada usando a abordagem conhecida como *transpiration*. O método Newmark-*beta* solver é usado para calcular a solução do sistema massa-mola-amortecedor. As análises de estabilidade e sensibilidade são feitas resolvendo problemas de autovalor generalizado, o qual é solucionado pelo método de Arnoldi.

Uma revisão de recentes resultados de análise de estabilidade linear para um cilindro montado-elasticamente é apresentada. Em seguida, análises de receptividade e sensibilidade baseadas no método adjunto são aplicadas para esse problema de IFS, onde novas análises de sensibilidade com relação a uma força externa são feitas. Em todos os casos são realizadas comparações com os resultados de sensibilidade para o escoamento em torno de um cilindro fixo, observando-se que os campos de receptividade e sensibilidade mostram diferentes configurações. Com base nos resultados de análise de sensibilidade em relação a uma força constante, são feitas simulações considerando que o sistema de IFS

está sujeito a um controle passivo, onde aplica-se uma força constante proporcional ao quadrado da velocidade do campo base. Esta modelagem da força é similar à inserção de um pequeno cilindro no domínio computacional. Nesta configuracão, conclui-se que um cilindro montado-elasticamente pode responder de forma diferente do cilindro fixo, isto é, podem ocorrer casos em que a inserção de uma força externa em um ponto do domínio estabiliza o sistema de escoamento, mas por outro lado, essa mesma força pode induzir a uma taxa de crescimento positiva do modo menos estável do sistema de IFS.

Esta tese também apresenta um estudo do caráter da bifurcação primária de um cilindro montado-elasticamente. Avaliando a bifurcação em torno de um número crítico de Reynolds, percebe-se que o caráter não linear da bifurcação muda completamente em alguns casos quando comparado ao que é observado no cilindro fixo. Nesses casos, a bifurcação do cilindro montado-elasticamente é subcrítica, enquanto para um cilindro fixo a bifurcação é supercrítica. Por fim, são feitos cálculos de crescimento ótimo da energia para números de Reynolds (Re) abaixo da instabilidade primária do cilindro fixo ($Re < 47$). Nesse casos, os resultados também são comparados com os aqueles obtidos para um cilindro fixo. A energias ótimas do cilindro fixo e do cilindro livre pra oscilar permanecem próximas. No entanto, as condições iniciais ótimas dos cilindro fixo e do montado-elasticamente podem ser notavelmente diferentes.

Palavras chaves: *Sensibilidade baseadas no método adjunto, estabilidade linear, bifurcação, interação fluid-estrutura.*

List of Symbols

$\mathbf{q}$ – State vector

$\mathbf{q}^\dagger$ – Adjoint vector

$\mathcal{J}$ – Objective functional

$\mathbf{f}$ – External forcing

Re – Reynolds number

m^* – Mass ratio (mass of the moving body divided by the mass of displaced fluid)

Re_{c_0} – Critical Reynolds of the flow around a fixed cylinder

$\mathbb{L}$ – Linearized Navier-Stokes operator

$\mathbb{L}^\dagger$ – Adjoint Navier-Stokes operator

Ω – Spatial domain

$\mathbf{x}$ – Spatial coordinates

t – time variable

τ – Period of time

ρ – Density

$\boldsymbol{\sigma}$ – Stress tensor

p – Pressure of nonlinear Navier-Stokes equations

$\mathbf{u}$ – Velocity of nonlinear Navier-Stokes equations

μ – Dynamic viscosity

$\mathbf{I}$ – Identity tensor

L – Reference length

U – Reference velocity

$\mathbb{N}(\mathbf{q})$ – non-dimensional nonlinear Navier-Stokes operator

$\mathcal{L}$ – Lagrangian functional

C_d – Drag coefficient

C_l – Lift coefficient

$\partial\Omega_w$ – Structure wall

$\partial\Omega_i$ – Structure inlet

$\partial\Omega_o$ – Structure outlet

$\partial\Omega$ – Boundary regions

$\mathbf{U}_c$ – Inlet velocity of the base flow

$\mathbf{U}$ – Velocity of the base flow

$\bar{\mathbf{U}}$ – Mean velocity

$\mathbf{U}_\infty$ – Stream velocity

$\mathbf{u}^\dagger$ – Adjoint velocity

P – Pressure of the base flow

$p^\dagger$ – Adjoint pressure

$\mathbf{n}$ – Unit outward normal vector

$\mathbf{e}_x$ – Unit vectors parallel to the x-axis

$\mathbf{e}_y$ – Unit vectors parallel to the y-axis

$\mathbf{q}'$ – Perturbation field

$\mathbf{v}'$ – Perturbation velocity

p' – Pressure velocity

$\mathbf{Q}$ – Base flow vector

λ – Eigenvalue

λ_1 – Less stable eigenvalue

$\widehat{\mathbf{q}}$ – Direct mode

$\widehat{\mathbf{q}}^{\dagger}$ – Adjoint mode

$\mathcal{B}$ – Bilinear concomitant

f_{st} – Strouhal frequency

D – Cylinder diameter

$\lambda_{1,r}$ – Real part of the less stable eigenvalue

$\lambda_{1,i}$ – Imaginary part of the less stable eigenvalue

$\mathbf{y}$ – Structure displacement

$\dot{\mathbf{y}}$ – Structure velocity

$\ddot{\mathbf{y}}$ – Structure acceleration

$\mathbf{u}_a$ – Absolute velocity in a nonlinear fluid-structure interaction problem

p_a – Absolute pressure in a nonlinear fluid-structure interaction problem

$\mathbb{E}$ – Perturbation energy

$\mathbf{x}_0$ – Equilibrium points of the a fluid structure problem

Ω_0 – Domain formed by equilibrium points $\mathbf{x}_0$

$\mathbf{u}'_a$ – Perturbation velocity in a nonlinear fluid-structure interaction problem

p'_a – Perturbation pressure in a nonlinear fluid-structure interaction problem

f_n – Natural frequency

V_r – Reduced velocity

ζ – Structural damping

$\mathbf{I}$ – Identity operator

List of Figures

List of Tables

Contents

Chapter

1 Introduction

The application of numerical techniques based on the adjoint method to perform stability, receptivity and sensitivity analyses has become common in fluid mechanics. Using these techniques, the flow fields can be characterized with respect to their stability, response to external forcing and to structural changes. Adjoint-based sensitivity analysis has a wide application in different physical problems. It was first applied for linear problems in nuclear reactor physics problem (Pendlebury, 1955), and later for aerodynamic design (Pironneau, 1974; Jameson, 1988), atmospheric phenomena (Hall & Cacuci, 1983) and commonly used in control theory (Gunzburger *et al.* , 1991; Gunzburger, 2003; Kim & Bewley, 2007; Marquet *et al.* , 2008; Meliga *et al.* , 2014). In fluid flow problems, adjoint-based stability and sensitivity analyses can provide guidance to help in the control of the vortex shedding (Marquet *et al.* , 2008), or control of the aerodynamic forces (Meliga *et al.* , 2014). Also, it can compute quantitative measures of sensitivity, like the variation of aerodynamic forces with respect to a non-geometric variable (Hayashi *et al.* , 2016), or be used in optimization problems, like finding the optimal energy of a linear perturbation (Blackburn *et al.* , 2008).

In a broad context, the sensitivity calculations assess the influence of one (or several) control variable(s) on one (or several) system output(s). Mathematically, this is done by calculating the gradient of the system parameter(s) with respect to the control variable(s). A way to perform these computations is by employing the adjoint method, which is particularly well-suited for cases in which the number of outputs is small and the number of control variables is large. In this thesis, the mathematical expressions of the adjoint-based sensitivity measures are obtained from a Lagrangian functional. A brief insight into this approach is introduced in the next section.

1.1 Adjoint-based sensitivity obtained by a Lagrangian functional

Based on the approach introduced by Cacuci (1981); Marquet *et al.* (2008); Meliga & Chomaz (2011), a way to carry out the sensitivity calculations is from the Lagrangian functional:

$$\mathcal{L}(\mathbf{q}, \mathbf{q}^{\dagger}, \mathbf{B}, \mathbf{B}^{\dagger}, \mathbf{I}_0, \mathbf{I}_0^{\dagger}, \alpha, \mathbf{f}) = \mathcal{J} - \langle \mathbf{q}^{\dagger}, \mathbf{S}(\mathbf{q}, \alpha) - \mathbf{f} \rangle - \langle \boldsymbol{B}^{\dagger}, \mathbf{B} \rangle - \langle \mathbf{I}_0^{\dagger}, \mathbf{I}_0 \rangle, \tag{1.1}$$

in which $\mathcal{J}$ is the objective functional, $\mathbf{q}$ represents the state vector, and α represents the parameters of a physical problem. The system $\mathbf{S}(\mathbf{q}, \alpha) - \mathbf{f} = \mathbf{0}$ represents the constraint that is enforced by the Lagrange multiplier $\mathbf{q}^{\dagger}$, where $\mathbf{f}$ represents an external forcing. The system $\mathbf{S}(\mathbf{q}, \alpha) - \mathbf{f} = \mathbf{0}$ satisfies the boundary conditions $\mathbf{B}$ and the initial conditions $\mathbf{I}_0$ that are explicitly enforced by $\mathbf{B}^{\dagger}$ and $\mathbf{I}_0^{\dagger}$, respectively. In some works, the boundary conditions and the initial conditions were not explicitly imposed as constraints in the Lagrangian functional (Marquet *et al.* , 2008; Meliga *et al.* , 2014). In this current case, the mathematical expressions of sensitivity are given by the gradient of the functional objective $\mathcal{J}$ with respect to the control variable, where the expression depends of the Lagrange multipliers also referred by adjoint variables. In this thesis, the control variables are non-geometric parameters which can be an external forcing $\mathbf{f}$, a parameter of the system α, the initial condition $\mathbf{I}_0$, or a boundary condition $\mathbf{B}$.

This thesis focuses on performing the adjoint-based stability and sensitivity analyses for fluid flow and fluid-structure interaction problems. Adjoint-based sensitivity is first used to verify its applicability on providing correct measures of aerodynamic forces sensitivity with respect to non-geometric variables for fluid flow problems. This way, the objective functional is the aerodynamic force and the control variables are the non-geometric variables: Reynolds number, inlet velocity and external forcing. The constraint of the Lagrangian functional is the non-linear Navier-Stokes system. In linear global analysis applied to a FSI system, this work introduces sensitivity with respect to external forcing and the sensitivity of optimal energy growth with respect to initial conditions. In the first case, the functional objective is the least stable eigenvalue and the control variable is an external forcing. In the second case, the functional objective is the perturbation energy, and the control variable is the initial condition. For both cases, the linearized FSI system appears as a constraint of the Lagrangian functional.

In the next sections, we will present a literature review of the main results of the adjoint-based stability and sensitivity analyses used as a theoretical base to perform the studies introduced in this thesis.

1.2 Adjoint-based stability and sensitivity in linear global analysis

Hydrodynamic stability theory is concerned with the response of a flow to a perturbation. In this context, if a laminar flow is subject to a small or moderate perturbation and returns to its original state, the flow is described as stable. Otherwise, the flow is described as unstable. Global linear stability analysis represents the most general form to study the instabilities of two and three-dimensional flows. This theory starts with the linearization of the Navier-Stokes equations around a base flow. Next, the linearized system is written as a generalized eigenvalue problem and modal analysis can be applied. In this case, the stability analysis is carried out by evaluating the eigenvalue of the least stable eigen-vector/direct modes. However, for some cases an asymptotically stable flow can exhibit non-negligible transient energy growth due to the non-normality of the linearized Navier-Stokes system (Chomaz, 2005; Schmid, 2007). Blackburn *et al.* (2008) showed that the optimal perturbation energy growth can be computed by a generalized eigenvalue problem, in which the optimal growth is given by the maximum singular value of the linearized Navier-Stokes operator $\mathbb{L}$, i.e., the maximum eigenvalue of the product of $\mathbb{L}$ by the its adjoint $\mathbb{L}^{\dagger}$. Mao *et al.* (2013) used an optimization approach to compute the optimal growth energy. The perturbation energy growth was the functional objective, and the initial condition was the control variable. Analogously to Blackburn *et al.* (2008), they showed that the optimal energy growth can be obtained from a generalized eigenvalue problem. The least stable eigenvalue gives the optimal energy and the least stable mode provides the optimal initial condition.

The non-normality of the linearized operator can also lead to a significant response or receptivity to external forcing (Trefethen *et al.* , 1993), and in a considerable sensitivity of the spectrum to perturbations (Chomaz, 2005). For fluid flow systems, several works have performed receptivity and sensitivity analyses using adjoint equations (Hill, 1992; Airiau *et al.* , 2002; Giannetti & Luchini, 2006, 2007; Giannetti *et al.* , 2010; Marquet *et al.* , 2008). Giannetti & Luchini (2007) were pioneers in the application of numerical techniques based on the direct and adjoint modes in sensitivity and receptivity analysis applied to open flows. The problem chosen was the flow around a circular cylinder with Reynolds number close to the primary instability of the flow. The authors identified the regions of the domain where the flow is more receptive to the presence of momentum forcing and mass injection. Besides that, based on the spatial distribution of the product between the direct and adjoint least stable eigen-vectors/modes, they identified the regions that are more sensitive to structural changes. Later on, Marquet *et al.* (2008) introduced eigenvalue sensitivity analysis with respect to a steady forcing imposed in the steady base flow. The Lagrangian functional was used to obtain the adjoint system and the mathematical expression of sensitivity. In those works (Giannetti & Luchini, 2007; Marquet *et al.* , 2008), the adjoint variables/Lagrange multipliers were the key tool for the receptivity and sensitivity analysis.

Although there are important results of stability, receptivity and sensitivity analysis for fluid flow problems in the literature, for fluid-structure interaction (FSI) problems, the studies are recent and still scarce. In the last few years, linear stability analysis has been employed for vortex-induced vibration (VIV) problems. Cossu & Morino (2000) were the first to apply this tool for the flow around a flexibly-mounted circular cylinder. They calculated the threshold for the primary instability to be $Re = 23.5$ for non-dimensional mass ratios (mass of the moving body divided by the mass of displaced fluid) $m^* = 7$ and $m^* = 70$ with the cylinder free to oscillate in the transverse direction. For a fixed cylinder, the primary bifurcation critical Reynolds number is $Re_{c_0} = 46.8$ (Jackson, 1987). Besides finding the critical Reynolds number, Cossu & Morino (2000) identified two unstable modes, referred in that work as nearly-structural and von-Kármán modes. For large mass ratio, m^*, the eigenvalue of the nearly-structural mode tended to the natural frequency of the structure and the eigenvalues of the von-Kármán mode corresponded to the leading eigenvalues of the flow past a fixed cylinder. More than one decade later, Meliga & Chomaz (2011), Zhang *et al.* (2015), Navrose & Mittal (2016), Yao & Jaiman (2017) and J. Kou & Li (2017) also showed results that confirmed instability for $Re < Re_{c_0} = 47$. Meliga & Chomaz (2011) presented a mapping of stable and unstable regions with respect to the parameter m^* for flow past a circular cylinder free to oscillate in both the transverse and in-line directions. Recently, Pfister *et al.* (2019) applied stability analysis for a flow around a circular cylinder with an attached elastic plate, for a flag immersed in a channel flow and a three-dimensional flexible plate perpendicular to the flow direction. In that work, the FSI system was formulated with Arbitrary Lagrangian-Eulerian (ALE) method. Its linearization was performed using the *transpiration* approach, which consists on writing the velocity and pressure at the boundary of the structure as an approximation around an equilibrium point. This *transpiration* approach in linear stability analysis of an FSI problem was first used by Fernández & Tallec (2002, 2003). Recently, Negi *et al.* (2019) also used the *transpiration* approach in stability analysis applied for a rotating circular cylinder with an attached splitter plate. Results of structural sensitivity were also introduced for an oscillating circular cylinder.

Receptivity and sensitivity analyses to external forcing applied to FSI problems have not yet been published in the literature. Bearing this in mind and departing from the previous developments and results of linear stability analysis of FSI problems, this thesis introduces a methodology and presents results of receptivity and sensitivity applied to low Reynolds number flow around an elastically-mounted circular cylinder. We compare the receptivity and sensitivity fields with the results obtained for a fixed cylinder. For this same FSI problem, calculations of optimal energy growth (receptivity of energy perturbation to initial conditions) are also introduced for $Re < 47$. Besides that, we also present a non-linear analysis, used to investigate the character of the primary bifurcation for the flow around a flexibly-mounted circular cylinder.

1.3 Adjoint-based sensitivity of the aerodynamic forces

Aerodynamic forces sensitivity using the adjoint method has been applied in control of the drag and lift forces. In previous works (Meliga *et al.* , 2014; Mao, 2015; Meliga *et al.* , 2018) the control variable was an external forcing. In Meliga *et al.* (2014), the sensitivity analysis was applied to a flow around fixed square and circular cylinders. In those works, the authors calculated the aerodynamic forces sensitivity with respect to variations of an external forcing applied in a localised point of the domain. The objective was to apply a force to decrease the drag force. Mao (2015) applied sensitivity calculations to a flow around a fixed airfoil, with the purpose of investigating the drag and lift sensitivity with respect to a surface forcing. Hayashi *et al.* (2016) introduced a method to calculate aerodynamic force sensitivity with respect to non-geometric control variables. The computations of sensitivity were applied for a two-dimensional channel flow, and the control variable was the Reynolds number. In that work, the calculations of sensitivity given by the adjoint method were verified by comparing with the sensitivity computed by the finite difference method. In this thesis, we applied calculations of sensitivity with respect to non-geometric variables for internal and external steady flows. Here, we want to verify the applicability of the adjoint-based sensitivity in providing correct measures. The control variables are the inlet velocity and Reynolds number. The fluid flow problems chosen were the fully-developed channel flow and backward-facing step flow for internal flows. For external flows, we applied the methodology for the flow around a flat plate parallel to the streamwise direction, square cylinder and NACA 0012 airfoil.

1.4 Outline of this thesis

Chapter 2 introduces the mathematical formulation to obtain measures of sensitivity of aerodynamic forces for steady base flows. Applications of this sensitivity are presented in the chapter 3. In most cases, the results of sensitivity measures are compared with the sensitivity computation using the finite differences method.

In the theory of global linear analysis, the methodology to calculate sensitivity is extended for a fluid-structure interaction system. To this end, a theoretical study of the analyses of stability, receptivity, and sensitivity for a fluid flow system was carried out and presented in chapter 4. Applications for the flow around a fixed cylinder are also presented in this chapter, with two objectives: of verifying the numerical methodology and to produce results which serve as benchmark for comparison against those obtained for the flow around an elastically-mounted cylinder (presented in chapter 6).

Chapter 5 delineates the mathematical formulation used to perform the stability and sensitivity analyses for flows around elastically-mounted bodies. We describe the Navier-Stokes equations coupled to a mass-spring-damper system and employ the non-inertial frame of reference method. Besides that, a mathematical formulation to obtain the linearized and adjoint FSI systems and the sensitivity measures are introduced. In chapter 6, these methods are applied in the flow around an elastically-mounted cylinder. We first present a review covering the main results from stability analysis for this kind of FSI problem. Next, we present a numerical verification of the adjoint system solution, by comparing its eigenvalues with the eigenvalues of the direct FSI system. Lastly, results of sensitivity analysis are presented and compared with sensitivity analyses for the flow around a fixed cylinder. In chapter 7, computations to assess the character of the primary bifurcation in the flow around fixed and elastically-mounted cylinders are shown, as well as computations of optimal energy growth for same FSI problem.

Finally, in chapter 8 we draw conclusions and suggest future works that could follow from this research. Figure 2 displays a chart illustrating the organization of this thesis. The asterisks indicate the new contributions of this thesis to the state-of-the-art.

The numerical simulations reported in this thesis were performed using the Nektar++ software, which is an open-source code which implements the Spectral/*hp* Element Method (Karniadakis & Sherwin, 2005). Appendix A.1 shows a concise description of this method. The Newmark-*beta* solver was used to integrate the mass-spring-damper system in time is also described in Appendix A, specifically in the section A.2. For low values of mass ratio and damping, we used the fictitious mass-damping method. A brief insight into it is described in section A.3. The Arnoldi method, used to solve the generalized eigenvalue problems, is described in Appendix B. In Appendix C, details about the computational meshes used in this thesis are presented. In this same appendix, we show the results from a mesh convergence analysis that was carried out for the flow around a fixed circular cylinder.

Figure 2: Organizational diagram of this thesis.

Chapter

2

Sensitivity of aerodynamic forces: Mathematical formulation

In this chapter, we present the mathematical formulations employed to calculate the sensitivity of aerodynamic forces with respect to a non-geometric parameters. We start by defining the constraint that is given by the governing equations for incompressible viscous flows, which constitute the nonlinear Navier-Stokes operator. Next, we introduce a general Lagrangian functional used to set the mathematical expressions to compute the aerodynamic sensitivities. The mathematical methodology introduced in this chapter is based in the Meliga *et al.* (2014, 2018). All the equations (Navier-Stokes and adjoint) are defined in a three-dimensional domain Ω, i. e, $\Omega \subset \mathbb{R}^3$.

2.1 Navier-Stokes equations

In this work, we consider incompressible and viscous flows, which are governed mathematically by the Navier-Stokes equations. They are written in dimensional form as

$$\begin{aligned} \nabla \cdot \mathbf{u}^* &= 0, && (2.1)\\ \rho\left(\frac{\partial \mathbf{u}^*}{\partial t} + \nabla\mathbf{u}^* \cdot \mathbf{u}^*\right) - \nabla\boldsymbol{\sigma}^* &= \mathbf{0}. && (2.2) \end{aligned}$$

The vector $\mathbf{u}^* = \mathbf{u}^*(\mathbf{x}^*, t^*)$ represents the velocity field, which depends on the spatial coordinates $\mathbf{x}^* \in \Omega$ and time $t^* \in [0, \tau] \subset \mathbb{R}$, ρ is the density and $\boldsymbol{\sigma}^*$ is the stress tensor. For Newtonian fluids, $\boldsymbol{\sigma}^*$ is written as

$$\boldsymbol{\sigma}^* = \mu\left[\nabla\mathbf{u}^* + (\nabla\mathbf{u}^*)^T)\right] - p^*\mathbf{I},$$

in which p^* is the pressure, the parameter μ represents the dynamic viscosity and $\mathbf{I}$ is the identity tensor.

In order to express equations (2.1)-(2.2) in non-dimensional form, we define the following non-dimensional variables:

$$\mathbf{x} = \frac{\mathbf{x}^*}{L}, \quad \mathbf{u} = \frac{\mathbf{u}^*}{U}, \quad t = \frac{t^* U}{L}, \quad p = \frac{p^*}{\rho U^2},$$

where L and U are the reference values for length and velocity, respectively. Substituting these non-dimensional variables in (2.1)-(2.2) and writing in a convenient form, we have the non-dimensional Navier-Stokes equations:

$$\nabla \cdot \mathbf{u} = 0, \tag{2.3}$$

$$\frac{\partial \mathbf{u}}{\partial t} + \nabla \mathbf{u} \cdot \mathbf{u} - \nabla \boldsymbol{\sigma} = \mathbf{0}. \tag{2.4}$$

The non-dimensional stress tensor $\boldsymbol{\sigma}$ is:

$$\boldsymbol{\sigma}(\mathbf{u}, p) = \frac{1}{Re}\left[\nabla \mathbf{u} + (\nabla \mathbf{u})^T)\right] - p\mathbf{I}.$$

The non-dimensional parameter $Re = \rho U L/\mu$ is the Reynolds number and $\mathbf{I}$ is the identity operator.

2.2 Lagrangian functional

The expressions of the sensitivity are obtained using the Lagrangian functional:

$$\mathcal{L}(\mathbf{q}, \mathbf{q}^\dagger, \mathbf{B}^\dagger, \mathbf{c}) = \mathcal{J} - \langle \mathbf{q}^\dagger, \mathbb{N}(\mathbf{q}) - \mathbf{f} \rangle - \langle \mathbf{B}^\dagger, \mathbf{B} \rangle_{\partial\Omega}. \tag{2.5}$$

Here, the objective functional, $\mathcal{J}$, is given by one of the aerodynamic force coefficients:

$$C_d = 2\int_{\partial\Omega_w} \{\boldsymbol{\sigma}(p, \mathbf{u}) \cdot \mathbf{n}\} \cdot \mathbf{e}_x \, \mathrm{d}S, \tag{2.6}$$

$$C_l = 2\int_{\partial\Omega_w} \{\boldsymbol{\sigma}(p, \mathbf{u}) \cdot \mathbf{n}\} \cdot \mathbf{e}_y \, \mathrm{d}S, \tag{2.7}$$

where C_d is the drag coefficient, C_l is the lift coefficient, $\partial\Omega_w$ denotes the structure wall, $\mathbf{n}$ indicates unit outward normal vector, $\mathbf{e}_x$ and $\mathbf{e}_y$ are unit vector parallel to the x and y axes, respectively. The control parameter is denoted by $\mathbf{c}$, and it can be a vector or a scalar. The constraints are given by the steady forced Navier-Stokes system

$$\mathbb{N}(\mathbf{q}) - \mathbf{f} = \begin{cases} \nabla \mathbf{u} \cdot \mathbf{u} - \nabla \boldsymbol{\sigma}(p, \mathbf{u}) - \mathbf{f} = \mathbf{0}, \\ \nabla \cdot \mathbf{u} = 0, \end{cases} \tag{2.8}$$

and their boundary conditions $\mathbf{B}(\mathbf{u}, p)$. The vector $\mathbf{q}^\dagger = [\mathbf{u}^\dagger, p^\dagger]^T$ and $\mathbf{B}^\dagger$ are the Lagrange multipliers, and well-know as adjoint variables. For steady flow $\mathbf{u} = \mathbf{u}(\mathbf{x})$, $p = p(\mathbf{x})$, and the inner product $\langle \cdot \rangle$ is defined as the integral $\int_\Omega \cdot \mathrm{d}\mathcal{V}$, in which Ω represents the spatial domain. The inner product $\langle \cdot \rangle_{\partial\Omega}$ is the integral $\int_{\partial\Omega} \cdot \mathrm{d}S$ over the boundary regions of the domain $\partial\Omega$. The methodology to obtain the sensitivity expressions is based on the approach introduced by Meliga *et al.* (2014, 2018). However, in this current case, the flow boundary conditions are also explicitly imposed as constraints in the Lagrangian functional.

In this work, the external forcing $\mathbf{f}$, Reynolds number Re and inlet velocity $\mathbf{U}_c$ are the control parameters used in the sensitivity studies. We will introduce the procedure to obtain the sensitivity of the drag force only (i.e., the drag force is the objective functional). Due to similarity, the process to obtain the sensitivity of the lift force is omitted.

2.3 Sensitivity to an external forcing

In the optimization problem (2.5) adapted to compute the drag sensitivity with respect to an external forcing. So the control variable $\mathbf{c} = \mathbf{f}$. The objective functional is given by the drag coefficient, expression (2.6). To compute the sensitivity, we start by inroducing the gradient of the Lagrangian functional, which at an optimal case is zero.

In this work, the gradient of the Lagrangian functional with respect to any variable s is given by the Gateaux derivative:

$$\frac{\partial \mathcal{L}}{\partial s} = \lim_{\epsilon \to 0} \frac{\mathcal{L}(s + \epsilon \delta s) - \mathcal{L}(s)}{\epsilon}. \tag{2.9}$$

So computing the derivative $\dfrac{\partial \mathcal{L}}{\partial \mathbf{q}^\dagger}$, we get:

$$\frac{\partial \mathcal{L}}{\partial \mathbf{q}^\dagger} = \lim_{\epsilon \to 0} \frac{\int_\Omega (\mathbf{q}^\dagger + \epsilon \delta \mathbf{q}^\dagger) \cdot (\mathbb{N}(\mathbf{q}) - \mathbf{f}) - \mathbf{q}^\dagger \cdot (\mathbb{N}(\mathbf{q}) - \mathbf{f})\, \mathrm{d}\mathcal{V}}{\epsilon} = \int_\Omega \delta \mathbf{q}^\dagger \cdot (\mathbb{N}(\mathbf{q}) - \mathbf{f}) \mathrm{d}\mathcal{V} = 0.$$

Therefore, the derivative $\dfrac{\partial \mathcal{L}}{\partial \mathbf{q}^\dagger} \delta \mathbf{q}^\dagger = 0$ is true if $\mathbb{N}(\mathbf{q}) - \mathbf{f} = \mathbf{0}$ for all $\mathbf{x}$ in the domain Ω. Analogously, the boundary conditions of the base flow are enforced by the calculating the derivative $\dfrac{\partial \mathcal{L}}{\partial \mathbf{B}^\dagger} \delta \mathbf{B}^\dagger$ and making it equal to zero.

2.3.1 Adjoint system

As was said in chapter 1, the expression of the sensitivity derived with the adjoint method is a function of the Lagrange multiplier that is the solution of an adjoint system. To determine the adjoint system, we calculate $\dfrac{\partial \mathcal{L}}{\partial \mathbf{q}} \delta \mathbf{q} = 0$. To apply the Gateaux derivative, first we write the Lagrangian functional $\mathcal{L}(\delta\mathbf{q}, \mathbf{q}^\dagger, \mathbf{B}^\dagger, \mathbf{f})$:

$$\begin{aligned}\mathcal{L}(\delta\mathbf{q}, \mathbf{q}^\dagger, \mathbf{B}^\dagger, \mathbf{f}) =& 2\int_{\partial\Omega_w} \{\boldsymbol{\sigma}(\delta\mathbf{u}, \delta p)\cdot\mathbf{n}\}\cdot\mathbf{e}_x \,\mathrm{d}S - \int_\Omega p^\dagger(\nabla\cdot\delta\mathbf{u})\,\mathrm{d}\mathcal{V} - \int_{\partial\Omega}\mathbf{B}^\dagger\cdot\delta\mathbf{B}\,\mathrm{d}S \\ &- \int_\Omega \mathbf{u}^\dagger\cdot\left(\nabla\mathbf{u}\cdot\delta\mathbf{u} + \mathbf{u}\cdot\nabla\delta\mathbf{u} - \frac{1}{Re}\nabla^2\delta\mathbf{u} + \nabla\delta p\right)\mathrm{d}\mathcal{V}\end{aligned}$$

On applying integral by parts in the domain integrals and after that the Divergence Theorem in the boundary integrals, we achieved:

$$\begin{aligned}\mathcal{L}(\delta\mathbf{q}, \mathbf{q}^\dagger, \mathbf{B}^\dagger, \mathbf{f}) =& \underbrace{-\int_\Omega\left(-\mathbf{u}\cdot\nabla\mathbf{u}^\dagger + \nabla\mathbf{u}\cdot\mathbf{u}^\dagger - \frac{1}{Re}\nabla^2\mathbf{u}^\dagger - \nabla p^\dagger\right)\cdot\delta\mathbf{u} + (\nabla\cdot\mathbf{u}^\dagger)\delta p\,\mathrm{d}\mathcal{V} +}_{I} \\ &\underbrace{-\int_{\partial\Omega_w}\left(2\mathbf{e}_x - \mathbf{u}^\dagger\right)\cdot\{-\boldsymbol{\sigma}(\delta\mathbf{u}, \delta p)\cdot\mathbf{n}\} + \delta\mathbf{u}\cdot\left\{\boldsymbol{\sigma}(-p^\dagger, \mathbf{u}^\dagger)\cdot\mathbf{n} + (\mathbf{u}\cdot\mathbf{n})\mathbf{u}^\dagger\right\}\mathrm{d}S+}_{II} \\ &\underbrace{-\int_{\partial\Omega_{i,o}}\left[(\mathbf{u}\cdot\mathbf{n})\,\mathbf{u}^\dagger + p^\dagger\mathbf{I}\cdot\mathbf{n} + \left(Re^{-1}\nabla\mathbf{u}^\dagger\right)\cdot\mathbf{n}\right]\cdot\delta\mathbf{u}\,\mathrm{d}S}_{III} \\ &\underbrace{+\int_{\partial\Omega_{i,o}}\mathbf{u}^\dagger\cdot\left(\delta p\mathbf{I} - Re^{-1}\nabla\delta\mathbf{u}\right)\cdot\mathbf{n}\,\mathrm{d}S}_{IV} - \int_{\partial\Omega}\mathbf{B}^\dagger\cdot\delta\mathbf{B}\,\mathrm{d}S\end{aligned}$$

From the term I, we set the steady adjoint system:

$$\mathbb{A}(\mathbf{u})\mathbf{q}^\dagger = \begin{cases} \nabla\cdot\mathbf{u}^\dagger = 0 \\ -\nabla\mathbf{u}^\dagger\cdot\mathbf{u} + \nabla\mathbf{u}\cdot\mathbf{u}^\dagger - \dfrac{1}{Re}\nabla^2\mathbf{u}^\dagger - \nabla p^\dagger = \mathbf{0}. \end{cases} \tag{2.10}$$

To solve this system, we have to impose boundary conditions. Assuming the boundary condition $\mathbf{u}^\dagger\cdot\mathbf{n} = 2\mathbf{e}_x$ at the wall ($\partial\Omega_w$), the term II is annulled, and $\dfrac{\partial\mathcal{L}}{\partial\mathbf{q}}\delta\mathbf{q}$ is reduced to:

$$\begin{aligned}\mathcal{L}(\delta\mathbf{q}, \mathbf{q}^\dagger, \mathbf{B}^\dagger, \mathbf{f}) =& \underbrace{-\int_{\partial\Omega_{i,o}}\left[(\mathbf{u}\cdot\mathbf{n})\,\mathbf{u}^\dagger + p^\dagger\mathbf{I}\cdot\mathbf{n} + \left(Re^{-1}\nabla\mathbf{u}^\dagger\right)\cdot\mathbf{n}\right]\cdot\delta\mathbf{u}\,\mathrm{d}S}_{III} \\ &\underbrace{+\int_{\partial\Omega_{i,o}}\mathbf{u}^\dagger\cdot\left(\delta p\mathbf{I} - Re^{-1}\nabla\delta\mathbf{u}\right)\cdot\mathbf{n}\,\mathrm{d}S}_{IV} - \int_{\partial\Omega}\mathbf{B}^\dagger\cdot\delta\mathbf{B}\,\mathrm{d}S\end{aligned}$$

In this work, the boundary conditions of the base flow are:

- Inlet ($\partial\Omega_i$): $\mathbf{u} = \mathbf{U}_c$;
- Outlet ($\partial\Omega_o$): $\nabla\mathbf{u}\cdot\mathbf{n} = p = \mathbf{0}$.
- Wall ($\partial\Omega_w$): $\mathbf{u} = \mathbf{0}$;

Therefore, the operator $\mathbf{B}$ at inlet, outlet and wall is given respectively by:

$$\mathbf{B}_i = \mathbf{U}_c, \quad \mathbf{B}_o = \nabla\mathbf{u}\cdot\mathbf{n} = \mathbf{0}, \quad \mathbf{B}_w = \mathbf{u} = \mathbf{0},$$

and $\dfrac{\partial\mathcal{L}}{\partial\mathbf{q}}\delta\mathbf{q}$ can be rewritten as:

$$\begin{aligned}\mathcal{L}(\delta\mathbf{q},\mathbf{q}^\dagger,\mathbf{B}^\dagger,c) = &-\underbrace{\int_{\partial\Omega_{i,o}}\left[(\mathbf{u}\cdot\mathbf{n})\,\mathbf{u}^\dagger + p^\dagger\mathbf{I}\cdot\mathbf{n} + \left(Re^{-1}\nabla\mathbf{u}^\dagger\right)\cdot\mathbf{n}\right]\cdot\delta\mathbf{u}\,\mathrm{d}S}_{III}\\ &+\underbrace{\int_{\partial\Omega_{i,o}}\mathbf{u}^\dagger\cdot\left(\delta p\mathbf{I} - Re^{-1}\nabla\delta\mathbf{u}\right)\cdot\mathbf{n}\,\mathrm{d}S}_{IV} - \int_{\partial\Omega_i}\mathbf{B}^\dagger\cdot\delta\mathbf{U}_c\,\mathrm{d}S\end{aligned}$$

Imposing $\mathbf{B}^\dagger = -\left[p^\dagger\mathbf{I} + Re^{-1}\nabla\mathbf{u}^\dagger\right]\cdot\mathbf{n}$ and assuming:

$$\mathbf{u}^\dagger = \mathbf{0} \qquad \text{at the inlet } (\partial\Omega_i), \tag{2.11}$$

$$p^\dagger\mathbf{n} + Re^{-1}\nabla\mathbf{u}^\dagger\cdot\mathbf{n} = -(\mathbf{u}\cdot\mathbf{n})\mathbf{u}^\dagger \qquad \text{at the outlet } (\partial\Omega_o), \tag{2.12}$$

we set the boundary conditions of the adjoint system. Next, applying the Gateaux derivative, we have:

$$\frac{\partial\mathcal{L}}{\partial\mathbf{q}}\delta\mathbf{q} = \int_\tau\int_\Omega(\mathbb{A}\mathbf{q}^\dagger)\cdot\delta\mathbf{q}\mathrm{d}\mathcal{V}\mathrm{d}t = 0.$$

So, we conclude that if the adjoint system is satisfied, the derivative of $\mathcal{L}$ with respect to $\mathbf{q}$ is zero.

2.3.2 Sensitivity

Finally, to determine a mathematical expression of the drag coefficient sensitivity with respect to $\mathbf{f}$, we calculate:

$$\frac{\partial\mathcal{L}}{\partial\mathbf{f}}\delta\mathbf{f} = \frac{\partial C_d}{\partial\mathbf{f}}\delta\mathbf{f} + \int_\Omega\mathbf{u}^\dagger\cdot\delta\mathbf{f}\,\mathrm{d}\mathcal{V} = 0 \quad\Rightarrow\quad \frac{\partial C_d}{\partial\mathbf{f}}\delta\mathbf{f} = -\langle\mathbf{u}^\dagger,\delta\mathbf{f}\rangle \tag{2.13}$$

Notice that the sensitivity is proportional to adjoint field $\mathbf{u}^\dagger$, i.e., this field indicates the regions that are more susceptible to external forcing, making it possible to evaluate the locations where the addition of force can increase or decrease the drag coefficient.

Analogously, we can get the lift sensitivity with respect to $\mathbf{f}$. In this case, the adjoint system is also given by the system (2.10). The change occurs only at the cylinder wall boundary: for sensitivity of lift coefficient, the boundary condition at $\partial\Omega_w$ is $\mathbf{u}^\dagger = 2\mathbf{e}_y$.

2.4 Sensitivity to Reynolds number

To obtain a mathematical expression of the sensitivity $\left(\dfrac{\partial C_d}{\partial Re}\right)$, the Lagrangian functional (2.5) is used with the control variable $\mathbf{c} = Re$ and $\mathbf{f} = \mathbf{0}$. In what follows, the functional objective is again the drag force (2.6), and the procedure for finding a sensitivity expression is similar to that used in the previous section. So we depart by enforcing the adjoint system and nonlinear Navier-Stokes system:

$$\mathbb{A}(\mathbf{u})\mathbf{q}^\dagger = 0 \quad \Rightarrow \quad \frac{\partial \mathcal{L}}{\partial \mathbf{q}}\delta\mathbf{q} = 0,$$

$$\mathbb{N}(\mathbf{q}) = 0 \quad \Rightarrow \quad \frac{\partial \mathcal{L}}{\partial \mathbf{q}^\dagger}\delta\mathbf{q}^\dagger = 0.$$

For a steady base flow, $\mathbb{N}(\mathbf{q})$ is given by the system (2.8) with $\mathbf{f} = 0$ and the adjoint system $\mathbb{A}(\mathbf{u})\mathbf{q}^\dagger = 0$ is given by the system (2.10). We define the boundary conditions of the adjoint system so as to make $\dfrac{\partial \mathcal{L}}{\partial \mathbf{B}^\dagger}\delta\mathbf{B}^\dagger = 0$.

At last, the expression of the sensitivity of the drag coefficient with respect Re is given by:

$$\begin{aligned} \frac{\partial C_d}{\partial Re}\delta Re \quad &= \quad -Re^{-2}\left\{2\int_{\partial\Omega_w}\left\{\left[\nabla\mathbf{u} + (\nabla\mathbf{u})^T\right]\cdot\mathbf{n}\right\}\cdot\mathbf{e}_x\,\mathrm{d}S + \right. \\ &\left. + \int_\Omega \nabla^2\mathbf{u}\cdot\mathbf{u}^\dagger\,\mathrm{d}\mathcal{V} + \int_{\partial\Omega_i}\mathbf{U}\cdot\left\{\left[\nabla\mathbf{u}^\dagger + (\nabla\mathbf{u}^\dagger)^T\right]\cdot\mathbf{n}\right\}\cdot\mathbf{e}_x\,\mathrm{d}S\right\}\delta Re. \end{aligned} \tag{2.14}$$

In a similar process, we obtain the lift sensitivity that is computed by the expression:

$$\begin{aligned} \frac{\partial C_l}{\partial Re}\delta Re \quad &= \quad -Re^{-2}\left\{2\int_{\partial\Omega_w}\left\{\left[\nabla\mathbf{u} + (\nabla\mathbf{u})^T\right]\cdot\mathbf{n}\right\}\cdot\mathbf{e}_y\,\mathrm{d}S + \right. \\ &\left. + \int_\Omega \nabla^2\mathbf{u}\cdot\mathbf{u}^\dagger\,\mathrm{d}\mathcal{V} + \int_{\partial\Omega_i}\mathbf{U}\cdot\left\{\left[\nabla\mathbf{u}^\dagger + (\nabla\mathbf{u}^\dagger)^T\right]\cdot\mathbf{n}\right\}\cdot\mathbf{e}_y\,\mathrm{d}S\right\}\delta Re. \end{aligned} \tag{2.15}$$

2.5 Sensitivity to inlet velocity

In this section, we want to find a mathematical expression for the sensitivity of the drag coefficient with respect to variations in the inlet velocity. We use the Lagrangian functional (2.5) setting the inlet velocity as the control variable $\mathbf{c} = \mathbf{U}_c$ and setting $\mathbf{f} = 0$. The Navier-Stokes equations, adjoint system and their respective boundary conditions are enforced by making $\dfrac{\partial \mathcal{L}}{\partial \mathbf{q}}\delta\mathbf{q} = 0$, $\dfrac{\partial \mathcal{L}}{\partial \mathbf{q}^\dagger}\delta\mathbf{q}^\dagger = 0$ and $\dfrac{\partial \mathcal{L}}{\partial \mathbf{B}^\dagger}\delta\mathbf{B}^\dagger = 0$, respectively.

For a steady base flow, the drag sensitivity with respect to inlet velocity is then given by:

$$\frac{\partial C_d}{\partial \mathbf{U}_c}\delta\mathbf{U}_c = \int_{\partial\Omega_i}\delta\mathbf{U}_c\cdot\left\{-p^\dagger\mathbf{I} + Re^{-1}\left(\nabla\mathbf{u}^\dagger + (\nabla\mathbf{u}^\dagger)^T\right)\cdot\mathbf{n}\right\}\cdot\mathbf{e}_x\,\mathrm{d}S.$$

while the lift sensitivity is computed by the expression:

$$\frac{\partial C_l}{\partial \mathbf{U}_c}\delta \mathbf{U}_c = \int_{\partial \Omega_i} \delta \mathbf{U}_c \cdot \left\{-p^\dagger \mathbf{I} + Re^{-1}\left(\nabla \mathbf{u}^\dagger + (\nabla \mathbf{u}^\dagger)^T\right) \cdot \mathbf{n}\right\} \cdot \mathbf{e}_y \, \mathrm{d}S.$$

Remind that the adjoint systems to compute the lift and drag sensitivity are very similar, only the boundary condition at the wall is modified. For lift sensitivity the boundary condition is $\mathbf{u}^\dagger = 2 \cdot \mathbf{e}_y$, and for drag sensitivity, $\mathbf{u}^\dagger = 2 \cdot \mathbf{e}_x$.

Chapter

3

Sensitivity of aerodynamic forces: Results

Meliga *et al.* (2014); Mao (2015); Meliga *et al.* (2018) investigated the sensitivity of the aerodynamic forces with respect to an external forcing. Recently, Hayashi *et al.* (2016) introduced a formulation to compute aerodynamic force sensitivity with respect Reynolds number and applied it for two-dimensional channel flow. In this chapter, we extend the calculations of sensitivity with respect to non-geometric variables for other fluid flow problems. The main objective is to verify the mathematical formulation introduced in the previous chapter for two-dimensional flows. Besides that, we want to verify the applicability of the adjoint-based sensitivity in providing quantitative measures. To do that, calculations of sensitivity are applied to internal and external steady flows.

3.1 Numerical methodology

The numerical results were obtained using the Nektar++ software, which is an open-source code based on the spectral/*hp* element method Karniadakis & Sherwin (2005). Sensitivity calculations were applied for steady flows. In the nektar++, Navier–Stokes (2.3) and adjoint systems were solved by the stiffly stable time-stepping scheme (Karniadakis *et al.* , 1991) that is described in Appendix A. We employed a second order scheme to advance the solution for a sufficiently long time to reach steady state.

Calculations of sensitivities were performed with respect to non-geometric parameters and applied to the following fluid flow problems: fully-developed channel flow, backward-facing step, flow around a square cylinder and flow around a NACA 0012 airfoil. For the first three cases, drag sensitivity was measured. For the NACA 0012 airfoil, we also computed the lift sensitivity. For fully-developed channel flow, the calculations of adjoint-based sensitivity were compared with the analytic solution. In other fluid flow

Figure 3: Schematic diagram of a representative channel geometry parallel to the x-axis.

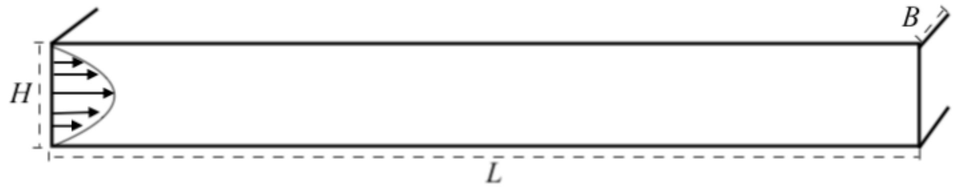

problems, the results of sensitivity given by the adjoint method (AM) were compared to the sensitivity obtained by the central finite difference method (FDM):

$$\frac{\mathrm{d}F}{\mathrm{d}P} = \frac{F|_{P+\delta P} - F|_{P-\delta P}}{2(\delta P)} + O(\delta P)^2 \tag{3.1}$$

where F represents the drag or lift coefficient. We considered that the shift δP corresponds to 1% of the value of the control variable P. Details of the computational mesh and polynomial order employed for each of the cases investigated in this chapter are given in Appendix C.

In this chapter, we are introducing measures of aerodynamic forces sensitivity with respect to Reynolds number, inlet velocity and external forcing. In some cases, mainly for external flow, the Reynolds number (Re) is defined as function of the inlet velocity. Therefore, to clarify, when we carry out computations of aerodynamic forces sensitivity with respect to Re, we consider that the reference velocity does not change. Besides that, we consider that the geometry length of reference does not change either.

3.2 Fully-developed channel flow

In this case, we calculate the drag sensitivity with respect to Reynolds number, Re, and mean inlet velocity $\bar{\mathbf{U}}$. Figure 3 illustrates a two-dimensional fully-developed channel flow parallel to the x-axis. The channel has height H, length L, depth B and the mean flow velocity is $\bar{\mathbf{U}}$. In the calculations we made, the channel was centred at $y = 0$, with the top and bottom walls at $y = \pm 0.5$ (i.e., height $H = 1.0$), length $L = 30$ and mean velocity $\bar{\mathbf{U}} = [\bar{U}, \bar{V}]^T = [1, 0]^T$.

For this fluid flow problem, we compare the sensitivity computed with the AM to the results obtained from the analytical expression of the sensitivity. To obtain the analytical sensitivity, we consider that the flow is fully developed. This means that the velocities, the stress tensor, and the pressure gradient do not vary along the channel. So, these properties are independent of the coordinate x, and the analytic velocity profile is given by:

$$u(y) = 2\bar{U}\left[1 - \left(\frac{2y}{H}\right)^2\right] \quad \text{and} \quad v = 0.$$

Figure 4: Velocity profile of the channel flow.

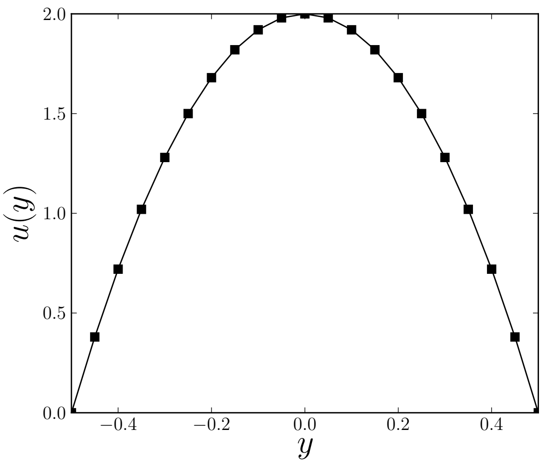

For this velocity profile (shown in Figure 4), the wall shear stress is

$$\tau_w = \mu \left.\frac{\mathrm{d}u}{\mathrm{d}y}\right|_{y=\pm H/2} = \mp\mu\frac{8\bar{U}}{H}.$$

Considering bottom and top walls, the drag coefficient is written as:

$$C_d = \frac{F_x}{\frac{1}{2}\rho\bar{U}^2 HB},$$

where

$$F_x = 2|\tau_w|BL = 16\frac{\mu\bar{U}}{H}BL.$$

Using $Re = \rho\bar{U}H/\mu$, the analytic expression for the drag coefficient considering the top and bottom channel walls is:

$$C_d = \frac{32\mu L}{\rho\bar{U}H^2} = \frac{32}{Re}\frac{L}{H}.$$

Therefore, the analytic drag sensitivities with respect to the mean velocity $\bar{U}$ and Re are given respectively by:

$$\frac{\partial C_d}{\partial \bar{U}} = -\frac{32\mu L}{\rho\bar{U}^2 H^2}, \tag{3.2}$$

$$\frac{\partial C_d}{\partial Re} = -\frac{32}{Re^2}\frac{L}{H}. \tag{3.3}$$

The same drag sensitivity measures obtained by the adjoint method are described by the equations (2.16) and (2.14), respectively. The steady base flow was solved with the following boundary conditions: $u = 2\bar{U}\left[1 - \left(\frac{2y}{H}\right)^2\right]$ and $v = 0$ at inlet, $\mathbf{u} = 0$ at wall and $\nabla\mathbf{u}\cdot\mathbf{n} = 0$ at outlet. The boundary conditions of the adjoint system are given in section 2.3.1.

Tables 3.1 and 3.2 show the drag sensitivity measures with respect to Re and $\bar{U}$, respectively. We noticed a good agreement, the largest error was 0.01%. Figures 5(a) and 5(b) display the curves of drag sensitivity given by the AM and by the analytic solution as functions of the parameter analyzed (Re and $\bar{U}$). For all values tested, we observe that the drag sensitivities with respect to Re and $\bar{U}$ are negative. As Re is increased, the absolute value of the sensitivity decreases. This means that an external forcing is more effective in changing the drag coefficient to lower Reynolds number.

It is important to say that when we are evaluating the drag sensitivity with respect to Re, the average velocity ($\bar{U}$) and height (H) of the channel are fixed. So the growth of Re implies that the dynamic viscosity decreases. This way, the drag force also decreases, implying in a negative sensitivity. In the drag sensitivity with respect to $\bar{U}$ and to each value of Re, the dynamic viscosity and the height (H) of the channel were fixed. This way, we observe in Table 3.2 and in Figure 5(b) that the sensitivity is negative with the growth of $\bar{\mathbf{U}}$.

Table 3.1: Drag coefficient sensitivity with respect to Re (Channel flow).

Re	Analytic sens. (AS)	AM	$(AS - AM)/AS$ (%)
30	$-0.035...$	-0.03555566	3.2×10^{-4}
60	$-8.88... \times 10^{-3}$	-8.8884×10^{-3}	3.76×10^{-3}
120	$-2.22... \times 10^{-3}$	-2.2212×10^{-3}	3.7×10^{-2}
200	-8×10^{-4}	-7.9904×10^{-4}	1×10^{-2}
400	-2×10^{-4}	-2.0002×10^{-4}	1×10^{-2}
800	-5×10^{-5}	-5.0028×10^{-5}	1×10^{-2}

Table 3.2: Drag coefficient sensitivity with respect to $\bar{U}$ (Channel flow).

Re	Analytic sens. (AS)	AM	$(AS - AM)/AS$ (%)
30	$-1.06...$	-1.066669	3×10^{-4}
60	$-0.53..$	-0.533304	5×10^{-3}
120	$-0.26...$	-0.266544	5×10^{-2}
200	-0.16	-0.1598	1×10^{-1}
400	-0.08	-0.07989	1×10^{-1}
800	-0.02	-0.0200112	6×10^{-2}

As previously said, the adjoint field provides the regions in which the drag force is more susceptible to external forcing. This way, we plotted in Figure 6 a field of the adjoint velocity magnitude at $Re = 400$. We then observe the stronger drag sensitivity to external forcing located at the wall of the channel and a weaker sensitivity closer to the center of the channel, at the region where the velocity achieves the maximum value. Also, notice that though the base flow velocity is uniform along of x-axis due to imposition of fully developed flow velocity profile, the same behaviour is not observed in the adjoint velocity magnitude. That occurs due to the boundary condition of the adjoint velocity, which is $\mathbf{u} = \mathbf{0}$ at inlet and $(u, v) = (2, 0)$ at wall of the channel.

Figure 5: Computations of drag coefficient sensitivity applied for fully-developed channel flow with respect to Re (a) and $\bar{U}(b)$.

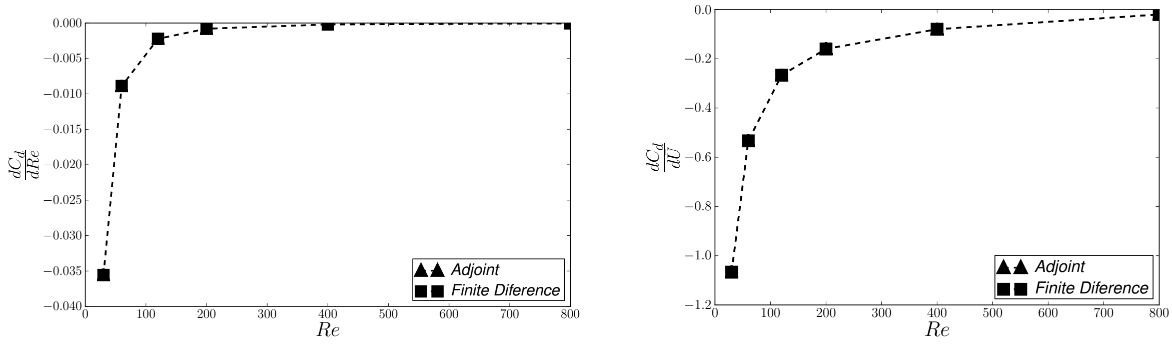

(a) (b)

Figure 6: Magnitude of adjoint velocity, at $Re = 400$.

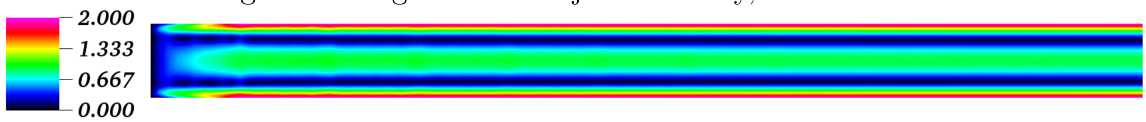

3.3 Backward-facing step

We now test the methodology for another internal flow, which is a channel flow with a sudden expansion, forming a backward facing step (BFS). The domain is illustrated in Figure 7, and comprises a channel inflow with height $H = 1$ and expansion $2H$. The length of the channel inflow is $li = 10$ and the and expansion has length $lo = 50$. Reynolds number was defined as $Re = \rho \bar{U} H/\mu$. At the inlet, we imposed the boundary condition $u = 1$ and $v = 0$. This case is reasonably more complex than the channel flow since the flow is truly two-dimensional. For the range of Reynolds number investigated in this section, a parabolic velocity profile develops along the inflow channel. As shown in Figure 9(b), after the expansion, shear layer separation occurs, giving rise to a recirculation region next to the step.

Tables 3.3 and 3.4 display the results of the drag coefficient sensitivity with respect to Reynolds number (Re) and to the inlet velocity ($\bar{U}$), respectively. In all the cases, the differences between the sensitivities were less than 1%. Sensitivity measures as function of Reynolds number obtained by the AM and FDM are also plotted in Figure 8. We can see that, in general, this flow is more sensitive to a change in $\bar{U}$ than to a change in Re. As in the plane channel flow, for lower Reynolds number, we notice in Figure 8(b) that

Figure 7: Schematic diagram of the backward-facing step.

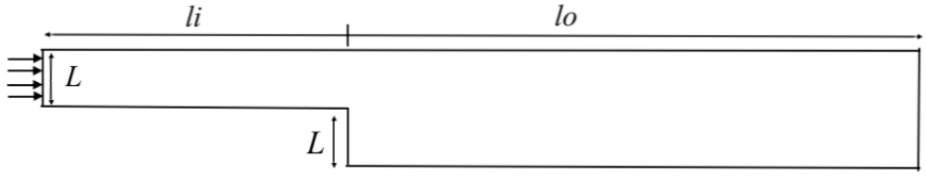

the drag sensitivity with respect to $\bar{U}$ or Re present a large variation. When the Reynolds number or the inlet velocity increase, the variation decreases.

Table 3.3: Drag coefficient sensitivity with respect to Re (Backward-facing step).

Re	FDM	AM	$(FDM - AM)/FDM$ (%)
50	-0.15168	-0.15636	0.02
100	-2.641×10^{-2}	-2.640×10^{-2}	0.01
200	-9.301×10^{-3}	-9.386×10^{-3}	0.09
300	-4.327×10^{-3}	-4.305×10^{-3}	0.50
400	-2.554×10^{-3}	-2.564×10^{-3}	0.32

Table 3.4: Drag coefficient sensitivity with respect to $\bar{U}$ (Backward-facing step).

Re	FDM	AM	$(FDM - AM)/FDM$ (%)
50	-7.585	-7.518	0.8
100	-2.642	-2.641	0.01
200	-1.861	-1.865	0.32
300	-1.238	-1.233	0.41
400	-1.021	-1.026	0.43

Figure 9 shows the adjoint velocity magnitude at $Re = 100$. Comparing it with the streamlines of the base flow (see Figure 9(b)), we observe that the drag force is most sensitive to an external forcing at the corner of the expansion, where the shear layer separates. Other regions of somewhat high drag sensitivity are also identified near the wall and at the wall of the outflow channel.

3.4 Flat plate

The first external flow presented is the laminar flow over a parallel flat plate with nondimensional length $D = 1$. The free stream velocity used in the simulations was $U_\infty = 1$ and the Reynolds number is defined as $Re = \rho U_\infty D/\mu$. Figure 10 shows an illustration of the current fluid flow problem, in which the origin of the coordinate system is at the center of the flat plate. The two-dimensional domain has the following dimensions:

Figure 8: Drag sensitivity calculations with respect to Re (a) and $\bar{U}$ (b) for Backward-facing step.

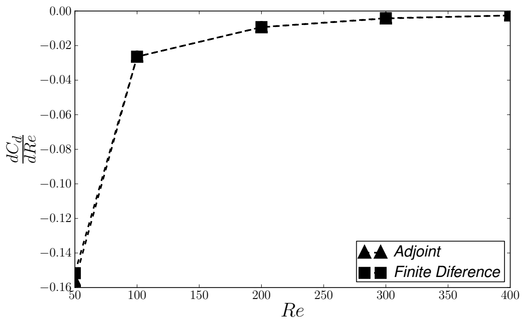

(a)

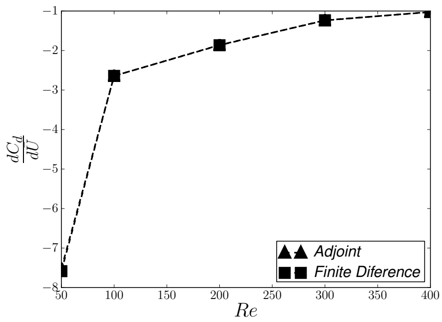

(b)

Figure 9: Adjoint velocity magnitude (a) and streamlines of the base flow (b) of the backward facing step, at $Re = 100$.

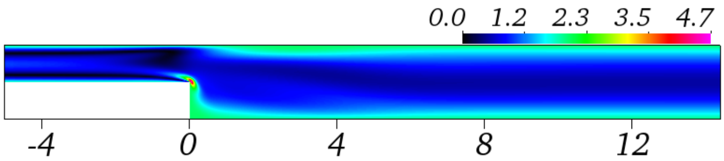

(a)

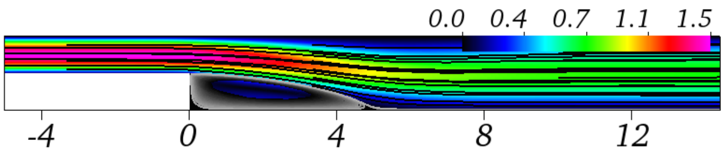

(b)

$x+ = 30$ to downstream, $x- = -30$ to upstream and vertical $y\pm = 25$. Figure 11 shows the streamlines of the base flow at $Re = 100$, in which we can see a laminar flow around of the flat plate.

Tables 3.5 and 3.6 show the measures of the drag sensitivity with respect to $\mathbf{U}_\infty$ and Re. Notice that the results from AM and central FDM exhibit good agreement. Although the difference increases when the Re increases, they remain below 1%. We also verify that the values of sensitivity are negative and the variations decrease with the growth of the Reynolds number.

Table 3.5: Drag sensitivity with respect to inlet velocity $\mathbf{U}_\infty$ (flat plate).

Re	Adjoint (A)	Finite Difference (FD)	(FD-A)/FD %
30	-4.506×10^{-1}	-4.495×10^{-1}	0.2%
60	-2.892×10^{-1}	-2.887×10^{-1}	0.2%
100	-2.162×10^{-1}	-2.122×10^{-1}	0.2%
200	-1.366×10^{-1}	-1.336×10^{-1}	0.2%
300	-1.062×10^{-1}	-1.056×10^{-1}	0.5%

Figure 10: Schematic diagram of a representative flow past a flat plate.

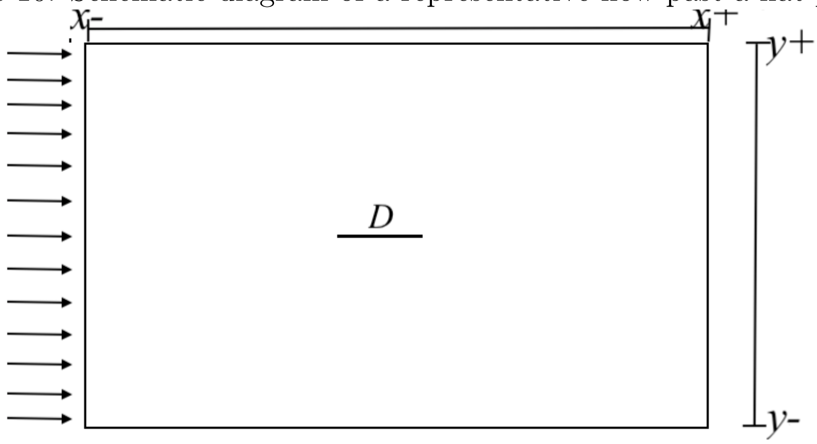

Figure 11: Streamlines of the flat plate, at $Re = 100$.

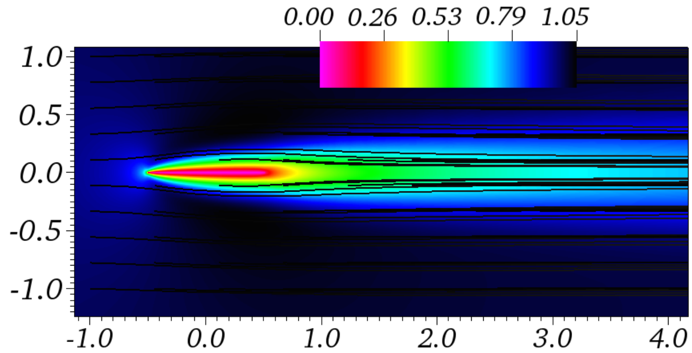

Table 3.6: Drag sensitivity with respect to Re (flat plate).

Re	Adjoint (A)	Finite Difference (FD)	(FD-A)/FD %
30	-1.503×10^{-2}	-1.497×10^{-2}	0.2%
60	-4.80×10^{-3}	-4.781×10^{-3}	0.2%
100	-2.082×10^{-3}	-2.076×10^{-3}	0.3%
200	-6.706×10^{-4}	-6.678×10^{-4}	0.3%
300	-3.539×10^{-4}	-3.551×10^{-4}	0.3%

The adjoint velocity magnitude plotted in Figure 12 shows that the drag force of the flat plat is most sensitive to external forcing at the region around of this body. Besides that, we verify that a weaker region of sensitivity is located upstream from the plate.

3.5 Square cylinder

The methodology was also tested for an external flow around a bluff body. A square cylinder with side length $D = 1$ was the geometry used. As illustrated in Figure 13, this solid body was immersed in an uniform flow with stream velocity $U_\infty = 1$ parallel to the x-axis, pointing to the $x+$ direction. The origin of the coordinate system was at the centre of the cylinder. The domain extended $x+ = 50$ to downstream, $x- = -35$ to

Figure 12: Adjoint velocity magnitude of the flat plate, at $Re = 100$.

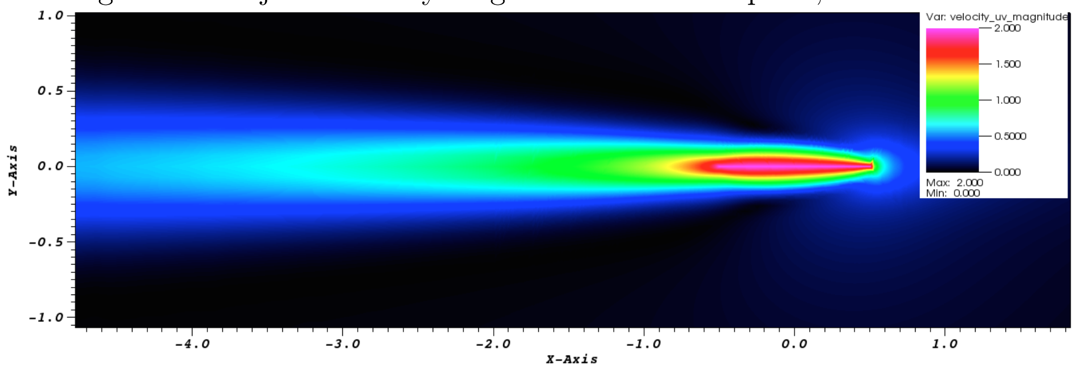

Figure 13: Schematic diagram of a square cylinder in a uniform flow.

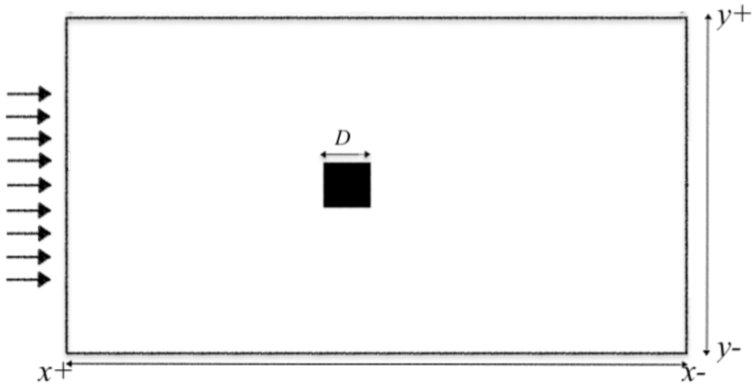

upstream and $y\pm = 50$ in the cross-stream direction. In this case, the Reynolds number was defined as $Re = \rho U_\infty D/\mu$. The sensitivity was calculated for a range of Reynolds number in which the fluid flow around a square cylinder is steady. In this case, the flow separates from the rear side of the square cylinder and a symmetric stable recirculation bubble is formed downstream. An illustration of this flow is observed in Figure 14(a), which shows the velocity magnitude and the streamlines of the base flow, at $Re = 40$.

3.5.1 Numerical verification – drag sensitivity with respect to a localized external forcing

We first present a numerical verification of the method applied to obtain the drag sensitivity with respect to an external forcing. The results obtained in our calculations are compared to the data obtained by Meliga *et al.* (2014). The calculation of the drag sensitivity with respect to an external forcing was carried out for a particular case in which the forcing is applied at a point of the domain. This external forcing is described analytically by the Gaussian function:

$$\mathbf{f}_\alpha(x,y) = \frac{\alpha}{2\pi X} e^{\left(-\frac{(x-x_c)^2+(y-y_c)^2}{2X^2}\right)}. \tag{3.4}$$

Figure 14: (a) Velocity magnitude and streamline of the base flow; and (b) magnitude of the adjoint velocity, at $Re = 40$

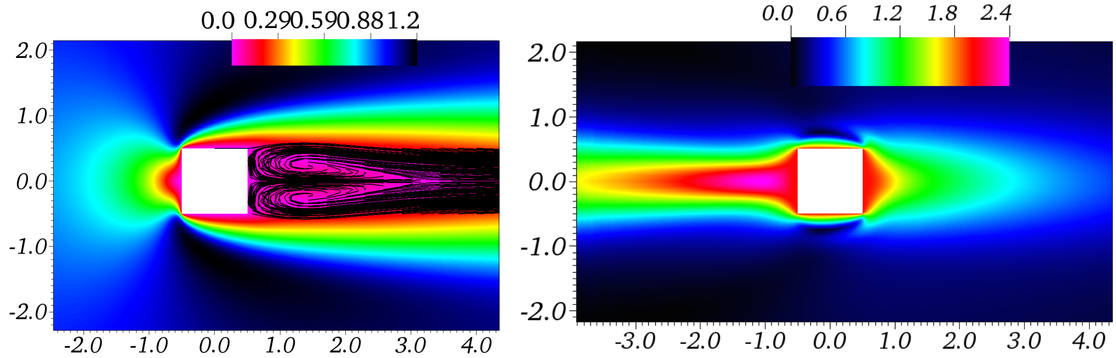

(a) (b)

To match the setup used by Meliga *et al.* (2014), we adopted $X = 6.25 \times 10^{-3}$ and $\alpha_0 = 10^{-3}$. The values x_c and y_c are the coordinates of the point at which the external forcing is applied. The Reynolds number was $Re = 40$. The sensitivity for this particular case is given by equation (2.13).

The drag coefficient computed from the numerical simulations was 1.66. This value agrees well with the result presented by Meliga *et al.* (2014), that was $C_d = 1.67$. Table 3.7 shows sensitivity results compared with those obtained by Meliga *et al.* (2014). The largest difference was around 2%, at $(x_c, y_c) = (4, 0)$ and $(x_c, y_c) = (0, 0.85)$. So we consider that the agreement was very good.

Table 3.7: Drag sensitivity to external forcing ($Re = 40$).

x_c	y_c	Meliga (2014)	Current work	Difference (%)
-1.5	0	2.32×10^{0}	2.31×10^{0}	0.5
0	0.65	7.10×10^{-1}	7.03×10^{-1}	0.9
0	0.85	-2.89×10^{-1}	-2.82×10^{-1}	2
1.5	0	1.24×10^{0}	1.24×10^{0}	–
2.5	0	8.96×10^{-1}	8.96×10^{-1}	–
4	0	5.68×10^{-1}	5.80×10^{-1}	2

Comparing the adjoint velocity magnitude (Figure 14(b)) with the base flow (Figure 14(a)), we see that the regions of stronger drag sensitivity are located upstream of the cylinder, in the shear layers, and in the recirculation bubble.

3.5.2 Sensitivity with respect to Reynolds number and inlet velocity

Despite the different configuration of the fluid flow problems, for the steady base flow the drag sensitivities computed by the adjoint method are precisely given by the

Figure 15: Drag coefficient sensitivity measures for flow past a square cylinder.

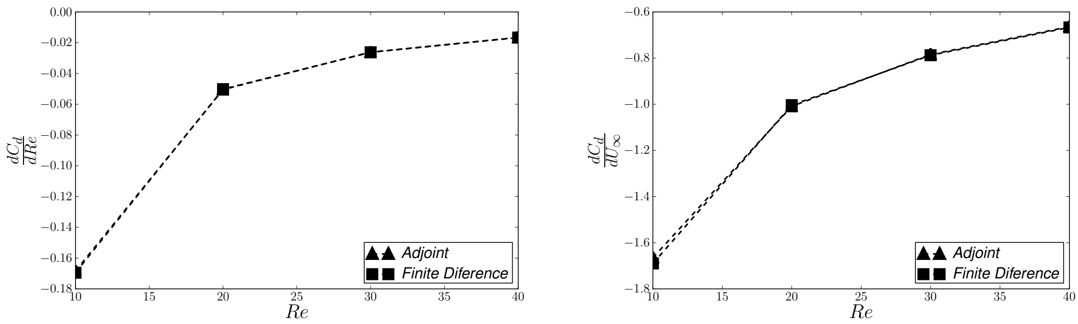

(a) (b)

equations (2.16) and (2.14). Results of drag coefficient sensitivity with respect to Re and inlet velocity U_∞ are shown in Tables 3.8 and 3.9. The sensitivities computed by the AM show good agreement with those obtained with the FDM. The differences between the measures are less than 1%. In Figure 15 the curves of sensitivities are plotted. For this range of Re, we observe that the drag sensitivity with respect to $\mathbf{U}_\infty$ is negative and present a smaller variation when Re increases.

Table 3.8: Drag coefficient sensitivity in respect to Re (square cylinder).

Re	FDM	AM	(FDM-AM)/FDM (%)
10	-1.6949×10^{-1}	-1.6838×10^{-1}	0.65
20	-5.0199×10^{-2}	-5.0489×10^{-2}	0.58
30	-2.6253×10^{-2}	-2.6135×10^{-2}	0.45
40	-1.6680×10^{-2}	-1.6602×10^{-2}	0.47

Table 3.9: Drag coefficient sensitivity in respect to U_∞ (square cylinder).

Re	FDM	AM	(FDM-AM)/FDM (%)
10	-1.665	-1.6899	1.4
20	-1.009	-1.004	0.5
30	-0.7845	-0.7876	0.4
40	-0.6641	-0.6672	0.5

3.6 Airfoil NACA 0012

Figure 16 illustrates the domain in which two-dimensional flows around an NACA 0012 airfoil were calculated. The free stream velocity used was $U_\infty = 1$, and the airfoil chord length was $c = 1$. The origin of the coordinate system was at the leading edge of the airfoil. The domain extended $x+ = 40$ to downstream, $x- = -40$ to upstream and $y\pm = 40$ on

Figure 16: Schematic diagram of a representative flow around an airfoil NACA 0012.

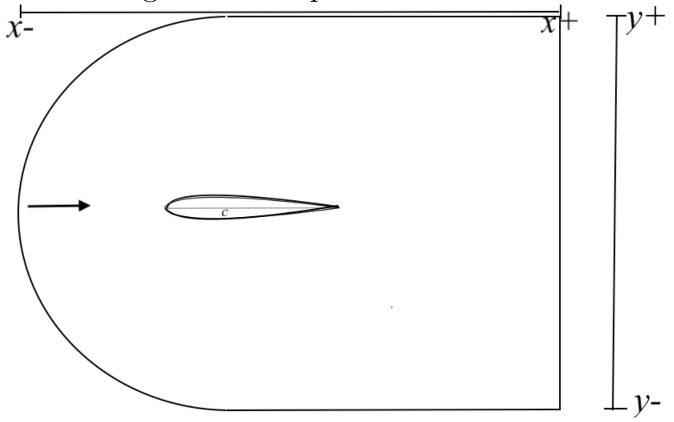

the cross-stream direction. Reynolds number was defined as $Re = \rho U_\infty c/\mu$. We set the components of the inlet velocity as $u = U_\infty \cos(2\pi\alpha/360)$ and $v = U_\infty \,\mathrm{sen}(2\pi\alpha/360)$, where α is the angle of attack (angle between the chord line and the incoming flow), in degrees. The numerical results were obtained for $Re = 500$.

We computed the drag coefficient and lift coefficient sensitivities. The control parameters used were U_∞, Re and the angle of attack α. The sensitivities with respect to Re and U_∞ computed by the adjoint method are given by (2.16) and (2.14), respectively. The sensitivity with respect to α is calculated with the equation:

$$\frac{\partial C_d}{\partial \alpha}_{adj} = \frac{\partial C_l}{\partial \alpha}_{adj} = -\frac{2\pi}{360}\int_{\partial\Omega_i} \frac{\partial \mathbf{u}}{\partial \alpha} \cdot \left\{-p^\dagger \mathbf{I} + Re^{-1}\left(\nabla \mathbf{u}^\dagger + (\nabla \mathbf{u}^\dagger)^T\right) \cdot \mathbf{n}\right\} \cdot \mathbf{e}\, \mathrm{d}S. \qquad (3.5)$$

Tables 3.10, 3.11 and 3.12 show the lift sensitivity with respect to α, Re and U_∞, respectively. The drag sensitivities with respect to α, Re and U_∞ are shown in Tables 3.13, 3.14 and 3.15. The largest difference between the sensitivities obtained by the AM and FDM was 3% for lift coefficient sensitivity with respect to U_∞ and drag coefficient sensitivity with respect to α. So we consider that the method works well also for this case. It is important to highlight that, due to the low Reynolds number of the flow in this case, C_l is not equal to $2\pi\alpha$.

Table 3.10: Lift coefficient sensitivity with respect to the angle of attack (airfoil).

α	Finite Difference (FD)	Adjoint (A)	$(DF - A)/DF(\%)$
3	4.63×10^{-2}	4.66×10^{-2}	0.7
5	4.04×10^{-2}	4.07×10^{-2}	0.8

Evaluating the results of lift coefficient sensitivity computations, we observe that for the angle of attack $\alpha = 3^\circ$ and $\alpha = 5^\circ$, the lift sensitivity with respect to α is positive with the growth of α. We notice that the values of sensitivity do not present considerable changes when we compare the sensitivities of $\alpha = 5^\circ$ with the sensitivities of $\alpha = 3^\circ$.

Table 3.11: Lift coefficient sensitivity with respect to Re (airfoil).

α	Finite Difference (FD)	Adjoint (A)	$(DF-A)/DF$ (%)
3	-5.27×10^{-5}	-5.22×10^{-5}	1
5	-9.86×10^{-5}	-9.65×10^{-5}	2

Table 3.12: Lift coefficient sensitivity with respect to U_∞ (airfoil).

α	Finite Difference (FD)	Adjoint (A)	$(DF-A)/DF$ (%)
3	-2.63×10^{-2}	-2.55×10^{-2}	3
5	-4.93×10^{-2}	-4.78×10^{-2}	3

Table 3.13: Drag coefficient sensitivity with respect to α (airfoil).

α	Finite Difference (FD)	Adjoint (A)	$(DF-A)/DF(\%)$
3	-2.93×10^{-3}	-2.84×10^{-3}	3
5	-3.65×10^{-3}	-3.78×10^{-3}	3

Table 3.14: Drag coefficient sensitivity with respect to Re (airfoil).

α	Finite Difference (FD)	Adjoint (A)	$(DF-A)/DF(\%)$
3	-1.91×10^{-4}	1.93×10^{-4}	1
5	-1.86×10^{-4}	-1.84×10^{-4}	0.9

Table 3.15: Drag coefficient sensitivity with respect to U_∞ (airfoil).

α	Finite Difference (FD)	Adjoint (A)	$(DF-A)/DF(\%)$
3	-0.95	-0.94	1
5	-0.93	-0.92	1

Lift sensitivities with respect to Re and $\mathbf{U}_\infty$ are negative with the growth of α. We also observe that with the growth of α, the variations increase.

Now, analyzing the drag sensitivities with the growth of α, we can see that the measures of sensitivity are negative for all control variables ($\mathbf{U}_\infty$, Re and α). Tables 3.13 shows that the variation of the drag force increases with the growth of the angle of attack. In Tables 3.14 and 3.15, we notice that the drag sensitivity with respect to Re and $\mathbf{U}_\infty$ do not present significant variation with the growth of α.

Figure (17) shows the adjoint velocity magnitude used for the calculations of drag and lift sensitivities at $\alpha = 3^\circ$. Figure 17(a) shows that the drag sensitivity to an external forcing is stronger at wall, mainly at the leading edge and at the trailing edge. Weaker drag sensitivity is verified close to the airfoil and to upstream of this body. Evaluating the adjoint velocity magnitude used to compute the lift sensitivity, we observe that the lift force is most susceptible to external forcing on top of airfoil, closer to the leading edge. A weaker sensitivity is verified at the trailing edge and above the airfoil.

Figure 17: (a) Fields of adjoint velocity magnitude used to obtain the drag force sensitivity; (b) lift force sensitivity; and (c) velocity magnitude with the streamlines of the flow around an airfoil, at $\alpha = 3°$.

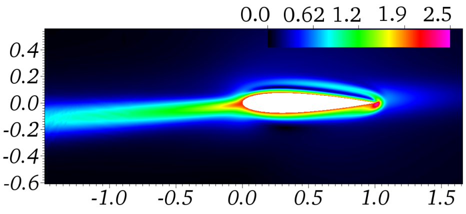

(a)

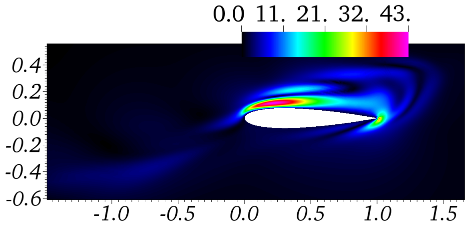

(b)

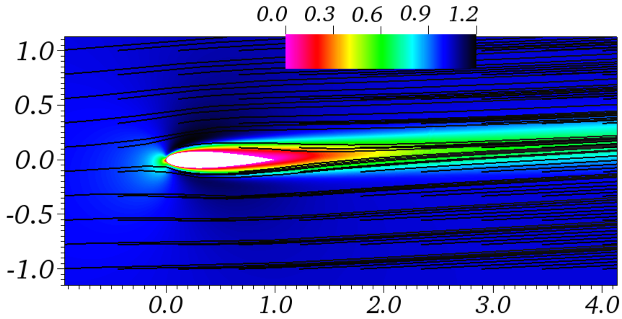

(c)

3.7 Conclusions

This work focused on computing sensitivities using the adjoint method for steady flows. On combining previous works, mainly the ones by Cacuci (1981) and Meliga & Chomaz (2011), it was possible to compute sensitivities with respect to non geometric control parameters (Reynolds number, inlet velocity and external forcing).

It was shown that the current approach is applicable for internal and external steady flows. The results for internal flows show excellent agreement between the sensitivities computed by the adjoint method and other sources like analytically sensitivity (fully-developed channel flow) and central finite difference. The errors were lower than 0.8%. Regarding external flows, the errors did not exceed 3%. We also presented the fields of adjoint velocity magnitude, which show the regions most receptive to external forcing. In the flow around a square cylinder, this kind of sensitivity calculation was verified comparing our results with the computations introduced by Meliga *et al.* (2014). We noticed a good agreement between the results; the largest difference was 2%.

In conclusion, the verification regarding the use of the adjoint method to compute sensitivities for low Reynolds flows with respect to non-geometric control parameters was completed. The results entice the extension of this alternative approach to computing sensitivities of new objective functional with respect to any kind of parameters in different applications including optimization problems.

CHAPTER

4

Global linear analysis applied for fluid flow systems

Based on a review of the literature, mathematical formulations for linear stability and sensitivity analyses of fluid flows are introduced in this chapter. The state vector $\mathbf{q}$ consists of the velocity vector field, $\mathbf{u}$, and the pressure field, p. Stability analysis is performed by considering an infinitesimal perturbation $\mathbf{q}'$ in the fluid flow fields. The governing equation for the perturbation is obtained from the linearization of the Navier-Stokes equations around a base flow $\mathbf{Q}$. In the context of linear global analysis, we introduce the mathematical process to perform the transient growth analysis. Next, the sensitivity expressions of the least stable eigenvalues with respect to an external forcing are described. In the last two cases, the adjoint field $\mathbf{q}^\dagger$ is used. Lastly, applications of stability and sensitivity analyses are carried out for a two-dimensional flow around a fixed circular cylinder.

4.1 Linear stability analysis

Hydrodynamic stability analysis consists of investigating the evolution of a small perturbation superimposed on a base flow $\mathbf{Q}$. So it is assumed that $\mathbf{q} = (\mathbf{u}, p)$ is given by the base flow $\mathbf{Q} = (\mathbf{U}, P)$ plus a perturbation $\mathbf{q}' = (\mathbf{u}', p')$. Substituting $\mathbf{q} = \mathbf{Q} + \mathbf{q}'$ in the Navier-Stokes equations (2.3), we have:

$$
\begin{aligned}
\nabla \cdot \mathbf{u}' + \nabla \cdot \mathbf{U} &= 0 \\
\underbrace{\frac{\partial \mathbf{u}'}{\partial t} + \nabla \mathbf{U} \cdot \mathbf{u}' + \mathbf{U} \cdot \nabla \mathbf{u}' - \boldsymbol{\sigma}(\mathbf{u}', p') + \nabla \mathbf{u}' \cdot \mathbf{u}'}_{\text{Non-linear equation of the perturbation evolution}} + \underbrace{\frac{\partial \mathbf{U}}{\partial t} + \mathbf{U} \cdot \nabla \mathbf{U} - \boldsymbol{\sigma}(\mathbf{U}, p)}_{\mathbb{N}(\mathbf{Q})} &= \mathbf{0}
\end{aligned}
$$

The base flow satisfies the nonlinear Navier-Stokes equations $\mathbb{N}(\mathbf{Q}) = \mathbf{0}$, and the evolution of the perturbation is governed by:

$$\nabla \cdot \mathbf{u}' = 0, \tag{4.1}$$

$$\underbrace{\frac{\partial \mathbf{u}'}{\partial t} + \nabla \mathbf{U} \cdot \mathbf{u}' + \mathbf{U} \cdot \nabla \mathbf{u}' - \boldsymbol{\sigma}'}_{\text{Linear equation of the perturbation evolution}} + \underbrace{\nabla \mathbf{u}' \cdot \mathbf{u}'}_{\text{Nonlinear term}} = \mathbf{0}. \tag{4.2}$$

The linearization process can be applied when the base flow is tested against an infinitesimal perturbation. This means to assume that the nonlinear term $\nabla \mathbf{u}' \cdot \mathbf{u}'$ in equation (4.2) is of a smaller order than the other terms in the short time scale. So it can be neglected and equation (4.2) becomes:

$$\frac{\partial \mathbf{u}'}{\partial t} + \nabla \mathbf{U} \cdot \mathbf{u}' + \mathbf{U} \cdot \nabla \mathbf{u}' - \frac{1}{Re} \nabla^2 \mathbf{u}' + \nabla p' = 0.$$

The set of linearized equations is conveniently written as:

$$\mathbb{H}\mathbf{q}' = \left(\begin{bmatrix} \partial_t & \\ & 0 \end{bmatrix} + \underbrace{\begin{bmatrix} (\mathbf{U} \cdot \nabla) + (\nabla \mathbf{U}) \cdot & -Re^{-1}\nabla^2 & \nabla \\ & \nabla \cdot & 0 \end{bmatrix}}_{\mathbb{L}} \right) \begin{bmatrix} \mathbf{u}' \\ p' \end{bmatrix} = \begin{bmatrix} \mathbf{0} \\ 0 \end{bmatrix}, \tag{4.3}$$

in which ∂_t represents partial derivative with respect to time.

An approach to evaluate hydrodynamic stability is checking whether a flow subject to a small perturbation returns to its original state or changes to a different state. In the first case, the flow is stable. In the second case, the flow is unstable. For linear stability analysis, the usual form to verify the stability is using the modal analysis. This approach will be introduced in the next subsection.

4.1.1 Modal Analysis

The main goal of the modal analysis is to evaluate the least stable mode. To do that, the linear system (4.3) is rewritten as a generalized eigenvalue problem by setting an asymptotic solution given by $\mathbf{q}' = \exp(\lambda t)\widehat{\mathbf{q}}$, so the system (4.3) can be rewritten as:

$$\mathbb{H}\mathbf{q}' = \left(\lambda \underbrace{\begin{bmatrix} \mathbf{I} & \\ & 0 \end{bmatrix}}_{\mathbb{B}} + \underbrace{\begin{bmatrix} (\mathbf{U} \cdot \nabla) + (\nabla \mathbf{U}) \cdot & -Re^{-1}\nabla^2 & \nabla \\ & \nabla \cdot & 0 \end{bmatrix}}_{\mathbb{L}} \right) \begin{bmatrix} \widehat{\mathbf{u}} \\ \widehat{p} \end{bmatrix} = \begin{bmatrix} \mathbf{0} \\ 0 \end{bmatrix}.$$

This can be written in compact form as the generalized eigenvalue problem:

$$(\boldsymbol{\lambda}\mathbb{B} - \mathbb{L})\widehat{\mathbf{q}} = \mathbf{0}. \tag{4.4}$$

Non-homogeneous solutions to this problem are pairs of eigenvalues (λ) and eigenvectors/direct modes ($\widehat{\mathbf{q}}$).

For a steady base flow ($\mathbf{U} = \mathbf{U}(\mathbf{x})$), the operator $\mathbb{L} = \mathbb{L}(\mathbf{U})$ is steady and the system stability can be assessed from the the sign of the real part of the eigenvalues. If there is at least one eigenvalue with positive real part, the perturbation energy grows with time and the system is unstable. On the other hand, if all eigenvalues have negative real part, the perturbation energy decreases with time and system is stable.

4.1.2 Non-modal analysis: Response to initial conditions

In the previous subsection, we saw that the stability of the system can be assessed from the eigenvalues of the linearized system. However, in some cases, there is a discrepancy between the stability analysis results and the response of the perturbation growth in a finite time interval (τ). This occurs when the system is asymptotically stable but not monotonically stable, i.e., $\dfrac{\mathrm{d}\mathbb{E}(\tau)}{\mathrm{d}t} = \dfrac{\mathrm{d}||\mathbf{u}'(\mathbf{x},\tau)||^2}{\mathrm{d}t} < 0$ does not hold for all time. For these cases, the modal analysis is not sufficient to characterize the dynamics of the flow in the time interval (τ) (Trefethen *et al.* , 1993; Chomaz, 2005) and the non-modal analysis is necessary.

To explain the non-modal analysis, let us consider the solution of the linearized system (4.3) given by

$$\mathbf{u}'(\mathbf{x},\tau) = \exp(\mathbb{L}t)\mathbf{u}'(\mathbf{x},0). \tag{4.5}$$

Using the energy norm $\mathbb{E}(\tau) = ||\mathbf{u}'(\mathbf{x},\tau)||^2$ at a generic time interval τ and normalising $\mathbb{E}(\tau)$ in order to obtain $\mathbb{E}(0) = 1$, we have the perturbation growth written as

$$\mathbb{G}(\tau) = \mathbb{E}(\tau) = ||\mathbf{u}'(\mathbf{x},\tau)||^2 = ||\exp(\mathbb{L}\tau)\mathbf{u}'(\mathbf{x},0)||^2 = ||\exp(\mathbb{L}\tau)||^2. \tag{4.6}$$

Applying the spectral decomposition to the operator $\mathbb{L}$, the growth $\mathbb{G}(\tau)$ may be evaluated of the following way:

$$\mathbb{G}(\tau) = ||\exp(\mathbb{L}\tau)||^2 = ||\exp(\mathbf{S}\boldsymbol{\Lambda}\mathbf{S}^{-1}\tau)||^2 = ||\mathbf{S}\exp(\boldsymbol{\Lambda}\tau)\mathbf{S}^{-1}||^2.$$

The columns of the matrix $\mathbf{S}$ are composed by the eigenvectors/modes of $\mathbb{L}$ and $\boldsymbol{\Lambda}$ is a diagonal operator which contains the eigenvalues of $\mathbb{L}$. To analyze the perturbation behaviour on a finite time interval τ, we estimate the inferior and superior limits of $\mathbb{G}(\tau)$. To do that, let us admit a stable flow system. This way, for the inferior limit we use the fact that the energy cannot decrease at a rate faster than that given by the least stable eigenvalue λ_1, i.e.,

$$||\exp(\lambda_1\tau)||^2 \leqslant ||\exp(\mathbb{L}\tau)||^2 .$$

For the superior limit, we consider the spectral decomposition

$$||\exp(\mathbb{L}\tau)||^2 = ||\mathbf{S}\exp(\mathbf{\Lambda}\tau)\mathbf{S}^{-1}||^2 \leqslant ||\mathbf{S}||^2||\mathbf{S}^{-1}||^2||\exp(\lambda_1\tau)||^2. \tag{4.7}$$

Analyzing the inequation (4.7) on finite time interval τ, we see that the system can show two different behaviours depending on the operator $\mathbb{L}$:

- If $\mathbb{L}$ is a normal operator then it is diagonalizable and $||\mathbf{S}||^2||\mathbf{S}^{-1}||^2 = 1$. Thus, superior and inferior limits are equivalent, and the stability will be given by the eigenvalue analysis, i.e., the modal analysis gives all the information about the evolution of small perturbations.

- If $\mathbb{L}$ is not a normal operator then the eigenvalue analysis is not sufficient for a finite time interval τ analysis, because we can have $||\mathbf{S}||^2||\mathbf{S}^{-1}||^2 \gg 1$. This makes the *transient growth* of perturbation energy possible, even though the system is asymptotically stable.

According to Schmid (2007), the non-modal analysis can be divided in two approaches: response to initial conditions and response to external forcing. The first approach is central to hydrodynamic stability theory and will be treated in this subsection, whereas the second ventures into the closely related field of sensitivity analysis (this approach will be studied in section 4.2).

The optimal growth over a finite time interval τ is defined as the maximum energy growth over all possible initial perturbations. So taking $\exp(\mathbb{L}\tau) = \mathcal{A}(\tau)$, this expression can be rewritten as

$$\mathbb{G}(\tau) = ||\mathcal{A}(\tau)\mathbf{u}'(\mathbf{x},0)||^2 =< \mathcal{A}(\tau)\mathbf{u}'(\mathbf{x},0), \mathcal{A}(\tau)\mathbf{u}'(\mathbf{x},0) >=< \mathbf{u}'(\mathbf{x},0), \mathcal{A}^{\dagger}(\tau)\mathcal{A}(\tau)\mathbf{u}'(\mathbf{x},0) >,$$

where the operator $\mathcal{A}^{\dagger}(\tau)$ is the adjoint of the operator $\mathcal{A}(\tau)$. The inner product $\langle\cdot\rangle$ is defined as the integral $\int_\tau\int_\Omega \cdot \mathrm{d}\mathcal{V}\mathrm{d}t$.

The largest possible transient growth is then dictated by the dominant eigenvalue of symmetric operator $\mathcal{A}^{\dagger}(\tau)\mathcal{A}(\tau)$. Therefore, we have an eigenvalue problem:

$$\mathcal{A}^{\dagger}(\tau)\mathcal{A}(\tau)\mathbf{v}_k = \lambda_k\mathbf{v}_k, \quad ||\mathbf{v}_k||^2 = 1$$

where $\mathbf{v}_k$ are the modes with non-negative growth λ_k on the time interval τ. Optimal growth is given by the maximal eigenvalue, $\max(\lambda_k) = \lambda_1$, of $\mathcal{A}^{\dagger}(\tau)\mathcal{A}(\tau)$, and the optimal initial condition $\mathbf{u}'(\mathbf{x},0)$ is given by the mode associated with λ_1. Therefore,

$$\mathbb{G}(\tau) = ||\mathcal{A}(\tau)\mathbf{u}'(\mathbf{x},0)||^2 = \langle\mathbf{u}'(\mathbf{x},0), \lambda_1\mathbf{u}'(\mathbf{x},0)\rangle = \lambda_1, \quad ||\mathbf{u}'(\mathbf{x},0)||^2 = 1.$$

4.1.2.1 Optimization approach

A typical optimization problem consists of state variables, control variables, objective functional, and constraints. Based on the work by Mao *et al.* (2013), an optimization approach is adopted to obtain the optimal initial perturbation and optimal energy growth. In this approach, we deal with the Lagrangian functional

$$\mathcal{L}(\mathbf{q}', \mathbf{q}^\dagger, \mathbf{u}'(\mathbf{x}, 0)) = \mathbb{E}(\tau) - \langle \mathbf{q}^\dagger, \mathbb{H}\mathbf{q}' \rangle - \langle \mathbf{u}^\dagger(\mathbf{x}, 0), \mathbf{u}'(\mathbf{x}, 0) - \mathbf{u}'_0 \rangle, \tag{4.8}$$

where $\mathbf{q}^\dagger = [\mathbf{u}^\dagger, p^\dagger]$ is the Lagrange multiplier also referred to as the adjoint variable. The linearized system $\mathbb{H}\mathbf{q}' = \mathbf{0}$ and the initial conditions $\mathbf{u}'(\mathbf{x}, 0)$ are the constraints. The gradient of the Lagrangian functional with respect to any variable s is defined by:

$$\frac{\partial \mathcal{L}}{\partial s} = \lim_{\epsilon \to 0} \frac{\mathcal{L}(s + \epsilon \delta s) - \mathcal{L}(s)}{\epsilon}. \tag{4.9}$$

At an optimum point, the gradient of $\mathcal{L}(\mathbf{q}', \mathbf{q}^\dagger, \mathbf{u}'(\mathbf{x}, 0))$ with respect to any variable is zero. If we express the first variation of $\mathcal{L}$ with respect to the adjoint/Lagrange multiplier $\mathbf{q}^\dagger$, we obtain

$$\frac{\partial \mathcal{L}}{\partial \mathbf{q}^\dagger} = \lim_{\epsilon \to 0} \frac{\int_\tau \left[\int_\Omega (\mathbf{q}^\dagger + \epsilon \delta \mathbf{q}^\dagger) \cdot (\mathbb{H}\mathbf{q}') - \mathbf{q}^\dagger \cdot (\mathbb{H}\mathbf{q}')\right] \mathrm{d}\mathcal{V}\mathrm{d}t}{\epsilon} = \int_\tau \int_\Omega \delta \mathbf{q}^\dagger \cdot (\mathbb{H}\mathbf{q}') \mathrm{d}\mathcal{V}\mathrm{d}t = 0,$$

because we require that the constraint $\mathbb{H}\mathbf{q}' = \mathbf{0}$ must be satisfied for all domain Ω and time τ.

Next, we compute the first variation of $\mathcal{L}$ with respect to the state vector $\mathbf{q}'$:

$$\frac{\partial \mathcal{L}}{\partial \mathbf{q}'} \delta \mathbf{q}' = \frac{\partial}{\partial \mathbf{q}'} \left(\int_\tau \int_\Omega \mathbf{q}^\dagger \cdot \mathbb{H}\mathbf{q}' \mathrm{d}\mathcal{V}\mathrm{d}t \right) \delta \mathbf{q}' = \frac{\partial}{\partial \mathbf{q}'} \left(\int_\tau \int_\Omega \mathbb{H}^\dagger \mathbf{q}^\dagger \cdot \mathbf{q}' \mathrm{d}\mathcal{V}\mathrm{d}t \right) \delta \mathbf{q}'$$

The adjoint system and its boundary and initial conditions are obtained from the integral by parts:

$$\begin{aligned}
\int_\tau \int_\Omega \mathbf{q}^\dagger \cdot \mathbb{H}\mathbf{q} \mathrm{d}\mathcal{V}\mathrm{d}t &= \int_\tau \int_\Omega \mathbb{H}^\dagger \mathbf{q}^\dagger \cdot \mathbf{q}' \,\mathrm{d}\mathcal{V}\mathrm{d}t \\
&= \int_\tau \int_\Omega \mathbf{u}^\dagger \cdot \left[\frac{\partial \mathbf{u}'}{\partial t} + \nabla \mathbf{U} \cdot \mathbf{u}' + \mathbf{U} \cdot \nabla \mathbf{u}' - \frac{1}{Re} \nabla^2 \mathbf{u}' + \nabla p' \right] + p^\dagger \left[\nabla \cdot \mathbf{u}' \right] \mathrm{d}\mathcal{V}\mathrm{d}t \\
&= \int_\tau \int_\Omega \left[-\frac{\partial \mathbf{u}^\dagger}{\partial t} - \mathbf{U} \cdot \nabla \mathbf{u}^\dagger + \nabla \mathbf{U} \cdot \mathbf{u}^\dagger - Re^{-1} \nabla^2 \mathbf{u}^\dagger - \nabla p^\dagger \right] \cdot \mathbf{u}' \,\mathrm{d}\mathcal{V}\mathrm{d}t + \\
&+ \int_\tau \int_\Omega \left[\nabla \cdot \mathbf{u}^\dagger \right] p' \,\mathrm{d}\mathcal{V}\mathrm{d}t + \int_\tau \int_\Omega \left[\mathbf{u}' \cdot \mathbf{u}^\dagger \right]_0^\tau \mathrm{d}\mathcal{V}\mathrm{d}t + \\
&+ \int_\tau \int_\Omega \nabla \cdot \left\{ \mathbf{U}\mathbf{u}'\mathbf{u}^\dagger + \mathbf{u}^\dagger p' + p^\dagger \mathbf{u}' \right\} \mathrm{d}\mathcal{V}\mathrm{d}t + \\
&+ \int_\tau \int_\Omega \nabla \cdot \left\{ Re^{-1} \left[\mathbf{u}' \cdot \nabla \mathbf{u}^\dagger - \nabla \mathbf{u}' \cdot \mathbf{u}^\dagger \right] \right\} \mathrm{d}\mathcal{V}\mathrm{d}t.
\end{aligned}$$

Assuming that the adjoint system $\mathbb{H}^\dagger \mathbf{q}^\dagger = \mathbf{0}$, we can write:

$$\mathbb{H}^\dagger \mathbf{q}^\dagger = \left\{ \begin{array}{rcl} -\dfrac{\partial \mathbf{u}^\dagger}{\partial t} - \mathbf{U} \cdot \nabla \mathbf{u}^\dagger + \nabla \mathbf{U} \cdot \mathbf{u}^\dagger - Re^{-1} \nabla^2 \mathbf{u}^\dagger - \nabla p^\dagger & = & \mathbf{0}, \\ \nabla \cdot \mathbf{u}^\dagger & = & 0. \end{array} \right. \tag{4.10}$$

Besides that, employing the Divergence Theorem, we have:

$$< \mathbb{H}\mathbf{q}, \mathbf{q}^\dagger > - < \mathbf{q}, \mathbb{H}^\dagger \mathbf{q}^\dagger >= \int_\Omega \left[\mathbf{u}' \cdot \mathbf{u}^\dagger \right]_0^\tau \mathrm{d}\mathcal{V} + \mathcal{B},$$

in which the term $\mathcal{B}$, called bilinear concomitant, is

$$\mathcal{B} = \int_\tau \int_{\partial\Omega} \mathbf{n} \cdot \left\{ (\mathbf{U} \cdot \mathbf{u}')\mathbf{u}^\dagger + \mathbf{u}^\dagger p + p^\dagger \mathbf{u}' + Re^{-1} \left[\mathbf{u}' \cdot \nabla \mathbf{u}^\dagger - \nabla \mathbf{u}' \cdot \mathbf{u}^\dagger \right] \right\} \mathrm{d}S \mathrm{d}t.$$

with $\mathbf{n}$ a unit outward normal on the spatial boundary of the domain $\partial\Omega$.

In this work, the boundary conditions adopted for the perturbation velocity field are:

- $\mathbf{u}' = 0$ at inlet ($\partial\Omega_i$) and wall ($\partial\Omega_w$);
- $\nabla \mathbf{u}' \cdot \mathbf{n} = \mathbf{0}$ and $p' = 0$ at outlet ($\partial\Omega_o$).

Therefore, the concomitant bilinear is reduced to:

$$\begin{aligned} \mathcal{B} \;=\; & \int_\tau \int_{\partial\Omega_{i,w}} \mathbf{n} \cdot \left\{ \mathbf{u}^\dagger \cdot p - Re^{-1} \nabla \mathbf{u}' \cdot \mathbf{u}^\dagger \right\} \mathrm{d}S \mathrm{d}t + \\ & + \int_\tau \int_{\partial\Omega_o} \mathbf{n} \cdot \left\{ (\mathbf{U} \cdot \mathbf{u}')\mathbf{u}^\dagger + \mathbf{u}^\dagger p + p^\dagger \mathbf{u}' + Re^{-1} \mathbf{u}' \cdot \nabla \mathbf{u}^\dagger \right\} \mathrm{d}S \mathrm{d}t \end{aligned}$$

Taking $\mathcal{B} = 0$, the boundary conditions for the adjoint system are given by:

- $\mathbf{u}^\dagger = \mathbf{0}$ at inlet ($\partial\Omega_i$) and wall ($\partial\Omega_w$);
- $(\mathbf{U} \cdot \mathbf{n})\mathbf{u}^\dagger + Re^{-1} \nabla \mathbf{u}^\dagger = p = \mathbf{0}$ at outlet ($\partial\Omega_o$).

The term $\int_{\partial\Omega} \left[\mathbf{u}' \cdot \mathbf{u}^\dagger \right]_0^\tau d\Omega$ vanishes if the constraint $\langle \mathbf{u}'(\mathbf{x}, \tau), \mathbf{u}^\dagger(\mathbf{x}, \tau) \rangle = \langle \mathbf{u}'(\mathbf{x}, 0), \mathbf{u}^\dagger(\mathbf{x}, 0) \rangle$ is satisfied. As a result of the simplifications, $< \mathbb{H}\mathbf{q}, \mathbf{q}^\dagger > - < \mathbf{q}, \mathbb{H}^\dagger \mathbf{q}^\dagger >= \mathbf{0}$ is achieved. Therefore,

$$\begin{aligned} \frac{\partial \mathcal{L}}{\partial \delta \mathbf{q}'} \delta \mathbf{q}' &= \frac{\partial}{\partial \delta \mathbf{q}'} \left(\int_\tau \int_\Omega \mathbb{H}^\dagger \mathbf{q}^\dagger \cdot \mathbf{q} \mathrm{d}\mathcal{V} \mathrm{d}t \right) \delta \mathbf{q}' \\ &= \lim_{\epsilon \to 0} \frac{\int_\tau \int_\Omega \mathbb{H}^\dagger \mathbf{q}^\dagger \cdot (\mathbf{q}' + \epsilon \delta \mathbf{q}') - (\mathbb{H}^\dagger \mathbf{q}^\dagger) \cdot \mathbf{q}' \mathrm{d}\mathcal{V} \mathrm{d}t}{\epsilon} \delta \mathbf{q}' = \int_\tau \int_\Omega (\mathbb{H}^\dagger \mathbf{q}^\dagger) \cdot \delta \mathbf{q}' \mathrm{d}\mathcal{V} \mathrm{d}t \delta \mathbf{q}' = 0 \end{aligned}$$

By making $\dfrac{\partial \mathcal{L}}{\partial \delta \mathbf{u}'(\mathbf{x},0)}\delta \mathbf{u}'(\mathbf{x},0) = 0$, it is possible to set an expression to compute the optimal energy as follows:

$$\frac{\partial \mathcal{L}}{\partial \mathbf{u}'(\mathbf{x},0)}\delta \mathbf{u}'(\mathbf{x},0) = \nabla_{\mathbf{u}'(\mathbf{x},0)}\mathbb{E}(\tau)\delta \mathbf{u}'(\mathbf{x},0) - \langle \delta \mathbf{u}'(\mathbf{x},0), \mathbf{u}^{\dagger}(\mathbf{x},0)\rangle = 0 \Rightarrow$$
$$\Rightarrow \quad \nabla_{\mathbf{u}'(\mathbf{x},0)}\mathbb{E}(\tau) = \mathbf{u}^{\dagger}(\mathbf{x},0)$$

Therefore, the energy growth gradient with respect to $\mathbf{u}'(\mathbf{x},0)$ is given by the adjoint variable $\mathbf{u}^{\dagger}(\mathbf{x},0)$. The optimal energy and optimal initial condition can be obtained from an eigenvalue problem by evaluating the constraint:

$$\begin{aligned}\langle \mathbf{u}'(\mathbf{x},\tau), \mathbf{u}^{\dagger}(\mathbf{x},\tau)\rangle - \langle \mathbf{u}'(\mathbf{x},0), \mathbf{u}^{\dagger}(\mathbf{x},0)\rangle &= \langle \mathcal{A}(\tau)\mathbf{u}'(\mathbf{x},0), \mathbf{u}^{\dagger}(\mathbf{x},\tau)\rangle - \langle \mathbf{u}'(\mathbf{x},0), \mathbf{u}^{\dagger}(\mathbf{x},0)\rangle \\ &= \langle \mathbf{u}'(\mathbf{x},0), \mathcal{A}^{\dagger}(\tau)\mathbf{u}^{\dagger}(\mathbf{x},\tau)\rangle - \langle \mathbf{u}'(\mathbf{x},0), \mathbf{u}^{\dagger}(\mathbf{x},0)\rangle = 0\end{aligned}$$

Thus, $\mathbf{u}^{\dagger}(\mathbf{x},0) = \mathcal{A}^{\dagger}(\tau)\mathbf{u}^{\dagger}(\mathbf{x},\tau)$ and $\mathcal{A}(\tau)\mathbf{u}'(\mathbf{x},0) = \mathbf{u}^{\dagger}(\mathbf{x},\tau)$. From these two equations, we can explain the relationship between optimal energy growth and the eigenvalues of the symmetric operator $\mathcal{A}^{\dagger}(\tau)\mathcal{A}(\tau)$, i.e:

$$\mathcal{A}(\tau)\mathbf{u}'(\mathbf{x},0) = \mathbf{u}^{\dagger}(\mathbf{x},\tau) \quad \Rightarrow \quad \mathcal{A}^{\dagger}(\tau)\mathcal{A}(\tau)\mathbf{u}'(\mathbf{x},0) = \mathcal{A}^{\dagger}(\tau)\mathbf{u}^{\dagger}(\mathbf{x},\tau) = \lambda \mathbf{u}^{\dagger}(\mathbf{x},\tau) = \mathbf{u}^{\dagger}(\mathbf{x},0)$$

Using Arnoldi modified method (presented in Appendix B), the optimal energy growth can be obtained by carrying out the following steps:

1. Integrate the linearized system forward in time interval τ, where the initial condition is the adjoint velocity $\mathbf{u}^{\dagger}(\mathbf{x},0)$;

2. The perturbation velocity $\mathbf{u}'(\mathbf{x},\tau)$ is used as initial condition for the adjoint system that is integrated backwards in the same time interval τ.

3. Next, the optimal energy growth is obtained by computing the growth rate λ_1 of the adjoint vector $\mathbf{u}^{\dagger}(\mathbf{x},0)$.

4.2 Sensitivity analysis

In the context of global linear stability analysis, sensitivity analysis is given by the eigenvalue gradient with respect to an arbitrary variable, such as an external forcing, for example (Giannetti & Luchini (2007), Marquet *et al.* (2008)). A mathematical expression to compute this gradient can be found by using an optimization problem formulated with the Lagrangian functional. In the global linear stability analysis, the base flow $\mathbf{Q}$ and the perturbation $\mathbf{q}'$ fields are the state variables, $\mathcal{J}$ is the least stable eigenvalue λ_1 and the control variable is the external forcing.

In this section, two approaches to sensitivity analysis will be introduced: firstly, the eigenvalue sensitivity with respect to an external forcing added to the perturbation field (structural sensitivity); secondly, the eigenvalue sensitivity with respect to an external forcing added to the base flow (sensitivity to steady forcing).

4.2.1 Structural sensitivity

Following the work introduced by Giannetti & Luchini (2007), the structural changes are due to an external forcing added in the linearized momentum equation. For this case, the goal is to find a structural modification which produces the greatest least stable eigenvalue drift $\delta\lambda_1$. To obtain this sensitivity field, let us consider a Lagrangian functional defined as

$$\mathcal{L}(\lambda_1, \widehat{\mathbf{q}}, \widehat{\mathbf{f}}, \widehat{\mathbf{q}}^\dagger) = \lambda_1 - \langle \widehat{\mathbf{q}}^\dagger, (\boldsymbol{\lambda}\mathbb{B} - \mathbb{L})\widehat{\mathbf{q}} - \widehat{\mathbf{f}} \rangle.$$

Here, the forced generalized eigenvalue problem $(\boldsymbol{\lambda}\mathbb{B} - \mathbb{L})\widehat{\mathbf{q}} - \widehat{\mathbf{f}} = 0$ is the constraint, the least stable eigenvalue λ_1 is the objective functional, and $\widehat{\mathbf{q}}^\dagger$ is the Lagrange multiplier.

At an optimum point, the gradient $\nabla\mathcal{L}(\lambda_1, \widehat{\mathbf{q}}, \widehat{\mathbf{f}}, \widehat{\mathbf{q}}^\dagger) = 0$. The procedure to reach the zero gradient is similar to that introduced in section 2.3. The treatment of each partial derivative is explained below.

- $\dfrac{\partial \mathcal{L}}{\partial \widehat{\mathbf{q}}^\dagger}\delta\widehat{\mathbf{q}}^\dagger$

  Taking the first variation with respect to the adjoint/Lagrange multiplier $\widehat{\mathbf{q}}^\dagger$ by using the eq. (4.9), we have:

$$\begin{aligned}
\frac{\partial \mathcal{L}}{\partial \widehat{\mathbf{q}}^\dagger} &= \lim_{\epsilon \to 0} \frac{\int_\tau \int_\Omega \left(\widehat{\mathbf{q}}^\dagger + \epsilon\delta\widehat{\mathbf{q}}^\dagger\right) \cdot \left[(\boldsymbol{\lambda}\mathbb{B} - \mathbb{L})\widehat{\mathbf{q}} - \widehat{\mathbf{f}}\right] + \widehat{\mathbf{q}}^\dagger \cdot \left[(\boldsymbol{\lambda}\mathbb{B} - \mathbb{L})\widehat{\mathbf{q}} - \widehat{\mathbf{f}}\right] \mathrm{d}\mathcal{V}\mathrm{d}t}{\epsilon} \\
&= \int_\tau \int_\Omega \delta\widehat{\mathbf{q}}^\dagger \cdot \left[(\boldsymbol{\lambda}\mathbb{B} - \mathbb{L})\widehat{\mathbf{q}} - \widehat{\mathbf{f}}\right] \mathrm{d}\mathcal{V}\mathrm{d}t = 0.
\end{aligned}$$

  Therefore, the partial derivative $\dfrac{\partial \mathcal{L}}{\partial \widehat{\mathbf{q}}^\dagger}\delta\widehat{\mathbf{q}}^\dagger = 0$ requires that the constraint $(\boldsymbol{\lambda}\mathbb{B} - \mathbb{L})\widehat{\mathbf{q}} - \widehat{\mathbf{f}} = \mathbf{0}$ must be satisfied in all domain Ω.

- $\dfrac{\partial \mathcal{L}}{\partial \widehat{\mathbf{q}}}\delta\widehat{\mathbf{q}}$

  On carrying out the first variation with respect to the direct mode $\widehat{\mathbf{q}}$, we have:

$$\begin{aligned}
\frac{\partial \mathcal{L}}{\partial \widehat{\mathbf{q}}}\delta\widehat{\mathbf{q}} &= \langle \widehat{\mathbf{q}}^\dagger, (\boldsymbol{\lambda}\mathbb{B} - \mathbb{L})\delta\widehat{\mathbf{q}} \rangle \\
&= -\int_\Omega p^\dagger (\nabla \cdot \delta\widehat{\mathbf{u}})\mathrm{d}\mathcal{V} + \\
&\quad -\int_\Omega \widehat{\mathbf{u}}^\dagger \cdot \left(\lambda\widehat{\mathbf{u}} + \nabla\mathbf{U} \cdot \delta\widehat{\mathbf{u}} + \mathbf{U} \cdot \nabla\delta\widehat{\mathbf{u}} - \frac{1}{Re}\nabla^2\delta\widehat{\mathbf{u}} + \nabla\delta\widehat{p}\right) \mathrm{d}\mathcal{V}
\end{aligned}$$

Applying integration by parts and then the Divergence Theorem:

$$
\begin{aligned}
\frac{\partial \mathcal{L}}{\partial \widehat{\mathbf{q}}}\delta\widehat{\mathbf{q}} &= \langle \widehat{\mathbf{q}}^{\dagger}, (\boldsymbol{\lambda}\mathbb{B} - \mathbb{L})\delta\widehat{\mathbf{q}}\rangle \\
&= \int_{\tau}\int_{\Omega}\left[\lambda\widehat{\mathbf{u}}^{\dagger} + \nabla\mathbf{U}\cdot\widehat{\mathbf{u}}^{\dagger} - \mathbf{U}\cdot\nabla\widehat{\mathbf{u}}^{\dagger} - Re^{-1}\nabla^{2}\widehat{\mathbf{u}}^{\dagger} - \nabla\widehat{p}^{\dagger}\right]\cdot\delta\widehat{\mathbf{u}}\,\mathrm{d}\mathcal{V}\mathrm{d}t + \\
&\quad + \int_{\tau}\int_{\Omega}\left[\nabla\cdot\widehat{\mathbf{u}}^{\dagger}\right]\delta\widehat{p}\,\mathrm{d}\mathcal{V}\mathrm{d}t + \\
&\quad + \underbrace{\int_{\tau}\int_{\partial\Omega}\mathbf{n}\cdot\left\{(\mathbf{U}\cdot\delta\widehat{\mathbf{u}})\widehat{\mathbf{u}}^{\dagger} + \widehat{\mathbf{u}}^{\dagger}\delta\widehat{p} + \widehat{p}^{\dagger}\delta\widehat{\mathbf{u}}\right\}\mathrm{d}\mathcal{V}\mathrm{d}t}_{I} + \\
&\quad + \underbrace{\int_{\tau}\int_{\partial\Omega}\mathbf{n}\cdot\left\{Re^{-1}\left[\delta\widehat{\mathbf{u}}\cdot\nabla\widehat{\mathbf{u}}^{\dagger} - \nabla\delta\widehat{\mathbf{u}}\cdot\widehat{\mathbf{u}}^{\dagger}\right]\right\}\mathrm{d}\mathcal{V}\mathrm{d}t}_{II}.
\end{aligned}
$$

Assuming that:

$$\lambda\widehat{\mathbf{u}}^{\dagger} + \nabla\mathbf{U}\cdot\widehat{\mathbf{u}}^{\dagger} - \mathbf{U}\cdot\nabla\widehat{\mathbf{u}}^{\dagger} - Re^{-1}\nabla^{2}\widehat{\mathbf{u}}^{\dagger} - \nabla\widehat{p}^{\dagger} = \mathbf{0} \tag{4.11}$$

$$\nabla\cdot\widehat{\mathbf{u}}^{\dagger} = 0 \tag{4.12}$$

we have an adjoint generalized eigenvalue problem, whose solution is the Lagrange multiplier $\widehat{\mathbf{q}}^{\dagger} = [\widehat{\mathbf{u}}^{\dagger}, \widehat{p}^{\dagger}]$. In this work, for flows around a fixed structure, we set $\widehat{\mathbf{u}} = \mathbf{0}$ at inlet $(\partial\Omega_i)$ and wall $(\partial\Omega_w)$, and $\nabla\widehat{\mathbf{u}}\cdot\mathbf{n} = 0$ at outlet $(\partial\Omega_o)$. So the terms I and II are reduced to:

$$
\begin{aligned}
I + II &= \int_{\tau}\int_{\partial\Omega_{i,w}}\mathbf{n}\cdot\left\{\widehat{\mathbf{u}}^{\dagger}\delta\widehat{p} - Re^{-1}\nabla\delta\widehat{\mathbf{u}}\cdot\widehat{\mathbf{u}}^{\dagger}\right\}\mathrm{d}\mathcal{V}\mathrm{d}t + \\
&+ \int_{\tau}\int_{\partial\Omega}\mathbf{n}\cdot\left\{(\mathbf{U}\cdot\delta\widehat{\mathbf{u}})\widehat{\mathbf{u}}^{\dagger} + \widehat{p}^{\dagger}\delta\widehat{\mathbf{u}} + Re^{-1}\delta\widehat{\mathbf{u}}\cdot\nabla\widehat{\mathbf{u}}^{\dagger}\right\}\mathrm{d}\mathcal{V}\mathrm{d}t
\end{aligned}
$$

Assuming $\widehat{\mathbf{u}}^{\dagger} = \mathbf{0}$ at inlet and wall, and $(\mathbf{U}\cdot\mathbf{n})\widehat{\mathbf{u}}^{\dagger} + \widehat{p}^{\dagger} + Re^{-1}\nabla\widehat{\mathbf{u}}^{\dagger} = 0$ at outlet, we arrive at $I + II = 0$ and $\dfrac{\partial \mathcal{L}}{\partial \widehat{\mathbf{q}}}\delta\widehat{\mathbf{q}} = 0$.

- $\dfrac{\partial \mathcal{L}}{\partial \lambda_1}\delta\lambda_1$

  Computing the gradient of the Lagrangian functional with respect to λ_1, we get:

$$\frac{\partial \mathcal{L}}{\partial \lambda_1}\delta\lambda_1 = \delta\lambda_1 - \langle\widehat{\mathbf{u}}^{\dagger}, \delta\lambda_1\widehat{\mathbf{u}}\rangle = \delta\lambda_1 - \langle\widehat{\mathbf{u}}^{\dagger}, \widehat{\mathbf{u}}\rangle\delta\lambda_1. \tag{4.13}$$

  Taking $\langle\widehat{\mathbf{u}}^{\dagger}, \widehat{\mathbf{u}}\rangle = 1$, $\dfrac{\partial \mathcal{L}}{\partial \lambda_1}\delta\lambda_1 = 0$ holds true.

Lastly, we work out the derivative of $\mathcal{L}$ with respect to $\widehat{\mathbf{f}}$ to achieve:

$$\frac{\partial \mathcal{L}}{\partial \widehat{\mathbf{f}}}\delta\widehat{\mathbf{f}} = \frac{\partial \lambda}{\partial \widehat{\mathbf{f}}}\delta\widehat{\mathbf{f}} = \langle \widehat{\mathbf{q}}^{\dagger}, \delta\widehat{\mathbf{f}} \rangle. \tag{4.14}$$

So we conclude that the first variation of the least stable eigenvalue, $\dfrac{\partial \lambda_1}{\partial \widehat{\mathbf{f}}}\delta\widehat{\mathbf{f}}$, is proportional to the Lagrange multiplier/adjoint mode $\widehat{\mathbf{q}}^{\dagger}$. In the optimal case, the adjoint mode corresponds to the least stable eigenvalue.

Giannetti & Luchini (2007) identified the *wavemaker* region as the region in space susceptible to structural modifications that produce the strongest drift of the eigenvalue. The *wavemaker* region was determined by assuming $\delta\widehat{\mathbf{f}} = C(\mathbf{x}) \cdot \delta\widehat{\mathbf{u}}$, i.e., the force applied on the system is proportional to velocity mode $\delta\widehat{\mathbf{u}}$. Besides that, it is supposed that the force $\delta\widehat{\mathbf{f}}$ has a localized feedback mechanism in space by setting $C(\mathbf{x}) = \delta(\mathbf{x} - \mathbf{x}_0)\mathbf{C}_0$. In this last expression, $\mathbf{C}_0$ is a constant coefficient, $\mathbf{x}_0$ is the cartesian position where the forcing acts and $\delta(\mathbf{x} - \mathbf{x}_0)$ is a Dirac delta function.

To determine the *wavemaker* region, we can rewrite the eigenvalue sensitivity in respect to external forcing (4.14) as:

$$\frac{\partial \lambda}{\partial \widehat{\mathbf{f}}}\delta\widehat{\mathbf{f}} = \langle \widehat{\mathbf{u}}^{\dagger}, \delta\widehat{\mathbf{f}} \rangle = \langle \widehat{\mathbf{u}}^{\dagger}, C(\mathbf{x})\widehat{\mathbf{u}} \rangle \leqslant ||\widehat{\mathbf{u}}^{\dagger}||^2 ||\widehat{\mathbf{u}}||^2 ||\mathbf{C}_0||^2. \tag{4.15}$$

Therefore, the eigenvalue sensitivity due to the localized feedback mechanism is limited by the product between the direct and adjoint fields $||\widehat{\mathbf{u}}^{\dagger}||^2 ||\widehat{\mathbf{u}}||^2$.

4.2.2 Sensitivity to a steady forcing

Marquet *et al.* (2008) also introduced a sensitivity study of the flow with respect to an external forcing. However, differently from the previous case, they suggest that the presence of a control cylinder also modifies the base flow and can change its dynamics. So they proposed that the sensitivity to base flow modifications should be considered. Therefore, the goal was to evaluate the modifications induced by a steady force acting on the base flow. In this case, the sensitivity had the objective of showing the regions at which the eigenvalues were more susceptible to change with the imposition of a steady force $\mathbf{f}$ in the base flow. This problem was solved using the Lagrangian functional in which the state variables were $\mathbf{Q}$ and $\widehat{\mathbf{q}}$ and the constraints were given by the forced base flow system:

$$\mathbb{N}(\mathbf{Q}) - \mathbf{f} = \left\{ \begin{array}{rcl} \nabla\mathbf{U} \cdot \mathbf{U} - \dfrac{1}{Re}\nabla^2\mathbf{U} + \nabla P - \mathbf{f} & = & \mathbf{0}, \\ \nabla \cdot \mathbf{U} & = & 0, \end{array} \right. \tag{4.16}$$

and by the generalized eigenvalue problem $(\lambda\mathbb{B} - \mathbb{L})\widehat{\mathbf{q}} = \mathbf{0}$. This Lagrangian functional is written as:

$$\mathcal{L}(\mathbf{Q}, \mathbf{f}, \widehat{\mathbf{q}}, \lambda, \mathbf{Q}^\dagger, \widehat{\mathbf{q}}^\dagger) = \lambda - \langle \widehat{\mathbf{q}}^\dagger, (\lambda\mathbb{B} - \mathbb{L})\widehat{\mathbf{q}} \rangle - \langle \mathbf{Q}^\dagger, \mathbb{N}(\mathbf{Q}) - \mathbf{f} \rangle, \tag{4.17}$$

in which $\widehat{\mathbf{q}}^\dagger$ and $\mathbf{Q}^\dagger$ are the Lagrange multipliers.

In the optimal case, all the derivatives of the Larangean functional are annulled. So analogous to the process introduced in the previous section, Fréchet derivative (4.9) is used to compute the derivatives. The explanation of how to set each of the partial derivatives to zero is the following:

- $\dfrac{\partial \mathcal{L}}{\partial \widehat{\mathbf{q}}^\dagger}\delta\widehat{\mathbf{q}}^\dagger$, $\dfrac{\partial \mathcal{L}}{\partial \widehat{\mathbf{Q}}^\dagger}\delta\widehat{\mathbf{Q}}^\dagger$ and $\dfrac{\partial \mathcal{L}}{\partial \lambda}\delta\lambda$

  When the Lagrangian derivatives with respect to Lagrange multipliers $\mathbf{q}^\dagger$ and $\mathbf{Q}^\dagger$ are computed, the constraints are enforced:

$$\frac{\partial \mathcal{L}}{\partial \widehat{\mathbf{q}}^\dagger}\delta\widehat{\mathbf{q}}^\dagger = \mathbf{0} \quad \Rightarrow \quad (\lambda\mathbb{B} - \mathbb{L})\widehat{\mathbf{q}} = \mathbf{0},$$

$$\frac{\partial \mathcal{L}}{\partial \mathbf{Q}^\dagger}\mathbf{Q}^\dagger = \mathbf{0} \quad \Rightarrow \quad \mathbb{N}(\mathbf{Q}) - \mathbf{f} = \mathbf{0}.$$

  As explained in the previous subsection, when we take the gradient $\dfrac{\partial \mathcal{L}}{\partial \widehat{\mathbf{q}}}\delta\widehat{\mathbf{q}} = 0$, we obtain the adjoint generalized eigenvalue problem (4.11). If we employ the normalization $\langle \widehat{\mathbf{u}}^\dagger, \lambda\widehat{\mathbf{u}} \rangle = \lambda\langle \widehat{\mathbf{u}}^\dagger, \widehat{\mathbf{u}} \rangle = 1$, it results in $\dfrac{\partial \mathcal{L}}{\partial \lambda}\delta\lambda = 0$.

- $\dfrac{\partial \mathcal{L}}{\partial \mathbf{Q}}\delta\mathbf{Q}$

$$\begin{aligned} \frac{\partial \mathcal{L}}{\partial \mathbf{Q}}\delta\mathbf{Q} \;&=\; -\int_\Omega \widehat{\mathbf{u}}^\dagger \cdot (\nabla\delta\mathbf{U} \cdot \widehat{\mathbf{u}} + \nabla\widehat{\mathbf{u}} \cdot \delta\mathbf{U})\,\mathrm{d}\mathcal{V} - \int_\Omega P^\dagger\,(\nabla \cdot \delta\mathbf{U})\,\mathrm{d}\mathcal{V} + \\ &\quad - \int_\Omega \mathbf{U}^\dagger \cdot \left(\nabla\delta\mathbf{U} \cdot \mathbf{U} + \delta\mathbf{U} \cdot \nabla\mathbf{U} - \frac{1}{Re}\nabla^2\delta\mathbf{U} + \nabla\delta P\right)\mathrm{d}\mathcal{V}. \end{aligned}$$

  Applying integral by parts and the divergence theorem, we arrive at:

$$\begin{aligned} \frac{\partial \mathcal{L}}{\partial \mathbf{Q}}\delta\mathbf{Q} \;&=\; -\int_\Omega \left(\nabla\widehat{\mathbf{u}} \cdot \widehat{\mathbf{u}}^\dagger - \nabla\widehat{\mathbf{u}}^\dagger \cdot \widehat{\mathbf{u}}\right) \cdot \delta\mathbf{U}\mathrm{d}\mathcal{V} - \int_\Omega \left(\nabla \cdot \mathbf{U}^\dagger\right)\delta P\mathrm{d}\mathcal{V} + \\ &\quad - \int_\Omega \left(\nabla\mathbf{U} \cdot \mathbf{U}^\dagger - \nabla\mathbf{U}^\dagger \cdot \mathbf{U} - \frac{1}{Re}\nabla^2\mathbf{U}^\dagger - \nabla P^\dagger\right) \cdot \delta\mathbf{U}\mathrm{d}\mathcal{V} - \mathcal{B}, \end{aligned}$$

where the bilinear concomitant is:

$$\mathcal{B} = \int_{\partial\Omega} \mathbf{n} \cdot \left\{ \hat{\mathbf{u}} \cdot (\delta \mathbf{U} \hat{\mathbf{u}}^\dagger) + \mathbf{U} \cdot (\delta \mathbf{U} \mathbf{U}^\dagger) + \mathbf{U}^\dagger P + P^\dagger \delta \mathbf{U} + \right.$$
$$\left. + \, Re^{-1} \left[\delta \mathbf{U} \cdot \nabla \mathbf{U}^\dagger - \nabla \delta \mathbf{U} \cdot \mathbf{U}^\dagger \right] \right\} \mathrm{d}S.$$

Therefore, we obtain the adjoint system:

$$\nabla \mathbf{U} \cdot \mathbf{U}^\dagger - \nabla \mathbf{U}^\dagger \cdot \mathbf{U} - Re^{-1} \nabla^2 \mathbf{U}^\dagger - \nabla P^\dagger = \nabla \hat{\mathbf{u}} \cdot \hat{\mathbf{u}}^\dagger - \nabla \hat{\mathbf{u}}^\dagger \cdot \hat{\mathbf{u}}, \tag{4.18}$$
$$\nabla \cdot \mathbf{U}^\dagger = 0. \tag{4.19}$$

We then set boundary conditions for this system such that $\mathcal{B} = 0$. To obtain these boundary conditions, we first consider the boundary conditions of the base flow system (4.16) and of the GEP system (4.4), and impose the following boundary conditions for the adjoint velocity:

- $\mathbf{U}^\dagger = \mathbf{0}$ at inlet ($\partial\Omega_i$) and wall ($\partial\Omega_w$);
- $(\hat{\mathbf{u}} \cdot \mathbf{n})\mathbf{u}^\dagger + (\mathbf{U} \cdot \mathbf{n})\mathbf{U}^\dagger + P^\dagger + Re^{-1} \nabla \mathbf{U}^\dagger = \mathbf{0}$ at outlet ($\partial\Omega_w$).

Therefore, $\dfrac{\partial \mathcal{L}}{\partial \mathbf{Q}} \delta \mathbf{Q} = 0$ is satisfied.

After following the steps delineated above, the total variation of the least stable eigenvalue is reduced to

$$\delta\lambda_1 = \frac{\partial \mathcal{L}}{\partial \mathbf{f}} \delta \mathbf{f} = \frac{\partial \lambda_1}{\partial \mathbf{f}} \delta\lambda_1 = \langle \mathbf{Q}^\dagger, \delta \mathbf{f} \rangle, \tag{4.20}$$

so the eigenvalue sensitivity to a steady force applied in the base field is given by $\nabla_{\mathbf{f}} \lambda_1 = \mathbf{Q}^\dagger$. The Langrange multiplier $\mathbf{Q}^\dagger$ is the solution of the adjoint system (4.18) - (4.19).

The adjoint mode $\hat{\mathbf{u}}^\dagger$ is obtained by solving the generalized eigenvalue adjoint problem (4.11), and the perturbation velocity $\hat{\mathbf{u}}$ is calculated with the generalized eigenvalue direct problem (4.4). For the optimal case, the direct ($\hat{\mathbf{u}}$) and adjoint ($\hat{\mathbf{u}}^\dagger$) modes correspond to the least stable eigenvalue λ_1.

Therefore, to obtain the eigenvalue sensitivity to a steady forcing, it is necessary to carry out the following steps:

1. Compute the steady base flow $\mathbf{Q}$ by solving the system (4.16);

2. Compute the direct modes $\hat{\mathbf{q}}$ by solving the direct generalized eigenvalue problem (4.4);

3. Compute the adjoint modes $\hat{\mathbf{q}}^\dagger$ by solving the adjoint generalized eigenvalue problem (4.11);

4. Normalize the adjoint mode $\hat{\mathbf{u}}^\dagger$ in order to obtain $\int_\Omega \hat{\mathbf{u}} \cdot \hat{\mathbf{u}}^\dagger \, \mathrm{d}\mathcal{V} = 1$.

5. Compute the eigenvalue sensitivity with respect to base flow modification by the expression (4.21);

6. Compute the adjoint field $\mathbf{Q}^\dagger$ given by the system (4.18) - (4.19).

4.2.3 Sensitivity to base flow modifications

The term on the right side of the equation (4.18) is interpreted as the base flow sensitivity (Marquet *et al.* , 2008). This can be explained by considering the Lagrangian functional:

$$\mathcal{L}(\mathbf{Q}, \mathbf{q}, \hat{\mathbf{q}}^\dagger, \lambda_1) = \lambda_1 - \langle \hat{\mathbf{q}}^\dagger, (\lambda \mathbb{B} - \mathbb{L}) \cdot \hat{\mathbf{q}} \rangle.$$

We obtain $\dfrac{\partial \mathcal{L}}{\partial \hat{\mathbf{q}}^\dagger} \delta \hat{\mathbf{q}}^\dagger = 0$ if the constraint $(\lambda \mathbb{B} - \mathbb{L}) \cdot \hat{\mathbf{q}} = \mathbf{0}$ is satisfied. We then compute the gradient of $\mathcal{L}$ with respect to base flow $\mathbf{Q}$ to arrive at

$$\frac{\partial \mathcal{L}}{\partial \mathbf{Q}} \delta \mathbf{Q} = \frac{\partial \lambda_1}{\partial \mathbf{Q}} \delta \mathbf{Q} = -\langle \nabla \hat{\mathbf{u}} \cdot \hat{\mathbf{u}}^\dagger - \nabla \hat{\mathbf{u}}^\dagger \cdot \hat{\mathbf{u}}, \delta \mathbf{U} \rangle.$$

Therefore, the eigenvalue sensitivity to base flow modifications is

$$\nabla_{\mathbf{Q}} \lambda_1 = -\nabla \hat{\mathbf{u}} \cdot \hat{\mathbf{u}}^\dagger + \nabla \hat{\mathbf{u}}^\dagger \cdot \hat{\mathbf{u}}. \tag{4.21}$$

4.3 Global linear analysis applied for flow around a fixed circular cylinder

This section has the goal to exemplify the application of the linear stability analysis and sensitivity analysis for the flow around a fixed structure. Base flow, modal analysis, and the sensitivity calculations are verified by making comparisons with results from previous works.

4.3.1 Numerical methodology

The partial differential equations were discretized and solved using the spectral/*hp* element method Karniadakis & Sherwin (2005) (a brief description of this method can be found in Appendix A). Seventh-degree polynomials were employed as basis functions in the two-dimensional simulations. A second-order stiffly-stable time-stepping scheme (Karniadakis *et al.* , 1991) was employed to advance the solution in time. The eigenvalues were obtained by solving a generalized eigenvalue problem with the Arnoldi method (Saad, 1992), as described in Appendix B. In the case of steady base flow, the Navier-Stokes system was solved for a sufficiently large time to reach the steady state.

Figure 18: Schematic diagram of a representative flow past a circular cylinder.

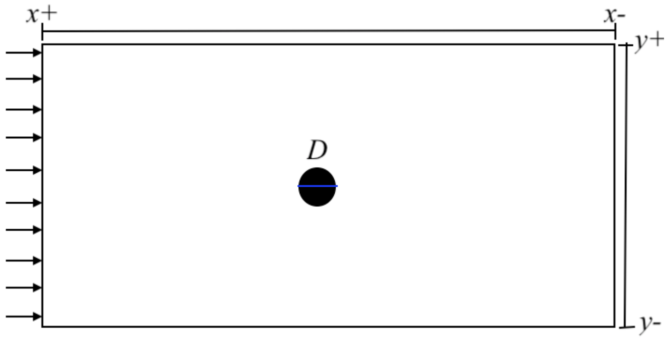

Figure 18 shows the geometry of interest. We considered a circular cylinder of diameter $D = 1$. This solid body was immersed in an uniform flow of magnitude U parallel to the x-axis, pointing to the $x+$ direction. The origin of the coordinate system was at the centre of the cylinder with dimensions: $x+ = 45D$ downstream, $x- = -25D$ upstream and $y\pm = 25D$ cross-stream. For the base and perturbation fields, Neumann high-order boundary conditions for pressure (Karniadakis *et al.* , 1991) and Dirichlet boundary conditions for the velocity were imposed at inlet and cylinder wall. The velocity boundary conditions were: at the inlet, $\mathbf{U} = (1, 0)$ for the base flow calculations, $\mathbf{u}' = \mathbf{u}^\dagger = \mathbf{U}^\dagger = \mathbf{0}$ for the linear stability analysis and for sensitivity analysis; at the cylinder wall, $\mathbf{U} = \mathbf{u}' = \mathbf{u}^\dagger = \mathbf{U}^\dagger = \mathbf{0}$; at the outlet, $\nabla\mathbf{U} \cdot \mathbf{n} = \nabla\mathbf{u}' \cdot \mathbf{n} = \nabla\mathbf{u} \cdot \mathbf{n} = 0$ and $P = p' = p^\dagger = P^\dagger = 0$ were imposed for all calculations.

4.3.2 Base flow

It is well-known that for very low Reynolds numbers, the flow follows the contour of the cylinder (see Figure 19(a)). This flow regime occurs for Reynolds numbers up to 5. As shown in Figure 19(b), when the Reynolds number increases, the steady flow separates from the rear side of the cylinder and a symmetric stable recirculation bubble is formed. For the critical Reynolds number $Re_{c0} \cong 47$, the flow undergoes a supercritical Hopf bifurcation (primary instability) that leads to a two-dimensional time-periodic laminar flow (Figure 19(c)). The two-dimensional time-periodic flow produces a vortex wake observed downstream of the cylinder, which is known as von-Kármán wake. This wake is two-dimensional for $47 \geqslant Re \leqslant 190$ (Williamson, 1989; Barkley & Henderson, 1996). The vortices are shed at a fixed non-dimensional frequency f_{st} called Strouhal frequency, which depends on the Reynolds number.

Figure 19: Flow regimes around a cylinder. Extracted from Dyke (1988).

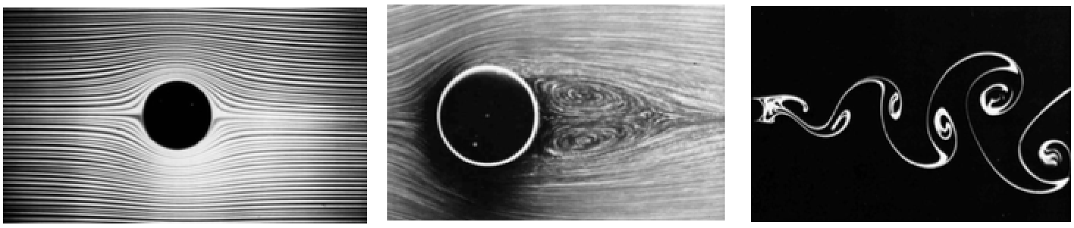

(a) $Re \lesssim 5$. (b) $5 \lesssim Re \lesssim 47$. (c) $Re \approx 50$.

As a numerical verification of the steady base flow ($Re < 47$), we compare the length of the wake bubble L_w and drag coefficient C_d measured for $Re = 20$ and $Re = 40$ with results from the literature (Table 4.1). The comparisons with Ye *et al.* (1999) and Giannetti & Luchini (2007) show good agreement. The time-periodic base flow is verified by comparing the Strouhal number for $47 < Re < 180$ with experimental data from Williamson (1989). In Figure 20, we can notice a good agreement with the results of that paper.

Table 4.1: Length of the wake bubble L_w (measured from the rear stagnation point) and drag coefficient C_D.

	$Re = 20$		$Re = 40$	
	L_w	$\overline{C_d}$	L_w	$\overline{C_d}$
Ye et al. (1999)	0.92	2.03	2.27	1.52
Ganetti & Luchini (2007)	0.92	2.05	2.24	1.54
Current work	0.95	2.06	2.25	1.54

4.3.3 Stability analysis

In order to check the methodology used to perform linear stability analysis, this section shows the comparison of the critical Re obtained for the primary instability with results found in the literature. Table 4.2 shows the growth rate λ_r and eigenfrequency $\lambda_i/(2\pi)$ associated to the leading global mode as a for Reynolds numbers between $Re = 46$ and $Re = 47$. As explained in Section 4.1, the stability can be assessed by the sign of the real part of the eigenvalue λ_r. We observed that the system changes from stable (λ_r negative) to unstable (λ_r positive) for Reynolds number between $Re = 46.5$ and $Re = 46.6$, being thus reasonable to affirm that the first instability occurs for $Re_{c0} \cong 46.6$. This value of the critical Reynolds number Re_{c0} agrees with results from the literature (Jackson, 1987; Dusěk & Fraunie, 1994). Besides that, the frequency given by the global stability analysis for this Reynolds number is $\lambda_i \cong 0.118$, which is also in good agreement with Giannetti

Figure 20: Strouhal number (St) as a function of Reynolds number (Re) for two-dimensional time-periodic flow.

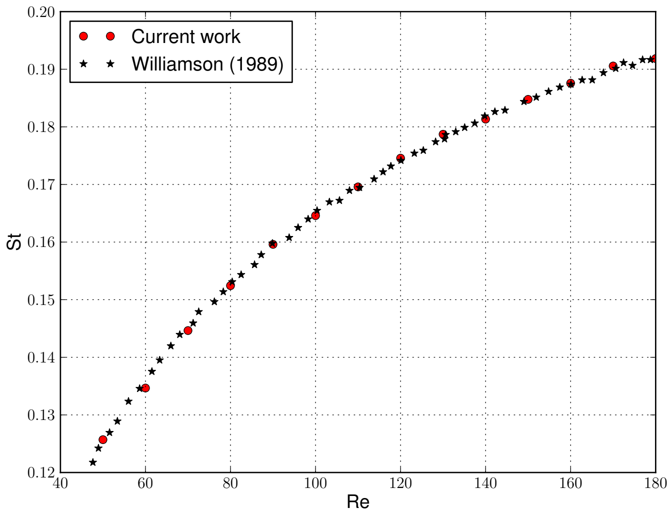

& Luchini (2007) ($\lambda_i \cong 0.118$) and Marquet *et al.* (2008) ($\lambda_i \cong 0.116$). The magnitude of the real and imaginary parts of the least stable modes are shown in figure 21.

Table 4.2: Eigenvalues for Reynolds numbers Re around of the first instability.

Re	λ_r	$\lambda_i/2\pi$
46.4	-6.7714×10^{-4}	0.11873
46.5	-2.4954×10^{-4}	0.11875
46.6	1.7694×10^{-4}	0.11878
46.7	6.0212×10^{-4}	0.1188
46.8	1.0262×10^{-3}	0.11882
47	1.8708×10^{-3}	0.11887

4.3.4 Structural sensitivity: *Wavemaker*

According to the mathematical formulation introduced in section 4.2.1, the structural sensitivity evaluates the greatest drift of the eigenvalue with respect to an external forcing added to the perturbation field. For a particular case, it was assumed in Giannetti & Luchini (2007) that this forcing was localized and proportional to mode $\hat{\mathbf{u}}$. Under this assumption, we can conclude that the expression given by $||\hat{\mathbf{u}}^{\dagger}||||\hat{\mathbf{u}}||$ provides the *wavemaker* region. The modes are computed by solving the adjoint generalized eigenvalue problem.

Figures 22 and 23 display the magnitudes of the adjoint and direct modes respectively, and they are compared with the results from Giannetti & Luchini (2007). A good agreement between the fields is observed. The direct are very different from the adjoint modes.

Figure 21: Spatial distribution of the leading global mode magnitude for critical Reynolds $Re = 46.6$.

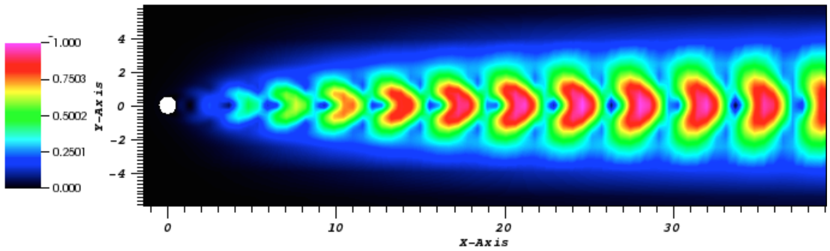

(a) Magnitude of the real part.

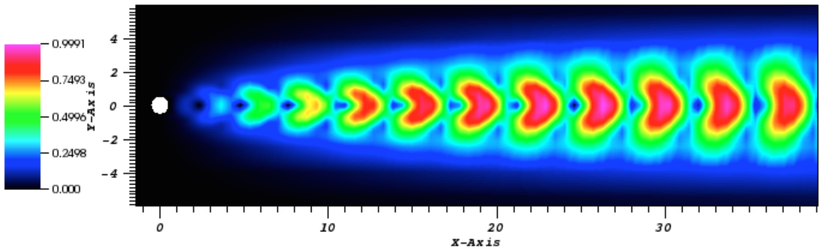

(b) Magnitude of the imaginary part.

This can be explained by the non-normality of the linearized operator $\mathbb{L}$ (Chomaz, 2005; Schmid, 2007; Trefethen *et al.* , 1993).

Figure 22: Spatial distribution of receptivity $||\widehat{\mathbf{u}}^{\dagger}||$, at $Re = 50$.

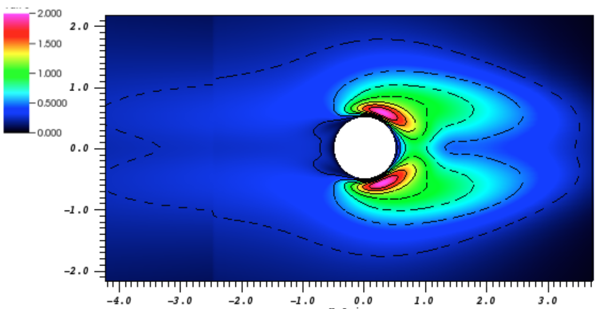

(a) Current work.

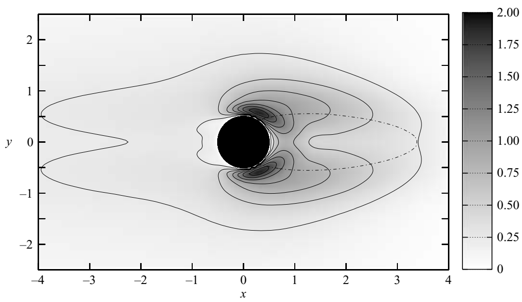

(b) Giannetti & Luchini (2007).

Comparing the adjoint magnitude field $||\widehat{\mathbf{u}}^{\dagger}||$ shown in figure 22 with the base flow shown in figure 24, we notice that the maximum responses to an external forcing (receptivity) are localized slightly downstream of the cylinder, close to the separation point of the boundary layer on the cylinder surface.

Figure 23: Spatial distribution of the perturbation velocity magnitude $||\hat{\mathbf{u}}||$.

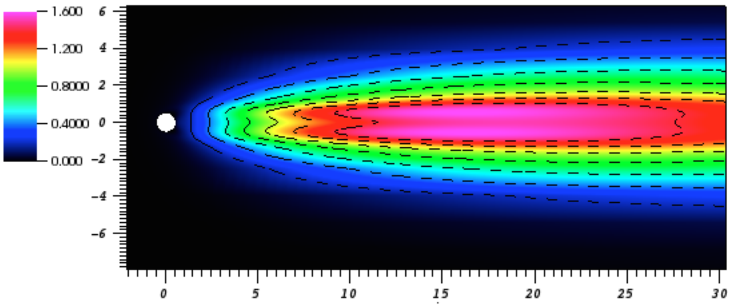

(a) Current work

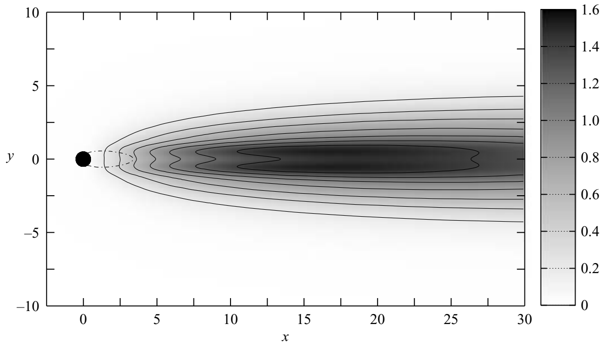

(b) Giannetti & Luchini (2007).

Figure 24: Contours of velocity magnitude and streamlines for the steady base flow at $Re = 50$

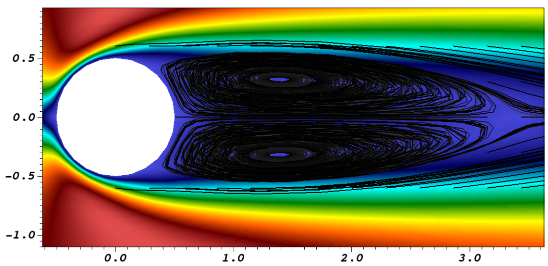

Figure 25 shows the spatial distribution of the inner product $||\hat{\mathbf{u}}^{\dagger}||^2 \cdot ||\hat{\mathbf{u}}||^2$. The regions in which a feedback control actuation can be most effective are symmetrically localized downstream of the cylinder, into the recirculation bubble. Giannetti & Luchini (2007) noticed that these regions were similar to those regions where the placement of a small control cylinder suppressed the vortex shedding in the experiments introduced by Strykowski & Sreenivasan (1990).

4.3.5 Sensitivity to base flow modifications

Figure 27 shows a qualitative comparison of the growth rate sensitivity $\nabla_{\mathbf{U}}\lambda_{1r}$ and the eigenfrequency sensitivity $\nabla_{\mathbf{U}}\lambda_{1i}$ with results from Marquet *et al.* (2008). For $Re = 46.8$, the optimal growth rate and frequency sensitivities to base flow modifications are localized

Figure 25: *Wavemaker* at $Re = 50$.

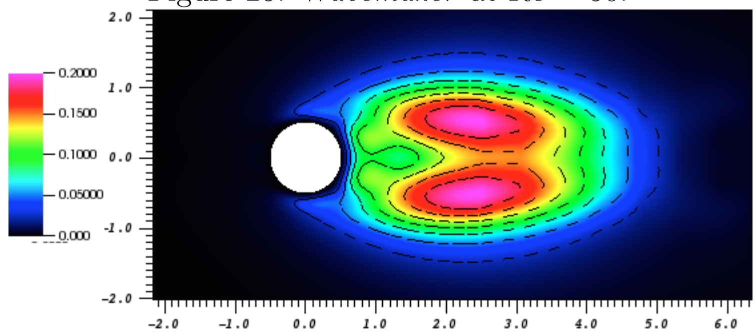

Figure 26: Streamlines of the steady base flow, at $Re = 46.8$

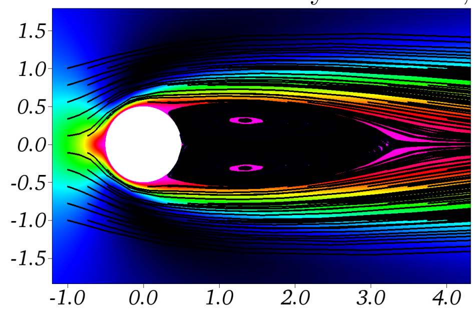

in the vicinity of the separation point and in the recirculation bubble of the steady flow, which is plotted in figure 26. The greatest variation of the eigenvalue with respect to base flow modifications is computed by the inner product $\langle \nabla_{\lambda_1} \mathbf{Q}, \delta \mathbf{f} \rangle$.

To explain the effect of a forcing $\delta \mathbf{f}$ imposed at some point of the two-dimensional domain, let us admit that $\delta \mathbf{f}$ is oriented in the same direction of the sensitivity $\nabla_{\mathbf{U}} \lambda_{1r}$ and is localized on the centerline of the recirculation bubble. So observing the streamlines of $\nabla_{\mathbf{U}} \lambda_{1r}$ and $\nabla_{\mathbf{U}} \lambda_{1i}$ plotted in figures 27(a) and 27(c) respectively, it can be noticed that $\delta \lambda_{1r}$ is positive, while $\delta \lambda_{1i}$ is negative. In contrast, if $\delta \mathbf{f}$ is oriented in the opposite direction of the sensitivity $\nabla_{\mathbf{U}} \lambda_{1r}$, $\delta \lambda_{1r}$ is negative, and $\delta \lambda_{1i}$ is positive. Therefore, in the second case, $\delta \mathbf{f}$ can stabilize the flow and increase the frequency.

4.3.6 Sensitivity to a steady forcing

Figures 28(a) and 28(b) display the growth rate and frequency sensitivities to a steady forcing. Optimal responses are localized in the vicinity of the separation point and in the centre of the recirculation bubble. A weaker region of sensitivity was identified out of the recirculation bubble, at the top and the bottom.

By evaluating the streamlines of the sensitivity fields and on considering a particular case in which a local forcing is imposed in the vicinity of the separation point or in the center of the recirculation bubble, we can see that this force has an opposite direction (downstream direction) of the sensitivity $\nabla_{\mathbf{f}} \lambda_{1r}$. So this local forcing can stabilize the flow.

Figure 27: Sensitivity to base flow modifications $\nabla_{\mathbf{U}}\lambda_1$ at $Re = 46.8$. Comparison of the spatial distribution of the growth rate sensitivity $\nabla_{\mathbf{U}}\lambda_{1r}$ (a)-(b) and the frequency sensitivity $\nabla_{\mathbf{U}}\lambda_{1i}$ (c)-(d) with results introduced by Marquet *et al.* (2008).

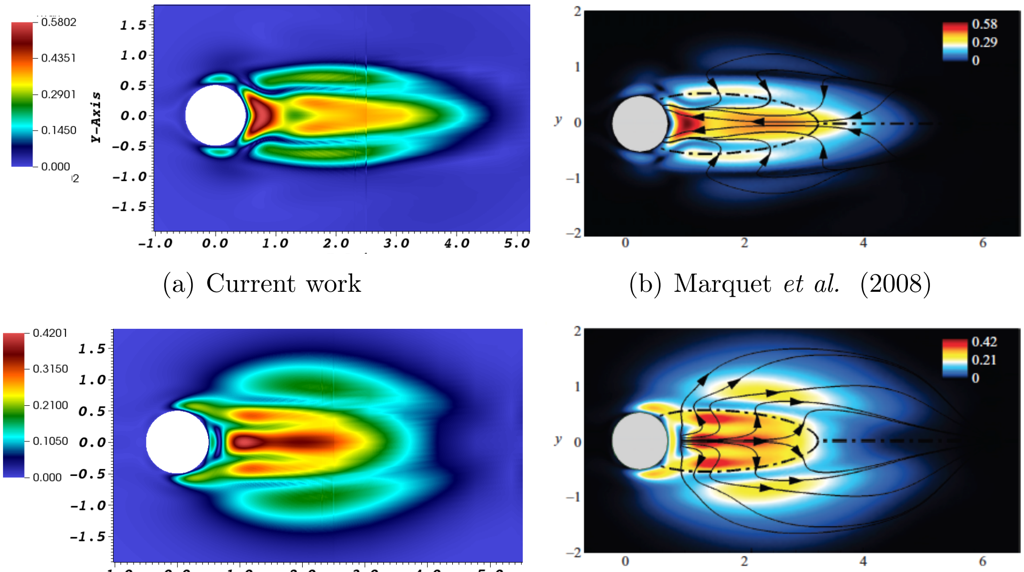

(a) Current work

(b) Marquet *et al.* (2008)

(c) Current work

(d) Marquet *et al.* (2008)

On the other hand, this forcing can destabilize the flow if applied out of the recirculation bubble, at the top or the bottom.

Marquet *et al.* (2008) considered an external forcing exerted on the base flow at a point $(x0, y0)$, where this forcing was given by the insertion of a small cylinder of diameter $d = 0.1$. Analytically, this kind of control was modelled by the following expression:

$$\delta\mathbf{f} = -0.5dC_d(Re_l)||\mathbf{U}||\mathbf{U}\delta(x_0, y_0). \tag{4.22}$$

In this equation, $C_d(Re_l)$ is the drag coefficient and is a function of the local Reynolds number Re_l. Therefore, for a steady forcing proportional to base flow velocity $\mathbf{U}$, an

Figure 28: Sensitivity to a steady forcing at $Re = 46.8$

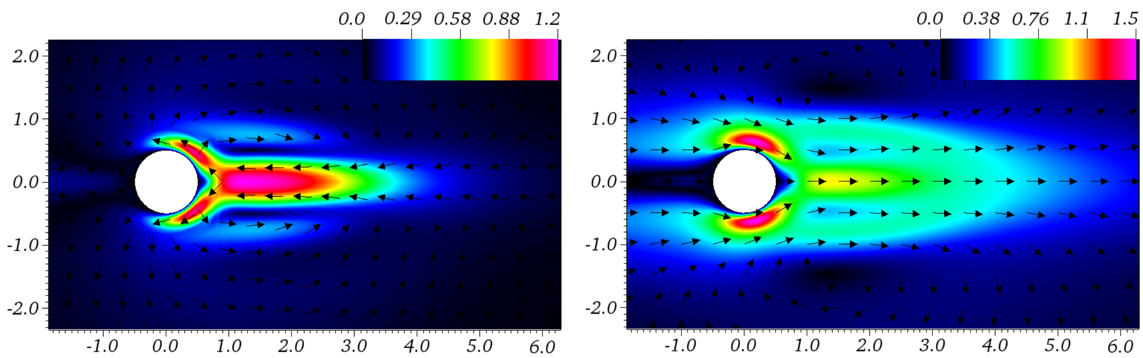

(a) $\nabla_{\mathbf{f}}\lambda_r$

(b) $\nabla_{\mathbf{f}}\lambda_i$

optimal variation of the least stable eigenvalue ($\delta\lambda_1$) can be evaluated by the expression:

$$\delta\lambda_1 = -0.5d\langle \mathbf{U}^\dagger, C_d(Re_l)||\mathbf{U}||\mathbf{U}\rangle. \tag{4.23}$$

Figure 29: Spatial distribution of the growth rate variation $\delta\lambda_{1,r}/C_d(Re_l)$ (a) and the frequency variation $\delta\lambda_{1,f}/\alpha$ (b).

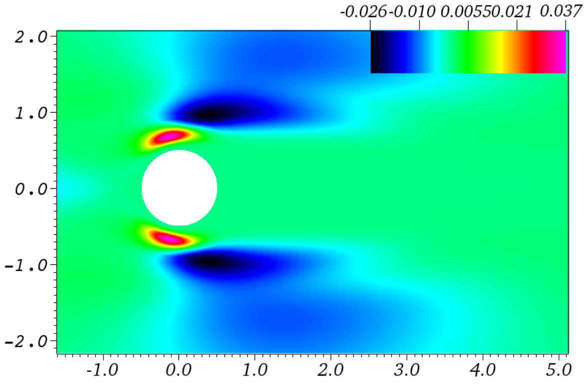

(a)

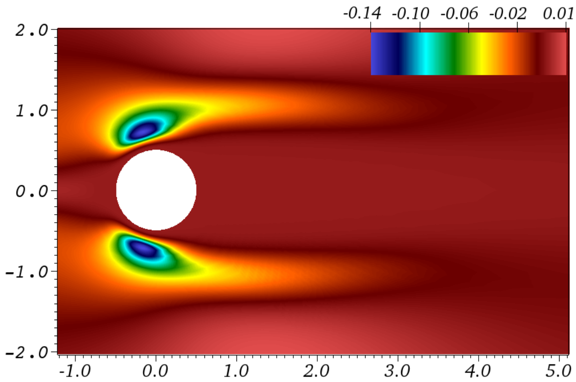

(b)

Figure 29 shows the variation $\delta\lambda_1/C_d(Re_l)$, in which an external forcing modelled by the expression (4.22) can stabilize the flow system if applied in the region where the growth rate variation $\delta\lambda_{1,r}$ is negative. Otherwise, this forcing can destabilize if applied on the regions where $\delta\lambda_{1,r} > 0$. Therefore, the growth rate increases and the frequency decreases if a local steady forcing is applied at the top and at the bottom of the cylinder. On the other hand, the growth rate decreases when the local forcing is imposed at the limit of the recirculation bubble, slightly above or below. In this same region, the frequency also decreases. These results agree with the experimental analysis introduced by Strykowski & Sreenivasan (1990). In that work, the authors present a mapping of the regions in which the insertion of small cylinder with diameter $d = 0.1$ stabilizes the system, i.e., suppress the vortex shedding.

Chapter

5

Global linear analysis: mathematical formulation for flexibly-mounted bluff bodies

In this chapter, we introduce the fluid-structure interaction (FSI) systems used to carry out linear stability analysis and sensitivity analysis. We consider the movement of a flexibly-mounted bluff body, which is governed by a mass-spring damper system. To model the linearized and adjoint FSI systems we employ the non-inertial frame of reference method.

5.1 Mass-spring-damper system

For a viscous two-dimensional flow around a flexibly-mounted structure free to oscillate in streamwise (in-line) and cross-stream (transverse) directions, the structure is governed by the mass-spring-damper system:

$$M\ddot{\mathbf{y}} + C\dot{\mathbf{y}} + K\mathbf{y} = \mathbf{F}(t). \tag{5.1}$$

The variables $\mathbf{y} = \mathbf{y}(t)$, $\dot{\mathbf{y}} = \dot{\mathbf{y}}(t)$ and $\ddot{\mathbf{y}} = \ddot{\mathbf{y}}(t)$ represent respectively the vectors of displacement, velocity and acceleration of the structure. The constant coefficients M, C and K are the mass, damping and stiffness of the system, and $\mathbf{F}$ is the fluid force described by:

$$\mathbf{F} = \int_{\partial\Omega_w} \mathbf{n} \cdot \left\{-p\mathbf{I} + Re^{-1}(\nabla\mathbf{u} + (\nabla\mathbf{u})^T)\right\} \mathrm{d}S_w = \int_{\partial\Omega_w} \mathbf{n} \cdot \boldsymbol{\sigma}(\mathbf{u}, p)\mathrm{d}S_w. \tag{5.2}$$

The subscript w indicates that the integral is calculated along the structure wall $(\partial\Omega_{w,0})$.

To make the structure equation (5.1) non-dimensional, consider the dimensional constant coefficients (M, K, C), the force $\mathbf{F}$, the variables of the system $\mathbf{y}$, $\dot{\mathbf{y}}$, $\ddot{\mathbf{y}}$ and the time t written in dimensionless form:

$$M^* = \frac{M}{\rho D^2 L}, \quad C^* = \frac{C}{\rho U_\infty D L}, \quad K^* = \frac{K}{\rho U_\infty^2 L}, \quad F^* = \frac{F}{\rho U_\infty^2 D L},$$

$$\mathbf{y}^* = \frac{\mathbf{y}}{D}, \quad \dot{\mathbf{y}}^* = \frac{\dot{\mathbf{y}}}{U_\infty}, \quad \ddot{\mathbf{y}}^* = \frac{\ddot{\mathbf{y}} D}{U_\infty^2}, \quad t^* = \frac{t U_\infty}{D}.$$

In these expressions, D and L are the diameter and the length of the cylinder, respectively, ρ is the fluid density and U_∞ is the free stream speed. Substituting these non-dimensional expressions in (5.1) and writing in convenient form, we have the non-dimensional mass-spring-damper forced system (for simplicity, the asterisks of the displacement, velocity and acceleration vectors were omitted):

$$M^* \ddot{\mathbf{y}} + C^* \dot{\mathbf{y}} + K^* \mathbf{y} = \mathbf{F}^*. \tag{5.3}$$

The system given by (5.3) and Navier-Stokes equations (2.3) govern the flow around a flexibly-mounted structure.

5.2 Non-inertial frame of reference

In this method, the system of coordinates is fixed to the structure and the mesh is not modified. We adopt the approach described in Li & Bearman (2002), but in this work we restrain the structure motion to translation $\mathbf{y}(t)$. For a two-dimensional motion, we have the following coordinate transformation between the absolute and relative frame of references:

$$x_{1,a} = y_1 + x_1, \quad x_{2,a} = y_2 + x_2. \tag{5.4}$$

The illustration of this coordinate transformation is shown in Figure 30. The coordinates $\mathbf{x}_a = [x_{1,a}, x_{2,a}, x_{3,a}]^T$ denotes an arbitrary point described in the absolute frame of reference, $\mathbf{x} = [x_1, x_2, x_3]^T$ are the coordinates of the point P described in the relative frame of reference, and $\mathbf{y}(t) = [y_1(t), y_2(t)]^T = [y_1, y_2]^T$ are the coordinates of the origin of the relative frame of reference (fixed to the structure), described in the absolute frame of reference. This coordinate transformation can be written in vector form:

$$\mathbf{x}_a = \mathbf{y} + \mathbf{x} \tag{5.5}$$

Figure 30: Coordinate transformation of the non-inertial frame of reference method.

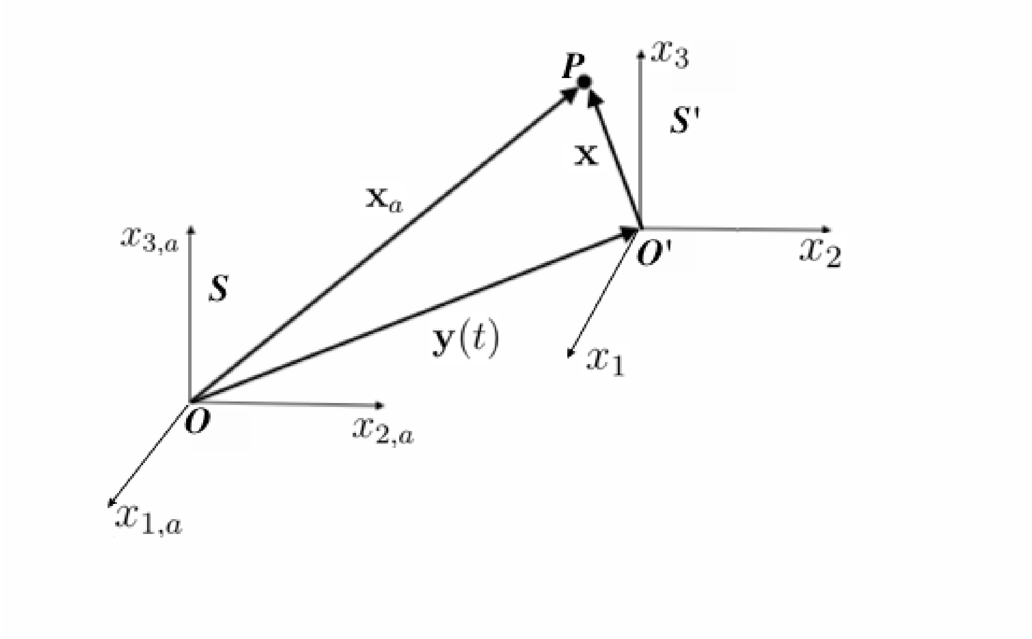

In this mapping, the velocity components are given by the time derivative of the expression (5.5). So the absolute velocity vector is described by:

$$\mathbf{u}_a = \dot{\mathbf{y}} + \mathbf{u}, \tag{5.6}$$

where $\dfrac{\partial \mathbf{x}}{\partial t} = \mathbf{u}$, $\mathbf{u}$ the relative velocity. For the two-dimensional FSI system, the non-inertial spatial derivatives have the following form:

$$\begin{aligned}
\frac{\partial}{\partial x_{1,a}} &= \frac{\partial}{\partial x_1}\frac{\partial x_1}{\partial x_{1,a}} + \frac{\partial}{\partial x_2}\frac{\partial x_2}{\partial x_{1,a}} = \frac{\partial}{\partial x_1}, \\
\frac{\partial}{\partial x_{2,a}} &= \frac{\partial}{\partial x_1}\frac{\partial x_1}{\partial x_{2,a}} + \frac{\partial}{\partial x_2}\frac{\partial x_2}{\partial x_{2,a}} = \frac{\partial}{\partial x_2}.
\end{aligned}$$

Therefore, the gradient and laplacian operators in the non-inertial form are given respectively by:

$$\nabla_a = \nabla, \tag{5.7}$$

$$\nabla_a^2 = \nabla^2. \tag{5.8}$$

To calculate the time derivative, we have to take the structure translation into account. So the absolute time derivative is:

$$\left.\frac{\partial}{\partial t}\right|_a = \left.\frac{\partial x_1}{\partial t}\right|_a \frac{\partial}{\partial x_1} + \left.\frac{\partial x_2}{\partial t}\right|_a \frac{\partial}{\partial x_2} + \left.\frac{\partial}{\partial t}\right|_r = -\dot{\mathbf{y}} \cdot \nabla + \left.\frac{\partial}{\partial t}\right|_r . \tag{5.9}$$

We now proceed to describe the motion of the fluid in the relative frame of reference. We start by writing the non-dimensional Navier-Stokes equations in absolute coordinates:

$$\begin{aligned} \left.\frac{\partial \mathbf{u}_a}{\partial t}\right|_a + \nabla_a \mathbf{u}_a \cdot \mathbf{u}_a - Re^{-1}\nabla_a^2 \mathbf{u}_a + \nabla_a p_a &= \mathbf{0}, \\ \nabla_a \cdot \mathbf{u}_a &= 0. \end{aligned}$$

Then, we rewrite the time and spatial derivatives of the Navier-Stokes equations using (5.7), (5.8) and (5.9). Besides that, we write the absolute velocity in terms of the relative velocity by using (5.6), so:

$$\left.\frac{\partial \mathbf{u}_a}{\partial t}\right|_a = -\dot{\mathbf{y}} \cdot \nabla \mathbf{u}_a + \left.\frac{\partial \mathbf{u}_a}{\partial t}\right|_r = -\dot{\mathbf{y}} \cdot \nabla \mathbf{u} + \frac{\partial \mathbf{u}}{\partial t} + \frac{\mathrm{d}\dot{\mathbf{y}}}{\mathrm{d}t},$$

$$\nabla_a \mathbf{u}_a = \nabla \mathbf{u} \quad \Rightarrow \quad \nabla \mathbf{u}_a \cdot \mathbf{u}_a = \nabla \mathbf{u} \cdot (\mathbf{u} + \dot{\mathbf{y}}), \quad \nabla_a^2 \mathbf{u}_a = \nabla^2 \mathbf{u}, \quad \nabla_a p = \nabla p.$$

After these transformations, we obtain the Navier-Stokes equations and the mass-spring-damper system equation (5.3) described in the non-inertial frame of reference:

$$\frac{\partial \mathbf{u}}{\partial t} + \nabla \mathbf{u} \cdot \mathbf{u} - \frac{1}{Re}\nabla^2 \mathbf{u} + \nabla p + \frac{\mathrm{d}\dot{\mathbf{y}}}{\mathrm{d}t} = 0, \tag{5.10}$$

$$\nabla \cdot \mathbf{u} = 0, \tag{5.11}$$

$$M^* \frac{\mathrm{d}\dot{\mathbf{y}}}{\mathrm{d}t} + C^* \dot{\mathbf{y}} + K^* \mathbf{y} = \mathbf{F}(\mathbf{u}, p). \tag{5.12}$$

The system above is used in this work to model the behaviour of the flow and the elastically-mounted structure. Here we consider external flows (uniform flow around the structure), which employ the following boundary conditions:

- Inlet: Dirichlet boundary conditions are used at inlet. Therefore, $\mathbf{u}_a = \mathbf{u} + \dot{\mathbf{y}}$, implying at $\mathbf{u} = \mathbf{u}_a - \dot{\mathbf{y}}$.
- Structure wall: At this boundary it is assumed that $\mathbf{u}_a = \dot{\mathbf{y}}$. Thus, with the change of coordinates, we have $\mathbf{u} = \mathbf{0}$.
- Outlet: Neumann boundary condition for the velocities $\mathbf{U}$ and $\mathbf{u}'$ are applied at the outlet. Hence, $\nabla \mathbf{u} \cdot \mathbf{n} = \mathbf{0}$.

5.3 Linearized fluid-structure system

As we saw in section 4.1, hydrodynamic stability analysis consists in evaluating the evolution of a perturbation $\mathbf{q}'$ superimposed to the base flow $\mathbf{Q}$. For fluid-structure interaction (FSI) problems, the same approach is adopted. However, the main difference is in the domain where the system is defined. In the "flow only" case, the Navier-Stokes system is defined in a fixed domain (Ω). Therefore, base flow and perturbation are solved in the same domain. For a FSI system, this hypothesis does not hold. Assuming $\mathbf{q} = \mathbf{Q} + \mathbf{q}'$, the steady base field $\mathbf{Q}$ is solved in a fixed domain, but the perturbation field is computed in a domain that can vary in the time.

To explain that, let us linearize the FSI system with the same approach used for the "flow only" problem. Consider the vector state $\mathbf{q} = \mathbf{Q}+\mathbf{q}' = [\mathbf{u}, p, \mathbf{y}, \dot{\mathbf{y}}] = [\mathbf{U}, P', \mathbf{Y}, \dot{\mathbf{Y}}]^T + [\mathbf{u}, p', \mathbf{y}', \dot{\mathbf{y}}']^T$, in which the structure has two degrees of freedom. Substituting this in the FSI system (5.10)-(5.12), we get:

$$
\begin{aligned}
\frac{\partial \mathbf{u}'}{\partial t} + \mathbf{U}\cdot\nabla\mathbf{u}' + \nabla\mathbf{U}\cdot\mathbf{u}' + \nabla\mathbf{u}'\cdot\mathbf{u}' - \frac{1}{Re}\nabla^2\mathbf{u}' + \nabla p' + \ddot{\mathbf{y}}' & \\
+ \underbrace{\nabla\mathbf{U}\cdot\mathbf{U} - \frac{1}{Re}\nabla^2\mathbf{U} + \nabla P + \ddot{\mathbf{Y}}}_{\text{Evolution equation for the base field}} &= 0, \\
\nabla\cdot\mathbf{u}' + \nabla\cdot\mathbf{U} &= 0, \\
M^*\ddot{\mathbf{y}}' + C^*\dot{\mathbf{y}}' + K^*\mathbf{y}' &= \mathbf{F}(\mathbf{u}', p').
\end{aligned}
$$

For a steady base flow $\mathbf{Y} = \dot{\mathbf{Y}} = \ddot{\mathbf{Y}} = \mathbf{0}$ and for small perturbation the non-linear term $(\nabla\mathbf{u}'\cdot\mathbf{u}')$ is negligible. For FSI problems, the Navier-Stokes system is described using a coordinate system $\mathbf{x}$ that is time dependent. However, the base field $\mathbf{Q}$ is defined in a fixed domain $\mathbf{x}_0$. So it is necessary to evaluate time and spatial derivatives of $\mathbf{Q}$ in the relative frame of reference $\mathbf{x}$. To work with this kind of problem, we adopted a strategy introduced in previous works (Fernández, 2001; Fernández & Tallec, 2002, 2003).

5.3.1 Flow equations

To carry out the stability analysis of a two-dimensional FSI system, let us write the velocity $\mathbf{u}$ and pressure p as a Taylor series expansion of first order around an equilibrium point $\mathbf{x}_0$. So the velocity and pressure fields are written as:

$$
\begin{aligned}
\mathbf{u} &= \mathbf{u}(\mathbf{x}_0, t) + \nabla_0\mathbf{u}(\mathbf{x}_0, t)\cdot\delta\mathbf{x} \\
p &= p(\mathbf{x}_0, t) + \nabla_0 p(\mathbf{x}_0, t)\cdot\delta\mathbf{x},
\end{aligned}
$$

where $\nabla_0 = \left[\frac{\partial}{\partial x_0}, \frac{\partial}{\partial y_0}\right]^T$. Imposing $\mathbf{q} = \mathbf{Q} + \mathbf{q}'$, velocity and pressure fields become

$$
\begin{aligned}
\mathbf{u} &= \mathbf{U}(\mathbf{x}_0) + \nabla_0\mathbf{U}(\mathbf{x}_0, t)\cdot\delta\mathbf{x} + \mathbf{u}'(\mathbf{x}_0, t) + \nabla_0\mathbf{u}'(\mathbf{x}_0, t)\cdot\delta\mathbf{x}, \\
p &= P(\mathbf{x}_0) + \nabla_0 P(\mathbf{x}_0, t)\cdot\delta\mathbf{x} + p'(\mathbf{x}_0, t) + \nabla_0 p'(\mathbf{x}_0, t)\cdot\delta\mathbf{x}.
\end{aligned}
$$

Using the hypothesis that $\delta\mathbf{x}$ is a small perturbation, the terms $\nabla_0\mathbf{u}'(\mathbf{x}_0, t)\cdot\delta\mathbf{x}$ and $\nabla_0 p'(\mathbf{x}_0, t)\cdot\delta\mathbf{x}$ can be neglected. Consequently, the velocity and pressure are described by

$$\mathbf{u} = \mathbf{U}(\mathbf{x}_0) + \nabla_0 \mathbf{U}(\mathbf{x}_0, t) \cdot \delta\mathbf{x} + \mathbf{u}'(\mathbf{x}_0, t), \tag{5.13}$$

$$p = P(\mathbf{x}_0) + \nabla_0 P(\mathbf{x}_0, t) \cdot \delta\mathbf{x} + p'(\mathbf{x}_0, t). \tag{5.14}$$

On using Taylor expansion around of $\mathbf{x}_0$, the velocity and pressure are defined in the fixed domain. However, in the FSI system (5.10)-(5.12) the domain points can move in the time. Therefore, for the correct application of the spatial gradients, it is necessary to perform coordinate transformations from/to the relative frame of reference $\mathbf{x}$ to/from the absolute frame of reference $\mathbf{x}_0$. To do that, we employ the following assumption:

$$\mathbf{x} = (\mathbf{I} + \mathbf{R}')\mathbf{x}_0.$$

This means that the coordinates of each domain point in the relative frame of reference is given by the coordinates of that point in the absolute frame of reference plus a perturbation represented by the application of a perturbation matrix $\mathbf{R}'$ in $\mathbf{x}_0$, i.e., $\delta\mathbf{x} = \mathbf{R}'\mathbf{x}_0$. In the non-inertial frame of reference method, the relative frame of reference is attached to the structure. So $\delta\mathbf{x}$ corresponds to the structure translation and is uniform for all points in the domain at a given time instant.

If we substitute eqs. (5.13) and (5.14) into eqs. (5.10) and (5.11), the spatial derivatives will give rise to terms that will include $\dfrac{\partial \mathbf{x}_0}{\partial \mathbf{x}}$ and $\dfrac{\partial \delta\mathbf{x}}{\partial \mathbf{x}}$. To find an expression for $\dfrac{\partial \mathbf{x}_0}{\partial \mathbf{x}}$, we start by expressing:

$$\frac{\partial \mathbf{x}_0}{\partial \mathbf{x}} = \left(\frac{\partial \mathbf{x}}{\partial \mathbf{x}_0}\right)^{-1} = (\mathbf{I} + \mathbf{R}')^{-1}.$$

We then write $(\mathbf{I} + \mathbf{R}')^{-1}$ as a Neumann series to obtain:

$$(\mathbf{I} + \mathbf{R}')^{-1} = \mathbf{I} - \mathbf{R}' + \mathbf{R}'^2 - \mathbf{R}'^3 + ... - ...$$

For a small perturbation ($\mathbf{R}' \ll 1$), we arrive at:

$$\frac{\partial \mathbf{x_0}}{\partial \mathbf{x}} = (\mathbf{I} + \mathbf{R}')^{-1} = \mathbf{I} - \mathbf{R}'$$

implying in $\dfrac{\partial \delta\mathbf{x}}{\partial \mathbf{x}} = \dfrac{\partial}{\partial \mathbf{x}}(\mathbf{R}'\mathbf{x}_0) = \mathbf{R}'(\mathbf{I} - \mathbf{R}')$. Retaining only the first order terms, we arrive at $\dfrac{\partial \delta\mathbf{x}}{\partial \mathbf{x}} = \mathbf{R}'$.

So the spatial gradient $\nabla \mathbf{u}$ is rewritten as:

$$\begin{aligned}
\nabla \mathbf{u} &= \nabla \left(\mathbf{U} + \nabla_0 \mathbf{U} \cdot \delta \mathbf{x} + \mathbf{u}'\right) \\
&= \nabla_0 \mathbf{U} \cdot \frac{\partial \mathbf{x}_0}{\partial \mathbf{x}} + \nabla_0 \mathbf{u}' \cdot \frac{\partial \mathbf{x}_0}{\partial \mathbf{x}} + \nabla_0 (\nabla_0 \mathbf{U}) \cdot \left(\frac{\partial \mathbf{x}_0}{\partial \mathbf{x}} \delta \mathbf{x}\right) + \nabla_0 \mathbf{U} \cdot \frac{\partial \delta \mathbf{x}}{\partial \mathbf{x}} \\
&= \nabla_0 \mathbf{U} \cdot (\mathbf{I} - \mathbf{R}') + \nabla_0 \mathbf{u}' \cdot (\mathbf{I} - \mathbf{R}') + \left(\delta x \frac{\partial}{\partial x_0} + \delta y \frac{\partial}{\partial y_0}\right) \nabla_0 \mathbf{U} \cdot (\mathbf{I} - \mathbf{R}') + \nabla_0 \mathbf{U} \cdot \mathbf{R}' \\
&= \nabla_0 \mathbf{U} + \nabla_0 \mathbf{u}' \cdot (\mathbf{I} - \mathbf{R}') + \left(\delta x \frac{\partial}{\partial x_0} + \delta y \frac{\partial}{\partial y_0}\right) \nabla_0 \mathbf{U} \cdot (\mathbf{I} - \mathbf{R}')
\end{aligned}$$

For small perturbations, the terms of second order can be neglected and we arrive at:

$$\nabla \mathbf{u} = \nabla_0 \mathbf{U} + \nabla_0 \mathbf{u}' + \left(\delta x \frac{\partial}{\partial x_0} + \delta y \frac{\partial}{\partial y_0}\right) \nabla_0 \mathbf{U}$$

Using the same procedure, the pressure gradient is:

$$\nabla p = \nabla_0 P + \nabla_0 p' + \left(\delta x \frac{\partial}{\partial x_0} + \delta y \frac{\partial}{\partial y_0}\right) \nabla_0 p$$

The divergence of the velocity is:

$$\begin{aligned}
\nabla \cdot \mathbf{u} &= \nabla \cdot \left(\mathbf{U} + \nabla_0 \mathbf{U} \cdot \delta \mathbf{x} + \mathbf{u}'\right) \\
&= \nabla_0 \cdot \mathbf{U} \frac{\partial \mathbf{x}_0}{\partial \mathbf{x}} + \nabla_0 \cdot \mathbf{u}' \cdot \frac{\partial \mathbf{x}_0}{\partial \mathbf{x}} + \nabla_0 \cdot (\nabla_0 \mathbf{U}) \cdot \left(\frac{\partial \mathbf{x}_0}{\partial \mathbf{x}} \delta \mathbf{x}\right) + \nabla_0 \cdot \mathbf{U} \cdot \frac{\partial \delta \mathbf{x}}{\partial \mathbf{x}} \\
&= (\nabla_0 \cdot \mathbf{U} + \nabla_0 \cdot \mathbf{u}') \frac{\partial \mathbf{x}_0}{\partial \mathbf{x}} + \nabla_0 (\nabla_0 \cdot \mathbf{U}) \cdot \left(\frac{\partial \mathbf{x}_0}{\partial \mathbf{x}} \delta \mathbf{x}\right)
\end{aligned}$$

The base flow and perturbed flow are divergence free, i.e., $\nabla_0 \cdot \mathbf{U} = 0$ and $\nabla \cdot \mathbf{u} = 0$. If we use that in the equation above, we conclude that $\nabla_0 \cdot \mathbf{u}' = 0$.

Regarding the Laplacian term, we have:

$$\begin{aligned}
\nabla^2 \mathbf{u} &= \nabla \cdot (\nabla \mathbf{u}) = \nabla \cdot \left(\nabla_0 \mathbf{U} + \nabla_0 \mathbf{u}' \cdot (\mathbf{I} - \mathbf{R}') + \left(\delta x \frac{\partial}{\partial x} + \delta y \frac{\partial}{\partial y}\right) \cdot \nabla_0 \mathbf{U} (\mathbf{I} - \mathbf{R}')\right) \\
&= \nabla_0^2 \mathbf{U} \cdot \frac{\partial \mathbf{x}_0}{\partial \mathbf{x}} + \nabla_0^2 \mathbf{u}' \cdot (\mathbf{I} - \mathbf{R}') \frac{\partial \mathbf{x}_0}{\partial \mathbf{x}} + \left(\frac{\partial \delta x}{\partial x} \frac{\partial}{\partial x_0} + \frac{\partial \delta y}{\partial y} \frac{\partial}{\partial y_0}\right) \nabla_0 \mathbf{U} \cdot (\mathbf{I} - \mathbf{R}') + \\
&\quad + \left(\delta x \frac{\partial}{\partial x_0} + \delta y \frac{\partial}{\partial y_0}\right) \nabla_0^2 \mathbf{U} \cdot (\mathbf{I} - \mathbf{R}') \frac{\partial \mathbf{x}_0}{\partial \mathbf{x}} \\
&= \nabla_0^2 \mathbf{U} (\mathbf{I} - \mathbf{R}') + \nabla_0^2 \mathbf{u}' \cdot (\mathbf{I} - \mathbf{R}')^2 + \left(\mathbf{R}'_0 \frac{\partial}{\partial x_0} + \mathbf{R}'_1 \frac{\partial}{\partial y_0}\right) \nabla_0 \mathbf{U} \cdot (\mathbf{I} - \mathbf{R}') + \\
&\quad + \left(\delta x \frac{\partial}{\partial x_0} + \delta y \frac{\partial}{\partial y_0}\right) \nabla_0^2 \mathbf{U} \cdot (\mathbf{I} - \mathbf{R}')^2
\end{aligned}$$

For small perturbations, we neglect the second and higher order terms, so the Laplacian is given by:

$$\begin{aligned}\nabla^2\mathbf{u} &= \nabla_0^2\mathbf{U}\cdot(\mathbf{I}-\mathbf{R}') + \nabla_0^2\mathbf{u}' + \mathbf{R}'\cdot\nabla_0^2\mathbf{U} + \left(\delta x\frac{\partial}{\partial x_0} + \delta y\frac{\partial}{\partial y_0}\right)\nabla_0^2\mathbf{U} \\ &= \nabla_0^2\mathbf{U} + \nabla_0^2\mathbf{u}' + \left(\delta x\frac{\partial}{\partial x_0} + \delta y\frac{\partial}{\partial y_0}\right)\nabla_0^2\mathbf{U}.\end{aligned}$$

The mapping of the time derivative for points $\mathbf{x}$ described in the relative frame of reference from the description in the absolute frame of reference is:

$$\left.\frac{\partial}{\partial t}\right|_{\mathbf{x}} = \frac{\partial\delta\mathbf{x}_0}{\partial t}\cdot\nabla_0 + \left.\frac{\partial}{\partial t}\right|_{\mathbf{x}_0} = \left.\frac{\partial}{\partial t}\right|_{\mathbf{x}_0}.$$

Next, substituting the velocity by (5.13), and remembering that the base flow is steady, we reach:

$$\frac{\partial\mathbf{u}}{\partial t} = \frac{\partial}{\partial t}\left(\mathbf{U}(\mathbf{x}_0) + \frac{\partial\mathbf{U}(\mathbf{x}_0,t)}{\partial x}\delta x + \frac{\partial\mathbf{U}(\mathbf{x}_0,t)}{\partial y}\delta y + \mathbf{u}'(\mathbf{x}_0,t)\right) = \left.\frac{\partial\mathbf{u}'}{\partial t}\right|_{\mathbf{x}_0} + \frac{\partial\delta\mathbf{x}}{\partial t}\cdot\nabla_0\mathbf{U}$$

Substituting the velocity field by (5.13) and using the derivatives introduced above, the momentum equation (5.10) is rewritten as:

$$\begin{aligned}&\underbrace{\left.\frac{\partial\mathbf{u}'}{\partial t}\right|_{\mathbf{x}_0} + \mathbf{U}\cdot\nabla_0\mathbf{u}' + \mathbf{u}'\cdot\nabla_0\mathbf{U} + \frac{\partial\delta\mathbf{x}}{\partial t}\cdot\nabla_0\mathbf{U} - \frac{1}{Re}\nabla_0^2\mathbf{u}' + \nabla_0 p' + \frac{\partial\dot{\mathbf{y}}'}{\partial t} + \nabla_0\mathbf{u}'\cdot\mathbf{u}' +}_{\text{Non-linear evolution equation for the perturbation}} \\ &+\delta\mathbf{x}\cdot\nabla_0\left[\underbrace{\nabla_0\mathbf{U}\cdot\mathbf{U} - \frac{1}{Re}\nabla_0^2\mathbf{U} + \nabla_0 P}_{\text{Steady base field}}\right] + \left[\underbrace{\nabla_0\mathbf{U}\cdot\mathbf{U} - \frac{1}{Re}\nabla_0^2\mathbf{U} + \nabla_0 P}_{\text{Steady base field}}\right] = 0.\end{aligned} \tag{5.15}$$

Therefore, the steady base flow is governed by:

$$\nabla_0\mathbf{U}\cdot\mathbf{U} - \frac{1}{Re}\nabla_0^2\mathbf{U} + \nabla_0 P = \mathbf{0}, \tag{5.16}$$

$$\nabla_0\cdot\mathbf{U} = 0, \tag{5.17}$$

While the momentum and mass conservation equations that govern the perturbation are described by:

$$\left.\frac{\partial\mathbf{u}'}{\partial t}\right|_{\mathbf{x}_0} + \mathbf{U}\cdot\nabla_0\mathbf{u}' + \left(\mathbf{u}' + \frac{\partial\delta\mathbf{x}}{\partial t}\right)\cdot\nabla_0\mathbf{U} - \frac{1}{Re}\nabla_0^2\mathbf{u}' + \nabla_0 p' + \left.\frac{\partial\dot{\mathbf{y}}'}{\partial t}\right|_{\mathbf{x}_0} + \underbrace{\nabla_0\mathbf{u}'\cdot\mathbf{u}'}_{\text{Non-linear term}} = 0.$$

$$\nabla\cdot\mathbf{u}' = 0,$$

To obtain the linearized system, we assume the same hypothesis used in the Section 4.1, i.e., the $\nabla_0\mathbf{u}'\cdot\mathbf{u}'$ has a smaller order than the other terms in the short time scale. Therefore, the momentum equation is rewritten as:

$$\left.\frac{\partial \mathbf{u}'}{\partial t}\right|_{\mathbf{x}_0} + \mathbf{U}\cdot\nabla_0\mathbf{u}' + \left(\mathbf{u}' + \frac{\partial \delta\mathbf{x}}{\partial t}\right)\cdot\nabla_0\mathbf{U} - \frac{1}{Re}\nabla_0^2\mathbf{u}' + \nabla_0 p' + \left.\frac{\partial \dot{\mathbf{y}}'}{\partial t}\right|_{\mathbf{x}_0} = \mathbf{0}.$$

In the non-inertial frame of reference method, $\delta\mathbf{x} = \mathbf{y}$ for all $\mathbf{x} \in \Omega$, implying in $\dfrac{\partial \delta\mathbf{x}}{\partial t} = \dot{\mathbf{y}}$. From now the notation $\frac{\partial}{\partial t}\big|_{\mathbf{x}_0} = \frac{\partial \mathbf{u}'}{\partial t}$ will be considered.

Notice that $\mathbf{u}'$ and p' are the relative velocity and pressure, respectively. However, we are interested in carrying out the stability analysis using the absolute velocity $\mathbf{u}_a'$ and p_a'. Reminding that $\mathbf{u}_a' = \mathbf{u}' + \dot{\mathbf{y}}'$ and $p_a' = p'$, the linearized Navie-Stokes system can be written as the action of the linear operator on the perturbation $\mathbf{u}_a'$ and p_a', i.e.,

$$\begin{bmatrix} \frac{\partial}{\partial t} + (\mathbf{U}\cdot\nabla_0) + (\nabla_0\mathbf{U})\cdot \quad -Re^{-1}\nabla_0^2 & \nabla_0 \\ \nabla_0\cdot & 0 \end{bmatrix} \begin{bmatrix} \mathbf{u}' + \dot{\mathbf{y}}' \\ p \end{bmatrix} =$$

$$= \begin{bmatrix} \frac{\partial}{\partial t} + (\mathbf{U}\cdot\nabla_0) + (\nabla_0\mathbf{U})\cdot \quad -Re^{-1}\nabla_0^2 & \nabla_0 \\ \nabla_0\cdot & 0 \end{bmatrix} \begin{bmatrix} \mathbf{u}_a' \\ p_a \end{bmatrix} = \begin{bmatrix} \mathbf{0} \\ 0 \end{bmatrix},$$

5.3.1.1 Structure equations

After linearizing the Navier-Stokes, the next step is to find a mass-spring-damper equation for the perturbation. To do so, we write the mass displacement as $\mathbf{y} = \mathbf{Y} + \mathbf{y}'$. For steady base flow, we have $\mathbf{Y} = \mathbf{0}$. Next, we have to deal with the force $\mathbf{F}$ given by (5.2) and considering a steady base flow:

$$\mathbf{F}(\mathbf{u}, p) = \int_{\partial\Omega_w} \mathbf{n}\cdot\sigma(\mathbf{u}, p)\mathrm{d}S_w = \int_{\partial\Omega_{w,0}} \mathbf{n}\cdot\sigma(\mathbf{u}', p')\mathrm{d}S_{w_0} + \int_{\partial\Omega_{w,0}} \mathbf{n}\cdot\nabla\sigma(\mathbf{U}, P)\delta\mathbf{x}\mathrm{d}S_{w_0}.$$

Therefore, the mass-spring-damper system that governs the displacement of the structure due to a perturbation is given by:

$$M^*\frac{\mathrm{d}\dot{\mathbf{y}}'}{\mathrm{d}t} + C^*\dot{\mathbf{y}}' + \left(K^* + \int_{\partial\Omega_{w,0}} \mathbf{n}\cdot\nabla\sigma(\mathbf{U}, P)\mathrm{d}S_{w_0}\right)\mathbf{y}' = \int_{\partial\Omega_{w,0}} \mathbf{n}\cdot\sigma(\mathbf{u}_a', p_a')\mathrm{d}S_{w_0}. \quad (5.18)$$

To conduct the stability analysis of the FSI system, it is convenient to write the mass-spring-damper system (5.18) as a system of two first order differential equations:

$$\frac{\mathrm{d}\mathbf{y}'}{\mathrm{d}t} = \mathbf{y}_1' \quad (5.19)$$

$$\frac{\mathrm{d}\mathbf{y}_1'}{\mathrm{d}t} + \frac{C^*}{M^*}\mathbf{y}_1' + \frac{K_1^*}{M^*}\mathbf{y}' = \frac{1}{M^*}\int_{\partial\Omega_{w,0}} \mathbf{n}\cdot\sigma(\mathbf{u}_a', p_a')\mathrm{d}S_{w_0}, \quad (5.20)$$

where

$$K_1^* = K^* + \int_{\partial\Omega_{w,0}} \mathbf{n} \cdot \nabla\sigma(\mathbf{U}, P)\mathrm{d}S_{w_0}$$

5.3.2 Boundary conditions

Applying the first order Taylor expansion around an equilibrium point $\mathbf{x}_0$ and using $\mathbf{u} = \mathbf{U} + \mathbf{u}'$, we describe the boundary conditions adopted for linearized FSI system:

- Inlet ($\partial\Omega_{i,0}$):

$$\mathbf{u}_a = \mathbf{U}_c + \frac{\partial \mathbf{U}_c}{\partial x_0}\delta x + \frac{\partial \mathbf{U}_c}{\partial y_0}\delta y + \mathbf{u}_a'(\mathbf{x}_0, t)$$

  In this work, we imposed a uniform velocity at inlet ($\mathbf{U}_c$). Therefore,

$$\frac{\partial \mathbf{U}_c}{\partial x_0}\delta x + \frac{\partial \mathbf{U}_c}{\partial y_0}\delta y = \mathbf{0},$$

  and the boundary condition at inlet for the perturbation velocity is $\mathbf{u}_a'(\mathbf{x}_0, t) = \mathbf{0}$.

- Structure wall ($\partial\Omega_{w,0}$):
  At this boundary $\mathbf{u}_a = \dot{\mathbf{y}}$ and $\mathbf{U} = \mathbf{0}$. Thus,

$$\mathbf{u}_a = \dot{\mathbf{y}} = \frac{\partial \mathbf{U}}{\partial x_0}\delta x + \frac{\partial \mathbf{U}}{\partial y_0}\delta y + \mathbf{u}_a'(\mathbf{x}_0, t) \quad \Rightarrow \quad \mathbf{u}_a'(\mathbf{x}_0, t) = \dot{\mathbf{y}} - \frac{\partial \mathbf{U}}{\partial x_0}\delta x - \frac{\partial \mathbf{U}}{\partial y_0}\delta y$$

- Outlet ($\partial\Omega_{o,0}$):
  Neumann boundary condition is applied at outlet. In other words, $\nabla\mathbf{u}_a \cdot \mathbf{n} = 0$, implying at $\nabla_0\mathbf{u}_a' \cdot \mathbf{n} = 0$.

5.3.3 Final system

In conclusion, the linearized FSI system that governs the perturbation fields and its boundary conditions are given by:

$$\frac{\partial \mathbf{u}_a'}{\partial t} + \mathbf{U} \cdot \nabla_0\mathbf{u}_a' + \nabla_0\mathbf{U} \cdot \mathbf{u}_a' - \frac{1}{Re}\nabla_0^2\mathbf{u}_a' + \nabla p_a' = 0 \tag{5.21}$$

$$\nabla_0 \cdot \mathbf{u}' = 0, \tag{5.22}$$

$$\frac{\mathrm{d}\mathbf{y}'}{\mathrm{d}t} = \mathbf{y}_1' \tag{5.23}$$

$$\frac{\mathrm{d}\mathbf{y}_1'}{\mathrm{d}t} + \frac{C^*}{M^*}\mathbf{y}_1' + \frac{K_1^*}{M^*}\mathbf{y}' = \frac{1}{M^*}\int_{\partial\Omega_{w,0}} \mathbf{n} \cdot \sigma(\mathbf{u}_a', p_a')\mathrm{d}S_{w_0} \tag{5.24}$$

$$\mathbf{u}' = \mathbf{0} \quad \text{at} \quad \partial\Omega_{i,0} \tag{5.25}$$

$$\mathbf{u}_a' = \dot{\mathbf{y}} - \nabla_0\mathbf{U} \cdot \delta\mathbf{x} \quad \text{at} \quad \partial\Omega_{w,0} \tag{5.26}$$

$$\nabla_0\mathbf{u}_a' \cdot \mathbf{n} = \mathbf{0} \quad \text{at} \quad \partial\Omega_{o,0} \tag{5.27}$$

Since this is a linear system, for modal analysis, we can assume the following solution for the perturbation:

$$\mathbf{q}'_a(\mathbf{x}_0, t) = \widehat{\mathbf{q}}\exp(\lambda t) = \left[\widehat{\mathbf{u}}(\mathbf{x}_0)\exp(\lambda t), \quad \widehat{p}(\mathbf{x}_0)\exp(\lambda t), \quad \widehat{\mathbf{y}}\exp(\lambda t), \quad \widehat{\mathbf{y}}_1\exp(\lambda t)\right]^T,$$

in which λ is the eigenvalue and $\widehat{\mathbf{q}}$ is the respective direct mode. Considering solutions fo this form, the linearized FSI system can be rewritten as:

$$(\boldsymbol{\lambda}\mathbb{B} - \mathbb{L})\widehat{\mathbf{q}} = \begin{cases} \lambda\widehat{\mathbf{u}} + \mathbf{U}\cdot\nabla_0\widehat{\mathbf{u}} + \nabla_0\mathbf{U}\cdot\widehat{\mathbf{u}} - \frac{1}{Re}\nabla_0^2\widehat{\mathbf{u}} + \nabla_0\widehat{p} &= 0 \\ \nabla_0\cdot\widehat{\mathbf{u}} &= 0, \\ \lambda\widehat{\mathbf{y}} - \widehat{\mathbf{y}}_1 &= \mathbf{0} \\ \lambda\widehat{\mathbf{y}}_1 + \dfrac{C^*}{M^*}\widehat{\mathbf{y}}_1 + \dfrac{K_1^*}{M^*}\widehat{\mathbf{y}} - \dfrac{1}{M^*}\mathbf{F}(\widehat{\mathbf{u}}, \widehat{p}) &= \mathbf{0}. \end{cases} \tag{5.28}$$

Satisfying the boundary conditions $\widehat{\mathbf{u}} = 0$ at inlet $(\partial\Omega_{i,0})$, $\nabla_0\widehat{\mathbf{u}}\cdot\mathbf{n} = \widehat{p} = \mathbf{0}$ at outlet $(\partial\Omega_{o,0})$ and $\widehat{\mathbf{u}} = \dot{\widehat{\mathbf{y}}} - \nabla_0\mathbf{U}\cdot\delta\mathbf{x}$ at wall of the structure $(\partial\Omega_{w,0})$.

5.4 Optimal perturbation energy growth

We have seen that even linearly stable systems can present perturbation growth for finite time. In order to assess the maximum possible growth a perturbation can have for a given time, we can formulate and solve an optimization problem, following the the methodology introduced by Mao *et al.* (2013). In this approach, we look for an initial condition (perturbation) that will give the maximum growth for finite time interval τ. Here, we adapt this methodology for a flow around an elastically-mounted cylinder.

For the FSI system we are considering, the Lagrangian functional is written as:

$$\begin{aligned} \mathcal{L}(\mathbf{q}', \mathbf{q}^\dagger, \mathbf{u}'_a(0)) = \mathbb{E}(\tau) &- \int_\tau\int_{\Omega_0}\left[\frac{\partial\mathbf{u}'_a}{\partial t} + \mathbf{U}\cdot\nabla_0\mathbf{u}'_a + \nabla_0\mathbf{U}\cdot\mathbf{u}'_a - \frac{1}{Re}\nabla_0^2\mathbf{u}'_a + \nabla_0 p'_a\right]\cdot\mathbf{u}^\dagger \mathrm{d}\mathcal{V}_0\mathrm{d}t + \\ &- \int_\tau\int_{\Omega_0}(\nabla_0\cdot\mathbf{u}'_a)\,\mathbf{p}^\dagger\mathrm{d}\mathcal{V}_0\mathrm{d}t - \int_\tau\left(\frac{\mathrm{d}\mathbf{y}'}{\mathrm{d}t} - \dot{\mathbf{y}}'_1\right)\cdot\mathbf{y}^\dagger\mathrm{d}t + \\ &- \int_\tau\left[M^*\frac{\mathrm{d}\mathbf{y}'_1}{\mathrm{d}t} - C^*\mathbf{y}'_1 + K_1^*\mathbf{y}' - \mathbf{F}(\mathbf{u}'_a, p'_a)\right]\cdot\mathbf{y}_1^\dagger\mathrm{d}t \\ &- \int_\tau\int_{\Omega_0}\mathbf{u}'_a(0)\cdot\mathbf{u}^\dagger(0)\mathrm{d}\mathcal{V}_0\mathrm{d}t - \int_\tau\mathbf{y}'(0)\cdot\mathbf{y}^\dagger(0)\mathrm{d}t - \int_\tau\dot{\mathbf{y}}'(0)\cdot\dot{\mathbf{y}}^\dagger(0)\mathrm{d}t, \end{aligned}$$

where $\mathbb{E}(\tau) = ||\mathbf{u}'_a(\mathbf{x}_0, \tau)||^2$ measures the perturbation energy which is normalized in order to satisfy $\mathbb{E}(0) = ||\mathbf{u}'_a(\mathbf{x}_0, 0)||^2 = 1$, and the vector $\mathbf{q}^\dagger = \left[\mathbf{u}^\dagger, p^\dagger, \mathbf{y}^\dagger, \dot{\mathbf{y}}^\dagger\right]^T$ is the Lagrange multiplier/adjoint variable. Like we did for the "flow only" system, we will look for function extreme by making the gradient $\dfrac{\partial\mathcal{L}(\mathbf{q}', \mathbf{q}^\dagger, \mathbf{u}'_a(0))}{\partial\mathbf{q}^\dagger}\delta\mathbf{q}^\dagger = 0$, so the linerized system (5.10–5.12) must be satisfied.

5.4.1 Adjoint system

We start by writing the expression of the variation of the Lagrangian functional with respect to a perturbation $\mathbf{q}'$:

$$\begin{aligned}\frac{\partial \mathcal{L}}{\partial \mathbf{q}'}\delta\mathbf{q}' = &-\frac{\partial}{\partial \mathbf{q}'}\int_\tau\int_{\Omega_0}\left[\frac{\partial \mathbf{u}'_a}{\partial t} + \mathbf{U}\cdot\nabla_0\mathbf{u}'_a + \nabla_0\mathbf{U}\cdot\mathbf{u}'_a - \frac{1}{Re}\nabla_0^2\mathbf{u}'_a + \nabla_0 p'_a\right]\cdot\mathbf{u}^\dagger \mathrm{d}\mathcal{V}_0\mathrm{d}t\delta\mathbf{q}' + \\ &-\frac{\partial}{\partial \mathbf{q}'}\int_\tau\int_{\Omega_0}(\nabla_0\cdot\mathbf{u}'_a)\,\mathbf{p}^\dagger\mathrm{d}\mathcal{V}_0\mathrm{d}t\delta\mathbf{q}' - \frac{\partial}{\partial \mathbf{q}'}\int_\tau\left(\frac{\mathrm{d}\mathbf{y}'}{\mathrm{d}t} - \dot{\mathbf{y}}'_1\right)\cdot\mathbf{y}^\dagger\mathrm{d}t\delta\mathbf{q}' + \\ &-\frac{\partial}{\partial \mathbf{q}'}\int_\tau\left[M^*\frac{\mathrm{d}\mathbf{y}'_1}{\mathrm{d}t} - C^*\mathbf{y}'_1 + K_1^*\mathbf{y}' - \mathbf{F}(\mathbf{u}'_a, p'_a)\right]\cdot\mathbf{y}_1^\dagger\mathrm{d}t\delta\mathbf{q}'.\end{aligned}$$

The adjoint FSI system is obtained by applying the integral by parts:

$$\begin{aligned}&\int_\tau\int_{\Omega_0}\left[\frac{\partial \mathbf{u}'_a}{\partial t} + \mathbf{U}\cdot\nabla_0\mathbf{u}'_a + \nabla_0\mathbf{U}\cdot\mathbf{u}'_a - \frac{1}{Re}\nabla_0^2\mathbf{u}'_a + \nabla_0 p'_a\right]\cdot\mathbf{u}^\dagger\mathrm{d}\mathcal{V}_0\mathrm{d}t + \\ &+\int_\tau\int_{\Omega_0}(\nabla_0\cdot\mathbf{u}'_a)\cdot\mathbf{p}^\dagger\mathrm{d}\mathcal{V}_0\mathrm{d}t + \int_\tau\left(\frac{\mathrm{d}\mathbf{y}'}{\mathrm{d}t} - \dot{\mathbf{y}}'_1\right)\cdot\mathbf{y}^\dagger\mathrm{d}t + \\ &+\int_\tau\left[M^*\frac{\mathrm{d}\mathbf{y}'_1}{\mathrm{d}t} - C^*\mathbf{y}'_1 + K^*\mathbf{y}' - \mathbf{F}(\mathbf{u}'_a, p'_a)\right]\cdot\mathbf{y}_1^\dagger\mathrm{d}t \\ &= \underbrace{\int_\tau\int_{\Omega_0}\mathbf{u}'_a\cdot\left[-\frac{\partial\mathbf{u}^\dagger}{\partial t} - \mathbf{U}\nabla_0\mathbf{u}^\dagger + \nabla_0\mathbf{U}\mathbf{u}^\dagger - Re^{-1}\nabla_0^2\mathbf{u}^\dagger - \nabla_0 p^\dagger\right]\mathrm{d}\mathcal{V}_0\mathrm{d}t}_{I} + \\ &+\underbrace{\int_\tau\int_{\Omega_0}p'_a\cdot\left[\nabla_0\cdot\mathbf{u}^\dagger\right]\mathrm{d}\mathcal{V}_0\mathrm{d}t}_{II} + \underbrace{\int_\tau\mathbf{y}'\cdot\left[-\dot{\mathbf{y}}^\dagger + K_1^*\mathbf{y}_1^\dagger\right]\mathrm{d}t}_{III} + \\ &+\underbrace{\int_\tau\mathbf{y}'_1\cdot\left[-M^*\dot{\mathbf{y}}_1^\dagger + C^*\mathbf{y}_1^\dagger - \mathbf{y}^\dagger\right]\mathrm{d}t}_{IV} - \underbrace{\int_\tau\mathbf{F}(\mathbf{u}'_a, p'_a)\cdot\mathbf{y}_1^\dagger\mathrm{d}t}_{V} + \\ &+\underbrace{\int_\tau\int_{\partial\Omega_{o,0}}\mathbf{n}\cdot\left\{(\mathbf{U}\cdot\mathbf{u}'_a)\mathbf{u}^\dagger + \mathbf{u}^\dagger p'_a + p^\dagger\mathbf{u}'_a + Re^{-1}\left[\mathbf{u}'_a\cdot\nabla_0\mathbf{u}^\dagger - \nabla_0\mathbf{u}'_a\cdot\mathbf{u}^\dagger\right]\right\}\mathrm{d}S_{o,0}\mathrm{d}t}_{VI} + \\ &+\underbrace{\int_\tau\int_{\partial\Omega_{i,0}}\mathbf{n}\cdot\left\{(\mathbf{U}\cdot\mathbf{u}'_a)\mathbf{u}^\dagger + \mathbf{u}^\dagger p'_a + p^\dagger\mathbf{u}'_a + Re^{-1}\left[\mathbf{u}'_a\cdot\nabla_0\mathbf{u}^\dagger - \nabla_0\mathbf{u}'_a\cdot\mathbf{u}^\dagger\right]\right\}\mathrm{d}S_{i,0}\mathrm{d}t}_{VII} + \\ &+\underbrace{\int_\tau\int_{\partial\Omega_w}\mathbf{n}\cdot\left\{\mathbf{U}\cdot\left(\mathbf{u}'_a\mathbf{u}^\dagger\right) - \sigma(\mathbf{u}'_a, p'_a)\cdot\mathbf{u}^\dagger + \mathbf{u}'_a\cdot\sigma(\mathbf{u}^\dagger, -p^\dagger)\right\}\mathrm{d}S_w\mathrm{d}t}_{VIII} \\ &-\underbrace{\left[\mathbf{y}'\cdot\mathbf{y}^\dagger + M^*\mathbf{y}'_1\cdot\mathbf{y}_1^\dagger\right]_0^\tau}_{IX} - \underbrace{\left[\int_{\Omega_0}\mathbf{u}'_a\cdot\mathbf{u}^\dagger\mathrm{d}\mathcal{V}\right]_0^\tau}_{X}.\end{aligned}$$

Using the boundary condition $\nabla_0\mathbf{u}'_a\cdot\mathbf{n} = \mathbf{0}$ at outlet ($\partial\Omega_{o,0}$) and assuming that this boundary is sufficiently far way of structure, we set $p' = 0$. Besides that, on imposing

$p_a^\dagger = 0$ and $(\mathbf{U}\cdot\mathbf{n})\mathbf{u}^\dagger + Re^{-1}\nabla_0\mathbf{u}^\dagger\cdot\mathbf{n} = \mathbf{0}$, the terms in bracket VI vanishes. At the inlet, on using $\mathbf{u}'_a = \mathbf{0}$ and on setting $\mathbf{u}^\dagger = \mathbf{0}$, the term in the bracket VII vanishes. For the terms V and $VIII$, we can impose a boundary condition for the adjoint velocity $\mathbf{u}^\dagger$ at the wall structure. Besides that, we can set the adjoint aerodynamic force added in adjoint mass-spring-damper system. So on using the boundary condition $\mathbf{U} = \mathbf{0}$ at $\partial\Omega_{w,0}$, the sum V + $VIII$ is reduced to:

$$\begin{aligned} V + VIII &= -\int_\tau\int_{\partial\Omega_{w,0}} \{\sigma(\mathbf{u}'_a, p'_a)\cdot\mathbf{n}\}\cdot\mathbf{y}_1^\dagger \mathrm{d}S_{w,0}\mathrm{d}t + \\ &\int_\tau\int_{\partial\Omega_{w,0}} \mathbf{n}\cdot\left\{-\sigma(\mathbf{u}'_a, p'_a)\cdot\mathbf{u}^\dagger + \mathbf{u}'_a\cdot\sigma(\mathbf{u}^\dagger, -p^\dagger)\right\}\mathrm{d}S_{w,0}\mathrm{d}t \end{aligned}$$

Taking the boundary condition $\mathbf{u}^\dagger = -\mathbf{y}_1^\dagger$ and using $\mathbf{u}'_a = \dot{\mathbf{y}}' - \nabla_0\mathbf{U}\delta x = \mathbf{y}'_1 - \nabla_0\mathbf{U}\cdot\mathbf{y}'$ at the structure wall ($\partial\Omega_{w,0}$), the terms II + IV + V + $VIII$ are reduced to:

$$\begin{aligned} II + IV + V + VIII = &\int_\tau \mathbf{y}'\cdot\left[-\dot{\mathbf{y}}^\dagger + K_1^*\mathbf{y}_1^\dagger - \int_{\partial\Omega_{w,0}}\left[\frac{\partial U}{\partial\mathbf{x}_0} + \frac{\partial V}{\partial\mathbf{x}_0}\right]\sigma(\mathbf{u}^\dagger, -p^\dagger)\cdot\mathbf{n}\mathrm{d}S_{w,0}\right]\mathrm{d}t + \\ &+\int_\tau \mathbf{y}'_1\cdot\left[-M^*\dot{\mathbf{y}}_1^\dagger + C^*\mathbf{y}_1^\dagger - \mathbf{y}^\dagger + \int_{\partial\Omega_{w,0}}\left\{\sigma(\mathbf{u}^\dagger, -p^\dagger)\right\}\cdot\mathbf{n}\mathrm{d}S_w\right]\mathrm{d}t \end{aligned}$$

Thus, considering the terms above and the terms I and II, the adjoint FSI system is given by:

$$-\frac{\partial\mathbf{u}^\dagger}{\partial t} - \mathbf{U}\cdot\nabla_0\mathbf{u}^\dagger + \nabla_0\mathbf{U}\mathbf{u}^\dagger - Re^{-1}\nabla_0^2\mathbf{u}^\dagger - \nabla_0 p^\dagger = \mathbf{0} \tag{5.29}$$

$$\nabla_0\cdot\mathbf{u}^\dagger = 0 \tag{5.30}$$

$$-\dot{\mathbf{y}}^\dagger + K_1^*\mathbf{y}_1^\dagger - \int_{\partial\Omega_{w,0}}\left[\frac{\partial U}{\partial\mathbf{x}_0} + \frac{\partial V}{\partial\mathbf{x}_0}\right]\sigma(\mathbf{u}^\dagger, -p^\dagger)\cdot\mathbf{n}\mathrm{d}S_{w,0} = \mathbf{0} \tag{5.31}$$

$$-M^*\dot{\mathbf{y}}_1^\dagger + C^*\mathbf{y}_1^\dagger - \mathbf{y}^\dagger + \int_{\partial\Omega_{w,0}}\left\{\sigma(\mathbf{u}^\dagger, -p^\dagger)\right\}\cdot\mathbf{n}\mathrm{d}S_w = \mathbf{0}, \tag{5.32}$$

subject to the following boundary conditions:

$$\mathbf{u}^\dagger = \mathbf{0} \quad \text{at} \quad \partial\Omega_{i,0} \tag{5.33}$$

$$\mathbf{u}^\dagger = -\mathbf{y}_1^\dagger \quad \text{at} \quad \partial\Omega_{w,0} \tag{5.34}$$

$$(\mathbf{U}\cdot\mathbf{n})\mathbf{u}^\dagger + Re^{-1}\nabla\mathbf{u}^\dagger\cdot\mathbf{n} = p^\dagger = \mathbf{0} \quad \text{at} \quad \partial\Omega_{o,0} \tag{5.35}$$

Therefore, $\dfrac{\partial\mathcal{L}}{\partial\mathbf{q}'}\delta\mathbf{q}' = 0$ if

$$\underbrace{\left[\mathbf{y}'\cdot\mathbf{y}^\dagger + M^*\mathbf{y}'_1\cdot\mathbf{y}_1^\dagger\right]_0^\tau}_{IX} - \underbrace{\left[\int_{\Omega_0}\mathbf{u}'_a\cdot\mathbf{u}^\dagger\mathrm{d}\mathcal{V}\right]_0^\tau}_{X} = 0$$

Writing $\mathbf{u}'_a(\mathbf{x}_0, \tau)$ as the action of the linearized Navier-Stokes equation in the initial conditions $\mathbf{u}'_a(\mathbf{x}_0, \tau)$, we reach $\mathcal{A}(\mathbf{x}_0, \tau)\mathbf{u}'_a(\mathbf{x}_0, 0) = \mathbf{u}^\dagger(\mathbf{x}_0, \tau)$ and $\mathcal{A}^\dagger(\mathbf{x}_0, \tau)\mathbf{u}^\dagger(\mathbf{x}_0, \tau) = \mathbf{u}^\dagger(\mathbf{x}_0, 0)$ for all $\mathbf{x}_0$ in Ω. Therefore, the term in bracket X is zero. At the structure wall, for all times, $\mathbf{u}^\dagger(\mathbf{x}_{0,w}, t) = -\mathbf{y}_1^\dagger(t)$ and $\mathbf{u}'_a(\mathbf{x}_{0,w_i}, t) = \mathbf{y}'_1(t)$ ($\mathbf{x}_{0,w}$ are the coordinates at the wall). So the second term of IX is zero by the same reason that the term X is zero. This way, we arrive at:

$$\left[\mathbf{y}' \cdot \mathbf{y}^\dagger\right]_0^\tau = 0$$

5.4.2 Optimal initial perturbation

Making $\dfrac{\partial \mathcal{L}}{\partial \delta \mathbf{u}'_a(\mathbf{x}_0, 0)} \delta \mathbf{u}'_a(\mathbf{x}_0, 0) = 0$ it is possible to get an expression to compute the optimal initial perturbation as follows:

$$\begin{aligned} \frac{\partial \mathcal{L}}{\partial \mathbf{u}'_a(\mathbf{x}_0, 0)} \delta \mathbf{u}'_a(\mathbf{x}_0, 0) &= \nabla_{\mathbf{u}'_a(\mathbf{x}_0,0)} \mathbb{E}(\tau) \delta \mathbf{u}'_a(\mathbf{x}_0, 0) - \langle \delta \mathbf{u}'_a(\mathbf{x}_0, 0), \mathbf{u}^\dagger(\mathbf{x}_0, 0) \rangle = 0 \\ \Rightarrow \quad & \nabla_{\mathbf{u}'_a(\mathbf{x}_0,0)} \mathbb{E}(\tau) = \mathbf{u}^\dagger(\mathbf{x}_0, 0). \end{aligned}$$

Therefore, for flow around an elastically-mounted cylinder, the optimal energy growth for a given time τ, and the initial perturbation that will result in it can be obtained carrying out the following steps:

1. Integrate the linearized system forward in time from $t = 0$ to $t = \tau$;

2. Use the final solution $\mathbf{q}'_1(\tau) = [\mathbf{u}'(\mathbf{x}_0, \tau), p'(\mathbf{x}_0, \tau), \mathbf{y}'(\tau), \mathbf{y}'_1(\tau)]$ as the initial condition for the adjoint system and integrate this system backwards in time from $t = \tau$ to $t = 0$.

3. Finally, the optimal energy growth is obtained by computing the growth rate λ of the adjoint vector $\mathbf{u}^\dagger(\mathbf{x}_0, 0)$.

5.5 Sensitivity

5.5.1 Structural sensitivity

In a process analogous to that introduced in section 4.2, structural sensitivity is obtained from an optimization problem. We want to adopt this methodology for the case in which the constraint is given by the forced perturbation FSI system:

$$\lambda\hat{\mathbf{u}} + \mathbf{U}\cdot\nabla_0\hat{\mathbf{u}} + \nabla_0\mathbf{U}\cdot\hat{\mathbf{u}} - \frac{1}{Re}\nabla^2\hat{\mathbf{u}} + \nabla_0\hat{p} = \hat{\mathbf{f}} \tag{5.36}$$

$$\nabla_0\cdot\hat{\mathbf{u}} = 0, \tag{5.37}$$

$$\lambda\hat{\mathbf{y}} = \hat{\mathbf{y}}_1 \tag{5.38}$$

$$\lambda M^*\hat{\mathbf{y}}_1 + C^*\hat{\mathbf{y}}_1 + K_1^*\hat{\mathbf{y}} = \hat{\mathbf{F}}. \tag{5.39}$$

In order to obtain the eigenvalue sensitivity with respect to an external forcing ($\hat{\mathbf{f}} = \hat{\mathbf{f}}(\mathbf{x}_0)$) added to the momentum equation (5.36), the least stable eigenvalue is the objective functional and Lagrangian functional is written as:

$$\begin{aligned}\mathcal{L}(\lambda,\hat{\mathbf{q}},\hat{\mathbf{q}}^\dagger) = \lambda - \int_\tau\int_{\Omega_0}\left[\lambda\hat{\mathbf{u}} + \mathbf{U}\cdot\nabla_0\hat{\mathbf{u}} + \nabla_0\mathbf{U}\cdot\hat{\mathbf{u}} - \frac{1}{Re}\nabla^2\hat{\mathbf{u}} + \nabla_0\hat{p} - \mathbf{f}\right]\cdot\hat{\mathbf{u}}^\dagger \mathrm{d}\mathcal{V}_0\mathrm{d}t \,+\\ -\int_\tau\int_{\Omega_0}[\nabla_0\cdot\hat{\mathbf{u}}]\cdot\hat{p}^\dagger\mathrm{d}\mathcal{V}_0\mathrm{d}t \,+\\ -\int_\tau[\lambda\hat{\mathbf{y}} - \hat{\mathbf{y}}_1]\cdot\hat{\mathbf{y}}^\dagger\mathrm{d}t - \int_\tau\left[\lambda M^*\hat{\mathbf{y}}_1 + C^*\hat{\mathbf{y}}_1 + K_1^*\hat{\mathbf{y}} - \hat{\mathbf{F}}\right]\cdot\hat{\mathbf{y}}_1^\dagger\mathrm{d}t.\end{aligned}$$

The treatment of each partial derivative is introduced below.

- $\dfrac{\partial\mathcal{L}}{\partial\hat{\mathbf{q}}^\dagger}\delta\hat{\mathbf{q}}^\dagger = \mathbf{0}$
  Analogous to "flow only" problems, by expressing this term using the definition given by eq. (4.9), the constraint given by the system (5.36)-(5.39) is enforced.

- $\dfrac{\partial\mathcal{L}}{\partial\hat{\mathbf{q}}}\delta\hat{\mathbf{q}}$:
  Applying the derivative (4.9), then the integral by parts and finally the Divergence Theorem, we have:

$$\begin{aligned}\frac{\partial\mathcal{L}}{\partial\hat{\mathbf{q}}}\delta\hat{\mathbf{q}} = -\int_\tau\int_{\Omega_0}\delta\hat{\mathbf{u}}\cdot\left[-\lambda\hat{\mathbf{u}}^\dagger - \mathbf{U}\nabla_0\hat{\mathbf{u}}^\dagger + \nabla_0\mathbf{U}\hat{\mathbf{u}}^\dagger - Re^{-1}\nabla^2\hat{\mathbf{u}}^\dagger - \nabla_0 p^\dagger\right]\mathrm{d}\mathcal{V}_0\mathrm{d}t \,+\\ \int_\tau\int_{\Omega_0}\hat{p}\cdot\left[\nabla_0\cdot\hat{\mathbf{u}}^\dagger\right]\mathrm{d}\mathcal{V}_0\mathrm{d}t - \mathcal{B} \,+\\ -\int_\tau\hat{\mathbf{y}}\cdot\left[-\dot{\mathbf{y}}^\dagger + K_1^*\hat{\mathbf{y}}_1^\dagger\right]\mathrm{d}t - \int_\tau\hat{\mathbf{y}}_1'\cdot\left[-M^*\dot{\mathbf{y}}_1^\dagger + C^*\hat{\mathbf{y}}_1^\dagger - \hat{\mathbf{y}}^\dagger\right]\mathrm{d}t + \int_\tau\mathbf{F}(\hat{\mathbf{u}},\hat{p})\cdot\hat{\mathbf{y}}_1^\dagger\mathrm{d}t\end{aligned}$$

  If we enforce that the adjoint FSI system:

$$-\lambda\hat{\mathbf{u}}^\dagger - \mathbf{U}\nabla_0\hat{\mathbf{u}}^\dagger + \nabla_0\mathbf{U}\hat{\mathbf{u}}^\dagger - Re^{-1}\nabla^2\hat{\mathbf{u}}^\dagger - \nabla_0 p^\dagger = \mathbf{0} \tag{5.40}$$

$$\nabla_0\cdot\hat{\mathbf{u}}^\dagger = 0, \tag{5.41}$$

$$\lambda\hat{\mathbf{y}}^\dagger + K_1^\dagger\hat{\mathbf{y}}_1^\dagger - \int_{\partial\Omega_{w,0}}\nabla_0\mathbf{U}\cdot\sigma(\hat{\mathbf{u}}^\dagger,-p^\dagger)\cdot\mathbf{n}\mathrm{d}S_{w,0} = \mathbf{0} \tag{5.42}$$

$$-M^\dagger\lambda\hat{\mathbf{y}}_1^\dagger + C^\dagger\hat{\mathbf{y}}_1^\dagger - \hat{\mathbf{y}}^\dagger - \int_{\partial\Omega_{w,0}}\sigma(\hat{\mathbf{u}}^\dagger,-p^\dagger)\cdot\mathbf{n}\mathrm{d}S_{w,0} = \mathbf{0}, \tag{5.43}$$

subject to boundary conditions:

$$\widehat{\mathbf{u}}^{\dagger} = \mathbf{0} \quad \text{at} \quad \partial\Omega_{i,0} \tag{5.44}$$

$$\widehat{\mathbf{u}}^{\dagger} = -\widehat{\mathbf{y}}_1^{\dagger} \quad \text{at} \quad \partial\Omega_{w,0} \tag{5.45}$$

$$(\mathbf{U}\cdot\mathbf{n})\widehat{\mathbf{u}}^{\dagger} + Re^{-1}\nabla_0\widehat{\mathbf{u}}^{\dagger}\cdot\mathbf{n} = p^{\dagger} = \mathbf{0} \quad \text{at} \quad \partial\Omega_{o,0}. \tag{5.46}$$

We reach $\mathcal{B} = \mathbf{0}$ and $\dfrac{\partial\mathcal{L}}{\partial\widehat{\mathbf{q}}}\delta\widehat{\mathbf{q}} = 0$.

Details of how to obtain the adjoint system and its boundary conditions are omitted due to similarly with the process introduced on previous section.

- $\dfrac{\partial\mathcal{L}}{\partial\lambda}\delta\lambda$:

$$\frac{\partial\mathcal{L}}{\partial\lambda}\delta\lambda = \delta\lambda - \langle\widehat{\mathbf{u}}^{\dagger},\widehat{\mathbf{u}}\rangle\delta\lambda - (\widehat{\mathbf{y}}\cdot\widehat{\mathbf{y}}^{\dagger} + \widehat{\mathbf{y}}_1\cdot\widehat{\mathbf{y}}_1^{\dagger})\delta\lambda. \tag{5.47}$$

Taking $\langle\widehat{\mathbf{u}}^{\dagger},\widehat{\mathbf{u}}\rangle = 1$ and $(\widehat{\mathbf{y}}\cdot\widehat{\mathbf{y}}^{\dagger} + \widehat{\mathbf{y}}_1\cdot\widehat{\mathbf{y}}_1^{\dagger}) = 0$, the gradient $\dfrac{\partial\mathcal{L}}{\partial\lambda}\delta\lambda = 0$ is satisfied.

Finally, the sensitivity of the less stable eigenvalue with respect to an external forcing imposed in the perturbations field is computed by the expression:

$$\frac{\partial\mathcal{L}}{\partial\mathbf{f}}\delta\mathbf{f} = \frac{\partial\lambda}{\partial\mathbf{f}}\delta\widehat{\mathbf{f}}, \tag{5.48}$$

in which

$$\frac{\partial\mathcal{L}}{\partial\mathbf{f}}\delta\mathbf{f} = \int_{\Omega_0}\widehat{\mathbf{u}}^{\dagger}\cdot\delta\mathbf{f}\,\mathrm{d}\mathcal{V}_0 = \langle\widehat{\mathbf{u}}^{\dagger},\delta\mathbf{f}\rangle.$$

Analogous to the "flow only" problems, the structural sensitivity of a FSI case is proportional to adjoint mode $\widehat{\mathbf{u}}^{\dagger}$.

5.5.2 Sensitivity to a steady forcing

Adapting the methodology introduced in section 4.2.2 for an FSI system, the Lagrangian functional is written as:

$$\begin{aligned}
\mathcal{L}(\mathbf{Q},\mathbf{f},\widehat{\mathbf{q}},\lambda,\mathbf{Q}^{\dagger},\widehat{\mathbf{q}}^{\dagger}) = \lambda - \int_{\tau}\int_{\Omega_0}\left[\lambda\widehat{\mathbf{u}} + \mathbf{U}\cdot\nabla_0\widehat{\mathbf{u}} + \nabla_0\mathbf{U}\cdot\widehat{\mathbf{u}} - \frac{1}{Re}\nabla^2\widehat{\mathbf{u}} + \nabla_0\widehat{p} - \mathbf{f}\right]\cdot\widehat{\mathbf{u}}^{\dagger}\mathrm{d}\mathcal{V}_0\mathrm{d}t + \\
- \int_{\tau}\int_{\Omega_0}[\nabla_0\cdot\widehat{\mathbf{u}}]\cdot\widehat{p}^{\dagger}\mathrm{d}\mathcal{V}_0\mathrm{d}t + \\
- \int_{\tau}[\lambda\widehat{\mathbf{y}} - \widehat{\mathbf{y}}_1]\cdot\widehat{\mathbf{y}}^{\dagger}\mathrm{d}t - \int_{\tau}[\lambda M^*\widehat{\mathbf{y}}_1 + C^*\widehat{\mathbf{y}}_1 + K_1^*\widehat{\mathbf{y}} - \mathbf{F}(\widehat{\mathbf{u}},\widehat{p})]\cdot\widehat{\mathbf{y}}_1^{\dagger}\mathrm{d}t + \\
- \int_{\tau}\int_{\Omega_0}\mathbf{Q}^{\dagger}\cdot[\mathbb{N}(\mathbf{Q}) - \mathbf{f}]\,\mathrm{d}\mathcal{V}_0\mathrm{d}t
\end{aligned}$$

in which $\widehat{\mathbf{q}}^\dagger$ and $\mathbf{Q}^\dagger$ are the Lagrange multipliers. The constraint $\mathbb{N}(\mathbf{Q}) - \mathbf{f}$ is the forced steady base flow (4.16).

The constraints are enforced carrying out $\dfrac{\partial \mathcal{L}}{\partial \widehat{\mathbf{q}}^\dagger}\delta\widehat{\mathbf{q}}^\dagger = 0$ and $\dfrac{\partial \mathcal{L}}{\partial \mathbf{Q}^\dagger}\delta\mathbf{Q}^\dagger = 0$. Like in section 4.2.2, making the gradient $\dfrac{\partial \mathcal{L}}{\partial \mathbf{Q}}\delta\mathbf{Q} = 0$ we obtain the adjoint system (4.18–4.19), and the mathematical expression of the sensitivity to a steady force is $\nabla_{\lambda_1}\mathbf{f} = \mathbf{Q}^\dagger$. The difference from this kind of sensitivity computation to an FSI global analysis is only in the solution of the eigenmode $\widehat{\mathbf{u}}$. In the current case, the mode $\widehat{\mathbf{u}}$ and $\widehat{\mathbf{u}} * \dagger$ are solution of an FSI eigensystem.

Chapter

6

Eigenvalue sensitivity for flow around an elastically-mounted cylinder

Recent studies have applied global linear stability analysis for the flow around elastically-mounted bluff bodies (Cossu & Morino, 2000; Meliga & Chomaz, 2011; Zhang *et al.* , 2015; Navrose & Mittal, 2016; Yao & Jaiman, 2017). For a circular cylinder free to oscillate, it was shown from non-linear (Mittal & Singh, 2005) and linear analysis (Cossu & Morino, 2000; Zhang *et al.* , 2015; Navrose & Mittal, 2016) that the first instability can occur for $Re < 47$. Figure 31(a) shows the stability regions on a (Re, m^*) map (m^* is the mass of the moving body divided by the mass of displaced fluid) introduced by Meliga & Chomaz (2011). In this figure, the regions in which the flow was unstable (U) are shaded, and the regions in which the flow was stable (S) are clear. Cossu & Morino (2000), Meliga & Chomaz (2011), Zhang *et al.* (2015) and Navrose & Mittal (2016) performed linear stability analysis and found two least stable modes. For high mass ratio ($m^* \geqslant 20$), Navrose & Mittal (2016) named these modes as elastic mode (EM) and fluid mode (FM). For low mass ratio ($m^* \leqslant 5$), the two least stable modes were referred to as fluid elastic mode I (FEMI) and fluid elastic mode II (FEMII). These modes satisfied the following characteristics: the frequency of the eigenvalue of the EM tends to the natural frequency of the structure and the eigenvalues of the FM are similar to the leading eigenvalues of the flow past a fixed cylinder; the modes FEMI and FEMII do not present a clear definition, i.e., these modes cannot be defined as a EM or a FM. Navrose & Mittal (2016) described the modes as decoupled when there was a clear distinction of the two least stable modes as EM or FM. Otherwise, these modes were named as coupled. Figure 31(b) shows a diagram of (Re, m^*) with the regions in which the modes are coupled and decoupled.

Departing from the linear stability analysis results, this chapter introduces the results of sensitivity analysis in the flow around an elastically-mounted circular cylinder. We start verifying the mathematical and numerical methodology by comparing our results of

Figure 31: (a) Linear stability map for (Re, m^*) pairs. Shaded regions are those for which the system is unstable (U), the clear regions indicate the parameter space for which the system is stable (S); (b) Mapping of coupled and decoupled modes, as a function of Re and m^*). Re_0 represents the critical Reynolds number of the fixed cylinder.

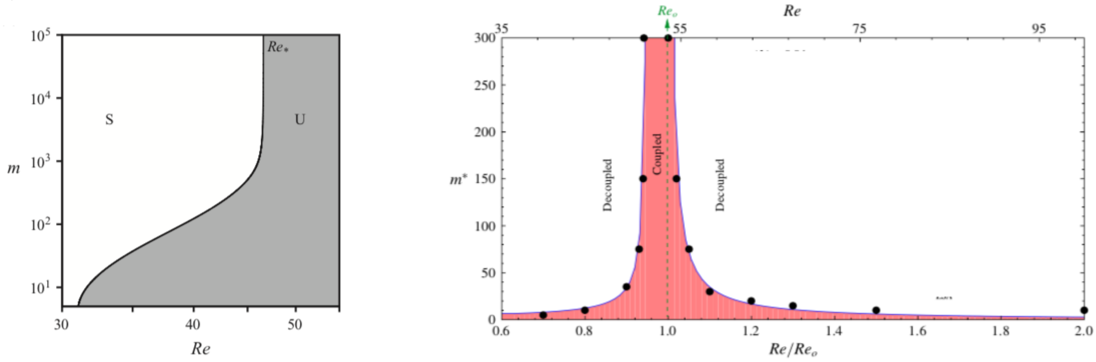

(a) Extracted from Meliga & Chomaz (2011) (b) Extracted from Navrose & Mittal (2016)

linear stability analysis with data published in the literature. Next, the solution of the adjoint FSI system is verified by comparisons of its eigenvalues with the eigenvalues of the direct FSI system. Sensitivity measures are then performed to evaluate the regions that are more receptive to an external forcing for cases inside and outside of the lock-in range, for low and high values of mass ratio m^*.

6.1 Numerical methodology

Numerical simulations were carried out in a two-dimensional domain with the settings presented in section 4.3.1. Seventh-degree polynomials were employed as basis functions in the two-dimensional simulations. A second-order stiffly stable time-stepping scheme Karniadakis *et al.* (1991) was employed to advance the solution in time. The eigenvalues were obtained by solving a generalized eigenvalue problem with the Arnoldi method Saad (1992). For the steady base flow case, the Navier-Stokes system was solved for a sufficiently large time to reach the steady state. For the flow around an elastically-mounted cylinder, the non-linear FSI system was solved for a time interval long enough for the structure displacement to reach a constant amplitude of oscillation. The displacement of the circular cylinder is governed by the non-dimensional mass-spring-damper system:

$$\frac{\pi m^*}{4}\ddot{\mathbf{y}} + \frac{\pi^2 \zeta m^*}{V_r}\dot{\mathbf{y}} + \frac{\pi^3 m^*}{V_r^2}\mathbf{y} = \mathbf{F}(\mathbf{u}, p), \tag{6.1}$$

where $m^* = \dfrac{4M}{\rho \pi D^2 L} = 4M^*/\pi$ is the mass ratio, $\zeta = \dfrac{C}{2\sqrt{KM}}$ represents the damping ratio, $V_r = \dfrac{U_\infty}{f_n D}$ is the reduced velocity and $f_n = \dfrac{\sqrt{KM}}{2\pi}$ is the natural frequency of the structure in vacuum.

All the results presented in this chapter are applied for an elastically-mounted cylinder free to oscillate only in transverse direction. The Newmark-*beta* algorithm (Newmark, 1959) was adopted to integrate the mass-spring-damper equation in time. For low mass ratio, the fictitious mass-method was employed (Baek & Karniadakis, 2012).

6.2 Stability analysis

First of all, numerical verification was carried out by performing computational simulations of the flow around a circular cylinder allowed to vibrate in the transverse direction at $Re = 33$ for a range of reduced velocities. The mass ratio was $m^* = 4.73$ and structural damping $\zeta = 0$ were chosen to match the setup used by Mittal & Singh (2005). Figure 32(a) shows results of cylinder amplitude oscillation y_{max} as a function of V_r obtained by Mittal & Singh (2005) and from the current work; the agreement is good. We also verified the modal analysis methodology by comparing the least stable eigenvalues we obtained for a range of V_r to the results provided by Zhang *et al.* (2015) at $(Re, m^*, \zeta) = (33, 50, 0)$ (Figure 32(b)) and $(Re, m^*, \zeta) = (60, 10, 0)$ (Figure 33). Results from Navrose & Mittal (2016) are also used in comparisons for $(Re, m^*, \zeta) = (60, 10, 0)$ as can be seen in Figure 33.

Figure 32(b) shows real and imaginary parts with respect to V_r of the least stable eigenvalue for $(Re, m^*, \zeta) = (33, 50, 0)$, where the results present a good concordance with Zhang *et al.* (2015). In this particular case, the eigen-frequencies $\lambda_i/(2\pi)$ tend to natural frequency f_n. Therefore, the least stable eigenvalues correspond to the EM. Figure 33 displays comparisons of the two least stable eigenvalues. Results introduced by Navrose & Mittal (2016) and Zhang *et al.* (2015) are used to verify our results for a range of V_r, at $(Re, m^*, \zeta) = (60, 10, 0)$. The eigen-frequencies $\lambda_i/(2\pi)$ match those from Navrose & Mittal (2016) and Zhang *et al.* (2015), but the real part presents some discrepancies. However, the general behaviour of λ_r with respect to V_r agrees with Navrose & Mittal (2016) and Zhang *et al.* (2015). In this case, the eigen-frequencies $\lambda_i/(2\pi)$ of the least stable eigenvalue tend to the frequency of the cylinder. In contrast, the eigen-frequencies $\lambda_i/(2\pi)$ of the second least stable eigenvalues tend to the natural frequency (f_n) of the cylinder. Therefore, the least stable eigenvalues correspond to FM, and the second least stable eigenvalues correspond to EM.

To explain the relation between the lock-in range and the least unstable modes, we consider two cases: $(Re, m^*, \zeta) = (33, 50, 0)$ and $(Re, m^*, \zeta) = (60, 10, 0)$. For $(Re, m^*, \zeta) = (33, 50, 0)$, only the EM is unstable. So we compare the range in which $\lambda_r > 0$ with the lock-in range as shown in Figure 34. It was verified that these two ranges match, i.e., for $6.8 < V_r < 10.3$ the eigenvalue of EM is positive and the cylinder presents non zero oscillation amplitude. For $(Re, m^*, \zeta) = (60, 20, 0)$, the FSI system is unstable for all V_r. However, in Figure 35 we see that the transverse oscillation starts at the same value of

Figure 32: (a) Amplitude of cylinder oscillation (y_{max}) compared with Mittal & Singh (2005), at $Re = 33$, $m^* = 4.73$ and $\zeta = 0$; (b) real part λ_r (left) and eigen-frequencies $\lambda_i/(2\pi)$ (right) of the least stable eigenvalues compared with data from Zhang *et al.* (2015), at $Re = 33$, $m^* = 50$ and $\zeta = 0$.

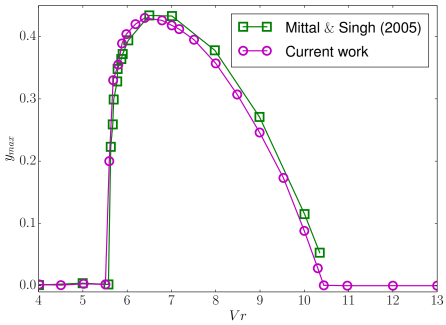

(a)

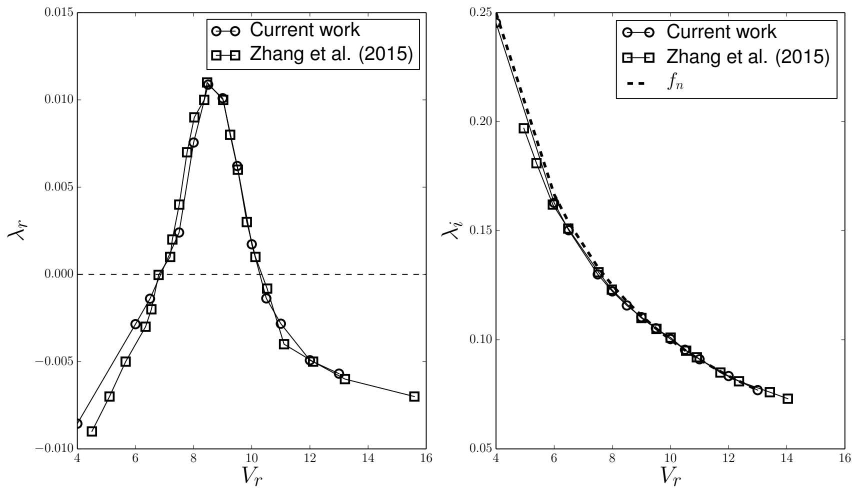

(b)

Figure 33: Real and imaginary part if the less two stable modes compared with Navrose & Mittal (2016); Zhang *et al.* (2015), at $(Re = 60, m^*, \zeta) = (60, 10, 0)$.

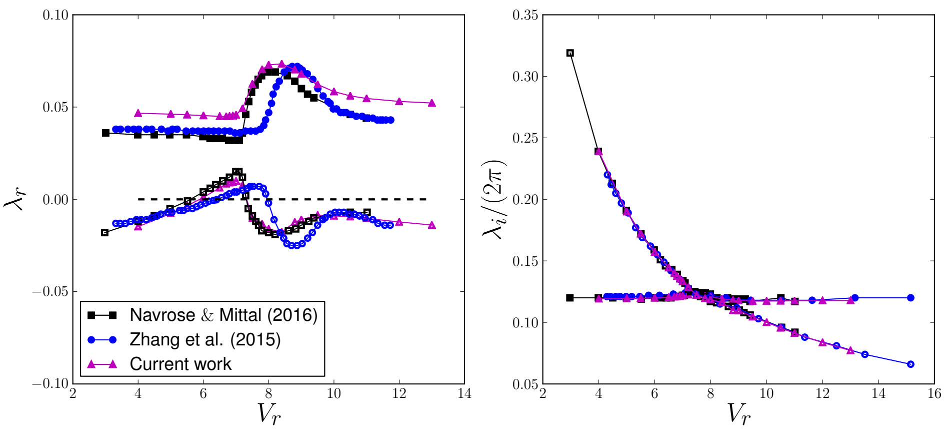

Figure 34: Comparison of lock-in range with the real part of the least stable eigenvalue, at $(Re, m^*, \zeta) = (33, 50, 0)$.

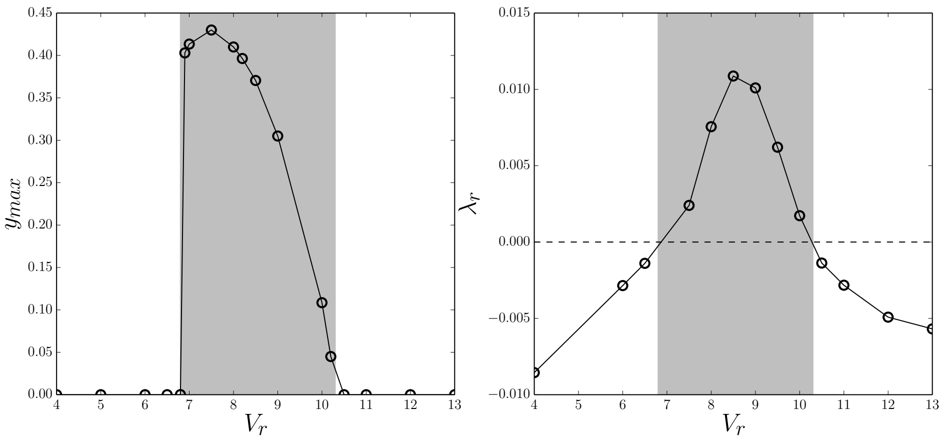

Figure 35: Comparison of lock-in range with the real part of two least stable eigenvalues, at $(Re, m^*, \zeta) = (60, 20, 0)$.

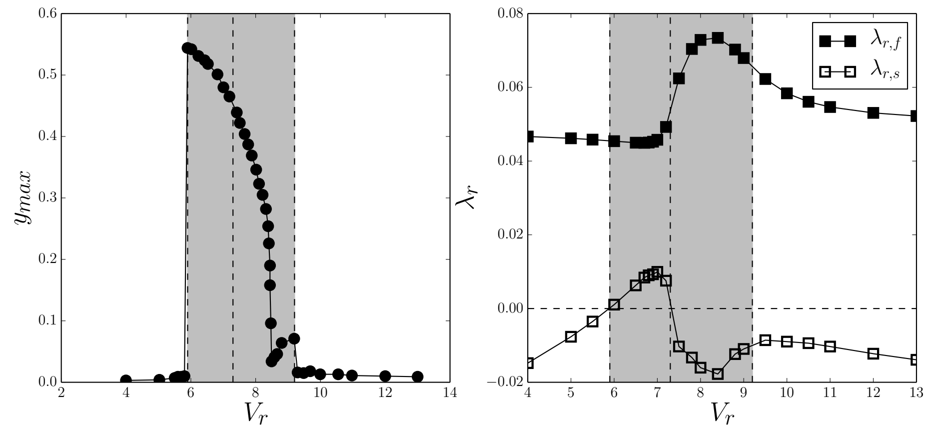

V_r at which the EM becomes unstable. This behaviour was discussed by Zhang *et al.* (2015). They argued that the sign change (from negative to positive) of the eigenvalue of EM is the root cause of the occurrence of lock-in outside the resonance region. Figure 36 shows that the eigen-frequencies of the two least unstable modes are not close in the initial branch of lock-in ($5.8 < V_r < 7.2$). Therefore, the cylinder oscillation in this range of V_r is due to instability of the EM mode, which was referred to by Zhang *et al.* (2015) as flutter instability. In the range $7.2 \leqslant V_r < 9.2$, only FM remains unstable. It is verified that the eigen-frequencies of FM and EM are close, and the cylinder remains oscillating even for stable EM. So in this case, it is said that the cylinder oscillates due to resonance instability (Zhang *et al.* , 2015). For $V_r > 9.2$, FM remains unstable, EM remains stable, the eigen-frequencies of EM and FM depart, and the cylinder stays in rest.

Figure 36 also shows the effect of the mass ratio m^* in the behaviour of two least stable eigenvalues. Figure 37 displays only the eigen-frequencies. For $(Re, m^*, \zeta) = (60, 20, 0)$,

Figure 36: Eigenvalues of the two least stable modes for $(Re, \zeta) = (60, 0)$.

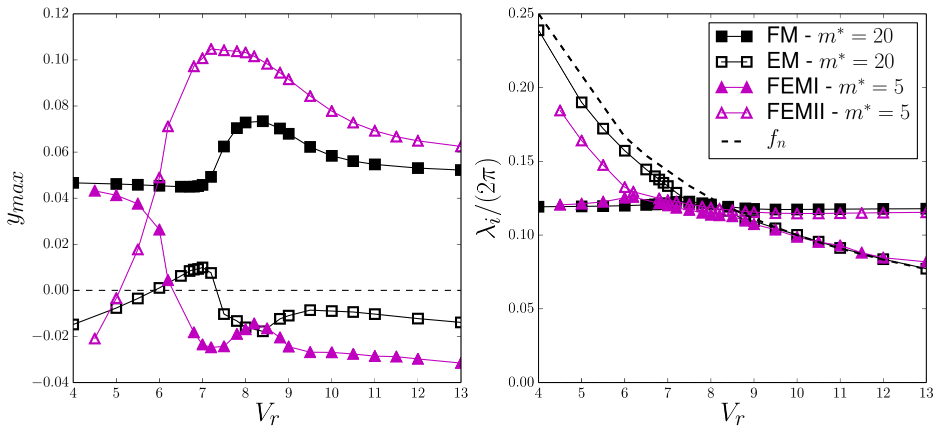

it is possible to distinguish the two least stable modes as FM and EM. In these cases, the eigen-frequencies of the least stable mode tend to the vortex shedding frequency observed for a fixed cylinder, and the eigen-frequencies of the second least stable modes tend to natural frequency of the structure, f_n. Therefore, the modes are decoupled. At $(Re, m^*, \zeta) = (60, 5, 0)$ and for low reduced velocity ($V_r < 5.6$), the eigen-frequencies of FEMI are closer to the FM and the eigen-frequencies of FEMII are closer to the EM. For $5.8 < V_r < 9.5$, we observe a resonance (see Figure 37), i.e., the eigen-frequencies of FEMI and FEMII match. In this range of V_r, the real part of the eigenvalue of FEMI decreases and becomes stable, while the FEMII presents a significant growth rate. Next, the eigen-frequencies of FEMI and FEMII depart and the eigen-frequencies of FEMI stay closer to the EM and the eigen-frequencies of FEMII stay closer to the FM. Therefore, for low V_r, the FEMI tends to the behaviour of FM and FEMII tends to the behaviour of EM. As shown in Figure 31(b), the coupling of modes are observed for low m^* and in the vicinity of the critical Reynolds $Re = 47$. In early work (Govardhan & Williamson (2002)), it was shown that for low m^* the circular cylinder can vibrate with larger amplitude, and for a large range of reduced velocity. So the coupling of modes can be explained by a stronger fluid-structure interaction.

6.3 Sensitivity analysis

In this section, we perform a series of sensitivity analyses for the flow around an elastically-mounted circular cylinder and compare the results with those obtained for a fixed cylinder, evaluating the differences in the fields of sensitivity for different configurations. The analyses performed were structural sensitivity and sensitivity to a steady forcing. The mathematical formulation for these cases are presented in sections 5.5.1 and 5.5.2 respectively.

Figure 37: Eigen-frequency of the two least stable modes for $(Re, \zeta) = (60, 0)$.

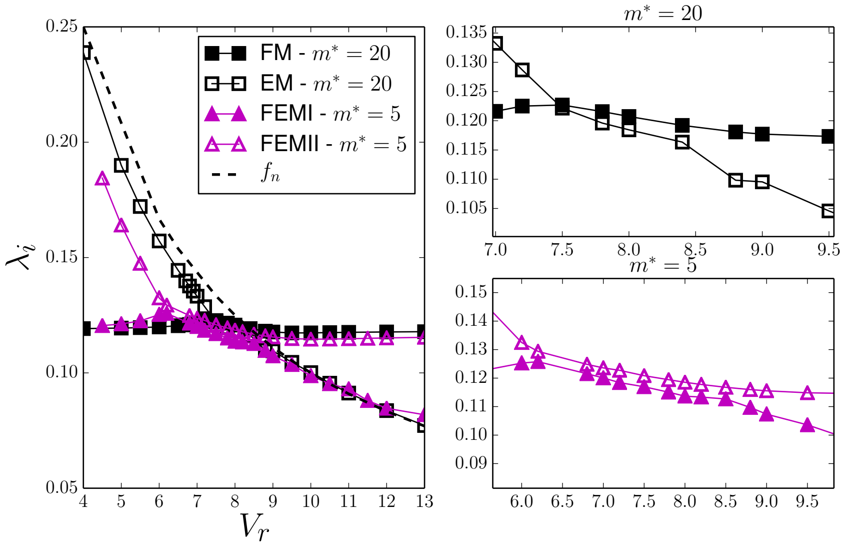

Sensitivity analysis was applied for the following cases: $(Re, m^*, \zeta) = (46.8, 20, 0)$, $(Re, m^*, \zeta) = (46.8, 5, 0)$ and $(Re, m^*, \zeta) = (33, 50, 0)$. Reynolds number $Re = 46.8$ was chosen because it is close to the critical Reynolds number for a fixed cylinder ($Re_c \approx 47$). The mass ratio values employed, $m^* = 5$ and $m^* = 20$, are representative of typical low and a high mass ratios. The calculations of sensitivity were also carried out for $Re < 47$. The goal was to evaluate the sensitivity for a case in which only the EM is unstable. Thus, $(Re, m^*, \zeta) = (33, 50, 0)$ was chosen.

Figures 38(a) and 38(b) show the amplitude of oscillation $y_{\max}$ with respect to V_r for $(Re, m^*, \zeta) = (46.8, 20, 0)$ and $(Re, m^*, \zeta) = (46.8, 5, 0)$, respectively. Figure 38(c) shows the two least stable eigenvalues of the coupled modes FEMI and FEMII for $(Re, m^*, \zeta) = (46.8, 20, 0)$. Based on the results of the amplitude of oscillation, for $m^* = 20$ we chose two values of V_r inside of lock-in range ($V_r = 6.3$ and $V_r = 9$), and a low value and a high value of V_r outside of lock-in range ($Vr = 5$ and $V_r = 13$). For $m^* = 5$, we chose two values of V_r inside of lock-in range ($V_r = 6.3$ and $V_r = 9$).

Figure 34 shows the least stable eigenvalue of the EM and the amplitude of oscillation with respect to V_r for $(Re, m^*, \zeta) = (33, 50, 0)$. For this case, we chose a low and high value of V_r outside the lock-in range ($V_r = 5$ and $V_r = 12$), and a value of V_r inside of lock-in range ($V_r = 8$). As described in the previous section, the range of V_r in which EM is unstable matches the region where the cylinder presents an oscillation amplitude.

In this work, calculations of sensitivity were performed using the adjoint modes. So before introducing results of sensitivity, the adjoint mode calculation routines were verified by comparing the eigenvalues obtained with the respective eigenvalues of the direct modes. Table 6.1 shows comparisons of the least stable eigenvalues for the direct and adjoint

Figure 38: Amplitude of cylinder oscillation for $(Re, m^*) = (46.8, 20)$ (a); and $(Re, m^*) = (46.8, 5)$, and the real part and frequency of two least stable eigenvalues (coupled modes) at $(Re, m^*) = (46.8, 20)$ (c).

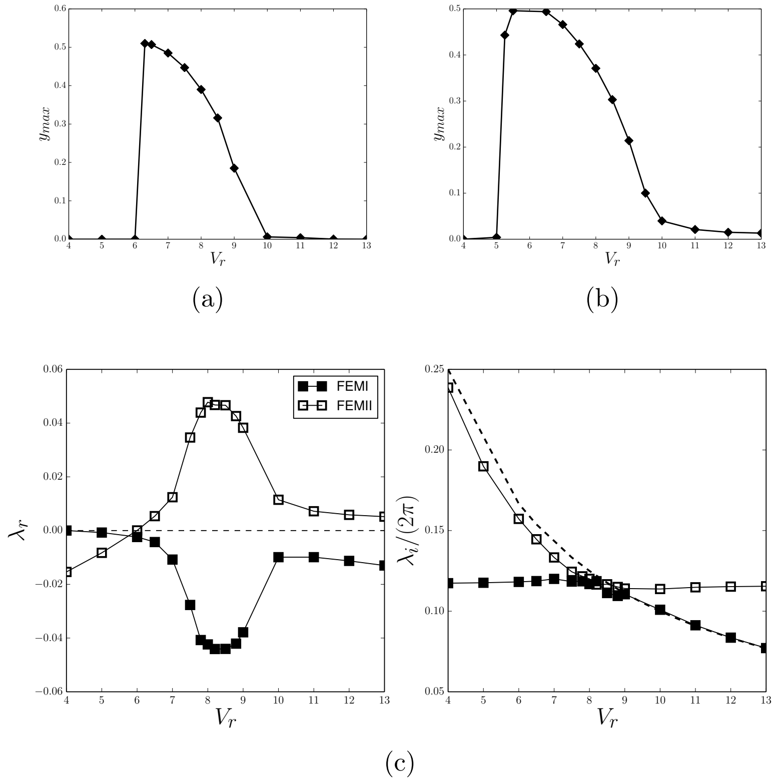

modes. The quantitative difference was computed using the expressions:

$$d_{\lambda_r} = \frac{\lambda_{r,d} - \lambda_{r,a}}{\lambda_{r,d}}, \quad d_{\lambda_i} = \frac{\lambda_{i,d} - \lambda_{i,a}}{\lambda_{i,d}},$$

where d_{λ_r} is the relative difference between the real part of the direct ($\lambda_{r,d}$) and adjoint ($\lambda_{r,a}$) eigenvalues, d_{λ_i} is the relative difference between the imaginary parts ($\lambda_{i,d}$ and $\lambda_{i,a}$) of these respective eigenvalues. According to Table 6.1, the highest difference was 4%. Although this difference could be considered a little high, we believe that the results of sensitivity using the adjoint and direct modes are satisfactory. Observe in Table 6.1 that the difference of 4.5% was verified for modes of a fixed cylinder. However, in section 4.3 we compared our results with previous works and we verified a good agreement. Therefore, these differences probably do not play a important role in the sensitivity analyses.

6.3.1 Structural sensitivity

6.3.1.1 Adjoint field

Before introducing results of sensitivity, let us evaluate the differences between the adjoint field of a flow around a cylinder free to oscillate in the transverse direction and

Table 6.1: Comparisons of less stable eigenvalue (λ_1) of direct and adjoint modes for flow around a fixed cylinder and flow around an elastically-mounted cylinder.

(Re, m^*, ζ)	V_r	λ_1 of $\widehat{\mathbf{u}}$	λ_1 of $\mathbf{u}^*$	$(d_{\lambda_r}, d_{\lambda_i})\%$
	Fixed cyl.	$-2.25 \times 10^{-5} + i0.736$	$-2.15 \times 10^{-5} + i0.736$	$(4, 0.0)$
	$V_r = 5$	$-1.586 \times 10^{-3} + i0.739$	$-1.625 \times 10^{-3} + i0.740$	$(2.5, 0.1)$
$(46.8, 20, 0)$	$V_r = 6.3$	$3.32 \times 10^{-3} + i0.937$	$3.17 \times 10^{-3} + i9.377$	$(4.5, 0.0)$
	$V_r = 9$	$3.85 \times 10^{-2} + i0.716$	$3.70 \times 10^{-2} + i0.73$	$(3.8, 0.5)$
	$V_r = 13$	$4.62 \times 10^{-3} + i0.725$	$4.74 \times 10^{-3} + i0.725$	$(2.5, 0.)$
$(46.8, 5, 0)$	$V_r = 6.3$	$6.71 \times 10^{-2} + i0.813$	$6.55 \times 10^{-2} + i0.813$	$(2.2, 0.0)$
	$V_r = 9$	$8.84 \times 10^{-2} + i0.635$	$8.53 \times 10^{-2} + i0.638$	$(3.5, 0.4)$
	Fixed cyl.	$-7.33 \times 10^{-2} + i0.714$	$-7.21 \times 10^{-2} + i0.717$	$(1.6, 0.4)$
	$V_r = 5$	$-6.24 \times 10^{-3} + i1.22$	$-6.13 \times 10^{-3} + i1.22$	$(1.8, 0.0)$
$(33, 50, 0)$	$V_r = 8$	$8.20 \times 10^{-3} + i0.772$	$8.45 \times 10^{-3} + i0.765$	$(3.0, 0.9)$
	$V_r = 12$	$4.17 \times 10^{-3} + i0.524$	$4.24 \times 10^{-3} + i0.523$	$(1.6, 0.2)$

the adjoint field of a fixed cylinder. It is well-know that the adjoint mode can provide the region of maximal receptivity to an external forcing imposed in the perturbation field (Giannetti & Luchini, 2007). Figures 39, 40 and 41 show the magnitude of least stable adjoint mode ($||\widehat{\mathbf{u}}^{\dagger}||^2$) for $(Re, m^*, \zeta) = (46.8, 20, 0)$, $(Re, m^*, \zeta) = (46.8, 5, 0)$ and $(Re, m^*, \zeta) = (33, 50, 0)$, respectively.

Comparing the adjoint velocity magnitude with the streamlines of the steady base flow (see Figure 42) for $Re = 46.8$, we observe in Figures 39 and 40 that the optimal regions of receptivity are localized close to the separation point, slightly downstream of the cylinder. When the receptivity of the elastically-mounted cylinder is compared with

Figure 39: Normalized adjoint velocity magnitude $||\widehat{\mathbf{u}}^{\dagger}||^2$ at $(Re, m^*, \zeta) = (46.8, 20, 0)$ compared with $||\widehat{\mathbf{u}}^{\dagger}||^2$ of the fixed cylinder at $Re = 46.8$.

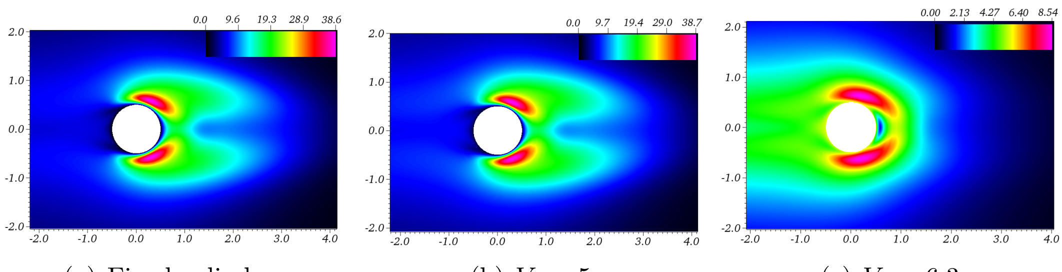

(a) Fixed cylinder (b) $V_r = 5$ (c) $V_r = 6.3$

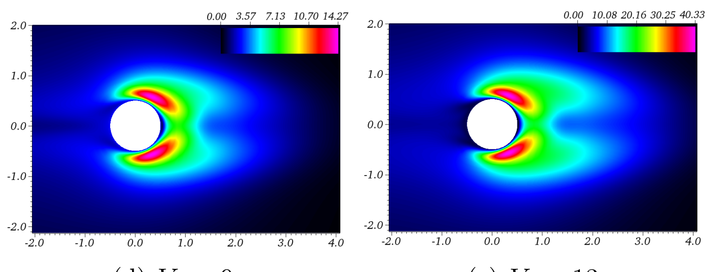

(d) $V_r = 9$ (e) $V_r = 13$

Figure 40: Normalized adjoint velocity magnitude $||\widehat{\mathbf{u}}^{\dagger}||^2$ at $(Re, m^*, \zeta) = (46.8, 5, 0)$ compared with $||\widehat{\mathbf{u}}^{\dagger}||^2$ of the fixed cylinder at $Re = 46.8$.

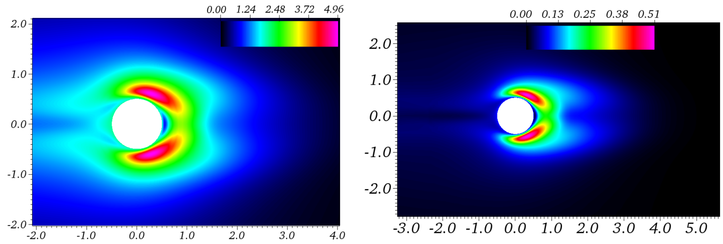

(a) $V_r = 6.3$ (b) $V_r = 9$

Figure 41: Normalized adjoint velocity magnitude $||\widehat{\mathbf{u}}^{\dagger}||^2$ at $(Re, m^*, \zeta) = (33, 50, 0)$ compared with $||\widehat{\mathbf{u}}^{\dagger}||^2$ of the fixed cylinder at $Re = 33$.

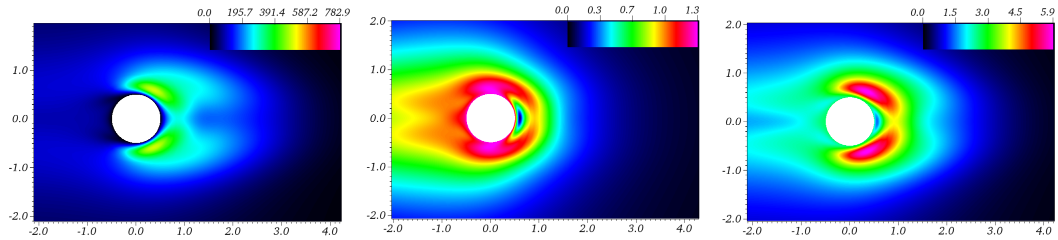

(a) Fixed cylinder (b) $V_r = 5$ (c) $V_r = 8$

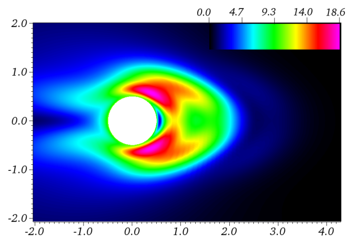

(d) $V_r = 12$

the receptivity of the fixed cylinder (plotted in Figure 39(b)), one observes the greatest difference between the receptivity fields for $(m^*, V_r) = (20, 6.3)$ and $(m^*, V_r) = (5, 6.3)$. Differently from the fixed cylinder, Figures 39(d) and 40(a) show fields of receptivity also located upstream of the cylinder. For both cases, the least stable eigenvalue corresponds to FEMII mode, which it has the eigen-frequency closer of the eigen-frequency of EM (see Figure 38(c)). In other cases, the field of receptivity of elastically-mounted cylinder are similar to that fixed cylinder receptivity. A small difference is observed downstream for $m^* = 5$ (see Figure 40), where we verify that a weaker receptivity stays closer to the elastically-mounted cylinder, until $x \approx 2$. For the fixed cylinder, a weaker receptivity is observed up to $x \approx 3$.

For $(Re, m^*) = (33, 50)$, when it is compared the receptivity regions with the streamlines of the steady base flow (plotted in Figure 43), we observe a stronger receptivity close to the separation point. This is similar to the result the fixed cylinder receptivity displayed in Figure 43 (a). On the other hand, differently of the fixed cylinder, regions of

Figure 42: Streamlines of the Steady base flow, at $Re = 46.8$

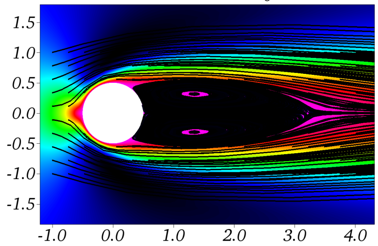

Figure 43: Streamlines of the steady base flow, at $Re = 33$

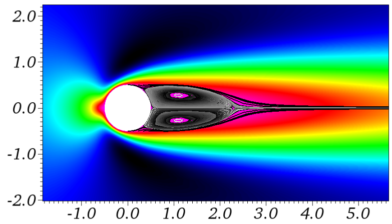

receptivity are also observed upstream from the elastically-mounted cylinder cylinder at $V_r = 5, 8, 12$ (see Figures 43 (a), 43(b), 43 (c)). For $V_r = 5$, these regions of receptivity upstream are stronger than the other cases ($V_r = 8, 12$). To remind, for $(Re, m^*) = (33, 50)$ the less stable eigenvalues at $V_r = 5, 8, 12$ correspond to EM.

6.3.1.2 Structural sensitivity: *Wavemaker*

Wavemaker regions are computed in the flow around an elastically-mounted circular cylinder free to oscillate in the transverse direction. As we showed in section 25, the expression to obtain these fields is given by $||\hat{\mathbf{u}}^{\dagger}||^2 \cdot ||\hat{\mathbf{u}}||^2$. For the current FSI problem, the direct and adjoint modes are solutions of a generalized eigenvalue problem of the respective systems (5.10 – 5.12).

Figures 44 and 45 show comparisons of the *wavemaker* regions of the fixed cylinder with the *wavemaker* regions of the elastically-mounted cylinder for $(Re, m^*, \zeta) = (46.8, 20, 0)$, $(Re, m^*, \zeta) = (46.8, 5, 0)$ and $(Re, m^*, \zeta) = (33, 50, 0)$. In the majority of the cases, the *wavemaker* regions of the elastically-mounted cylinder and those of the fixed cylinder are very different. For a fixed cylinder, a stronger sensitivity is localized to downstream, into the recirculation bubble. However, for an elastically-mounted cylinder, this behaviour is not observed for values of reduced velocity inside the lock-in range. At $(Re, m^*, \zeta) = (46.8, 20, 0)$, for $V_r = 6.3$ the stronger sensitivity is identified upstream of the separation point, at the cylinder wall. This behaviour is also verified for all results obtained for $(Re, m^*, \zeta) = (33, 50, 0)$ and at $(Re, m^*, \zeta, V_r) = (46.8, 5, 0, 6.3)$. For $(Re, m^*, \zeta, V_r) = (46.8, 20, 0, 9)$, $(Re, m^*, \zeta, V_r) = (46.8, 5, 0, 6.3)$, and for $(Re, m^*, \zeta, V_r) = (33, 50, 0)$, at $V_r = 8$ and $V_r = 12$, regions of stronger *wavemaker* are seen at the top and bottom of the wall cylinder. Only at $(Re, m^*, \zeta, V_r) = (46.8, 20, 0, 5))$ and

Figure 44: Comparisons of *wavemaker* regions of the fixed and elastically-mounted cylinder at $Re = 46.8$, $m^* = 5$ and $m^* = 20$.

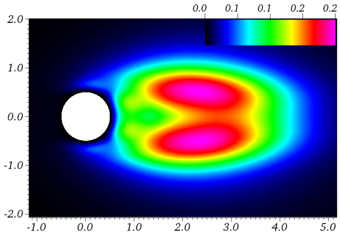

(a) Fixed

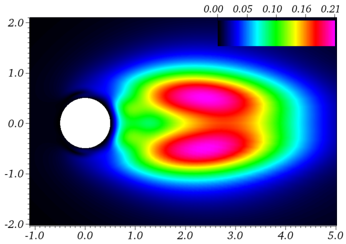

(b) $(m^*, V_r) = (20, 5)$

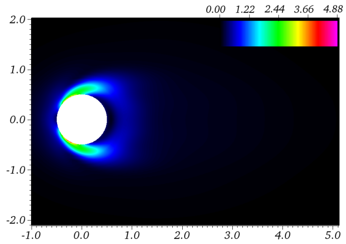

(c) $(m^*, V_r) = (20, 6.3)$

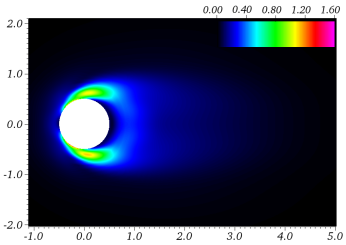

(d) $(m^*, V_r) = (5, 6.3)$

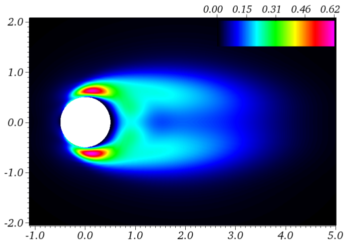

(e) $(m^*, V_r) = (20, 9)$

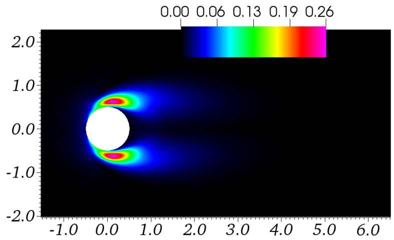

(f) $(m^*, V_r) = (5, 9)$

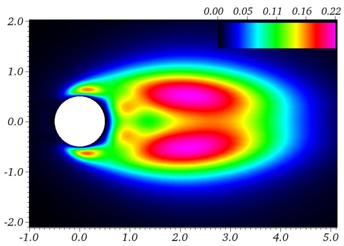

(g) $(m^*, V_r) = (20, 13)$

$(Re, m^*, \zeta, V_r) = (46.8, 20, 0, 13))$ the *wavemaker* region is very similar to the *wavemaker* of the fixed cylinder. In these cases, the cylinder is in rest and the eigen-frequency of the least stable mode tends to the frequency of the vortex shedding in flow around a fixed cylinder.

6.3.2 Sensitivity to a steady forcing

Before introducing the analyses of the receptivity to a steady force imposed in the base flow, we need to explain that the results are evaluated always referencing the separation point and bubble of recirculation of the base flow. For $Re = 46.8$ and $Re = 33$, these information are plotted in Figure 42 and 43, respectively.

6.3.2.1 Growth rate receptivity at $Re = 46.8$

Figure 46 displays comparisons of the growth rate receptivity to a steady forcing of the flow around fixed and elastically-mounted cylinders, at $Re = 46.8$. In the majority of the cases, the fields of growth rate receptivity are similar. That means, stronger receptivity close to the separation point and on the centre of the recirculation bubble.

Figure 45: Comparisons of *wavemaker* regions of the fixed and elastically-mounted cylinder at $Re = 33$, $m^* = 50$.

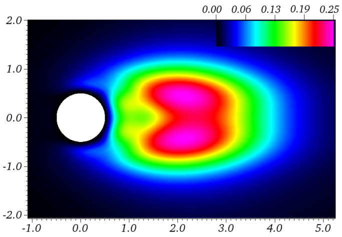

(a) Fixed cylinder

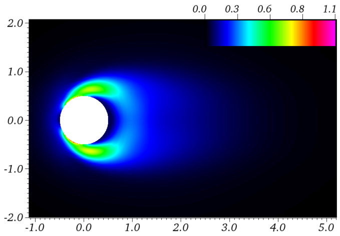

(b) $(m^*, V_r) = (50, 5)$

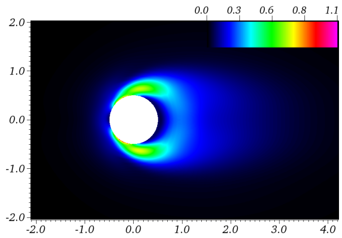

(c) $(m^*, V_r) = (50, 8)$

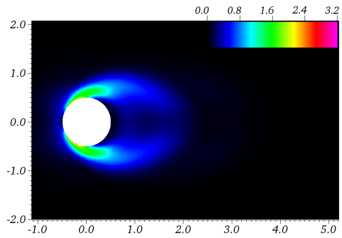

(d) $(m^*, V_r) = (50, 12)$

Figures 46(c) and 46(d) plot the fields of growth rate receptivity at $(m^*, V_r) = (20, 6.3)$ and at $(m^*, V_r) = (5, 6.3)$, respectively. Notice that the fields of receptivity change from a higher mass ratio ($m^* = 20$) to a lower mass ratio ($m^* = 5$). For $(m^*, V_r) = (5, 6.3)$, the growth rate receptivity stays closer to the structure and the stronger receptivity is located inside o the recirculation bubble. Figures 46(e) shows growth rate receptivity at $(m^*, V_r) = (20, 9)$, where it is verified that the stronger receptivity is located downstream, in the centre of the bubble. This region of receptivity is smaller than the region of stronger receptivity of the fixed cylinder. In other cases, regions of the elastically-mounted cylinder receptivity are very similar to the fixed cylinder receptivity.

In Figure 46 the black arrows represent the streamlines of the recpitivity at $Re = 46.8$. As explained in the section 4.3.6, a steady forcing imposed in the base flow can stabilize the system if has opposite direction to that streamlines. In general, the streamlines receptivity of the fixed and elastically-mounted cylinders have a similar behaviour on the regions inside of the recirculation bubble and close to the separation point. Some differences are identified for $(m^*, V_r) = (5, 6.3)$ (see Figure 46(d)).

6.3.2.2 Frequency receptivity at $Re = 46.8$

Figure 47 shows that the frequency receptivity for elastically-mounted and fixed cylinder. In all cases (fixed and elastically-mounted cylinders), stronger receptivity is located closer to the separation point. In general, the regions of weaker receptivity are also identified downstream of the cylinder: inside and outer of the recirculation bubble. At $(m^*, V_r) = (5, 6.3)$, a weaker receptivity is located only inside of the recirculation bubble.

Figure 46: Comparisons of the growth rate receptivity magnitude $|\nabla_{r,\mathbf{f}}\lambda_1|$ to the base flow of the elastically-mounted and fixed cylinders at $Re = 46.8$.

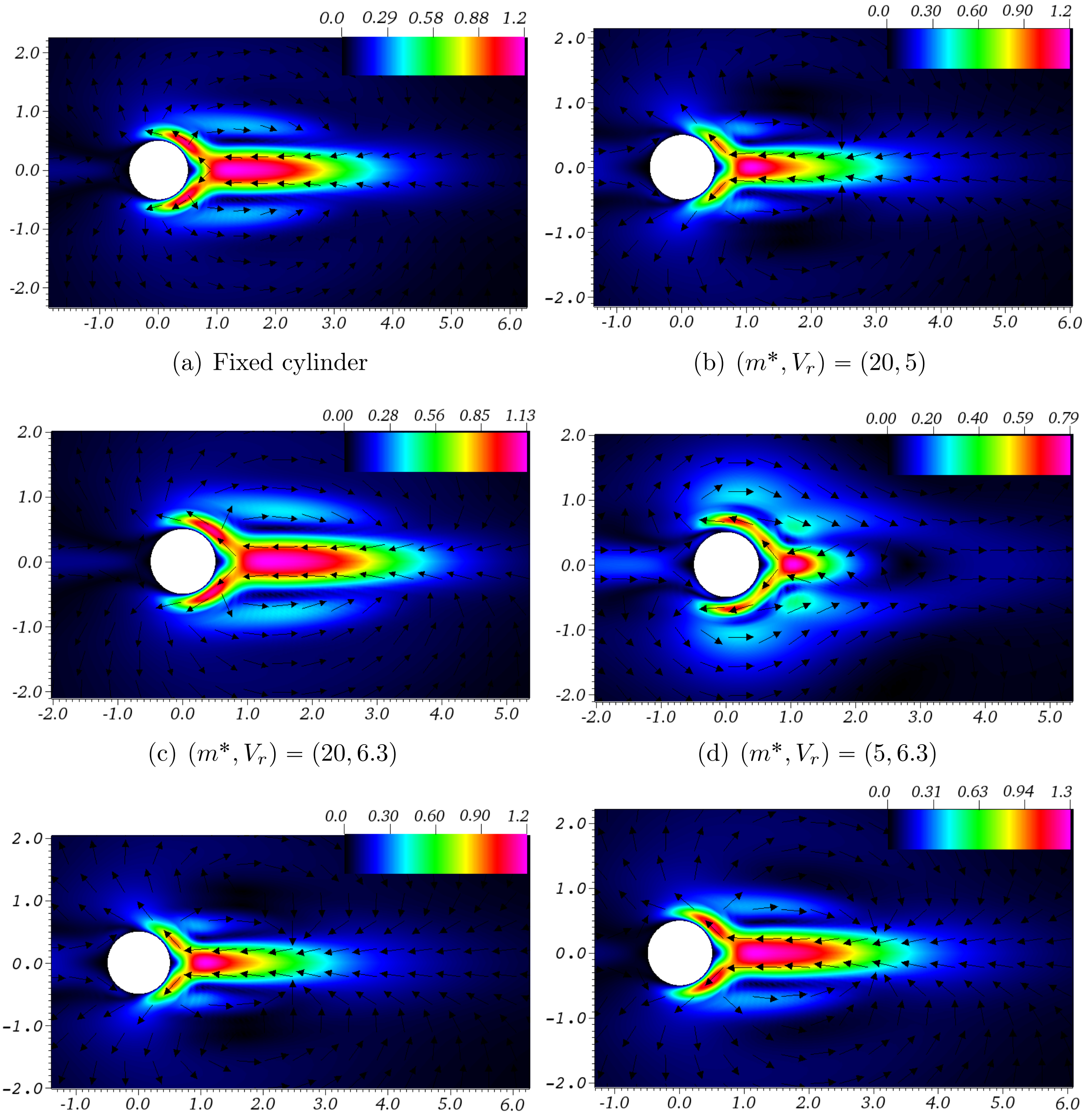

(a) Fixed cylinder

(b) $(m^*, V_r) = (20, 5)$

(c) $(m^*, V_r) = (20, 6.3)$

(d) $(m^*, V_r) = (5, 6.3)$

(e) $(m^*, V_r) = (20, 9)$

(f) $(m^*, V_r) = (20, 13)$

On bottom, on top and inside of the recirculation bubble, the streamlines of the fixed and elastically-mounted cylinder display similar behaviour.

6.3.2.3 Growth rate receptivity for $Re = 33$

Figure 48 shows the growth rate receptivity to an external forcing for $(Re, m^*, \zeta) = (33, 50, 0)$. In all cases, the settings of receptivity fields are really different from the fixed cylinder receptivity plotted in Figure 48(a). For $V_r = 5$ (see Figure 48(b)), the stronger receptivity is located close to the separation point and upstream to the structure. For $V_r = 8$ (see Figure 48(c)), stronger receptivity stay only close to the separation point, and

Figure 47: Comparisons of the frequency receptivity $|\nabla_{i,\mathbf{f}}\lambda_1|$ of the elastically-mounted and fixed cylinders at $Re = 46.8$.

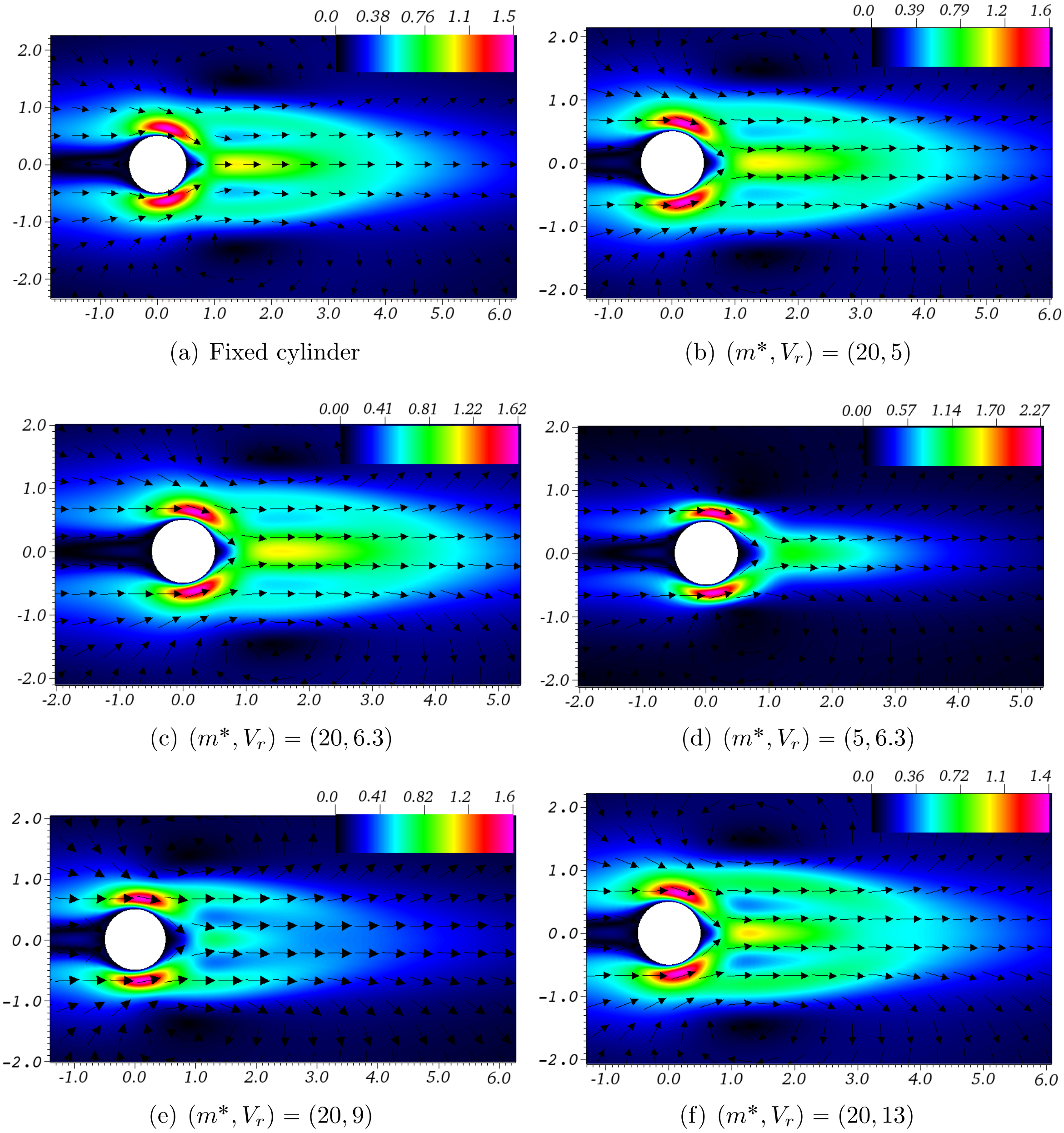

(a) Fixed cylinder

(b) $(m^*, V_r) = (20, 5)$

(c) $(m^*, V_r) = (20, 6.3)$

(d) $(m^*, V_r) = (5, 6.3)$

(e) $(m^*, V_r) = (20, 9)$

(f) $(m^*, V_r) = (20, 13)$

a weaker response to an steady forcing is location downstream, inside of the recirculation bubble region. For $V_r = 12$ (see Figure 48(d)), the greatest receptivity is identified closer to the cylinder, on the bottom and on top. Also, downstream on the region $0 \geqslant x \leqslant 2$ and $\pm 0.5 \leqslant y \leqslant \pm 1$.

For the elastically-mounted cylinder and for $V_r = 5, 8, 12$ (see Figure 48(b), 48(c), 48(d)), the receptivity streamlines have opposite direction than the streamlines of the fixed cylinder receptivity (see Figure 48(a)). Therefore, the responses of the fixed cylinder and the elastically-mounted cylinder to an external forcing can be different, maily on the top and bottom of the strucutre. To exemplify, let us consider an external forcing applied

Figure 48: Comparisons of the growth rate receptivity $|\nabla_{r,\mathbf{f}}\lambda_1|$ for elastically-mounted and fixed cylinders at $Re = 33$.

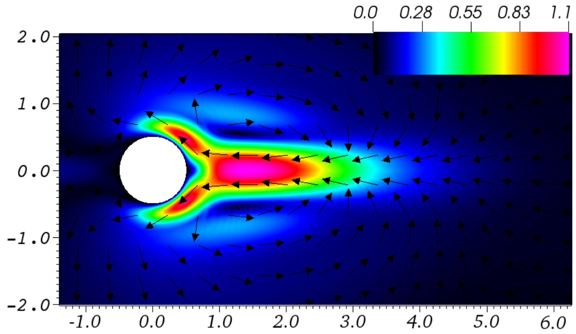

(a) Fixed cylinder

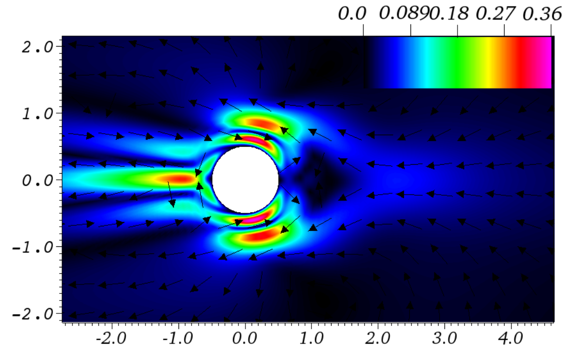

(b) $(m^*, V_r) = (50, 5)$

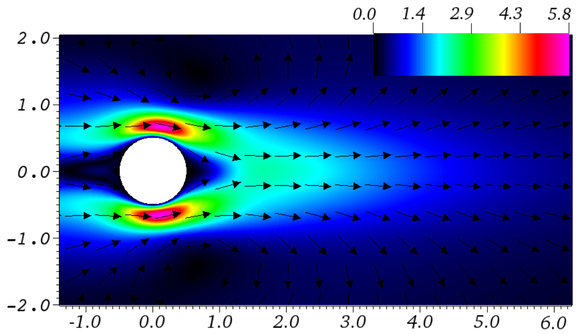

(c) $(m^*, V_r) = (50, 8)$

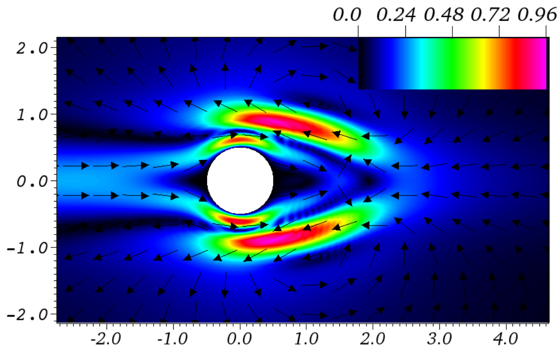

(d) $(m^*, V_r) = (50, 12)$

close to the separation point, such that this forcing is applied to upstream direction. This way, the real part of the least stable eigenvalue ($\lambda_{1,r}$) has a positive variation in the case in which the cylinder is fixed. While $\lambda_{1,r}$ of the elastically-mounted cylinder, real part of the least stable eigenvalue ($\lambda_{1,r}$) has a negative variation.

6.3.2.4 Frequency receptivity for $Re = 33$

Notice in Figure 49 that in both fixed and elastically-mounted cylinders, the stronger receptivity is located closer to the separation. In the fixed cylinder, a weaker receptivity is verified downstream, inside and outer of the recirculation bubble (see Figure 49(a)). For $V_r = 5$ and $V_r = 8$, Figures 49(b) and 49(c) show a weaker receptivity inside of recirculation bubble, on centre region closer to the cylinder. At $V_r = 12$, a weaker receptivity stays on the cylinder lateral regions of the recirculation bubble (see Figure 49(d)). On the region closer of the separation point, the streamlines have a similar behaviour for both fixed and elastically-mounted cylinders. On the centre of the recirculation bubble, the streamlines have also similar frame in the majority of the cases (except at $V_r = 12$).

Figure 49: Comparisons of the frequency receptivity to a steady forcing $|\nabla_{i,\mathbf{f}}\lambda_1|$ for elastically-mounted and fixed cylinders at $Re = 33$.

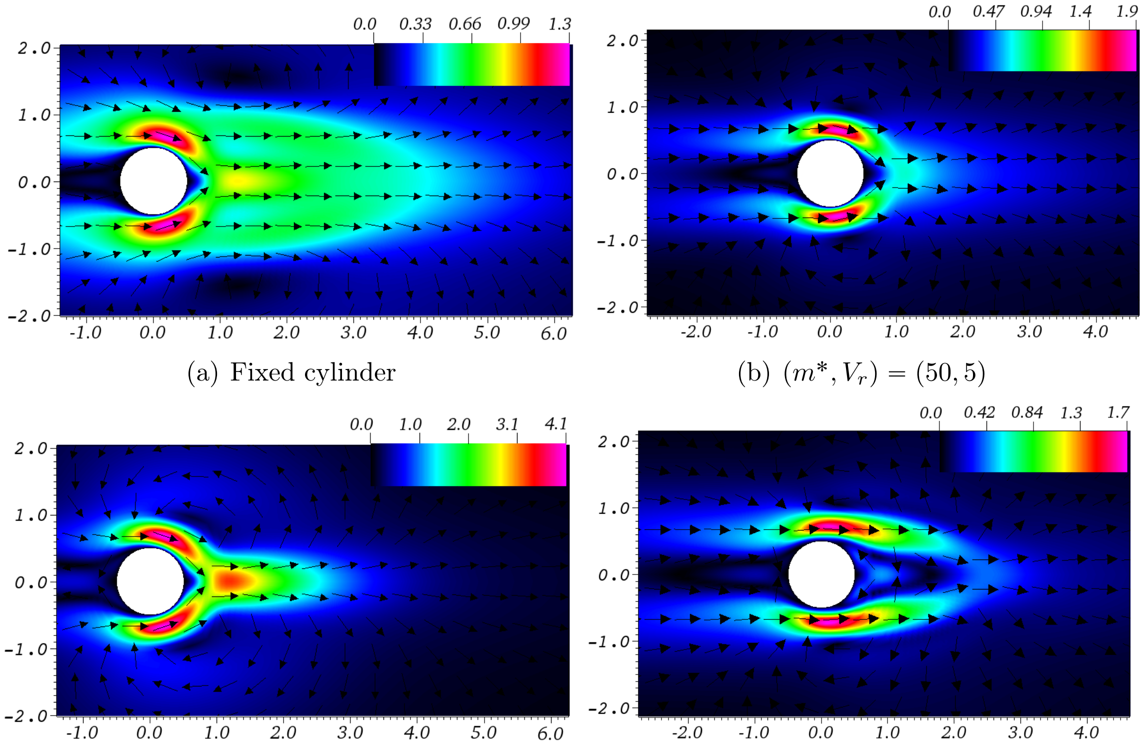

(a) Fixed cylinder

(b) $(m^*, V_r) = (50, 5)$

(c) $(m^*, V_r) = (50, 8)$

(d) $(m^*, V_r) = (50, 12)$

6.3.2.5 Passive control

In this section, we consider a passive control given by an external forcing modelled by the expression (4.22). This force was used in the work by Marquet *et al.* (2008). In that work, the objective was to investigate the variation of the least stable eigenvalue of the flow around a fixed circular cylinder. They verified that the field of growth rate variation agreed with the regions in which the insertion of a small cylinder suppressed the vortex shedding in the experiments introduced by Strykowski & Sreenivasan (1990). Here, we are interested in carrying out comparisons of the growth rate and frequency variations of the flow around an elastically-mounted cylinder and fixed cylinder. To do that, we have chosen values of V_r inside the lock-in range only. So for $(Re, m^*, \zeta) = (33, 50, 0)$, we investigate the eigenvalue variation only at $V_r = 8$. For $(Re, m^*, \zeta) = (46.8, 20, 0)$ and $(Re, m^*, \zeta) = (46.8, 5, 0)$, the variation fields are presented for $V_r = 6.3$ and $V_r = 9$. We are not interested in stabilizing the FSI systems. Actually, we want to evaluate the responses of the current FSI system stability with the imposition of a steady forcing and compare them with the stability responses of the flow around a fixed cylinder.

As explained previously in section 4.3.6, an external forcing modelled by the expression (4.22) can stabilize the flow system if applied in the region where the growth rate variation $\delta\lambda_{1,r}$ is negative. On the contrary, this forcing can destabilize the flow if applied at the

Figure 50: Variation of the growth rate $\delta\lambda_{1,r}/C_d(Re_l)$ for $Re = 46.8$.

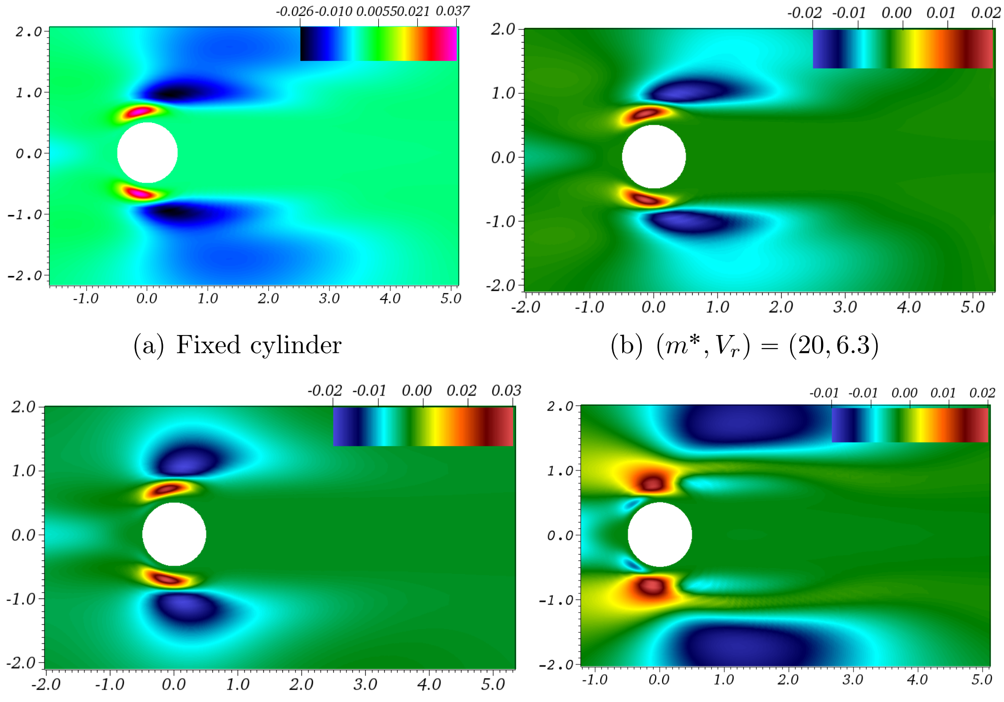

(a) Fixed cylinder

(b) $(m^*, V_r) = (20, 6.3)$

(c) $(m^*, V_r) = (5, 6.3)$

(d) $(m^*, V_r) = (20, 9)$

regions where $\delta\lambda_{1,r} > 0$. Figure 50 shows the growth rate variation for $Re = 46.8$. In all the cases, the greatest positive variation is located at the top and bottom of he cylinder. Figure 51 shows that the frequency variation of the fixed and elastically-mounted cylinders are similar. For $(m^*, V_r) = (5, 6.3)$ and $(m^*, V_r) = (5, 6.3)$, one verifies a difference in the value of the negative variation. Table 6.2 shows the variation of the least stable eigenvalue with the insertion of a small cylinder centred of diameter $d = 1$ and centred at the point $(x_0, y_0) = (1.2, 1)$. Similar to the fixed cylinder, at $(m^*, V_r) = (20, 9)$ the insertion of a small cylinder of diameter $d = 1$ makes a negative variation of the real and imaginary parts of the less stable eigenvalue. Theses results agree with the variation fields presented in Figures 50 and 51.

Table 6.2: Least stable eigenvalues of an unforced and forced steady base flow at $Re = 46.8$. The external forcing modelled by the expression (4.22) is applied at $(x_0, y_0) = (1.2, 1)$.

		Unforced	Forced	$(\delta\lambda_{1,r}, \delta\lambda_{1,i})$
$m^* = 20$	Fixed cyl.	$-2.25 \times 10^{-5} + i0.736$	$-2.92 \times 10^{-2} + i0.550$	(-0.03, -0.18)
	$V_r = 9$	$3.85 \times 10^{-2} + i0.736$	$2.03 \times 10^{-2} + i0.687$	(-0.018, -0.05)

Figure 52 shows comparisons of the growth rate variation $\delta\lambda_{1,r}/C_d(Re_l)$ and frequency variation $\delta\lambda_{1,i}/C_d(Re_l)$ of the less stable eigenvalue for $(Re, m^*, \zeta, V_r) = (33, 50, 0, 8)$. The growth rate variation of the elastically-mounted cylinder has different response than the growth rate variation of the fixed cylinder when a external forcing is modelled by the

Figure 51: Variation of the frequency $\delta\lambda_{1,i}/C_d(Re_l)$ for $(Re, m^*, \zeta) = (46.8, 20, 0)$.

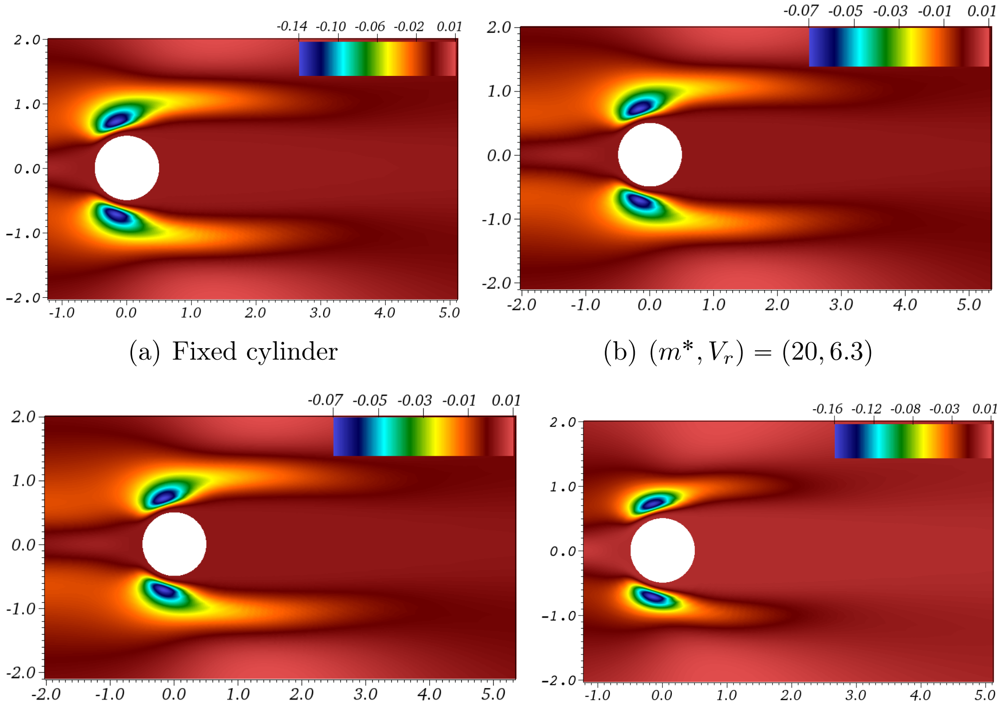

(a) Fixed cylinder (b) $(m^*, V_r) = (20, 6.3)$

(c) $(m^*, V_r) = (5, 6.3)$ (d) $(m^*, V_r) = (20, 9)$

expression (4.22) and is applied at the top and bottom of the cylinder. Notice that for an elastically-mounted cylinder, $\delta\lambda_{1,r}/C_d(Re_l)$ is negative whereas $\delta\lambda_{1,r}/C_d(Re_l)$ of the fixed cylinder is positive. For both elastically-mounted and fixed cylinders, the frequency variation $\delta\lambda_{1,i}/C_d(Re_l)$ has a similar behaviour in the regions closer to the structure. Table 6.3 shows the variation of the least stable eigenvalue with an insertion of a small cylinder of diameter $d = 1$ and centred at the point $(x_0, y_0) = (1.2, 1)$. According to Figure 52 (b-d), $\delta\lambda_{1,r}/C_d(Re_l)$ and $\delta\lambda_{1,i}/C_d(Re_l)$ are negative.

Table 6.3: Least stable eigenvalues of an unforced and forced steady base flow for $Re = 33$. The external forcing modelled by the expression (4.22) is applied at $(x_0, y_0) = (1.2, 1)$.

	Unforced	Forced	$(\delta\lambda_{1,r}, \delta\lambda_{1,i})$
$V_r = 8$	$8.20 \times 10^{-3} + i0.772$	$2.04 \times 10^{-3} + i0.70$	(-0.006, -0.072)

6.4 Conclusions

Regarding the linear stability analysis of the flow around an elastically-mounted cylinder, this chapter described the main results recently introduced in the literature. For this case, we saw that the primary instability occurs for $Re < 47$. Also, it was shown that we need to evaluate the two least stable modes to properly capture the dynamic of the system.

Figure 52: Variation of the growth rate $\delta\lambda_{1,r}/C_d(Re_l)$ and eigen-frequency $\delta\lambda_{1,i}/C_d(Re_l)$ for $Re = 33$.

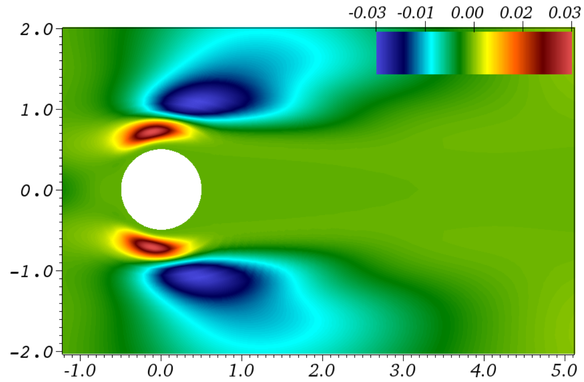

(a) $\delta\lambda_{1,r}/C_d(Re_l)$ – fixed cylinder

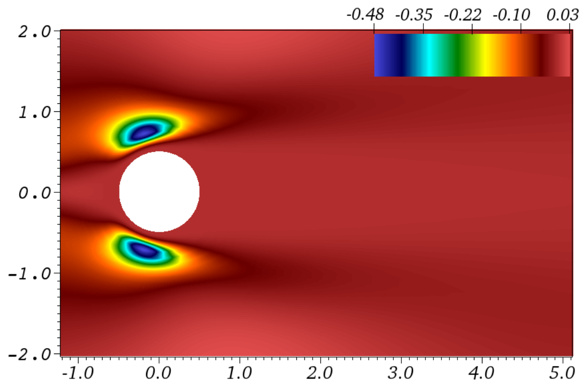

(b) $\delta\lambda_{1,r}/C_d(Re_l)$ – $(m^*, V_r) = (50, 8)$

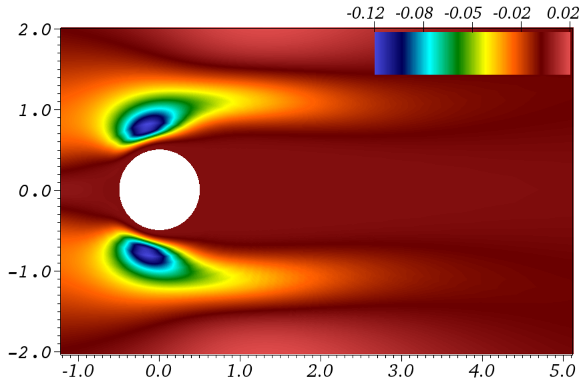

(c) $\delta\lambda_{1,i}/C_d(Re_l)$ – fixed cylinder

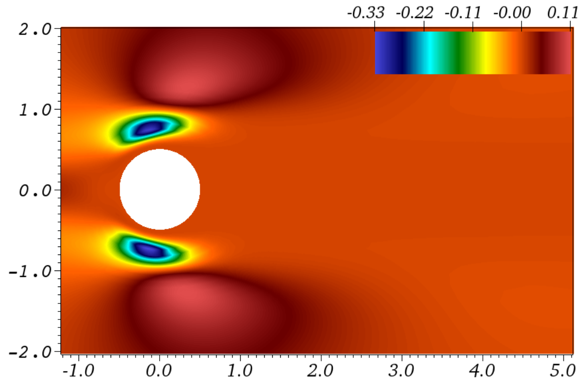

(d) $\delta\lambda_{1,i}/C_d(Re_l)$ – $(m^*, V_r) = (50, 8)$

Before introducing sensitivity calculations, we verified the adjoint modes by comparing its eigenvalues with the eigenvalues of the linearized/direct FSI system. Although the highest difference was 4.5%, we believe that it does not play a relevant role in the sensitivity analyses. Comparisons of the receptivity to an external forcing given by the adjoint model were carried out for an elastically-mounted cylinder and a fixed cylinder. In all the cases, the highest receptivity was localized close to the separation point. Differently from the fixed cylinder, for some cases regions of strong receptivity were also identified upstream of the cylinder. *Wavemaker* regions were also calculated for the flow around an elastically-mounted cylinder. For a fixed cylinder, the regions of stronger sensitivity were located downstream of the cylinder, into the recirculation bubble. However, for an elastically-mounted cylinder, this behaviour was generally not the same, particularly for values of reduced velocity inside of the lock-in range. In some cases, the regions of stronger *wavemaker* were upstream of the separation point, at the cylinder wall.

Finally, we presented calculations of sensitivity to a steady forcing. For the elastically-mounted cylinder, we have chosen the cases in which the reduced velocity was within the lock-in range. We observed different fields of sensitivity, maily for the cases in which the Elastic Mode was the less stavle. Differently from the fixed cylinder, in some cases, the highest sreceptivity was not observed in the centre of the recirculation bubble. Also, a weaker sensitivity was located slightly upstream, closer to the cylinder wall. We computed the variation of the least stable eigenvalue by considering a forcing proportional to the base flow. For $V_r = 9$, the insertion of a small cylinder makes a negative variation of $\lambda_{1,r}$. Differently of the fixed cylinder, we saw that this control is not able to suppress the vortex shedding when it is applied downstream outer of the recirculation bubble.

To the best author's knowledge, this kind of analysis was not yet reported for the lowest Reynolds numbers in the flow around an elastically-mounted cylinder. Therefore, more detailed analyses can be carried out to investigate if there is a relation with the less stable mode or with the frequencies of this FSI problem. In conclusion, for the lowest Reynolds number, sensitivity analyses and passive control for this FSI problem can be much more complex than the sensitivity analyses and passive control of the fixed cylinder.

Chapter

7

Bifurcation analysis of the primary instability and transient growth for flow around an elastically-mounted cylinder

As mentioned in section 4.1.2, the non-normality of the linear operator $\mathbb{L}$ may permit a transient growth of the perturbation in a time interval τ, even for stable systems, before the energy decays to zero. This energy growth is not predicted by the modal analysis, which is concerned with the asymptotic behaviour of the perturbation. This transient growth is especially important when it happens close to the critical point of a subcritical bifurcation. For this cases, the transient energy growth can be enough to trigger nonlinear mechanisms that sustain the perturbation energy, so the system transitions to another state, even for Reynolds numbers below the critical (predicted by the modal analysis).

For the flow around a fixed cylinder, the primary bifurcation (steady to time periodic two-dimensional laminar flow) has supercritical character, as shown by Provansal *et al.* (1987) and Sreenivasan *et al.* (1987), amongst others. However, for the flow around an oscillating cylinder, this analysis had not been carried out. We fill this gap in this work with the results of section 7.1, which have already been published (Dolci & Carmo, 2019).

Results presented by Abdessemed *et al.* (2009) and Cantwell & Barkley (2010) showed computations of optimal energy growth for a flow around a fixed cylinder. Cantwell & Barkley (2010) focused on evaluating the transient growth for $Re < 47$. They carried out analyses of the influence of the domain size in the results and evaluated the responses of transient growth. For the cylinder free to oscillate, this type of analysis has not yet been made. So in this chapter, section 7.2, we study the optimal energy growth for this kind of fluid-structure interaction problem. The optimal energy and optimal initial condition obtained for the cylinder free to oscillate are compared to the results obtained for the fixed cylinder.

7.1 Bifurcation analysis

The incompressible flow past a circular cylinder of diameter D can present different patterns, depending on the Reynolds number Re ($Re = \rho UD/\mu$, where ρ is the fluid density, U is the free stream speed and μ the fluid dynamic viscosity). If the cylinder is fixed, the flow is steady for low Reynolds number. The first instability occurs at Reynolds number $Re_{c_0} \cong 47$ (Jackson, 1987; Dusěk & Fraunie, 1994), when the von-Kármán wake develops and the flow becomes time-periodic. When the cylinder is free to oscillate, past studies have shown that the first instability can happen for lower Reynolds numbers. Mittal & Singh (2005) investigated the flow past a spring mounted cylinder, allowed to oscillate in both the transverse and in-line directions, for $Re < Re_{c_0}$. They observed vortex shedding and oscillation of the cylinder for some values of reduced velocity V_r ($V_r = U/(f_n D)$, where f_n is the natural frequency of the structure in vacuum). Lock-in was verified in all these cases.

For the flow around a fixed circular cylinder, the nonlinear character of the primary instability was also studied (Provansal *et al.* , 1987; Sreenivasan *et al.* , 1987), and it is known that it corresponds to a supercritical Hopf bifurcation. This means that the steady flow becomes time-periodic and that the bifurcation does not present hysteresis. However, to the best of the author's knowledge, no study has yet assessed the nonlinear character of the primary bifurcation in the flow around a flexibly-mounted circular cylinder. This section intends to fill this gap, and check if hysteresis can be observed for Reynolds numbers in the vicinity of the critical Reynolds number Re_c of the flow past a circular cylinder free to oscillate, thus characterising a subcritical bifurcation. To do that, different configurations are evaluated, by varying parameters and number of degrees of freedom.

The reduced velocity V_r, mass ratio m^* and number of degrees of freedom are all important in the structural response of flexibly-mounted cylinders immersed in a fluid flow for higher Reynolds numbers. For this reason, this work intends to verify if they also have influence in the nonlinear character of the primary bifurcation. The reduced velocity has a very clear importance in the response of the system, as the amplitude of vibration is significant in the lock-in range, and very small elsewhere. Therefore, to identify the primary bifurcation character inside and outside of the lock-in range, different values of reduced velocity are considered. Regarding the number of degrees of freedom, below a certain mass-ratio Jauvtis & Williamson (2003) have shown that the system responds differently in the lock-in range if it has 1 or 2 degrees of freedom. Finally, it has been well established in earlier works (Govardhan. & Willianson (2000)) that the mass ratio m^* parameter is of utmost importance for the structural response of the system in the lock-in regime at higher Reynolds number. This manuscript also investigates whether it changed character of the primary bifurcation by employing relatively high and low m^* values. For each combination of parameters, linear stability analysis is applied to find the critical Reynolds Re_c and nonlinear analysis is performed to determine the character of the bifurcation.

To investigate the flow regimes (steady or unsteady), the component of velocity v at an arbitrary point downstream of the cylinder was monitored. The point chosen was $(x_0, y_0) = (3, 0)$. The numerical simulations were carried out for long enough for the perturbation to settle at either a time periodic or steady state. The variation of the component v was used to classify the flow as steady or time periodic. We started the nonlinear simulations from a steady solution obtained for $Re < Re_c$ and gradually increased the Reynolds number until a few units beyond Re_c. At that point, and indeed for any $Re > Re_c$, the flow is time periodic. Next, we departed from that solution and performed simulations for gradually decreasing Reynolds numbers. If the bifurcation is subcritical, we should observe time periodic states for a range of $Re < Re_c$, which characterises hysteresis. If the bifurcation is supercritical, the amplitude should be zero for any $Re < Re_c$.

7.1.1 Results and discussions

We verified our mathematical and numerical methodology performing the convergence analysis evaluating the amplitude fluctuation A of the velocity component v at a chosen point in the wake, $(x_0, y_0) = (3, 0)$, with respect to the spectral element polynomial order for a flow around a flexibly-mounted circular cylinder free to oscillate in transverse and in-line directions, at $Re = 60$, $m^* = 5$, $\zeta = 0$ and $V_r = 5$. Table 7.1 shows that polynomials of degree 5 achieved excellent convergence results. To be rigorous, polynomials of degree 6 were used in all the numerical results introduced in this work. The numerical verification of a flow around a circular cylinder allowed to vibrate was carried out in section 6.2, where the cylinder amplitude oscillation y_{max} was compared to results from Mittal & Singh (2005). Linear stability analysis was also verified in the section 6.2.

Table 7.1: Fluctuation amplitude A convergence of the velocity component v with respect to the spectral element polynomial order P for a flow around a flexibly-mounted circular cylinder free to oscillate in transverse and in-line directions, at $Re = 60$, $m^* = 5$, $\zeta = 0$ and $V_r = 5$.

Polynomial order	A
$P = 4$	0.436
$P = 5$	0.446
$P = 6$	0.441
$P = 7$	0.441

Figure 53: Bifurcation diagram for the flow past a fixed cylinder, showing a supercritical character. A is the asymptotic amplitude of v (y component of velocity) at the point $(x_0, y_0) = (3, 0)$.

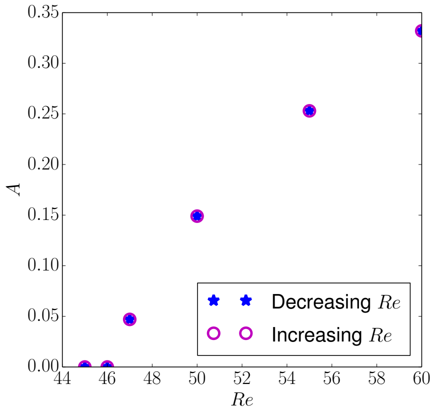

We have also checked our method of nonlinear analysis by applying it to the fixed cylinder case. To do that, first we performed a number of global linear stability analysis calculations to determine the critical Reynolds number. As showed in section 4.3.3, the primary instability occurs at $Re_{c_0} \cong 46.6$. This value is in good agreement with the numerical results presented by Jackson (1987) and Dusěk & Fraunie (1994). Next, we carried out nonlinear calculations in the vicinity of Re_c, for increasing and decreasing Re. Figure 53 shows a diagram of the asymptotic perturbation amplitude (amplitude of velocity component v at $(x_0, y_0) = (3, 0)$) as a function of Reynolds number, for both increasing and decreasing Reynolds number calculations. No hysteresis was identified, and the amplitude grows gradually as the Reynolds number is increased beyond Re_{c_0}. This behaviour characterises a supercritical bifurcation, agreeing with previous studies from the literature (Provansal *et al.* , 1987).

Having verified the numerical method, we proceeded to the selection of parameters to be used in the calculations of the fluid-structure interaction cases. Figure 32(a) shows that, for low Reynolds numbers, the lock-in happens for $5 \lessapprox V_r \lessapprox 11$. So we chose three different values of reduced velocity to investigate: one less than the lower limit of the lock-in range ($V_r = 5$), one inside the lock-in range ($V_r = 9$) and one higher than the upper limit of the lock-in range ($V_r = 13$). Regarding the mass ratio, we selected a low and a high value, $m^* = 5$ and $m^* = 50$, respectively. For all cases, the damping parameter, ζ, was set to zero. We performed simulations for a flexibly-mounted circular cylinder allowed to oscillate in the transverse direction only (1DoF) and in both transverse and in-line (2DoF) directions. In the 2DoF cases, the structural stiffness was the same for both directions. To find the critical Reynolds number Re_c, linear stability analysis was applied. Then nonlinear numerical simulations were carried out in the vicinity of Re_c to verify the bifurcation character. Like the flow around a fixed cylinder, this verification was carried out using the amplitude of velocity component v at $(x_0, y_0) = (3, 0)$.

Figure 54: Bifurcation diagrams at $V_r = 9$ in 1DoF ((a) and (b)) and 2DoF ((c) and (d)) cases, showing a subcritical behaviour. (a) and (c) are results for $m^* = 50$ with $Re_c \cong 22$; (b) and (d) are results for $m^* = 5$ with $Re_c \cong 23$.

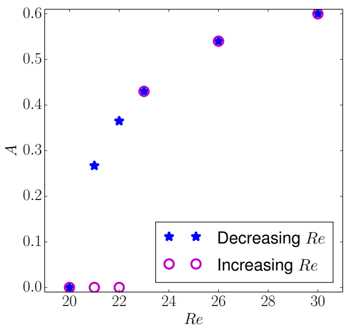

(a) $m^* = 50$

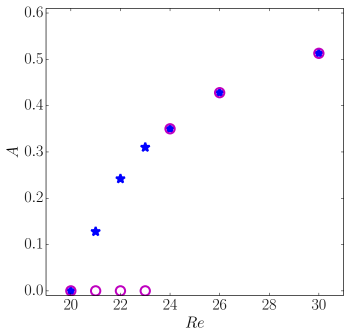

(b) $m^* = 5$

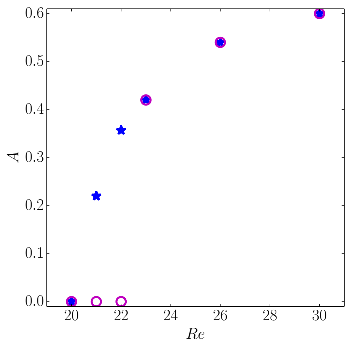

(c) $m^* = 50$

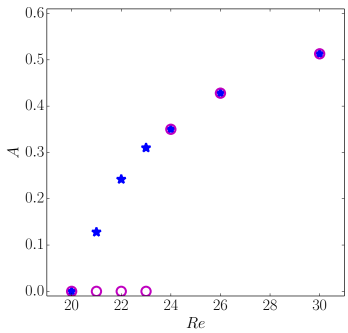

(d) $m^* = 5$

We start showing the results obtained for V_r in the lock-in range. Figure 54 displays the primary bifurcation diagram for $V_r = 9$. Differently from the fixed cylinder case, the subcritical character was verified in both high and low m^*, for 1DoF and 2DoF. For 1DoF and 2DoF, the critical Reynolds was $Re_c \cong 22$ for $m^* = 50$ and slightly higher, $Re_c \cong 23$, for $m^* = 5$. Figure 54 shows that the range of hysteresis is larger for $m^* = 5$ than for $m^* = 50$, but in both cases it covers only a few Reynolds number units. Figure 55 shows the vorticity fields for $Re = 22$ and $m^* = 50$, 1DoF. Figure 55(a) was obtained from a simulation using a steady flow as initial condition. On the other hand, figure 55(b) is the result from a simulation using a time periodic flow as initial condition, obtained from a simulation carried out at $Re > Re_c$. We can see that the steady and time-periodic characters of the initial condition remain in the final solution. In the time-periodic result (Figure 55b), the von-Kármán wake is developed, the flow is time-periodic and the flexibly-mounted circular cylinder presents a time-periodic oscillation of amplitude $y_{max} = 0.365$. For the sake of brevity, we only show results for $V_r = 9$, but we tested other V_r values inside the lock-in range and observed the same flow behaviour and subcritical character of the bifurcation.

Figure 55: Vorticity field for $Re = 22$, $V_r = 9$ and $m^* = 50$.

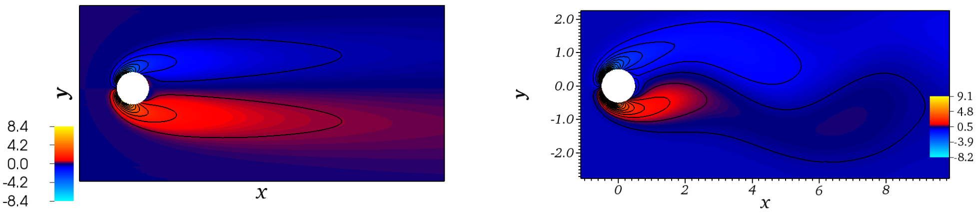

(a) Increasing Re

(b) Decreasing Re

Figures 56 and 57 show the bifurcation diagrams obtained for reduced velocities outside the lock-in range, $V_r = 5$ and $V_r = 13$. In all these cases, for 1DoF and 2DoF, the primary bifurcation was supercritical, like in the fixed cylinder case. For $m^* = 50$, $Re_c = Re_{c_0}$, i.e., the critical Reynolds number was the same as that for the fixed cylinder, for both $V_r = 5$ and $V_r = 13$, and for both 1DoF and 2DoF. In these cases, for $Re > Re_c$ we observed the von-Kármán wake time-periodic flow, but the cylinder did not show any appreciable motion. For $m^* = 5$, the behaviour was different. For $V_r = 13$ the primary instability happened for Re a little lower than Re_{c_0}, $Re_c \cong 44$, while for $V_r = 5$, the primary instability occurred for Reynolds number slightly larger than Re_{c_0}, at $Re_c \cong 48$. In both $m^* = 5$ cases, for $Re > Re_c$ the flow became time-periodic and small amplitude oscillations could be identified. These amplitudes were significantly lower than those observed for V_r in the lock-in range, $y_{max} \cong 10^{-2}$. It is important to highlight that we are referring to Reynolds numbers not very far from Re_{c_0} (we have tested Re up to 60). As the Reynolds number is further increased, the lock-in V_r range changes and shows a stronger dependency with the mass ratio too.

7.2 Optimal energy growth

Calculations of energy growth were carried out for time intervals up to $\tau = 100$ with free-stream velocity $U_\infty = 1$. We performed a convergence analysis to establish an appropriate domain size for flows around fixed and elastically-mounted cylinders using the followings meshes:

- M1: $x+ = 100D$, $x- = 15D$, $y\pm = 20D$;
- M2: $x+ = 125D$, $x- = 15D$, $y\pm = 20D$;
- M3: $x+ = 100D$, $x- = 25D$, $y\pm = 20D$;
- M4: $x+ = 100D$, $x- = 35D$, $y\pm = 20D$;
- M5: $x+ = 100D$, $x- = 25D$, $y\pm = 40D$;

Figure 56: Bifurcation diagram at $V_r = 5$ in 1DoF((a) and (b)) and 2DoF ((c) and (d)) cases, showing a supercritical behaviour in all cases. (a) and (b) are results for $m^* = 50$ with $Re_c \cong 46.6$; (b) and (d) are results for $m^* = 5$ with $Re_c \cong 48$.

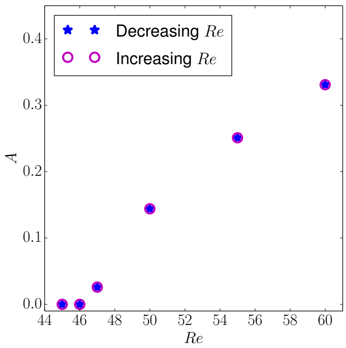

(a) $m^* = 50$

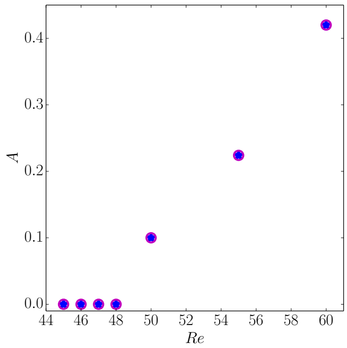

(b) $m^* = 5$

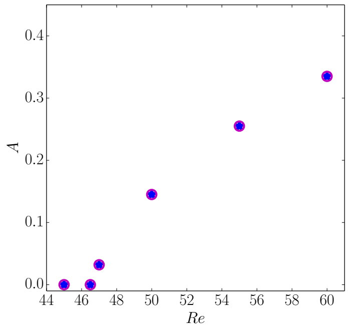

(c) $m^* = 50$

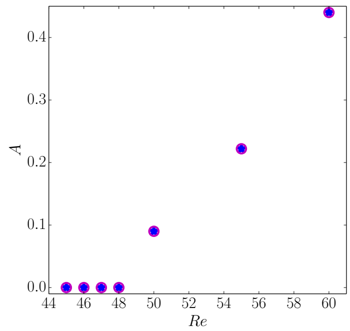

(d) $m^* = 5$

- M6: $x+ = 100D$, $x- = 25D$, $y\pm = 60D$;

For the elastically-mounted cylinder, the convergence of the domain size was performed for $(Re, m^*, \zeta, V_r) = (45, 50, 0, 7)$. For this setup, the system is unstable and the growth rate of least stable mode was $\lambda_{1,r} = 4.022 \times 10^{-2}$. On the other hand, for the fixed cylinder the rate growth of least stable mode was $\lambda_{1,r} = -7.659 \times 10^{-3}$. To perform the convergence analysis, we evaluated the relative difference in the highest energy growth. Results are in Table 7.2.

Meshes M1 and M2 were designed to evaluate the influence of the outflow length. For a cylinder centred in $x = 0$, the difference of the highest energy growth from M1 to M2 was around of 0.9%. This way, $x+ = 100$ was considered adequate for our optimal energy calculations. With the meshes M2, M3 and M4 we evaluated the inflow length. The difference in the highest energy growth between M3 and M2 was around of 1%. So we chose $x- = 25$. Next, we evaluated the influence of cross-stream length of the domain, in which the difference from M4 to M5 of the optimal energy growth was around of 1%, and the cross-stream length $y\pm = 25$ was considered enough for the energy growth

Figure 57: Bifurcation diagrams at $V_r = 13$ in 1DoF((a) and (b)) and 2DoF ((c) and (d)) cases, showing a supercritical behaviour in all cases. (a) and (c) are results for $m^* = 50$ with $Re_c \cong 46.6$; (b) and (d) are results for $m^* = 5$ with $Re_c \cong 44$.

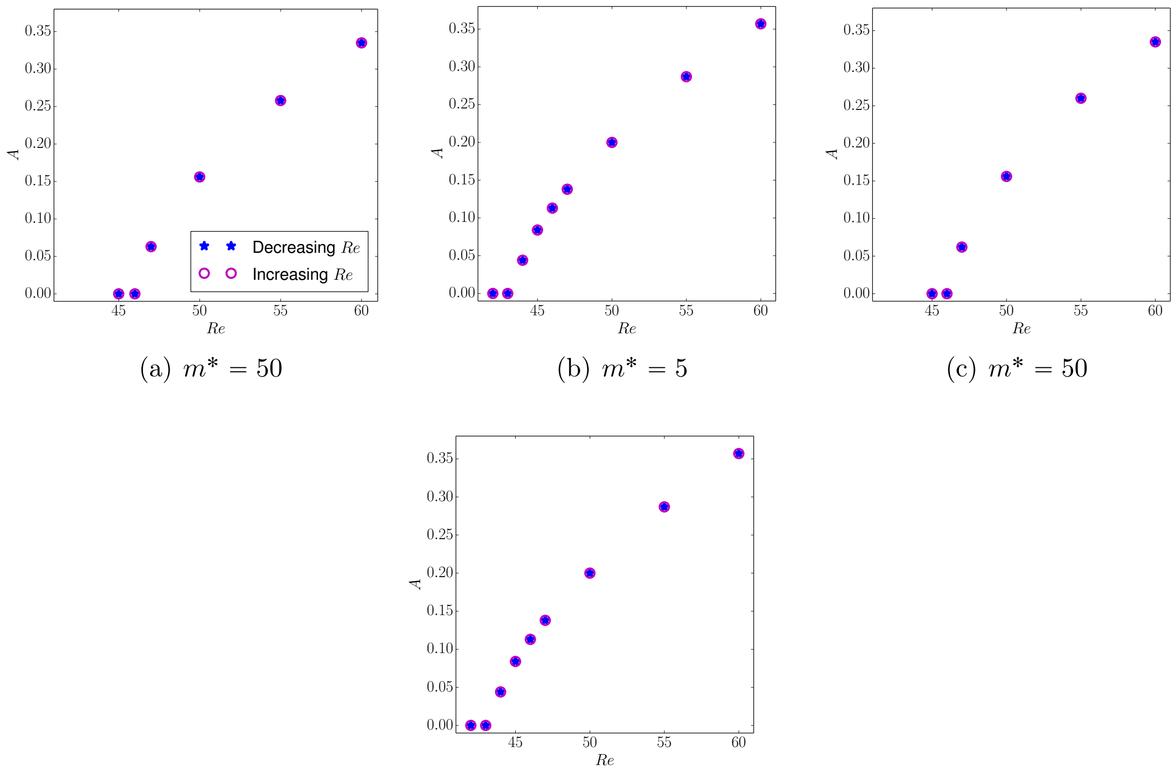

(a) $m^* = 50$ (b) $m^* = 5$ (c) $m^* = 50$

(d) $m^* = 5$

computations. So after the convergence analysis of the domain size, the mesh chosen was M5.

Table 7.2: Convergence analysis of the domain size for fixed cylinder and elastically-mounted cylinder.

Mesh	Fixed Cyl. ($E(100)$)	$V_r = 7$ ($E(100)$)
M1: $x+ = 100D$, $x- = 15D$, $y\pm = 20D$	2.4485×10^3	4.0770×10^3
M2: $x+ = 125D$, $x- = 15D$, $y\pm = 20D$	2.4492×10^3	4.0394×10^3
M3: $x+ = 100D$, $x- = 25D$, $y\pm = 20D$	2.3395×10^3	4.1169×10^3
M4: $x+ = 100D$, $x- = 35D$, $y\pm = 20D$	2.2993×10^3	4.1281×10^3
M5: $x+ = 100D$, $x- = 25D$, $y\pm = 40D$	2.2736×10^3	4.1226×10^3
M6: $x+ = 100D$, $x- = 25D$, $y\pm = 60D$	2.2655×10^3	4.1203×10^3

Firstly, we verified the energy growth computation of this FSI problem at a time τ. To perform that, it was simulated the perturbation initialized by the optimal initial condition $\mathbf{u}^{\dagger}(\mathbf{x}_0, 0)$ given by the formulation introduced in section 5.4. Next, it was compared the energy of the perturbation with the optimal growth energy $E(\tau)/E(0) = ||\mathbf{u}'_a(\mathbf{x}_0, \tau)||^2/||\mathbf{u}'_a(\mathbf{x}_0, 0)||^2$ at the same time τ. Figure 58 shows this comparison at $\tau = 2$,

Figure 58: Optimal energy growth and energy of the perturbation initialized with the optimal initial growth, for fixed (circle) and elastically-mounted cylinders (square).

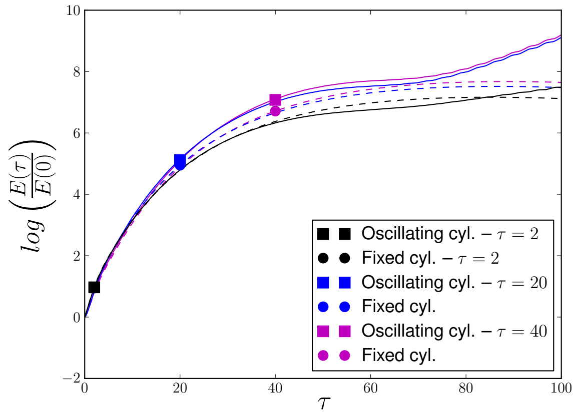

(a)

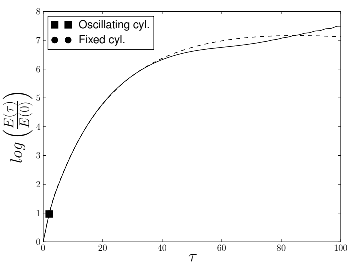

(b) $\tau = 2$

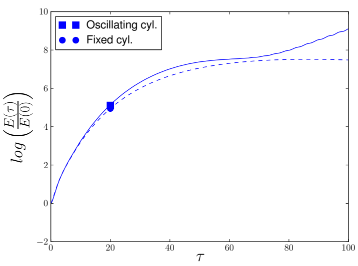

(c) $\tau = 20$

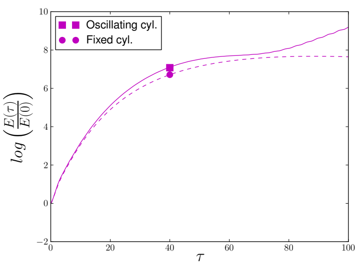

(d) $\tau = 40$

$\tau = 20$ and $\tau = 40$, for fixed cylinder and elastically-mounted cylinder and We have checked a good agreement between the results.

Figure 59 displays the optimal energy growth envelope for the fixed cylinder and elastically-mounted cylinder until $\tau = 100$. For the cases investigated here, we can see that the optimal energy growth of the fixed and elastically-mounted cylinders are similar. For fixed cylinder and at $Re = 45$, the flow system is stable and the optimal global energy was observed at $\tau = 100$, in which $\log(E(100)/E(0)) = 2.2736e + 03$. At the same Re and for elastically mounted cylinder, the FSI system is unstable. In Figure 59(a) is verified that the transient growth dominates until $Re \approx 80$, next the exponential growth rate of the less stable mode is observed. Figure 59(b) shows the optimal energy growth envelope for the fixed cylinder at $Re = 22$, and for elastically-mounted cylinder at $(Re, m^*, \zeta, V_r) = (22, 50, 0, 9)$. We can see that for elastically-mounted and fixed cylinder, the global maximum energy growth occurs in $\tau \approx 30$, in which for elastically-mounted cylinder $\log(E(\tau)/E(0)) = 6.047$ and for fixed cylinder $\log(E(\tau)/E(0)) = 6.241$. For elastically-mounted cylinder, we verified in previous section that the primary bifurcation had a subcritical character. So the transient growth play an important role for this kind of the bifurcation.

Figure 59: Comparisons of the optimal energy growth envelope for fixed cylinder (circle) and elastically-mounted cylinder (square). For $(Re, m^*, \zeta, V_r) = (45, 50, 0, 7)$, the predicted energy growth of the least stable mode for the fixed cylinder (traced line) and for the elastically-mounted cylinder (continuous line) are also shown.

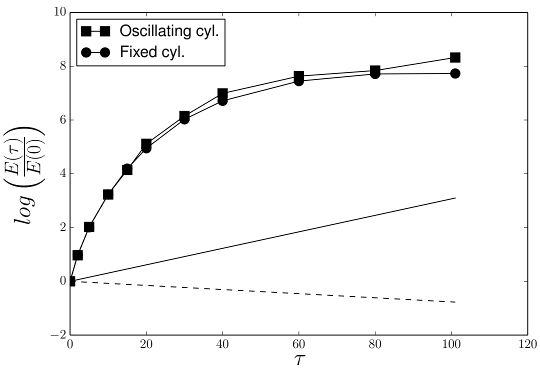

(a) $(Re, m^*, \zeta, V_r) = (45, 50, 0, 7)$

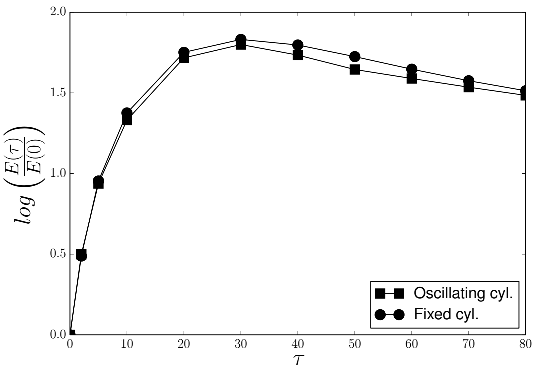

(b) $(Re, m^*, \zeta, V_r) = (22, 50, 0, 9)$

Figure 60 shows comparisons of the optimal initial conditions of fixed cylinder at $Re = 45$ and of the elastically-mounted cylinder at $(Re, m^*, \zeta, V_r) = (45, 50, 0, 7)$ for different time intervals, τ. The contours are all similar. In general, the higher energy is located close to the separation point, and a weaker energy is identified to downstream, near to the recirculation bubble. In the majority of the cases, the optimal initial energy of the fixed and elastically-mounted cylinders are similar, the highest difference is verified at $\tau = 5$, in which the maximal magnitude of the optimal initial condition is $|\mathbf{u}| = 0.05$ for the fixed cylinder and $|\mathbf{u}| = 0.07$ for the elastically-mounted cylinder. Also, at $\tau = 20$, we can see the difference in the region downstream of the cylinder, outer of the recirculation bubble. For the elastically-mounted cylinder, the energy distribution is stronger than the energy of the fixed cylinder.

Figure 61 shows the comparison of the optimal initial conditions for the flow around a fixed cylinder at $Re = 22$ and for the flow around an elastically-mounted cylinder at $(Re, m^*, \zeta, V_r) = (22, 50, 0, 9)$. In theses cases, the field of optimal initial conditions are different. For the fixed cylinder, the stronger energy is located close to the separation point. However, for the elastically-mounted cylinder, this behaviour is not verified for all time intervals. At $\tau = 20$, notice that the highest energy is located downstream, further from the separation point. At $\tau = 5$ and $\tau = 20$, the maximal energy stays closer to separation point and at the rear of the cylinder.

Figure 60: Optimal initial conditions for flow around a fixed cylinder (left side) and for flow around an elastically-mounted cylinder at $(m^*, V_r) = (50, 7)$ (right side).

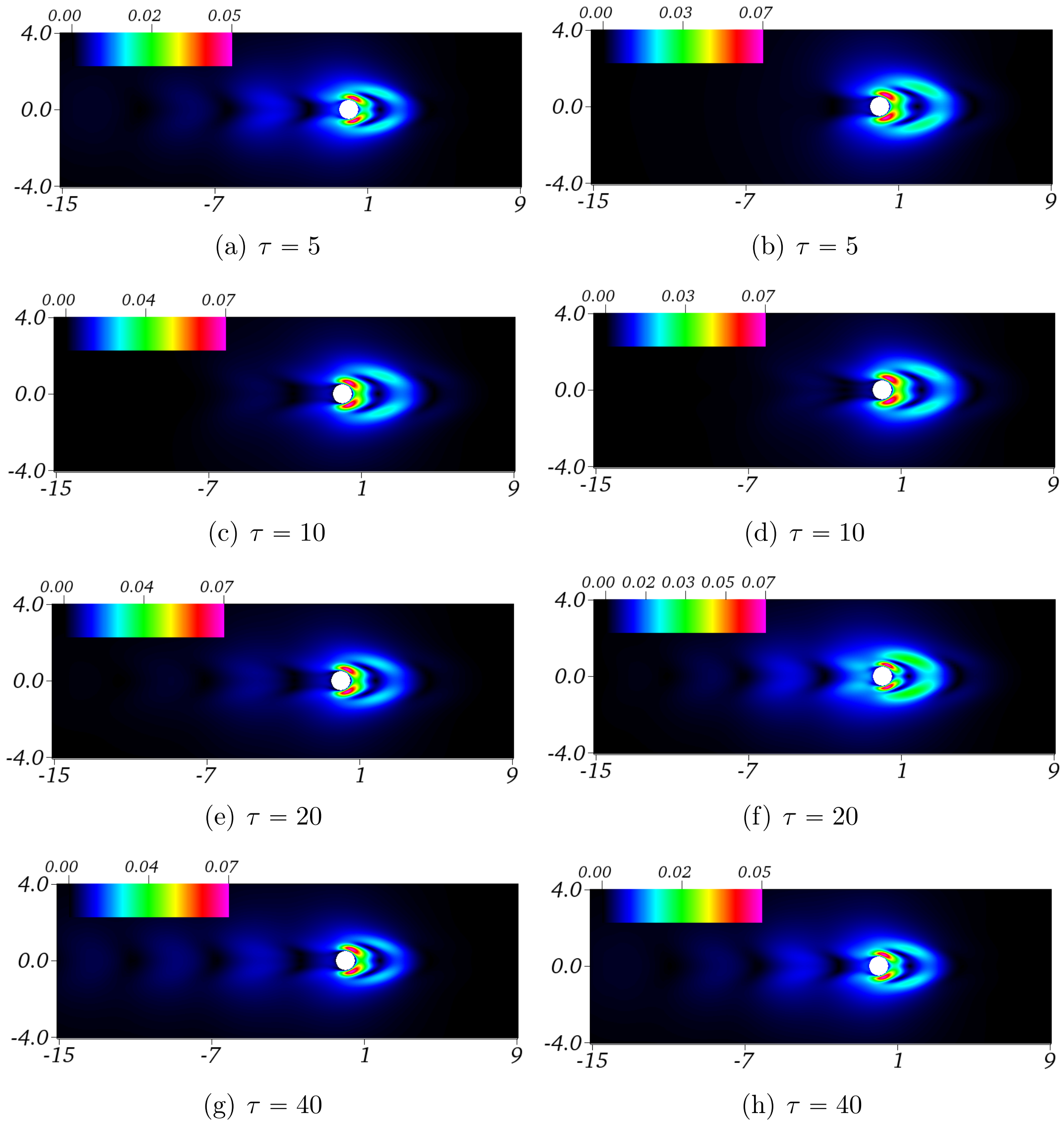

(a) $\tau = 5$ (b) $\tau = 5$

(c) $\tau = 10$ (d) $\tau = 10$

(e) $\tau = 20$ (f) $\tau = 20$

(g) $\tau = 40$ (h) $\tau = 40$

7.3 Conclusions

In this chapter, we have shown results from an investigation about the primary bifurcation in the flow around a flexibly-mounted circular cylinder. Also, computations of the optimal energy and optimal initial conditions.

To evaluate the bifurcation character, we have employed numerical linear stability analysis to find the critical Reynolds numbers. Next, nonlinear direct simulations in the vicinity of these critical Reynolds were performed to determine the primary bifurcation character. Different values of reduced velocities were tested, covering cases inside and outside the lock-in range. We also employed a low value and a high value of mass ratio ($m^* = 5$ and $m^* = 50$, respectively), and we considered transverse only (1DoF) and transverse and inline motion (2DoF). The main conclusion was that, like the critical

Figure 61: Optimal initial conditions for the flow around a fixed cylinder at $Re = 22$ (left side) and for the flow around an elastically-mounted cylinder at $(Re, m^*, \zeta, V_r) = (22, 50, 0, 9)$ (right side).

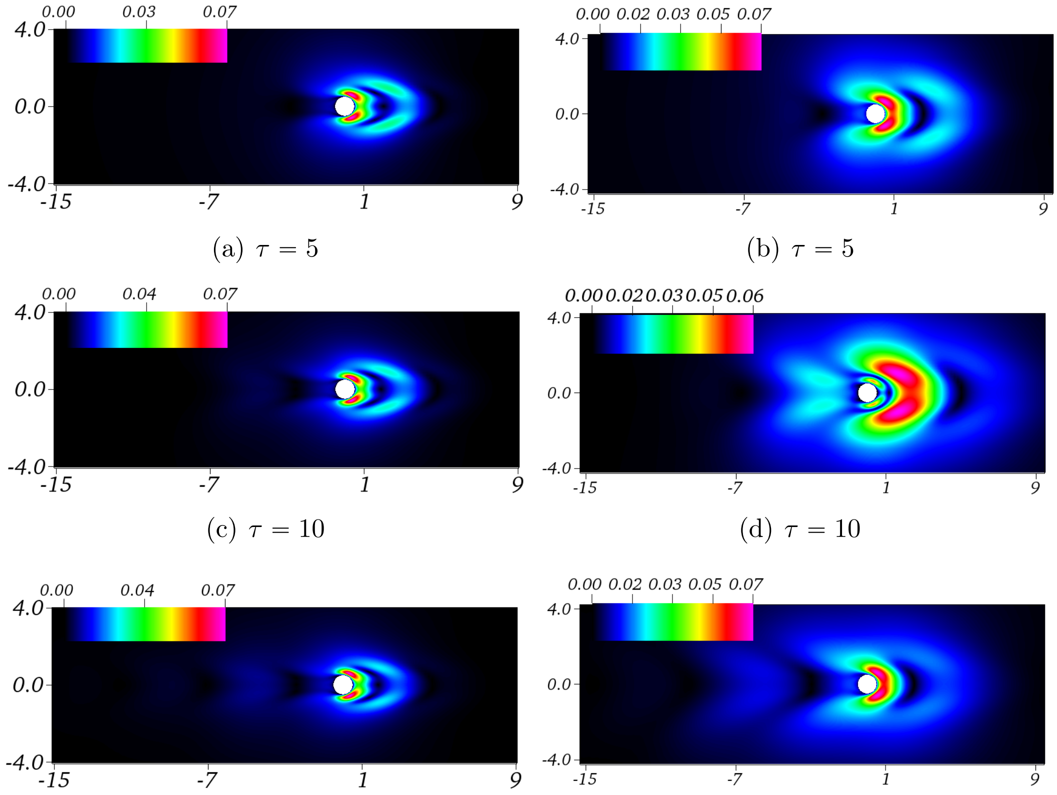

(a) $\tau = 5$ (b) $\tau = 5$

(c) $\tau = 10$ (d) $\tau = 10$

(e) $\tau = 20$ (f) $\tau = 20$

Reynolds number, the nonlinear character of the bifurcation changes completely if the reduced velocity is inside the lock-in range. For those cases, the critical Reynolds number is significantly lower than for the fixed cylinder ($\approx$ 22 vs. 47), and the bifurcation is subcritical, in contrast to the supercritical character observed for the fixed cylinder and flexibly-mounted cylinder with V_r outside the lock-in range. In the adopted configurations (range of Reynolds number, mass ratio and reduced velocity), the critical Reynolds do not differ in the cases of 1Dof and 2Dof. We saw that the mass ratio and number of degrees of freedom (1DoF or 2DoF) do not play a relevant role in the results. So we conclude that the changes in both linear and nonlinear responses are due mainly to the proximity of the natural frequencies of the structure and of the flow. It is interesting to notice that both the structure system and the coupling between structure and flow are linear, but the frequency tuning is able to change the nonlinear character of the coupled system.

Next, we have introduced computations of optimal energy growth and optimal initial condition for a flow around an elastically-mounted cylinder. The first step of this work was to compare the computations of the optimal growth energy and optimal initial condition of the elastically-mounted cylinder with the same computations applied for the fixed cylinder. In the cases investigated, we verified that the optimal energy of fixed and elastically-mounted cylinder stays close. At $Re = 45$, the flow system is stable, while the current FSI system is unstable. So the major difference in the growth energy was verified when the exponential growth rate of the less stable mode prevails in the elastically-mounted cylinder at the setup $(Re, m^*, \zeta, V_r) = (45, 50, 0, 7)$. At $Re = 22$, the flow and the FSI systems were stable and the optimal growth energy had similar results. However, the optimal initial conditions of the fixed and elastically-mounted cylinders were different. The major was at $\tau = 10$, in which we verified that stronger energy arises in different regions. Evaluating the Figure 31(b), we can see that for $(Re, m^*, \zeta, V_r) = (22, 50, 0)$ the modes are decoupled. Besides that, we verified that for $V_r = 9$ the less stable mode is the elastically mode (EM). So the difference of the optimal initial condition can be given by the less stable mode. Obviously, this affirmation must be better investigated by performing other analyses in the cases in which the less stable mode is the EM. In conclusion, we verified that the optimal initial conditions of the elastically-mounted cylinder can present different and similar configurations when compared with the fixed cylinder. In future works, more detailed analyses can be carried out to investigate in which configuration the fields are different or similar.

Chapter

8

Conclusion

This work introduced sensitivity calculations in global linear analysis for a fluid-structure interaction (FSI) system, and sensitivity of aerodynamic forces with respect to non-geometric variables. Besides that, we investigated the character of the primary bifurcation for the flow around a flexibly-mounted circular cylinder. Numerical simulations were carried out with the Nektar++ software, which is an implementation of the Spectral/*hp* Element Method (Karniadakis & Sherwin, 2005). Newmark-*beta* solver (Newmark, 1959) and fictitious mass method (Baek & Karniadakis, 2012) were used to integrate the mass-spring-damper system in time. The Arnoldi method was used to solve the generalized eigenvalue problems (Saad, 1992), and the FSI system was formulated using the non-inertial frame of reference method (Li & Bearman, 2002).

Adjoint-based sensitivity measures with respect to non-geometric variables for internal and external steady flows were presented in this thesis. The results showed good quantitative agreement with other methods like analytically-calculated sensitivity (applied for the fully-developed channel flow) and central finite difference. So, for steady base flows, the adjoint-based methodology to calculate sensitivity of aerodynamic forces with respect to non-geometric variables (Reynolds number, inlet velocity, external forcing) was verified.

Besides that, a theoretical study about the adjoint-based stability and sensitivity analysis for the fluid flow problem was made. Next, these analyses were applied for the flow around a fixed circular cylinder. The main objective was to verify the numerical methodology used in this work. Later on, the results of the fluid flow around a fixed cylinder were used as benchmark for comparisons against those obtained for the flow around an elastically-mounted cylinder. Based on the mathematical methodology used in the works by Fernández & Tallec (2002, 2003); Pfister *et al.* (2019); Negi *et al.* (2019), the linearization of the FSI system was carried out using the *transpiration* approach. In those works, the stability analysis was performed for a FSI system formulated with the ALE method. Here, we adapted the linearization for a FSI system formulated with the non-inertial frame of reference method. The mathematical formulations were done with the structure displacement governed by linear mass-spring-damper equations.

Linear stability analysis for the flow around an elastically-mounted circular cylinder was verified by comparisons with results from previous papers. Besides that, a review of the recent results was presented. Next, adjoint-based receptivity and sensitivity analyses were applied for this FSI problem. Unprecedented discussions about receptivity were put forward. Differently from the fixed cylinder, we saw that for the flow around an elastically-mounted cylinder, regions of receptivity were identified upstream of this structure. Structural sensitivity were also computed. This kind of analysis was first introduced by Negi *et al.* (2019) for $(Re, m^*, \zeta) = (50, 20, 0)$. In this current work, we presented structural sensitivity for $Re = 46.8$ and $Re = 33$, evaluating the responses for a high ($m^* = 20$) and a low ($m^* = 5$) value of mass ratio. Finally, results of sensitivity with respect to a steady forcing were introduced and with the results of this sensitivity, we performed computations of open-loop control for the flow around an elastically-mounted cylinder. Comparisons against those obtained for the flow around a fixed cylinder were carried out. We verify that this FSI problem can present distinct responses for the same external forcing, depending on the parameters of the system. Moreover, we saw that the responses to an external forcing can be different than that for the flow around a fixed cylinder.

Still in global analysis, the character of the primary bifurcation was investigated for an oscillating elastically-mounted cylinder. The main conclusion was that, like the critical Reynolds number, the nonlinear character of the bifurcation changes completely if the reduced velocity is inside the lock-in range. Differently from the fixed cylinder, the bifurcation showed a subcritical character. Later on, calculations of optimal energy growth were introduced for Reynolds numbers less than the critical for the primary instability of the fixed cylinder ($Re < 47$). We saw that the optimal energy growth of the fixed and elastically-mounted cylinders are similar. However, the optimal initial conditions of the fixed and elastically-mounted cylinders can be markedly different. We noticed this behaviour for the case in which the least stable eigenvalue corresponded to the elastic mode (EM).

To conclude, this thesis had the objective of developing adjoint-based analyses of stability and sensitivity analysis for fluid flow and fluid-structure interaction problems. To achieve the results of aerodynamic sensitivity, this work introduced a mathematical approach and calculations to verify if the adjoint-based sensitivity was able to provide quantitative sensitivity. In steady base flow, that was validated. Regarding global linear analysis, this work introduced analyses not yet assessed previously for an elastically-mounted cylinder. Computations of sensitivity, investigations over the bifurcation character of the primary instability, calculations of the optimal energy growth and optimal initial conditions were introduced firstly in this thesis.

8.1 Future work

In this thesis we introduced calculations of aerodynamic sensitivity for steady base flow. However, there is a wide field of research to advance. Meliga *et al.* (2014) introduced calculations of sensitivity with respect to an external forcing to control the drag force in the flow around a square cylinder. They investigated steady, time-periodic and turbulent base flows. Later on, the drag force sensitivity was revisited in Meliga *et al.* (2018), showing that for time-dependent base flow the adjoint-based sensitivity fails. The justification was that the error in the adjoint-based sensitivity occurred because the adjoint system does not adjust the time change of the velocity close to the cylinder. During this research, problems in computing aerodynamic forces for time-dependent base flows also happened. Therefore, we believe that there is a gap to explore algebraically and numerically to solve this kind of problem.

Besides that, adjoint-based sensitivity of the aerodynamic forces (or another functional objective) can be extended for FSI problem. This approach can be algebraically and numerically interesting. In the adjoint FSI system, it is necessary to deal with the gradients of the base flow defined in a coordinate system that can change in each time step.

Regarding the global analysis, adjoint-based stability and sensitivity analyses are scarce for FSI systems. In the last years, papers have introduced linear stability analysis for flow around elastically-mounted bluff bodies, where the structure undergoes only translation. In the first analyses of the sensitivity computations for elastically-mounted circular cylinder introduced in this thesis, we observed interesting results. When comparing against the flow around a fixed structure, we saw that the FSI problem can present responses to external forcing that are completely different. So these analyses can be extended for other FSI problem and in the cases in which the structure is free to rotate.

Besides that, computations of the stability and sensitivity can be extended for time-periodic base flow. With stability analysis, investigations of the secondary instability of a FSI problem can be done.

In conclusion, we believe that the adjoint-based stability and sensitivity analyses for time dependent flow systems and mainly for FSI systems open a range of opportunities.

Bibliography

ABDESSEMED, N. A. S., SHARMA, SHERWIN, S. J., & THEOFILIS, V. 2009. Transient growth analysis of the flow past a circular cylinder. *Phys. Fluid*, **21**.

AIRIAU, C., WALTHER, S., & BOTTARO, A. 2002. Boundary layer sensitivity and receptivity. *C. R. Mecanique*, **330**, 59–265.

BAEK, H., & KARNIADAKIS, G. E. 2012. A convergence study of a new partitioned fluid–structure interaction algorithm based on fictitious mass and damping. *J. of Comp. Physics*, **231**, 629–652.

BARKLEY, D., & HENDERSON, R. D. 1996. Three-dimensional Floquet stability analysis of the wake of a circular cylinder. *J. Fluid Mech.*, **322**, 215–241.

BLACKBURN, H. M., BARKLEY, D, & SHERWIN, S. J. 2008. Convective instability and transient growth in flow over a backward-facing step. *J. of Fluid Mech.*, **156**, 271–304.

CACUCI, D. G. 1981. Sensitivity Theory for Nonlinear Systems: II. Extensions to Additional. *J. Math. Phys.*, **22**, 2803.

CANTWELL, C. D., & BARKLEY, D. 2010. Computational study of subcritical response in flow past a circular cylinder. *Phys. Review*, **82**, 026315.

CARMO, B. S. 2009. *On wake interference in the flow around two circular cylinders: direct stability analysis and flow-induced vibrations.* Ph.D. thesis, Imperial College London.

CHOMAZ, J. M. 2005. Global instabilities in spatially developing flows: non-normality and nonlinearity. *Annu. Rev. Fluid Mech.*, **156**, 209–240.

COSSU, C., & MORINO, J. 2000. On the instability of a spring-mounted circular cylinder in a viscous flow at low Reynolds numbers. *Journal of Fluids and Structures*, **14**, (2) 183–196.

Dolci, Daiane I., & Carmo, Bruno S. 2019. Bifurcation analysis of the primary instability in the flow around a flexibly mounted circular cylinder. *Journal of Fluid Mechanics*, **880**, R5.

Dušěk, J., Le Gal P., & Fraunie, P. 1994. A numerical and theoretical study of the first Hopf bifurcation in a cylinder wake. *J. Fluid Mech.*, **264**, 59–80.

Dyke, Van. 1988. *An Album of Fluid Motion.* The Parabolic Press.

Fernández, M. A., & Tallec, P. Le. 2002. Linear stability analysis in fluid–structure interaction with transpiration. Part I: Formulation and mathematical analysis. *Technical Report, INRIA*, **4570**.

Fernández, M. A., & Tallec, P. Le. 2003. Linear stability analysis in fluid–structure interaction with transpiration. Part II: Numerical analysis and applications. Part II: Numerical analysis and applications. *Comput. Methods Appl. Mech*, **192**, 4837–4873.

Fernández, M.A. 2001. *Modèles simplifiés d'interaction fluide–structure.* M.Phil. thesis, Université de Paris IX.

Giannetti, F., & Luchini, P. 2006. Leading-edge receptivity by adjoint methods. *J. Fluid Mech*, **547**, 21–53.

Giannetti, F., & Luchini, P. 2007. Structural sensitivity of the first instability of the cylinder wake. *Fluid Mech*, **581**, 167–197.

Giannetti, F., Camarri, S., & Luchini, P. 2010. Structural sensitivity of the secondary instability in the wake of a circular cylinder. *Journal of Fluid Mechanics*, **651**, 319–337.

Golub, G. H., & Van Loan, C. F. 1996. *Matrix Computations.* Third ed. Baltimore, M.D.: Johns Hopkins University Press.

Govardhan, R., & Williamson, C. H. K. 2002. Resonance forever: existence of a critical mass and an infinite regime of resonance in vortex-induced vibration. *J. Fluid Mech.*, **473**, 147–166.

Govardhan., R., & Willianson, H. K. 2000. Modes of vortex formation and frequency response of a freely vibrating cylinder. *Journal of Fluids and Structures*, **420**, 85–130.

Gunzburger, M., Hou, L., & Svobodny, T. 1991. Boundary velocity control of incompressible flow with an application to viscous drag reduction. *SIAM J. Control Optim.*, **30**, 167–181.

GUNZBURGER, M. D. 2003. Perspectives in Flow Control and Optimization. *SIAM*.

HALL, M., & CACUCI, D. 1983. Physical interpretation of the adjoint functions for sensitivity analysis of atmospheric models. *J. of Atmospheric Sciences*, **40**, 2537–2546.

HAYASHI, M. T., LIMA, J. B. S., CHIEREGATTI, B. G., & VOLPE, E. V. 2016. Non–Geometric Sensitivities Using the Adjoint Method. *International Journal of Aerospace and Mechanical Engineering*, **10**(1), 155 – 163.

HILL, D. C. 1992. A theoretical approach for analyzing the restabilization of wakes. *AIAA*, **92-0067**.

J. KOU, W. ZHANG, Y. LIU, & LI, X. 2017. The lowest Reynolds number of vortex-induced vibrations. *Physics of Fluids*, **29**, 041701.

JACKSON, C. P. 1987. A finite-element study of the onset of vortex shedding in flow past variously shaped bodies. *J. Fluid Mech.*, **182**, 23–45.

JAMESON, A. 1988. Aerodynamic design via control theory. *J. of Scientific Comput.*, **3**, 233–260.

JAUVTIS, N., & WILLIAMSON, H.K. 2003. Vortex-induced vibration of a cylinder with two degrees of freedom. *Journal of Fluids and Structures*, **17**, (7) 1035–1042.

KARNIADAKIS, G. E., & SHERWIN, S. J. 2005. *Spectral/hp Element Methods for Computational Fluid Dynamics*. Oxford-UK: Oxford University Press.

KARNIADAKIS, G. E., ISRAELI, M., & ORSZAG, S. A. 1991. High-order splitting methods for the incompressible Navier–Stokes equations. *Journal of Computational Physics*, **97**, 414–443.

KIM, J., & BEWLEY, T. R. 2007. A linear systems approach to flow control. *Annu. Rev. Fluid Mech.*, **39**, 383–417.

LI, L., SHERWIN S. J., & BEARMAN, P. W. 2002. A moving frame of reference algorithm for fluid-structure interaction of rotating and translating bodies. *Int. J. Numer. Meth. Fluids*, **38**, 187–206.

MAO, X. 2015. Sensitivity of forces to wall transpiration in flow past an aerofoil. *The royal society*, **471**.

MAO, X., BLACKBURN, H. M., & SHERWIN, S. J. 2013. Calculation of global optimal initial and boundary perturbations for the linearised incompressible Navier–Stokes equations. *J. Comput. Phys.*, **235**, 258–273.

Marquet, O., Sipp, D., & Jacquin, L. 2008. Sensitivity analysis and passive control of cylinder flow. *J. Fluid Mech.*, **615**, 221–252.

Meliga, P., & Chomaz, J. 2011. An asymptotic expansion for the vortex-induced vibrations of a circular cylinder. *Journal of Fluid Mechanic*, **671**, 137–167.

Meliga, P., Boujo, E., Pujals, G., & Gallaire, F. 2014. Sensitivity of aerodynamic forces in laminar and turbulent flow past a square cylinder. *Phys. Fluids*, **26**, 104101.

Meliga, P, Boujo, E., Meldi, M., & Gallaire, F. 2018. Revisiting the drag reduction problem using adjoint-based distributed forcing of laminar and turbulent flows over a circular cylinder. *European J. of Mech. - B/Fluids*, **72**, 123–134.

Mittal, S., & Singh, S. 2005. Vortex-induced vibrations at subcritical *Re*. *J. of Fluid Mech.*, **534**, 185–194.

Navrose, & Mittal, S. 2016. Lock-in in vortex-induced vibration. *Journal of Fluid Mechanic*, **794**, 565–594.

Negi, P., Hanifi, A., & Henningson, D. S. 2019. Global Stability of rigid-body-motion fluid-structure-interaction problems. *Report at TRITA-SCI-RAP 2019:007.*

Newmark, N. M. 1959. A method of computation for structural dynamics. *Journal of the Engineering Mechanics Division of ASCE*, **85**, 67–94.

Pendlebury, E. D. 1955. General perturbation theory in neutronics. *Proc. Phys. Soc.*, **68**, 474–481.

Pfister, J.L., Marquet, O., & Carini, M. 2019. Linear stability analysis of strongly coupled fluid–structure problems with the Arbitrary-Lagrangian–Eulerian method. *Comput. Methods Appl. Mech. Engrg.*, **17**, (7) 663–689.

Pironneau, O. 1974. On optimum design in fluid mechanics. *J. Fluid Mech.*, **64**, 97–110.

Provansal, M., Mathis, C., & Boyer, L. 1987. The Benard-Von Kàrman instability : an experimental study near the threshold. *Journal of Fluid Mechanics*, **182**, 1–22.

Saad, Y. 1992. *Numerical Methods for Large Eigenvalue Problems*. Manchester, UK: Manchester University Press.

Schmid, P.J. 2007. Nonmodal stability theory. *Annu. Rev. Fluid Mech.*, **39**, 129–162.

Sreenivasan, K. R., Strykowski, P. J., & Olinger, D. J. 1987. Hopf bifurcation, Landau equation, and vortex shedding behind circular cylinders. *In Forum on Unsteady Flow Separation (ed. K. N. Ghia), p. 1. ASME FED vol. 52.*

Strykowski, P. J., & Sreenivasan, K. R. 1990. On the formation and suppression of vortex 'shedding' at low Reynolds number. *J. Fluid Mech.*, **218**, 71–107.

Trefethen, L. N., Trefethen, A. N., Reddy, S. C., & Driscoll, T. A. 1993. Hydrodynamic stability without eigenvalues. *Science*, **261**, 578–584.

Williamson, C. H. K. 1989. Oblique and parallel modes of vortex shedding in the wake of a circular cylinder at low Reynolds number. *J. Fluid Mech.*, **206**, 579–627.

Yao, W., & Jaiman, R. K. 2017. Model reduction and mechanism for the vortex-induced vibrations of bluff bodies. *J. of Fluid Mech.*, **827**, 357–393.

Ye, T., Mittal, S., Udaykumar, H. S., & Shyy, W. 1999. An accurate Cartesian grid method for viscous incompressible flows with complex immersed boundaries. *J. Comput. Phys.*, **156**, 209–240.

Zhang, W., Li, X., Ye, Z., & Jiang, Y. 2015. Mechanism of frequency lock-in in vortex-induced vibrations at low Reynolds numbers. *Journal of Fluid Mechanic*, **783**, 72–102.

Zienkiewicz, O. C., & Taylor, R. L. 2000. *The Finite Element Method. Volume 1: the basis.* 5^{th} edition ed. Butterworth-Heinemann Stoneham.

Appendix

A

Numerical methods

This chapter present a concise description of the numerical method employed to solve the Navier-Stokes system in this thesis. Besides that, we describe the numerical method to integrate the mass-spring-damper system in time.

A.1 The Spectral/*hp* Element Method

In this thesis, the numerical simulations are performed by employing the Spectral Element Method/*hp* (Karniadakis & Sherwin, 2005), which is a high-order method. To obtain a numerical solution by a computational algorithm, the system of partial differential equations composed of eqs. (2.3) must be discretized. The Spectral/*hp* Element Method is a discretization scheme derived from the Finite Element Method and the classical Spectral Method. From the Finite Element Method, it inherits the basic idea of subdividing the domain Ω into a set of juxtaposed subdomains known as elements Ω_e, and then construct the approximate solution of the equations from a sequence of local approximations defined in each element. These local approximations consist of linear combinations of functions that belong to a predefined set called base functions. Certain constraints are imposed to the base functions to ensure some degree of continuity in the global approximation in Ω. Usually, low order functions such as linear or quadratic polynomials are used as base functions and the solution converges through refinement of the subdivision of the Ω domain. This procedure is called mesh refinement is also known as h-refinement, since the letter h is usually employed to refer to the characteristic length of the mesh elements edges.

The classical Spectral Method employs a high-order basis of functions to approximate the solution of the differential equations in the entire domain, without making use of any spatial discretization. In this case, convergence is achieved by increasing the order of the approximation functions. This is known procedure as p-refinement, since p is usually employed to denote the degree of the polynomial of the base function.

The Spectral/hp Element Method uses the characteristic functions of the classical Spectral Method in the Finite Element Method formulation, thus combining the advantages of the geometric flexibility of the Finite Elements with the high accuracy of the classical Spectral Method. Therefore, convergence of the solution can be achieved through the refinement of the mesh (h convergence) or by increasing the order of the functions used as basis (p convergence), so the method name hp. This method is especially appropriate for simulations involving complex geometries and that require high accuracy. For this type of problem, the main advantage of the Spectral/hp Element Method is a lower computational effort when compared to low-order methods. In this sense, it is understood that the use of such methods in problems that are not yet fully solved in the literature may represent an advantage, since the influence of numerical errors is minimized. The code that is used in this research project employs Jacobi polynomials as basis of functions.

A.1.1 Weighted Residues Method and Galerkin Formulation

The idea of solving a set of partial differential equations in a spacial domain Ω is to find an approximation of the solution that satisfies a finite number of conditions. The choice of conditions that must be satisfied defines the numerical method. Analogous to the Finite Element Method, the Spectral/hp Element Method uses the weighted residues method to specify these conditions. This method can be described by considering a linear equation in a Ω domain denoted by:

$$\mathbb{L}(u) = 0, \tag{A.1}$$

Subject to appropriate initial and boundary conditions. The approximate solution sought has the form:

$$u^{\delta}(\mathbf{x}, t) = u_0(\mathbf{x}, t) + \sum_{j=1}^{N_{\text{dof}}} \hat{u}_j(t)\mathbf{\Phi}_j(\mathbf{x}), \tag{A.2}$$

where $\mathbf{\Phi}_j(\mathbf{x})$ are analytic functions called expansion functions, $\hat{u}_j(t)$ are the N_{dof} unknown coefficients and $u_0(\mathbf{x}, t)$ is chosen to satisfy the initial and boundary conditions. The functions $\mathbf{\Phi}_j(\mathbf{x})$ must satisfy homogeneous boundary conditions, i.e., they must be zero at the boundaries where Dirichlet conditions are imposed, since these boundary conditions are satisfied by $u_0(\mathbf{x}, t)$. Replacing the approximation (A.2) in (A.1) provides a non-zero residue, R:

$$\mathbb{L}(u^{\delta}) = R(u^{\delta}). \tag{A.3}$$

To obtain a unique form to determine the coefficients $\hat{u}_j(t)$, a constraint must be imposed on the residue R, so (A.3) is reduced to a system of ordinary differential equations in

$\hat{u}_j(t)$. If the original equation (A.1) is time independent, then the coefficients $\hat{u}_j$ can be determined directly from the solution of a system of algebraic equations.

The weighted residue method consists on imposing a constraint in R as the internal product of the residue with respect to an arbitrary *test function* (or *weight*) being zero. So,

$$(v(\mathbf{x}), R) = 0, \tag{A.4}$$

in which the function $v(\mathbf{x})$ is the test function and the internal product (f, g) over the domain Ω is defined as:

$$(f, g) = \int_\Omega f(\mathbf{x})g(\mathbf{x})\,\mathrm{d}\mathbf{x}. \tag{A.5}$$

If (A.4) is true for all $v(\mathbf{x})$, the approximation u^δ is exact. We relax this condition by choosing $v(\mathbf{x})$ to be represented by an arbitrary linear combination of a finite set of known functions,

$$v(\mathbf{x}) = \sum_{i=1}^{N_{\mathrm{dof}}} a_i v_i(\mathbf{x}), \tag{A.6}$$

where the coefficients a_i are arbitrary and $v_i(\mathbf{x})$ are know functions. Substituting (A.6) and (A.3) into (A.4) and using the definition (A.5), leads to

$$\int_\Omega \sum_{i=1}^{N_{\mathrm{dof}}} a_i v_i(\mathbf{x}) \mathbb{L}(u^\delta)\mathrm{d}\mathbf{x} = 0. \tag{A.7}$$

If we assume that $\mathbb{L}$ is time independent and use the approximation expression (A.2) in (A.7) explicitly, we obtain:

$$\int_\Omega \sum_{i=1}^{N_{\mathrm{dof}}} a_i v_i(\mathbf{x}) \mathbb{L}\left[u_0(\mathbf{x}) + \sum_{j=1}^{N_{\mathrm{dof}}} \hat{u}_j \boldsymbol{\Phi}_j(\mathbf{x})\right]\mathrm{d}\mathbf{x} =$$

$$\sum_{i=1}^{N_{\mathrm{dof}}} a_i \left\{\int_\Omega v_i(\mathbf{x})\mathbb{L}[u_0(\mathbf{x})]\mathrm{d}\mathbf{x} + \int_\Omega v_i(\mathbf{x})\mathbb{L}\left[\sum_{j=1}^{N_{\mathrm{dof}}} \hat{u}_j \boldsymbol{\Phi}_j(\mathbf{x})\right]\mathrm{d}\mathbf{x}\right\} = 0.$$

Since a_i is arbitrary, we have a set of algebraic equations which is sufficient to determine $\hat{u}_j$:

$$\sum_{j=1}^{N_{\mathrm{dof}}} \left\{\hat{u}_j \int_\Omega v_i(\mathbf{x})\mathbb{L}[\boldsymbol{\Phi}_j(\mathbf{x})]\right\}\mathrm{d}\mathbf{x} = -\int_\Omega v_i(\mathbf{x})\mathbb{L}[u_0(\mathbf{x})]\mathrm{d}\mathbf{x}, \qquad i = 1, 2, \ldots, N_{\mathrm{dof}}.$$

This set of equations can be written in matrix form

$$\mathbf{A}\hat{\mathbf{u}} = \mathbf{b}, \tag{A.8}$$

in which $\hat{\mathbf{u}}$ is the vector with the coefficients $\hat{u}_j$, the matrix components $\mathbf{A}$ are

$$A_{ij} = \int_\Omega v_i(\mathbf{x})\mathbb{L}[\mathbf{\Phi}_j(\mathbf{x})]\mathrm{d}\mathbf{x},$$

and the vector $\mathbf{b}$ is given by

$$b_i = -\int_\Omega v_i(\mathbf{x})\mathbb{L}[u_0(\mathbf{x})]\mathrm{d}\mathbf{x}.$$

In the weighted residual method, the choice of the expansion function $\mathbf{\Phi}_i(\mathbf{x})$ and test function $v_j(\mathbf{x})$ determine the numerical scheme. The Spectral/*hp* Element Method uses the Galerkin formulation, in which the set of test functions is equal to the set of expansion functions, i.e., $v_j(\mathbf{x}) = \mathbf{\Phi}_j(\mathbf{x})$. The Galerkin formulation has some significant mathematical properties, such as solution uniqueness, orthogonality of the error with respect of the solution space, energy norm test, and minimization of the error in the energy norm (for details, see Karniadakis & Sherwin, 2005).

A.1.2 Fundamental Concepts of the Spectral/*hp* Element Method discretization

In this section, we describe the two-dimensional base expansions that will be employed, as well as the procedures to perform the differentiation and integration necessary to evaluate the $\mathbf{A}$ matrix and the right side of (A.8), the vector $\mathbf{b}$. For details about the bases used in a three-dimensional discretization, please refer to Karniadakis & Sherwin (2005).

The base expansions are based on a one-dimensional modal basis. This basis is expressed as:

$$\phi_p(\xi) = \psi_p^a(\xi) = \begin{cases} \dfrac{1-\xi}{2}, & p = 0, \\ \left(\dfrac{1-\xi}{2}\right)\left(\dfrac{1+\xi}{2}\right)\mathcal{P}_{p-1}^{1,1}(\xi), & 0 < p < P, \\ \dfrac{1+\xi}{2}, & p = P, \end{cases} \tag{A.9}$$

where ξ is the one-dimensional coordinate, which ranges from -1 to 1, and $\mathcal{P}_p^{1,1}(\xi)$ is Jacobi polynomial of order p. This polynomial has the property of being orthogonal to all polynomials of order less than p of the same basis when integrated with respect to $(1-\xi)(1+\xi)$. For details on the definition of these polynomials, see Karniadakis & Sherwin (2005).

Figure 62: Standard regions for elements (a) quadrilaterals, and (b) triangular in terms of Cartesian coordinates (ξ_1, ξ_2). Extracted from Karniadakis & Sherwin (2005).

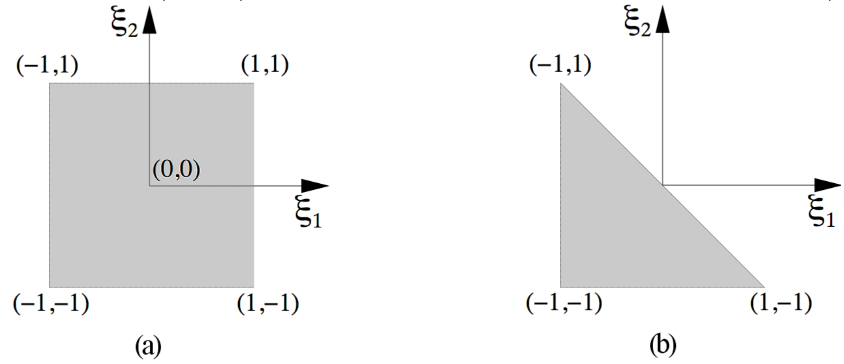

Figure 63: Two-dimensional base expansion for a quadrilateral element of order $P = 4$, constructed from a product of two one-dimensional tensor expansions. Extracted from Karniadakis & Sherwin (2005).

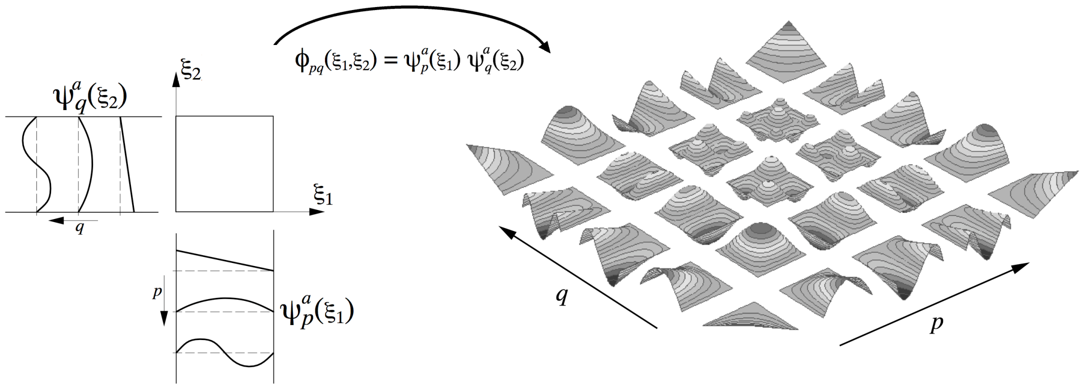

We define the standard two-dimensional region $\mathcal{Q}^2$ for quadrilateral elements as

$$\Omega_{\text{st}} = \mathcal{Q}^2 = \{-1 \leqslant \xi_1, \xi_2 \leqslant 1\}\,.$$

This region is trivially defined by the standard Cartesian coordinate system (figure 62(a)), then it is easy to construct a two-dimensional base with a one-dimensional base product (A.9), which can be understood as an one-dimensional tensor in each Cartesian direction, i.e.,

$$\phi_{pq}\left(\xi_1, \xi_2\right) = \psi_p^a(\xi_1)\psi_q^a(\xi_2), \qquad 0 \leqslant p, q, \;\; p \leqslant P, \;\; q \leqslant Q. \tag{A.10}$$

We note that the polynomial order of the multidimensional expansions can differ in each coordinate direction, i.e., P and Q can be different. However, in this project the same order in both directions will always be used. Figure 63 shows the base expansion for polynomial order $P = 4$.

An important property of modal expansion (A.10) is that it can be decomposed in *boundary* and *interior* modes. Boundary modes are all modes that are non zero at the boundaries of the standard region, while interior modes are those that are zero at the boundaries. This property is particularly convenient when a C^0 global base expansion is required, since the global expansion can be obtained from the local expansions by matching the boundary modes. In a two-dimensional expansion, the boundary modes are the vertex modes, which are those that have unitary magnitude at a vertex and are zero in all other vertices, and the edge modes, which are the modes that have support along one edge and have null value on all other edges and vertices.

In order to apply the same ideas to triangles, the expansion concept of the tensor product is generalized. This is possible if a *collapsed* coordinate system is used to represent the standard region Ω_{St} for triangles. This coordinate system is collapsed from the mapping of a square to a triangle, making two adjacent vertices of the square match. The resulting standard region $\mathcal{T}^2$ is shown in the figure 62(b), and can be expressed as

$$\Omega_{\mathrm{st}} = \mathcal{T}^2 = \left\{ (\xi_1, \xi_2) | -1 \leqslant \xi_1, \xi_2, \quad \xi_1 + \xi_2 \leqslant 0 \right\}.$$

To develop a suitable tensor base for this standard region, we need to adopt a coordinate system whose local coordinates have independent boundaries on $\mathcal{T}^2$. An appropriate coordinate system is defined by the transformation,

$$\begin{aligned} \eta_1 &= 2\frac{1+\xi_1}{1-\xi_2} - 1, \\ \eta_2 &= \xi_2, \end{aligned} \tag{A.11}$$

with inverse transformation:

$$\begin{aligned} \xi_1 &= \frac{(1+\eta_1)(1-\eta_2)}{2} - 1, \\ \xi_2 &= \eta_2. \end{aligned}$$

This new coordinate system (η_1, η_2) defines a standard triangular region by

$$\mathcal{T}^2 = \left\{ (\eta_1, \eta_2) | -1 \leqslant \eta_1, \eta_2 \leqslant 1 \right\},$$

which is identical to the definition of the quadrilateral standard region of the Cartesian coordinates. Using the collapsed coordinate system, the base expansions for a triangular region are defined as

$$\phi_{pq}(\xi_1, \xi_2) = \psi_p^a(\eta_1)\psi_{pq}^b(\eta_2), \tag{A.12}$$

Figure 64: Two-dimensional base expansion for a triangular element of order $P = 4$, constructed from a tensor product of two modified main functions $\psi^a_p(\eta_1)$ e $\psi^b_{pq}(\eta_2)$. Extracted from Karniadakis & Sherwin (2005).

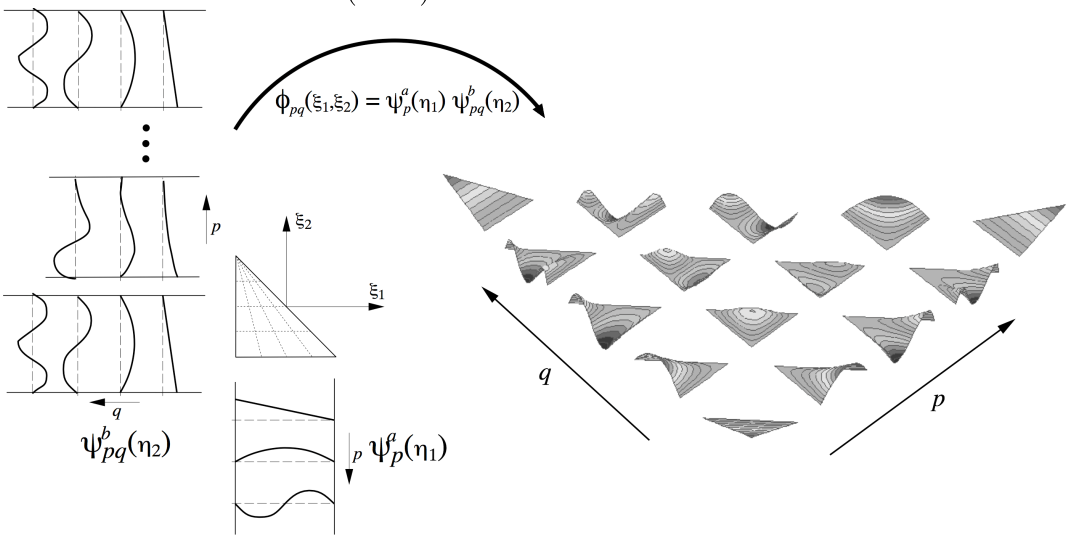

where the one-dimensional base expansion modified $\psi^b_{pq}(\eta)$ is given by:

$$\psi^b_{pq}(\eta) = \begin{cases} \psi^a_q(\eta), & p = 0,\ 0 \leqslant q \leqslant Q, \\ \left(\dfrac{1-\eta}{2}\right)^{p+1}, & 0 < p < P,\ q = 0, \\ \left(\dfrac{1-\eta}{2}\right)^{p+1} \dfrac{1+\eta}{2} \mathcal{P}^{2p+1,1}_{q-1}(\eta), & 0 < p < P,\ 0 < q < Q \\ \psi^a_q(\eta), & p = P,\ 0 \leqslant q \leqslant Q. \end{cases} \tag{A.13}$$

This expansion base is illustrated in Figure 64. Like the expansion base (A.10) used for quadrilateral elements, (A.12) can also be decomposed into boundary and interior modes.

The advantages of using tensor bases are due to decoupling of the expansion functions in each direction ξ_1 and ξ_2 (η_1 and η_2 to triangles). Therefore, techniques such as *sum-factorisation* (Karniadakis & Sherwin, 2005) can be applied in basic method operations, resulting in a significant gain in computational efficiency (Carmo, 2009).

A.1.2.1 Global Operations

The global domain Ω is decomposed into elemental subdomains Ω^e which can then be mapped to standard regions, in which a base expansion is defined. The Galerkin formulation requires that integration and differentiation are done at elementary level and then the contribution of each element is added during the assembly of the global matrix system.

In this work, the Gaussian quadrature will be employed to perform the numerical integration with high precision, consistent with the exact integration for polynomials. Gaussian quadrature defines a series of integration points on which the values of the function that is being integrated must be known at certain points, which are called quadrature points. Therefore, when we differentiate a function, we typically need the value of the derivative at the quadrature points.

In order to obtain the global solution in the Ω domain, the contribution of each element must be considered taking into account that the global approximation must be C^0 continuous. This is achieved by means of the final system assembly, which is in general the standard procedure used in the Finite Element Method(see Zienkiewicz & Taylor, 2000). Each global degree of freedom corresponds to one or more local degree of freedoms, and each local degree of freedom corresponds to only one global degree of freedom. The process of global assembly consists in summing equations generated for the local degrees of freedom corresponding to a single global degree of freedom. Thus as a global system with dimensions equal to the number of global degrees of freedom is produced. Once the global system is solved, the value of each global degree of freedom will correspond to the value of the local degrees of freedom associated.

A.1.3 Application in Computational Fluid Dynamics

The concepts presented in this appendix have been used to discretize the system (2.3) in space. To advance these equations in time, a rigorous stable time discretization scheme was employed (Karniadakis *et al.* , 1991). In this scheme, each time step is subdivided into three steps, and the solution of the discretized Navier-Stokes equation is advanced from the time step n to the time step $n+1$ as follows:

$$\frac{\check{\mathbf{u}} - \sum_{q=0}^{J_i-1} \alpha_q \mathbf{u}^{n-q}}{\Delta t} = \sum_{q=0}^{J_e-1} \beta_q \mathbf{N}(\mathbf{u}^{n-q}) \tag{A.14}$$

$$\nabla^2 \bar{p}^{n+1} = \nabla \cdot \left(\frac{\check{\mathbf{u}}}{\Delta t} \right) \tag{A.15}$$

$$\frac{\gamma_0 \mathbf{u}^{n+1} - \check{\mathbf{u}}}{\Delta t} + \nabla \bar{p}^{n+1} = \frac{1}{Re} \nabla^2 \mathbf{u}^{n+1} \tag{A.16}$$

where $\mathbf{N} = \mathbf{u}.\nabla\mathbf{u}$ denotes the advection operator, which is explicitly treated due its nonlinearity, J_i is the integration order for implicit terms and J_e is the integration order for explicit terms. The values of the coefficients γ_0, α_q and β_q for integration up to third order are given in the Table A.1.

This scheme requires that boundary conditions are defined for both velocity and pressure. High order Neumann conditions for pressure are imposed on (A.15) at the boundaries where Dirichlet boundary conditions are employed for the velocity. For these high-order

Table A.1: Stiffly-stable splitting scheme coefficients. Extracted from Karniadakis *et al.* (1991).

Coefficients	1^a order	2^a order	3^a order
γ_0	1	3/2	11/6
α_0	1	2	3
α_1	0	$-1/2$	$-3/2$
α_2	0	0	1/3
β_0	1	2	3
β_1	0	-1	-3
β_2	0	0	1

conditions we used a modified version of the expression given in Karniadakis *et al.* (1991) as below:

$$\frac{\partial \bar{p}^{n+1}}{\partial n} = \mathbf{n} \cdot \left\{ \sum_{q=0}^{J_e-1} \beta_q \left[\mathbf{N}(\mathbf{u}^{n-q}) - \frac{1}{Re}(\nabla \times (\nabla \times \mathbf{u}^{n-q})) \right] \right\} \tag{A.17}$$

The coefficients β_q in (A.17) are also given in the table A.1.

A.2 Newmark-*beta* solver

The interpolation equations for the Newmark-β scheme are given by:

$$\mathbf{y}^{n+1} = \mathbf{y}^n + \delta t \dot{\mathbf{y}}^n + \frac{\delta t^2}{2}\left[(1-2\beta)\,\ddot{\mathbf{y}}^n + 2\beta \ddot{\mathbf{y}}^{n+1}\right] \tag{A.18}$$

$$\dot{\mathbf{y}}^{n+1} = \dot{\mathbf{y}}^n + \delta t\left[(1-\gamma)\,\ddot{\mathbf{y}}^n + \gamma \ddot{\mathbf{y}}^{n+1}\right] \tag{A.19}$$

where the δt is the time step, β and γ are parameters that can be adjusted for accuracy order and stability of this numerical method. Using the approximations (A.18)-(A.19) and substituting in the the mass-spring-damper system (5.3), we have:

$$\mathbf{y}^{n+1} = \mathbf{y}^n + \delta t \dot{\mathbf{y}}^n + \frac{\delta t^2}{4}\left[-\frac{C^*}{M^*}\dot{\mathbf{y}}^n + \frac{K^*}{M^*}\mathbf{y} + \frac{\mathbf{F}^*}{M^*} + \frac{1}{2}\ddot{\mathbf{y}}^{n+1} \right], \tag{A.20}$$

$$\dot{\mathbf{y}}^{n+1} = \dot{\mathbf{y}}^n + \delta t\left[\frac{1}{2}\ddot{\mathbf{y}}^n + \frac{1}{2}\ddot{\mathbf{y}}^{n+1} \right]. \tag{A.21}$$

The accuracy of the method depends on the parameters (β, γ). In this thesis we used $(\beta, \gamma) = (1/4, 1/2)$. For these values, the Newmark scheme is of second order. In this case, the acceleration is constant in the interval $t \in [t_n, t_{n+1}]$.

A.3 Fictitious mass-damping method

For low values of M^* and C^* numerical instabilities may occur. So in these cases, this work uses the fictitious mass-damping method, introduced by Baek & Karniadakis (2012). In this method, a fictitious mass, M_f^*, times the acceleration and a fictitious damping, C_f^*, times the velocity are added to both sides of the structure equation:

$$\left(M^* + M_f^*\right) \ddot{\mathbf{y}} + \left(C + C_f^*\right) \dot{\mathbf{y}} + K^* \mathbf{y} = \mathbf{F} + M_f^* \ddot{\mathbf{y}} + C_f^* \dot{\mathbf{y}}. \tag{A.22}$$

More details of this method are found in Baek & Karniadakis (2012), where convergence analyses for coupled fluid and structure equations are presented.

Appendix

B

Solution of the generalized eigenvalue problem

In general, the solution of an eigenvalue problem can be obtained by means of classical techniques, such as the QZ algorithm (Golub & Van Loan, 1996), or by projection method, like the methods based on Krylov subspace. The first approach has the advantage of providing the full spectrum of eigenvalues, but has a high computational cost. This last fact makes it impractical the use in problems with many degrees of freedom, as is the case of flows with moderate Reynolds number occurring in complex domains. The second approach is iterative and allows focusing on a particular region of the spectrum, thus having an adjustable computational cost, depending on the precision and on number of eigenvalues that are sought. In general, for stability, receptivity and sensitivity analysis we require the leading eigenvalues only. Therefore, the projection techniques are more suitable for our applications.

The basic idea of the projection methods is to obtain an approximation of an eigenvalue using a specified smaller subspace, with some conditions to make the procedure feasible. After the projection, an eigenvalue problem of smaller size is obtained.

The projection method approximates the exact eigenvector $\mathbf{u}$ by a vector $\tilde{\mathbf{u}}$ that belongs to a subspace $\mathcal{K}$. If the subspace has dimension m, there will be m additional degrees of freedom, then it is necessary to define m conditions for a unique solution. This is done by imposing the Petrov-Galerkin condition, in which the residual vector must be perpendicular to some subspace $\mathcal{L}$, called the left subspace. In an orthogonal projection, $\mathcal{K} = \mathcal{L}$. In an oblique projection, $\mathcal{K} \neq \mathcal{L}$.

Normally we are interested in the least stable eigenvalues, so it is important to ensure that the approximation subspace contains the corresponding eigenvectors. This can be accomplished by taking a random initial vector $\mathbf{v}$, multiplying it by the matrix $\mathbf{A}$, and repeating this operation successively:

$$\mathcal{K}_m \equiv \text{span}\{\mathbf{v}, \mathbf{A}\mathbf{v}, \mathbf{A}^2\mathbf{v}, \ldots, \mathbf{A}^{m-1}\mathbf{v}\}.$$

The generated subspace is a Krylov subspace, $\mathcal{K}_m$, which is the subspace of all vectors in $\mathbb{C}^n$. $\mathbb{C}$ represents the set of complex numbers, which can be written as $\mathbf{x} = p(\mathbf{A})\mathbf{v}$, where p is a polynomial of degree less or equal to $m-1$. Among the methods of solving the eigenvalue problem based on subspaces of this type, we can cite the Arnoldi method and its variations, the Lanczos method for Hermitian matrices and the Lanczos method for non-Hermitian matrices (Saad, 1992). In this project, we will employ the Arnoldi method, which we shall outline below.

The method starts by constructing an orthogonal basis of a Krylov subspace $\mathcal{K}_m$. A variant of the method is:

Choose a vector $\mathbf{v}_1$ of unit norm.
for $j \leftarrow 1, m$ **do**
  $\mathbf{w}_j \leftarrow \mathbf{A}\mathbf{v}_j$ ▻ Compute the new vector of the subspace
  for $i \leftarrow 1, j$ **do**
    $h_{ij} \leftarrow (\mathbf{w}_j, \mathbf{v}_i)$
    $\mathbf{w}_j \leftarrow \mathbf{w}_j - h_{ij}\mathbf{v}_i$ ▻ Orthogonalization
  end for
  $h_{j+1,j} \leftarrow ||\mathbf{w}_j||_2$
  if $h_{j+1,j} = 0$ **then** ▻ Checks whether vector is linearly dependent
    break
  end if
  $\mathbf{v}_{j+1} \leftarrow \mathbf{w}_j / h_{j+1,j}$ ▻ Normalization
end for

The vectors of the matrix $\mathbf{V}_m = [\mathbf{v}_1, \mathbf{v}_2, \ldots, \mathbf{v}_m]$ form an orthonormal basis of $\mathcal{K}_m$ and the elements h_{ij} form a Hessenberg matrix $\mathbf{H}_m$. Since $\mathbf{e}_m$ is a vector of dimension m in the direction m,

$$\mathbf{A}\mathbf{V}_m = \mathbf{V}_m\mathbf{H}_m + h_{m+1,m}\mathbf{v}_{m+1}\mathbf{e}_m^H. \tag{B.1}$$

When $||\mathbf{w}_j|| = 0$, the algorithm stops because the vectors of the base have become linearly dependent. This means that the subspace $\mathcal{K}_j$ is invariant and the approximate eigenvalues are exact. Figure 65 helps to visualize the relationship between the dimensions of the matrices of eq. (B.1).

The approximate eigenvectors of $\mathbf{A}$ are called *Ritz eigenvectors* and are calculated by

$$\mathbf{u}_i^{(m)} = \mathbf{V}_m\mathbf{y}_i^{(m)}.$$

Figure 65: Schematic illustration of the arrays generated in the Arnoldi algorithm.

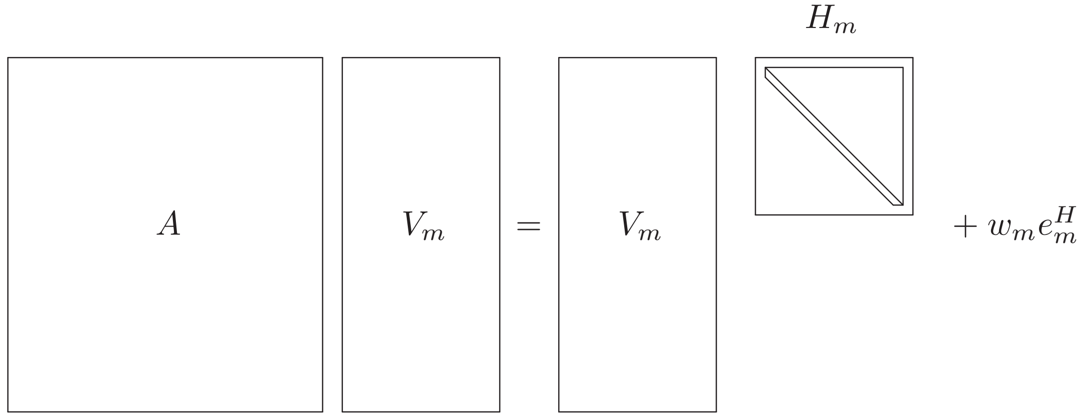

Only part of m eigenvalues will be good approximations, and the quality of these approximations usually grows with m. The residue of the method can be estimated using equation (B.1). We multiply all the terms on the right by $\mathbf{y}_i^{(m)}$, which is eigenvector of $\mathbf{H}_m$:

$$\begin{aligned}\mathbf{A}\mathbf{V}_m\mathbf{y}_i^{(m)} &= \mathbf{V}_m\mathbf{H}_m\mathbf{y}_i^{(m)} + h_{m+1,m}\mathbf{v}_{m+1}\mathbf{e}_m^H\mathbf{y}_i^{(m)} \\ &= \lambda_i^{(m)}\mathbf{V}_m\mathbf{H}_m\mathbf{y}_i^{(m)} + h_{m+1,m}\mathbf{v}_{m+1}\mathbf{e}_m^H\mathbf{y}_i^{(m)}.\end{aligned}$$

Therefore,

$$\mathbf{A}\mathbf{V}_m\mathbf{y}_i^{(m)} - \lambda_i^{(m)}\mathbf{V}_m\mathbf{H}_m\mathbf{y}_i^{(m)} = (\mathbf{A} - \lambda_i^{(m)}\mathbf{I})\mathbf{u}_i^{(m)} = h_{m+1,m}\mathbf{v}_{m+1}\mathbf{e}_m^H\mathbf{y}_i^{(m)}.$$

Taking the norm,

$$||(\mathbf{A} - \lambda_i^{(m)}\mathbf{I})\mathbf{u}_i^{(m)}||_2 = h_{m+1,m}|\mathbf{e}_m^H\mathbf{y}_i^{(m)}|.$$

The residue norm is equal to the last component of the eigenvector $\mathbf{y}_i^{(m)}$ multiplied by $h_{m+1,m}$.

Appendix

C

Meshes

In this appendix, we present the meshes employed in the calculations of this thesis. Figures are provided, along with general data like the number of elements and polynomial order employed. A mesh convergence analysis for the mesh employed to simulate the flow around a circular cylinder is also presented in section C.1.1

C.1 Circular cylinder

C.1.1 Mesh convergence analysis

A mesh convergence analysis was carried out for the flow around a fixed circular cylinder of diamater $D = 1$. The control parameters were: mesh discretization (number of elements), downstream lenght $x+$, upstream length $x-$ and vertical $y\pm$ length. The interpolation polynomial degree was also analyzed.

The boundary conditions used for the flow around a fixed cylinder were: no-slip boundary condition $\mathbf{u} = \mathbf{0}$ at the wall $\partial\Omega_w$; at the inflow ($\partial\Omega_i$) we imposed the Dirichlet condition $(u, v) = (1, 0)$; at the outflow ($\partial\Omega_o$) we applied the Neumann condition $\nabla\mathbf{u} \cdot \mathbf{n} = \mathbf{0}$ for the velocity field and Dirichlet $p = 0$ for the pressure. At inlet and at wall, Neumann high-order boundary condition was adopted for pressure (Karniadakis *et al.* , 1991). A second order stiffly-stable splitting scheme (described in A.1.3) was employed for time integration.

In the convergence analysis, the Strouhal number $St = f_{St}D/U_\infty$ (f_{St} is the vortex shedding frequency), the mean drag coefficient $\overline{C_d}$ and the RMS of the lift coefficient $C_{l_{RMS}}$ were evaluated. The numerical simulations were done for the following Reynolds numbers: $Re = 100$, $Re = 150$ and $Re = 200$.

We started by analyzing the effects of the mesh refinement in regions downstream and close to the cylinder. For these cases, seventh-degree polynomials were employed as basis function. The computational mesh was composed only of the quadrilateral elements. The length was $x+ = 45D$, $x- = 20D$ and $y \pm 20D$. Tables C.1 and C.2 present the number of elements (NE) in these respective regions. The meshes M1–M4 evaluate the refinement around to the cylinder. The meshes M5–M8 correspond to the refinement in the wake of the cylinder.

Table C.1: Mesh variation at $Re = 100$.

Mesh	NE	St	$C_{l_{RMS}}$	$\overline{C_d}$	Relative variation (%)
$M1$	421	0.16691	0.2295	1.3387	$[(C_{l_{RMS}})_{M1} - (C_{l_{RMS}})_{M2}] / (C_{l_{RMS}})_{M1} = 0.6$
$M2$	841	0.16614	0.2309	1.3420	$[(C_{l_{RMS}})_{M2} - (C_{l_{RMS}})_{M1}] / (C_{l_{RMS}})_{M2} = 0.17$
$M3$	1405	0.16615	0.2313	1.3433	$[(C_{l_{RMS}})_{M3} - (C_{l_{RMS}})_{M2}] / (C_{l_{RMS}})_{M3} = 0.17$
$M4$	2113	0.16615	0.2317	1.3439	
$M5$	224	0.16615	0.2314	1.3433	$[(C_{l_{RMS}})_{M5} - (C_{l_{RMS}})_{M6}] / (C_{l_{RMS}})_{M5} = 0$
$M6$	294	0.16615	0.2314	1.3433	$[(C_{l_{RMS}})_{M6} - (C_{l_{RMS}})_{M7}] / (C_{l_{RMS}})_{M6} = 0$
$M7$	364	0.16615	0.2314	1.3433	$[(C_{l_{RMS}})_{M7} - (C_{l_{RMS}})_{M8}] / (C_{l_{RMS}})_{M7} = 0$
$M8$	434	0.16615	0.2314	1.3433	

Table C.2: Mesh variation at $Re = 200$.

Mesh	NE	St	$C_{l_{RMS}}$	$\overline{C_d}$	Relative variation (%)
$M1$	421	0.19768	0.4802	1.3381	$[(C_{l_{RMS}})_{M1} - (C_{l_{RMS}})_{M2}] / (C_{l_{RMS}})_{M1} = 0.5$
$M2$	841	0.19768	0.4826	1.3413	$[(C_{l_{RMS}})_{M2} - (C_{l_{RMS}})_{M3}] / (C_{l_{RMS}})_{M2} = 0.17$
$M3$	1405	0.19768	0.4835	1.3427	$[(C_{l_{RMS}})_{M3} - (C_{l_{RMS}})_{M4}] / (C_{l_{RMS}})_{M3} = 0.04$
$M4$	2113	0.19768	0.4837	1.3433	
$M5$	224	0.19768	0.4841	1.3434	$[(C_{l_{RMS}})_{M5} - (C_{l_{RMS}})_{M6}] / (C_{l_{RMS}})_{M5} = 0.01$
$M6$	294	0.19768	0.4835	1.3428	$[(C_{l_{RMS}})_{M6} - (C_{l_{RMS}})_{M7}] / (C_{l_{RMS}})_{M6} = 0$
$M7$	364	0.19768	0.4835	1.3428	$[(C_{l_{RMS}})_{M7} - (C_{l_{RMS}})_{M8}] / (C_{l_{RMS}})_{M7} = 0$
$M8$	434	0.19768	0.4835	1.3428	

Tables C.1 and C.2 show the assessment of the dimensionless parameters with respect the number of elements close to the cylinder (meshes M1–M4). We noticed small variations for $Re = 100$ and $Re = 200$. From mesh M2 the variation is less than 0.2% in all cases. So the mesh M3 was judged to be suitable regarding the refinement close to the cylinder and will be used in the next simulations. With mesh refinement in the wake of the cylinder (meshes M5–M8), we observe for $Re = 100$ that the dimensionless parameters did not change. For $Re = 200$ (see Table C.2) from mesh M6 the parameters remained constant. Therefore, the mesh M6 can be considered a suitable mesh.

Using mesh M6, the interpolation polynomial degree was varied from 4 to 11 for a flow at $Re = 150$. The results are show in Table C.3, in which it is seen that the relative variation of the parameters for polynomial degree above 6 was less than 1%. Therefore, the polynomial degree 7 was considered adequate for the next simulations.

Tables C.4 and C.5 display the variations to upstream lenght $x-$ and in crossflow lenght $y\pm$. In all the cases, the relative variations of the dimensioneless parameters were less than 1%. So in the next numerical simulations, we employ $y\pm = \pm 25$ and $x- = 30$.

Table C.3: Polynomial degree interpolation − Re = 150.

Degree P	St	$\overline{C_d}$	$C_{l_{RMS}}$	Relative variation (%)
4	0.1792	1.3484	0.3876	$[(C_{l_{RMS}})_4 - (C_{l_{RMS}})_5] / (C_{l_{RMS}})_4 = 2.3$
5	0.1792	1.3327	0.3784	$[(C_{l_{RMS}})_5 - (C_{l_{RMS}})_6] / (C_{l_{RMS}})_6 = 1.5$
6	0.1792	1.3292	0.3723	$[(C_{l_{RMS}})_6 - (C_{l_{RMS}})_7] / (C_{l_{RMS}})_6 = 0.8$
7	0.1792	1.3247	0.3699	$[(C_{l_{RMS}})_7 - (C_{l_{RMS}})_8] / (C_{l_{RMS}})_7 = 0.6$
8	0.1792	1.3249	0.3674	$[(C_{l_{RMS}})_8 - (C_{l_{RMS}})_9] / (C_{l_{RMS}})_8 = 0.25$
9	0.1792	1.3247	0.3665	$[(C_{l_{RMS}})_9 - (C_{l_{RMS}})_{10}] / (C_{l_{RMS}})_9 = 0.16$
10	0.1792	1.3218	0.3659	$[(C_{l_{RMS}})_{10} - (C_{l_{RMS}})_{11}] / (C_{l_{RMS}})_{10} = 0.05$
11	0.1792	1.3218	0.3657	

Table C.4: Crossflow length variation.

Re	$y \pm /D$	St	$\overline{C_d}$	$C_{l_{RMS}}$
	20	0.16615	1.3464	0.2321
	25	0.16615	1.3433	0.2314
	30	0.16615	1.3423	0.2312
	20	0.1792	1.3448	0.4842
	25	0.1792	1.3428	0.4835
	30	0.1792	1.3419	0.4829

Table C.5: Upstream length variation.

Re	$x - /D$	St	$\overline{C_d}$	$C_{l_{RMS}}$
	20	0.16615	1.3428	0.2371
100	25	0.16615	1.3433	0.2361
	30	00.16615	1.3254	0.2348
	35	0.16615	1.3228	0.2342
	20	0.1792	1.3539	0.4874
200	25	0.1792	1.3469	0.4835
	30	0.1792	1.3428	0.4814
	35	0.1792	1.3407	0.4804

Figure 66 shows the maximum vorticity module during a cycle in various positions x_i. For each position x_i downstream to the cylinder, the vorticity along a parallel segment to the y-axis was extracted. These segments have length equal to 5 with center in $y = 0$, and contain 50 points. On each segment, the maximum value of the vorticity module along the segment was saved for each time-step. Next, the maximum value of this set (for each position x_i) was obtained. This process was applied for the downstream lengths: $x+ = 25$, $x+ = 35$ and $x+ = 60$. The results are shown in Figure 66, in which we can see that the maximal vorticity module does not present a relevant change for $x+ \geqslant 40$. Thus, $x+ = 45$ is considered sufficient.

Therefore, based in the convergence analysis the mesh M6 mesh using polynomial degree interpolation 7 was chosen. The distances of the inflow, lateral and outflow measured from the cylinder axis are equal to $x- = -25$, $y\pm = \pm 25$ e $x+ = 45$, respectively.

Figure 66: Convergence test for downstream length at $Re = 150$.

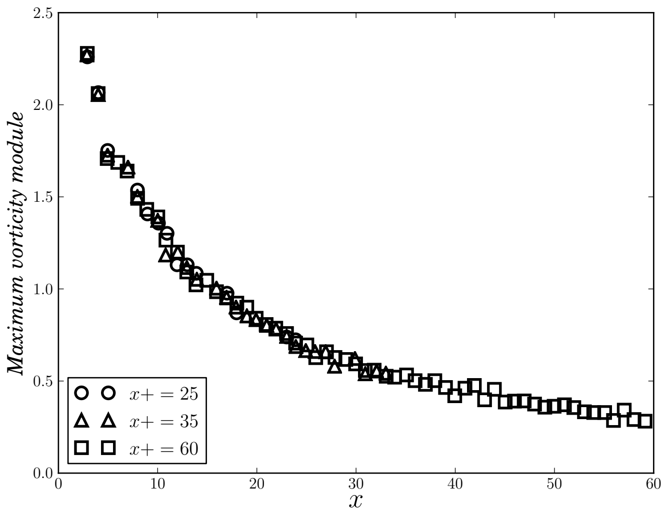

Figure 67: Final computational mesh with the polynomial interpolation of eleventh-degree.

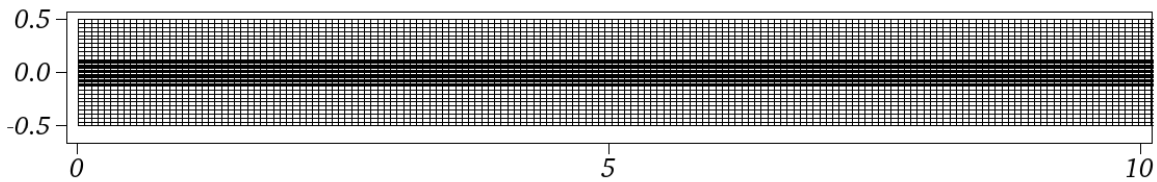

C.2 Channel

The two-dimensional channel was centred at $y = 0$. The height was $H = 1$ and the length was $L = 30$. The computational mesh was composed by 195 quadrilateral elements and eleventh-degree polynomials were employed as basis functions. Figure 67 shows a region ($0 \leqslant x \leqslant 10$) of the final computational mesh (with the polynomial interpolation) used to perform sensitivity calculations presented in the section 3.2.

C.3 Backward-facing step

In the section 3.3, the results were obtained for a backward-facing step with channel inflow of height $H = 1$ and the expansion with the height $2H$. The length of the channel inflow is $li = 10$ and the and expansion has length $lo = 50$. The mesh was built with 209 triangular elements and 220 quadrilateral elements. Tenth-degree polynomials were applied as basis functions. Figure 68 plots the computational mesh closer to the expansion region.

Figure 68: Final computational mesh with the polynomial interpolation of Tenth-degree in the region closer to the expansion.

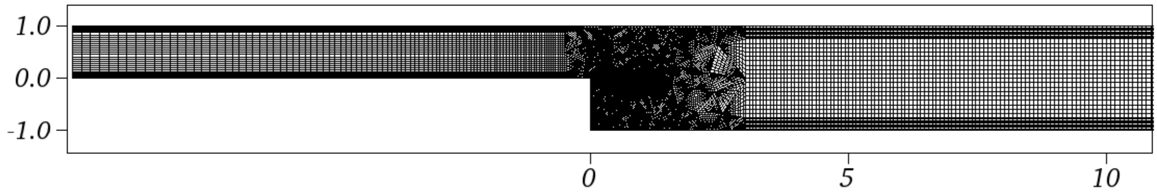

Figure 69: Final computational mesh with the polynomial interpolation of eleventh-degree in the region closer to the flat plat parallel to the flow direction.

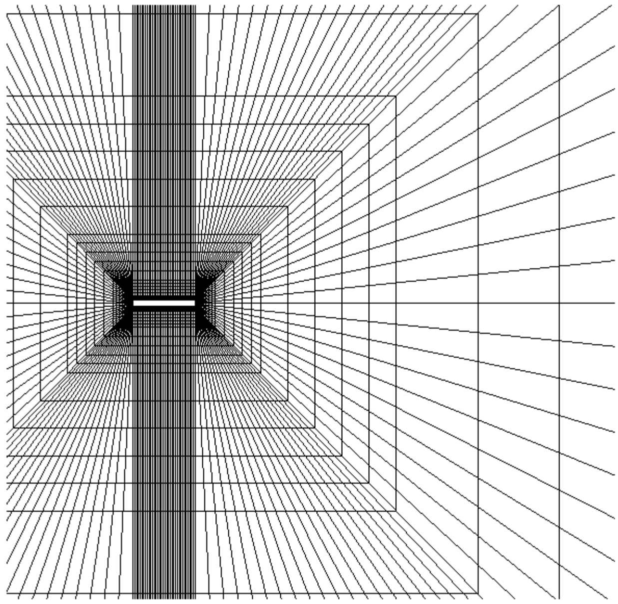

C.4 Flat plate

Figure 69 shows the mesh used in the sensitivity calculations reported in section 3.4 for the flow over a parallel flat plate with nondimensional length $D = 1$. The origin of the coordinate system is at the center of the flat plate. The two-dimensional domain has the following dimensions: $x+ = 30$ to downstream, $x- = -30$ to upstream and vertical $y\pm = 25$. The mesh was composed of the 413 quadrilateral elelements and polynomials of eleventh-degree were used in the spatial discretization.

C.5 Square cylinder

A square cylinder with side length $D = 1$ was the geometry used in the section 3.5. The origin of the coordinate system was at the center of the cylinder. The domain extended $x+ = 50$ to downstream, $x- = -35$ to upstream and $y\pm = 50$ in the cross-stream direction. The computational mesh was composed by 1059 quadrilateral elements and

Figure 70: Final computational mesh with the polynomial interpolation of eleventh-degree in the region closer to the square cylinder.

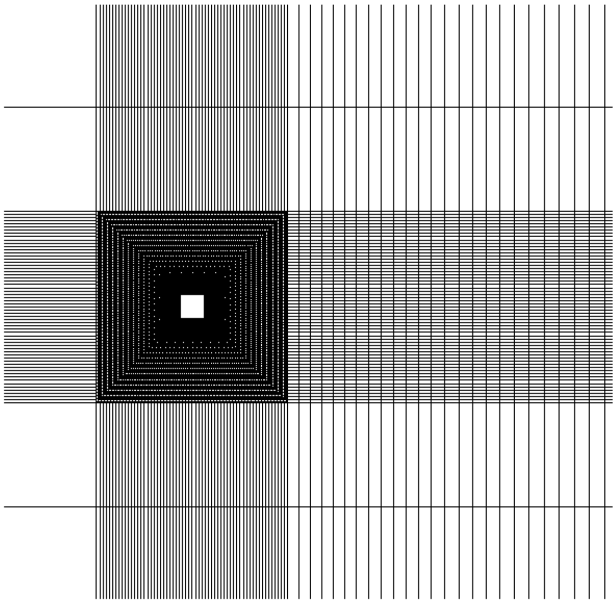

sixth-degree polynomials were employed as basis functions in the two-dimensional mesh which is plotted in Figure 70.

C.6 NACA 0012 airfoil

In this case, the origin of the coordinate system was at the leading edge of the airfoil, which had chord $c = 1$. The domain extended $x+ = 40$ to downstream, $x- = -40$ to upstream and $y\pm = 40$ in the cross-stream direction. The mesh was made with 423 triangular elements and 492 quadrilateral elements. Polynomials of the ninth-degree were used as base functions. Figure 71 displays the final mesh closer to the airfoil.

Figure 71: Final computational mesh with the polynomial interpolation of eleventh-degree in the region closer to the NACA 0012 airfoil.